How I Learned to Stop Worrying and Love Eclipsing Binaries

How I Learned to Stop Worrying and Love Eclipsing Binaries

A dissertation presented

by

Maxwell Cassady Moe

to

The Department of Astronomy

in partial fulfillment of the requirements

for the degree of

Doctor of Philosophy

in the subject of

Astronomy & Astrophysics

Harvard University

Cambridge, Massachusetts

July 2015

Dissertation Advisor: Dr. Rosanne Di Stefano Maxwell Cassady Moe

How I Learned to Stop Worrying and Love Eclipsing Binaries

Abstract

Relatively massive B-type stars with closely orbiting stellar companions can evolve to produce Type Ia supernovae, X-ray binaries, millisecond pulsars, mergers of neutron stars, gamma ray bursts, and sources of gravitational waves. However, the formation mechanism, intrinsic frequency, and evolutionary processes of B-type binaries are poorly understood. As of 2012, the binary statistics of massive stars had not been measured at low metallicities, extreme mass ratios, or intermediate orbital periods. This thesis utilizes large data sets of eclipsing binaries to measure the physical properties of B-type binaries in these previously unexplored portions of the parameter space. The updated binary statistics provide invaluable insight into the formation of massive stars and binaries as well as reliable initial conditions for population synthesis studies of binary star evolution.

We first compare the properties of B-type eclipsing binaries in our Milky Way Galaxy and the nearby Magellanic Cloud Galaxies. We model the eclipsing binary light curves and perform detailed Monte Carlo simulations to recover the intrinsic properties and distributions of the close binary population. We find the frequency, period distribution, and mass-ratio distribution of close B-type binaries do not significantly depend on metallicity or environment. These results indicate the formation of massive binaries are relatively insensitive to their chemical abundances or immediate surroundings.

Second, we search for low-mass eclipsing companions to massive B-type stars in the

Large Magellanic Cloud Galaxy. In addition to finding such extreme mass-ratio binaries, we serendipitously discover a new class of eclipsing binaries. Each system comprises a massive B-type star that is fully formed and a nascent low-mass companion that is still contracting toward its normal phase of evolution. The large low-mass secondaries discernibly reflect much of the light they intercept from the hot B-type stars, thereby producing sinusoidal variations in perceived brightness as they orbit. These nascent eclipsing binaries are embedded in the hearts of star-forming emission nebulae, and therefore provide a unique snapshot into the formation and evolution of massive binaries and stellar nurseries.

We next examine a large sample of B-type eclipsing binaries with intermediate orbital periods. To achieve such a task, we develop an automated pipeline to classify the eclipsing binaries, measure their physical properties from the observed light curves, and recover the intrinsic binary statistics by correcting for selection effects. We find the population of massive binaries at intermediate separations differ from those orbiting in close proximity. Close massive binaries favor small eccentricities and have correlated component masses, demonstrating they coevolved via competitive accretion during their formation in the circumbinary disk. Meanwhile, B-type binaries at slightly wider separations are born with large eccentricities and are weighted toward extreme mass ratios, indicating the components formed relatively independently and subsequently evolved to their current configurations via dynamical interactions. By using eclipsing binaries as accurate age indicators, we also reveal that the binary orbital eccentricities and the line-of-sight dust extinctions are anticorrelated with respect to time. These empirical relations provide robust constraints for tidal evolution in massive binaries and the evolution of the dust content in their surrounding environments.

Finally, we compile observations of early-type binaries identified via spectroscopy, eclipses, long-baseline interferometry, adaptive optics, lucky imaging, high-contrast photometry, and common proper motion. We combine the samples from the various surveys and correct for their respective selection effects to determine a comprehensive nature of the intrinsic binary statistics of massive stars. We find the probability distributions of primary mass, secondary mass, orbital period, and orbital eccentricity are all interrelated. These updated multiplicity statistics imply a greater frequency of low-mass X-ray binaries, millisecond pulsars, and Type Ia supernovae than previously predicted.

Contents

Acknowledgments

I am immensely grateful for my advisor, Rosanne Di Stefano. I thank her for sharing her passion of astrophysics with me and for inspiring me to understand the various aspects and nuances of binary stars. Her door was always open - even when it was physically closed. I thank her for all her advice, support, and encouragement over the years. I will always treasure our brain-storming sessions about new aspects of binary star evolution, sharing fun stories, and our heart-to-heart conversations that helped me to navigate my tenure as a graduate student. She is not only a great mentor in science, but also in life.

In addition, I thank Robert Kirshner, Josh Grindlay and Ramesh Narayan, who were also on my thesis advisory committee (TAC). I originally thought the TAC was to critique and evaluate my science. At my first TAC session, I was surprised to find they would advise me on *how* to do science, from what astrophysical questions are most important to consider, to how to share my work in the most efficient manner, to how to eventually get a job. I quickly realized their expertise, advise, and support on these subjects were invaluable, and I am most appreciative.

I thank all the other astronomers at the CfA, including Alicia Soderberg, Laura Chomiuk, Ryan Foley, Tassos Fragos, and Nancy Evans, who took the time to collaborate with me and discuss new ideas. I thank Peg Herlihy, Robb Scholten, Margaret Carroll, Debra Nickerson, Nina Zonnevylle, Mark Palmer, Lisa Catella, Donna Adams, Jean Collins for always greeting me with a smile and helping me to navigate all the logistics of graduate school. I also thank the CF help desk for helping me with all my computing resources, and Christine Pulliam for helping Rosanne and me to share our astronomical

discoveries to the public.

I thank all the astronomy graduate students for fun times at cookie hour, beer hour, Cambridge Commons, and just casual fun conversations in the hallway. I especially thank my officemates over the years, Dylan Nelson, Sukrit Ranjan, and Doug Ferrer. I also thank Ragnhild Lunnan, Tanmoy Laskar, Bekki Dawson, Yucong Zhu, Li Zeng, Ian Czekala, Courtney Dressing, Sarah Rugheimer, Nathan Sanders, Wen-fai Fong, Jack Steiner, Robert Harris, Paul Torrey, Bence Beky, Greg Snyder, Lauranne Lanz, Elisabeth Newton, Jason Dittman, Aaron Bray, Maria Drout, Chris Faesi, Meredith MacGregor, Lauren Woolsey, and Laura Schaefer.

I thank my parents, Ray and Lorraine Moe, for encouraging me to pursue my passion for astronomy. Even when I had my own car in high school to transport my telescope, they would still join me on trips to the mountains or the grasslands, just so they could stargaze with me into the wee hours of the night. I am eternally grateful for their long-term support and encouragement.

Finally, I am most appreciative for my wonderful wife, Miranda Moe. She has been my anchor and soulmate over the past eleven years. She always knows how to make me laugh and help me through the tough times. Her grace, passion, courage, and empathy she expresses with me, with her friends and family, and at her job are truly an inspiration. I thank her with all my heart.

For my binary star companion, Miranda.

Chapter 1

Introduction

On the evening of my senior prom in spring of 2004, I pointed upwards toward the night sky, a black canvas painted with a myriad of stars. I told my date for the evening, "See the brightest and bluest stars." I specifically pointed at Regulus in the heart of Leo the Lion and Spica in the hand of Virgo the Virgin. "Most of the brightest stars in the night sky are actually binary stars, two stars that orbit each other. They are destined to perform this cosmic dance and gaze into each others' eyes until death do they part." She smiled and blushed, obviously embarrassed by the romantic gesture. We then went inside and danced the night away. My partner that evening, who is now my wonderful wife, and I continue to dance and share our life journeys together.

1.1 Background and Motivation

Indeed, binary stars are ubiquitous (Abt 1983). Mizar and Alcor, a binary star system that forms the vertex of the handle in the Big Dipper, are barely distinguishable to the

unaided eye. The brightest star in the night sky, Sirius, looks like a single normal A-type main-sequence (MS) star with two times the mass of the sun. Upon closer inspection, we find it harbors a faint evolved white dwarf companion, i.e. the remnant core of a now-dead and originally more massive B-type MS star. The closest star to our solar system, Proxima Centauri, is a tertiary component that orbits the binary star Alpha Centauri. We see companions to low-mass M-dwarfs (Fischer & Marcy 1992), solar-type stars (Duquennoy & Mayor 1991), and massive O-type stars (Sana et al. 2012). The demon star Algol, which marks the eye of Medusa, periodically varies in brightness. We now know that Algol is an eclipsing binary star in which the two components pass in front of each other as viewed from earth in their highly inclined orbit. As we peer into the centers of the Orion, Lagoon, and Eagle Nebulae, we find these stellar nurseries are littered with baby stellar twins. And yes, even those bright spring-time stars, Regulus and Spica, contain stellar companions.

Binary stars cannot live forever. The more luminous and massive component eventually runs out of fuel and begins to expand toward its giant phase of evolution. It the binary companion is sufficiently nearby, it can affect the natural development of the more massive primary. Material can be stably transferred from the giant through an accretion disk onto the MS companion. The two components may instead merge into a single rejuvenated star. A third possibility is that the MS companion is engulfed by the outer atmosphere of the giant in a so-called common envelope. During this episode of binary evolution, the companion stirs up and ejects the envelope, spiraling inward before stabilizing into a short-period orbit with the hot remnant core of the giant.

If a component of a binary is an O-type or early-B star above ten solar masses, then it will eventually explode as a core collapse supernovae. In such an event, the companion

can be kicked out of its orbit as the recoiling core of the primary collapses into a neutron star or black hole. If the binary remains gravitationally bound, these physical processes repeat as the secondary star itself evolves toward the giant branch. During this second phase of binary evolution, however, one of the components is a compact remnant, i.e. a white dwarf, neutron star, or black hole. The various combinations and possibilities of binary star evolution are endless. In short, close binary stars can evolve to produce a plethora of astrophysical phenomena, including novae, blue stragglers, Type Ia supernovae, X-ray binaries, millisecond pulsars, neutron star mergers, and sources of gravitational waves (Paczyński 1971; Iben & Tutukov 1987; van den Heuvel 1984; Eggleton & Kiseleva-Eggleton 2002; Podsiadlowski et al. 2002).

When I began my thesis at Harvard University, I was particularly interested in the binary evolutionary pathways that produce Type Ia supernovae (SNe Ia). SNe Ia are the thermonuclear explosions of white dwarfs (WDs) in binary star systems (Whelan & Iben 1973). They are remarkable standardizeable candles in which we can accurately measure their distances based solely on the observed light curve properties (Phillips 1993). As precise distance indictors, SNe Ia have been utilized to discover the acceleration of the universe and probe the nature of dark energy (Schmidt et al. 1998).

Despite their importance for cosmology, we still do not know the progenitors of SNe Ia. What causes the WD to explode? Historically, the preferred theory has been the single-degenerate (SD) scenario in which a normal MS star or giant transfers some of its material to the WD (Whelan & Iben 1973). The WD increases in mass until it exceeds a critical limit, the so-called Chandrasekhar mass limit, at which point it can no longer gravitationally support itself via electron degeneracy pressure. The WD begins to collapse, eventually leading to a detonation that rapidly fuses most of the carbon and

oxygen in its interior into heavier elements like nickel and silicon.

An alternative theory that has been gaining momentum is the double-degenerate (DD) scenario (Webbink 1984). In this paradigm, two WDs coalesce via gravitational wave radiation, annihilating each other in a violent merger. It was originally believed that the merger of two WDs could not produce a normal-looking SNe Ia. However, updated numerical methods, nuclear reaction networks, and atomic opacities have produced models of merging WDs that match key features of the observed light curves and spectra (Pakmor et al. 2012). In fact, some double degenerate models predict that the detonation of a sub-Chandrasekhar mass WD may also produce normal SNe Ia (Woosley & Kasen 2011).

Several avenues have been explored to test the viability of these two theories. In the canonical SD scenario, for example, the donor companion is expected to be brightly shining before and after the explosion. Despite close inspection of pre-explosion images as well as deep observations of the centers of SN Ia remnants, there has not been a definitive detection of a MS or giant donor to a WD that produces a normal SN Ia. It is worth noting that a helium giant star was recently discovered to be the donor in SN 2012Z, an abnormal Type Iax supernovae (McCully et al. 2014). However, this subclass of SNe Ia are relatively faint, observationally rare in a magnitude-limited sample, and certainly not used as accurate distance indicators. Meanwhile, deep observations toward the center of the SN Ia remnant SNR 0509-67.5 certainly rule out the presence of a MS or giant companion (Schaefer & Pagnotta 2012). However, spectra of the light echoes, i.e. light from the supernova that has scattered off dust grains and is now reaching us, demonstrate that the supernova was not a normal SN Ia. Instead, the supernova that produced SNR 0509-67.5 belonged to the 1991T SN Ia subclass (Rest et al. 2008), which

are superluminous, intrinsically rare, and also not used as standard candles. In any case, when it comes to the search for companions, absence of evidence is not necessarily evidence of absence (Di Stefano et al. 2011).

Another method for testing these two theories derives from spectroscopic and photometric observations of the SN Ia explosion itself. In the SD scenario, the expanding shock wave slams into the MS or giant donor, possibly stripping some of its outer envelope. This interaction with the donor star and its gaseous circumstellar envelope may produce a signature at radio, optical, or X-ray wavelengths. Despite long observations of the closest SN Ia in decades, i.e. SN2011fe in the nearby galaxy M101, there was no detection of emission in X-rays (Margutti et al. 2012) or radio (Chomiuk et al. 2012). This indicates that SN2011fe exploded in a relatively low-density environment, opposite what you may expect if there was substantial amount of circumstellar material in the vicinity of the system. Nevertheless, optical spectroscopy of other supernovae has revealed variable sodium absorption lines (Patat et al. 2007), indicating interactions between the supernova shock wave and the surrounding circumstellar environment of a donor. Shortly after this detection, however, theories arose of how WD mergers in the DD scenario may also produce similar features (Shen et al. 2013). Recently, there were two *Nature* articles in the same issue on the early light curves of SNe Ia. One article found a small bump in the early light curve, indicating an interaction with a close companion in support of the SD scenario (Cao et al. 2015). Meanwhile, the other article did not find evidence for early rise times in the light curves of three different supernovae, providing support for the DD scenario (Olling et al. 2015). Indeed, all the caveats and various lines of inconclusive evidence when comparing observations to theories is what makes the SN Ia progenitor debate so challenging and exciting.

In any case, both SD and DD scenarios are likely to occur in nature. The question still remains: "Which evolutionary pathway is the dominant formation mechanism for producing normal Type Ia supernovae?" It therefore becomes necessary to estimate the rates of SNe Ia that derive from both of these channels, and compare these predictions to the observations. For example, observations of close WD binaries demonstrate the merger rate of Chandrasekhar-mass WDs is only 10% the observed SN Ia rate (Badenes & Maoz 2012). If you consider all WD binaries, including those with total systems masses well below the Chandrasekhar mass, then the sub-Chandrasekhar WD merger rate approaches the observed SN Ia rate. Estimating the SD SN Ia rate from observations proves more challenging. Some SD systems may be observed as recurrent novae, symbiotics, and/or supersoft X-ray emitters before they explode as SNe Ia. However, extrapolating the observed frequency of these systems to the rates of SNe Ia is quite unreliable as the duty cycles and timescales of these phases of binary evolution are highly uncertain (Di Stefano 2010).

One way of predicting the rates of both SD and DD SNe Ia is through binary population synthesis (BPS). BPS is a powerful Monte Carlo technique for modeling the evolution of a large population of stars and binaries. I personally divide BPS into two steps: (1) generating the initial conditions of a stellar population, and (2) evolving each system within the stellar population. The first step utilizes generating functions that describe the statistical properties and distributions of binary stars, e.g., the initial mass function, the binary star fraction, the orbital period distribution, the mass-ratio distribution, etc. In the second step, analytic prescriptions for physical processes, e.g. nuclear burning, binary mass transfer, tides, common envelope evolution, accretion onto WDs, etc., are incorporated to simulate the evolution of each system.

Various research groups have predicted the rates of SD and DD SNe Ia with BPS (see Nelemans et al. 2013 for an overview). They have also utilized their simulations to estimate the SN Ia delay time distribution. The delay time is simply the interval between the initial formation of the binary and the final explosion as an SN Ia. SNe Ia with small delay times $\tau \lesssim 1$ Gyr will explode in actively star-forming spiral galaxies. Meanwhile, binaries that wait $\tau \gtrsim 5$ Gyr to finally produce SNe Ia most likely occur in passive elliptical galaxies where star formation has since been quenched. In Fig. 1.1, I compare the observed SN Ia delay time distribution to the predicted SD and DD SN Ia delay time distribution based on six different studies as reported in Nelemans et al. (2013, see their Figs. 2-3). The error bars in the predicted rates of each bin derive from the spread in the values of the six different studies. Each research group assumed the same initial conditions, but different analytic prescriptions for the physical processes of binary evolution.

Even after considering the differences in the models and the resulting uncertainties in the predicted rates, three consistent key features can be seen in Fig. 1.1. First, the predicted rates of both SD and DD SNe Ia underestimate the observed rates at all delay times. Second, the SD and DD predictions are consistent with each at short delay times, corresponding to SNe Ia that explode in spiral galaxies. Finally, the predicted rates of SD systems at long delay times, i.e. those that occur in elliptical galaxies, dramatically underestimate the observed rate by two orders of magnitude! Despite the clear mismatch between both the SD and DD predictions to the observations, this last point has been one of the main arguments for the DD scenario. Namely, although the predicted DD rates are below the observed SN Ia rates, the DD delay time distribution follows the same τ^{-1} functional form of the observations (Maoz et al. 2010). Meanwhile, the predicted SD

delay time distribution exhibits an obvious kink toward extremely small rates at long delay times.

So I was intrigued as to why all the models predicted this downward bend in the SD delay time distribution. To understand the SD progenitors at long delay times, I must convey three steps of reasoning. First, in the SD scenario, the delay time is dictated by the nuclear burning lifetime of the donor, i.e. the original secondary. The initially more massive primary can evolve quickly into a WD, but it must still wait for the secondary to donate the needed additional mass to reach the Chandrasekhar limit $M_{Ch} \approx 1.4\,M_{\odot}$. To

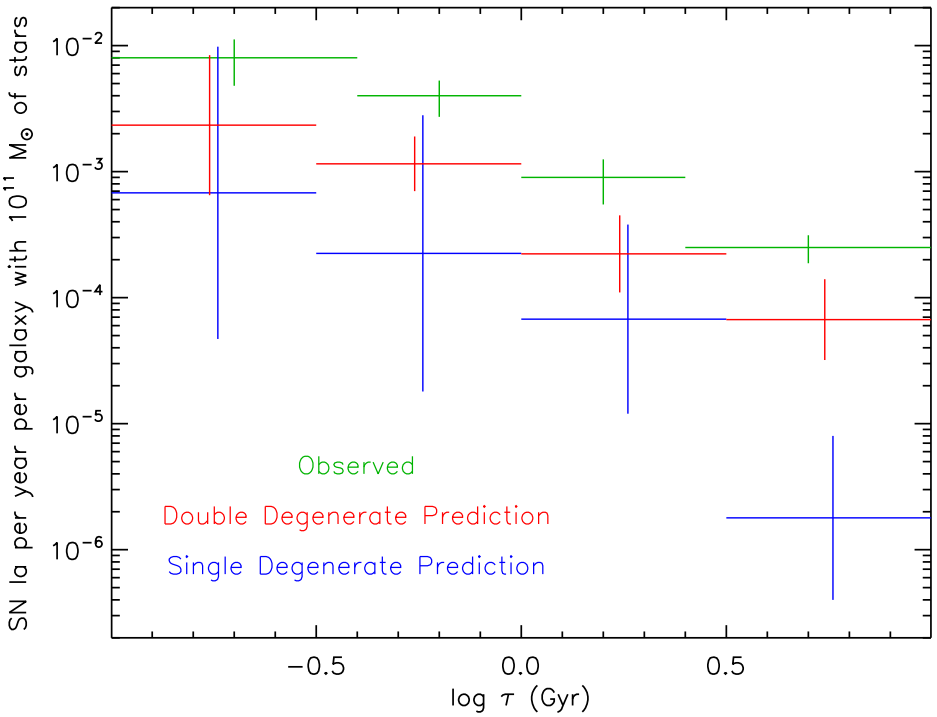

Figure 1.1: Delay time distribution of Type Ia supernovae. I compare the observations (green) to the predictions of the double degenerate scenario (red) and single degenerate scenario (blue) based on the compilation of BPS simulations reported in Nelemans et al. (2013).

form a SN Ia after a long 5 - 10 Gyr delay time in the SD scenario, the secondary must have a nuclear burning lifetime of 5 - 10 Gyr. Only solar-type stars with 1.0 - 1.3 $M_\odot$ have such long lifetimes. Hence, SD SNe Ia that explode in elliptical galaxies must have $M_2 = 1.0$ - $1.3\,M_\odot$ donors.

Second, a low-mass secondary with $M_2 = 1.0$ - $1.3\,M_\odot$ cannot donate a significant amount of mass to the WD. Mass transfer is never 100% efficient and most of the mass of the secondary is locked up in its core. The WD must therefore have an initial mass close to the Chandrasekhar mass to be capable of eventually reaching M_{Ch}. It cannot start off too close, between 1.1 - 1.4 $M_\odot$, because such massive WDs that form in the cores of intermediate-mass stars are likely to be composed of neon and oxygen. Neon-oxygen white dwarfs that gain enough material to reach the Chandrasekhar mass limit are expected to undergo accretion induced collapse into neutron star (Tutukov & Yungelson 1996). The WD needs to be composed of carbon and oxygen to be detonated, as the observed spectroscopic features of SNe Ia indicate. So our binary must contain a $M_{WD} \approx 1.0$ - $1.1 M_\odot$ carbon-oxygen WD in order for it to accrete the necessary mass $\Delta M = 0.3$ - $0.4 M_\odot$ from the $M_2 = 1.0$ - $1.3\,M_\odot$ secondary. According to the empirical initial to final mass relation (Weidemann 2000), carbon-oxygen WDs with $M_{WD} \approx 1.0$ - $1.1 M_\odot$ originally evolved from B-type MS stars with $M_1 = 6$ - $7\,M_\odot$. In the SD scenario, SNe Ia that explode after long delay times in elliptical galaxies derive from extreme mass-ratio $q = M_2/M_1 = 0.15$ - 0.20 binaries with mid-B MS primaries and solar-type MS secondaries.

Finally, not any B-type + solar-type MS binary will evolve into a WD + solar-type MS system capable of producing a SN Ia. Binaries that are too wide will not interact while systems that are too close will merge. In addition, the secondary must donate its

hydrogen-rich envelope to the WD in such a manner that the material stably accretes and burns into carbon as it accumulates onto the surface of the WD. For $M_{\rm WD} = 1.0$ - $1.1\,{\rm M}_{\odot}$ WDs, this nuclear burning stability criterion is met if the mass transfer rate is $2{\times}10^{-7}\,{\rm M}_{\odot}$ yr^{-1} (Nomoto et al. 2007). If the $M_2 = 1.0$ - $1.3\,{\rm M}_{\odot}$ secondary is still on the MS as it donates hydrogen-rich material, however, it will do so on its thermal timescale of $2{\times}10^{-8}\,{\rm M}_{\odot}$ yr^{-1} (Hurley et al. 2002). This is well below the stability criterion, and so this system would produce novae eruptions on the surface of the WD with no net increase in its mass. The secondary must therefore evolve into a red giant first in order to transfer mass at the necessary accretion rate. This SD channel of binary evolution is appropriately named the red giant channel (Ruiter et al. 2009). Because the donor is a red giant, the orbital period of the binary must be $P \approx 200$ - 2,000 days. The original B-type MS + solar-type MS binary must also have an orbital period in this interval. If the solar-type MS companion was closer to the B-type MS star as it enters its giant phase, the companion would entire common envelope evolution and spiral inward. If the MS binary was initially at longer orbital periods, the system would widen further due to the mass loss from the B-type star during the first phase of binary evolution.

So I have established that, in the SD scenario, SNe Ia that explode after long delay times in elliptical galaxies must evolve through the red giant channel in which a $M_2 = 1.0$ - $1.3\,{\rm M}_{\odot}$ giant stably transfers mass to a $M_{\rm WD} = 1.0$ - $1.1\,{\rm M}_{\odot}$ carbon-oxygen WD. This binary originally derived from a $M_1 = 6$ - $7\,{\rm M}_{\odot}$ B-type MS star with a $M_2 = 1.0$ - $1.3\,{\rm M}_{\odot}$ MS companion ($q = 0.15$ - 0.20) in an orbit of $P = 200$ - 2,000 days. In order to reliably predict the rates of SNe Ia through this channel, we need to know the intrinsic frequency of their progenitors in this cube of the parameter space.

Much of what we know about the statistics of close unresolved binaries derives from

spectroscopy (Abt 1983; Duquennoy & Mayor 1991; Sana et al. 2012). If the companion is sufficiently luminous, then both the primary and secondary can be visible in the combined spectrum, a so-called double-lined spectroscopic binary (SB2). Multi-epoch spectroscopy of an SB2 reveals the radial velocity variations of both sets of spectroscopic absorption features due to their mutual orbital motion. By fitting the radial velocities as a function of time, one can easily measure the orbital period P, masses M_1 and M_2, and eccentricity e. The mass ratio derives directly from the ratio of the observe velocity semi-amplitudes $q = M_2/M_1 = K_1/K_2$. If the companion is substantially less luminous, however, then only the spectral absorption features of the primary can be observed, a single-lined spectroscopic binary (SB1). Because MS stars follow a steep mass-luminosity relation, companions to massive O-type and B-type stars with mass ratios $q < 0.25$ will appear as SB1s. For an SB1, the reflex motion K_1 of the primary can be still be detected due to orbital motion with the secondary, and so the period P and eccentricity e can be measured. Although the inclination of an SB1 cannot be measured, a lower limit to the mass ratio q can be determined by inferring the mass of the primary from its spectral type. Assuming random orientations, a statistical mass-ratio distribution can be recovered for SB1s (Mazeh et al. 1992a).

Not all SB1s, however, are exclusively extreme mass-ratio stellar binaries. MS stars with companions that are compact remnants, e.g., white dwarfs, neutron stars, or black holes, will also appear to be SB1s. In fact, it was originally believed that the majority of SB1s with O-type and B-type primaries contained compact remnants. In a sample of spectroscopic B-type binaries, Wolff (1978) concluded that the few SB1s in her sample contained WD companions. Similarly, Garmany et al. (1980) found several SB1s with O-type primaries, and concluded they contained neutron star or black hole companions.

In fact, they speculated these O-type SB1s were the progenitors of high-mass X-ray binaries. Garmany et al. (1980) also suggested follow-up X-ray observations to determine if any of the systems are already producing X-rays due to accretion onto the compact remnants.

So why was it naturally assumed in the 1970's and 1980's that the majority of early-type SB1s contained compact remnants? The primary reason was due to our limited understanding of close binary star formation at the time. Closely orbiting binaries cannot form in situ (Tohline 2002). Instead, the components fragment from a gaseous molecular core on separations scales of 1,000s of AU, or the companion fragments from the primordial accretion disk on scales of 10s of AU (Bate & Bonnell 1997; Kratter & Matzner 2006). Some evolutionary process must occur to bring the components of close binaries together to their observed separations of 0.1 - 1.0 AU. The best hypothesis for close binary star formation at the time was through competitive accretion in the circumbinary disk (Bonnell & Bate 2005). If a companion fragmented near the edge of the disk, it would migrate inward, accreting material as it traveled toward the more massive primary. If it gained sufficient mass and orbital angular momentum, it could stabilize into a short orbit. Otherwise, the companion would migrate all the way inward and merge with the nascent primary star. Hence, close binary star formation via competitive accretion naturally produce correlated component masses with $q > 0.25$ and a deficit of extreme mass-ratio binaries with $q < 0.25$.

Indeed, the theory of competitive accretion has its merits. As we observe the population of close solar-type binaries, there is a clear overabundance of companions with $q > 0.25$ (Raghavan et al. 2010). In fact, many solar-type binaries appear to be twins with mass ratios $q \approx 1.0$ near unity (Tokovinin 2000). Toward extreme mass

ratios, solar-type $M_1 \approx 1.0\,\mathrm{M}_\odot$ MS stars exhibit of dearth of low-mass late-M dwarf companions with $M_2 = 0.08$ - $0.25\ \mathrm{M}_\odot$. Moreover, there is a complete absence of closely orbiting brown dwarf companions with $M_2 = 0.02$ - $0.08\ \mathrm{M}_\odot$ to solar-type MS primaries, commonly known as the brown dwarf desert (Grether & Lineweaver 2006). Close binary formation through competitive accretion correctly explains the observed statistics of solar-type primaries. However, more massive binaries may have formed differently, and may therefore have different binary statistics.

The notion that early-type SB1s contained primarily compact remnants permeated until the 1990's. It was then argued that low-mass X-ray binaries (LMXBs) must evolve from primordial extreme mass-ratio stellar binaries (Kalogera & Webbink 1998). To form a neutron star or black hole in an X-ray binary, the primary must be an O or early-B star with $M_1 \gtrsim 10\,\mathrm{M}_\odot$ to undergo core-collapse suprnovae. We currently see the donors in LMXBs to be F-K type stars with $M_{2,\mathrm{now}} < 1.5\,\mathrm{M}_\odot$. The donors may have evolved from intermediate mass A-type or late-B secondaries with $M_2 > 1.5\,\mathrm{M}_\odot$ and have since lost most of their mass to the compact remnant. However, A-type and late-B stars have convective cores and radiative envelopes, and must evolve to the upper MS or subgiant branch before they can transfer material to their companions. Meanwhile, F-K type stars with $M_2 < 1.5\,\mathrm{M}_\odot$ have radiative cores and convective envelopes, which produce strong, global magnetic fields and a hot ionized corona. As mass is lost from the F-K type star, it is ionized in the hot corona and then flows through the magnetic field lines, draining angular momentum from the star. Such a star in isolation would rapidly spin-down due to this magnetic braking. However, if it is tidally coupled to a closely orbiting companion, e.g, a compact remnant, angular momentum is drawn from the orbit and resupplied to the F-K type star, bringing the binary closer together (Hurley et al.

2002). Systems with primordial F-K type companions can therefore produce LMXBs with short orbital periods $P < 1$ day. In fact, the majority of observed LMXBs have such short orbital periods, dictating the donors must have originally been low-mass F-K type stars with $M_2 < 1.5$ $M_\odot$ (Fragos & McClintock 2015). Most LMXBs must therefore have evolved from $M_1 > 10$ $M_\odot$ primaries with $M_2 < 1.5$ $M_\odot$ secondaries, i.e. extreme mass-ratio binaries with $q < 0.15$.

Because of BPS, there was a rapid paradigm shift in the 1990's. It was now believed that most early-type SB1s contained low-mass stellar companions. Indeed, in order to explain LMXBs and related phenomenon, e.g. millisecond pulsars (MSPs), there must be primordial extreme mass-ratio close binaries. Observationally, however, it was still unclear what fraction of early-type SB1s have stellar companions compared to the fraction that contain compact remnants. Only SB2s, where the nature of the secondary is reliably known, can provide an uncontaminated census of close massive MS binaries.

In Fig. 1.2, I display the best statistics we had in 2012 of close binary companions to O-type and B-type stars based on observations of SB2s. Three things to consider. First, as previously stated, SB2s with O-type and B-type primaries can reveal only companions with $q > 0.25$. The observed population of SB1s can provide only an upper limit to the frequency of $q < 0.25$ stellar companions considering some may contain compact remnants. Because we do not know the intrinsic frequency of low-mass companions to massive stars, we cannot yet reliably test the role and significance of binary star formation via competitive accretion.

Second, all the SB2s in Fig. 1.2 are in our Galaxy and therefore have chemical abundances near solar metallicity $Z_\odot \approx 0.016$. Some models of binary star formation

predict close massive binaries with low metallicities should have different properties and statistical distributions (Machida 2008). It is therefore important to measure the properties of massive binaries at subsolar metallicities.

Finally, although the population of SB2s is well sampled at short orbital periods, the number of SB2s at intermediate orbital periods $P > 20$ days are rather small. The

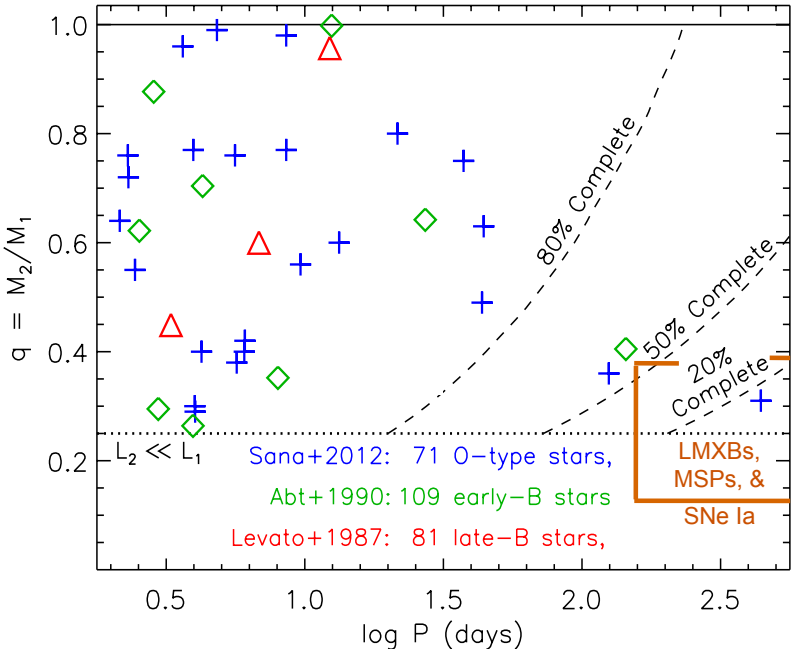

Figure 1.2: Comparison of mass ratio versus orbital period for the three best samples of early-type SB2s as of 2012. I display the completeness levels assuming random orientations and the sensitivity of the spectroscopic observations. Progenitors of LMXBs and MSPs that form in the galactic field as well as SNe Ia that explode after long delay times in elliptical galaxies derive from early-type stars with low-mass companions at intermediate orbital periods. The statistics of SB2s are rather poor in this corner of the parameter space. It is therefore difficult to reliably predict the intrinsic rates of these channels of binary evolution based solely on the SB2 data.

decrease in the number of early-type SB2s may be partially or entirely be due to selection effects. Namely, SB2s become less complete toward longer orbital periods and lower mass companions. This is simply because such systems have small velocity semi-amplitudes that are easily missed given the sensitive and cadence of the spectroscopic observations. Despite the selection effects, there appears to be a physically genuine trend that companions to massive stars with slightly longer orbital periods favor smaller mass ratios. Given the small sample sizes and selection effects of SB2s, however, it is difficult to determine the statistical significance of this trend based on the spectroscopic binary data alone.

I also display in Fig. 1.2 the parameter space for the progenitors of LMXBs, MSPs, and SD SNe Ia that explode in elliptical galaxies after long delay times via the red giant channel. All three of these systems derive from primordial extreme mass-ratio binaries at intermediate orbital periods. Sub-Chandrasekhar DD mergers that produce SNe Ia are also expected to derive from $q \approx 0.2$ - 0.3 companions with intermediate orbital periods (Ruiter et al. 2011). For the SNe Ia progenitors, the primaries are less massive mid-B stars with $M_1 \approx 6$ - $7\,M_\odot$ that evolve into 1.0 - $1.0\,M_\odot$ carbon-oxygen WDs, while the LMXBs and MSPs derive from more massive $M_1 > 10\,M_\odot$ primaries that evolve into neutron stars or black holes. At these intermediate orbital periods, the statistics of SB2s are rather small and significantly affected by selection affects. Moreover, SB2s provide no information on the frequency of extreme mass-ratio companions $q < 0.25$, where we expect these LMXBs, MSPs, and SNe Ia to derive. The fact that we have poor or no statistics in these portions of the parameter space should incite immediate worry and concern in our ability to test formation models of massive binaries as well as to reliably predict the rates of certain channels of binary evolution.

1.2 Eclipsing Binaries as Astrophysical Tools

Fortunately, we recently celebrated the 50th anniversary of Dr. Strangelove, and Peter Sellers taught me how to stop worrying and love eclipsing binaries. Eclipsing binaries (EBs) are wonderful astrophysical tools in which we can measure the intrinsic physical properties of binary stars. These measurements, in turn, provide invaluable insight and diagnostics into the formation, environments, and fates of binary stars.

There are many types and subclasses of EBs, which I will divide into three main groups. First, detached EBs are well separated, as is indicated by their narrow eclipse widths with respect to their orbital periods. If both components are unevolved MS stars in a detached EB, then each component is effectively evolving along its respective single-star evolutionary track. Second, the primary eventually evolves and fills its Roche lobe, beginning to donate matter to its companion in a semi-detached configuration. These semi-detached EBs have moderately wide eclipses because one component is filling its Roche lobe. If mass transfer is stable, then the MS companion can become more massive and luminous than the giant primary. In fact, the demon star, Algol, belongs to this subclass of semi-detached EBs with mass ratios that have been inverted due to binary mass transfer. Finally, if mass transfer is unstable, the binary will evolve toward a contact configuration. The companion cannot accrete all the material that has been donated to it, and so much of the mass leaves the system. As mass is lost, it carries away some orbital angular momentum, and so the binary comes even closer together. These contact EBs have very wide and sinusoidal eclipse features, and are expected to eventually merge into a single star.

Because components in detached EBs are effectively evolving along their respective

single-star tracks, they provide important diagnostics for stars in general. It was realized decades ago that the combination of spectroscopy and light curve photometry of detached eclipsing binaries can provide the fundamental stellar relations (Huang & Struve 1956). Multi-epoch spectroscopy is used to measure the orbital period P and masses M_1 and M_2 by fitting the radial velocities of an SB2 (see above). Spectroscopy also provides the effective temperatures T_1 and T_2 according to the observed spectral absorption features. Meanwhile, by fitting the EB photometric light curve, we gain two additional parameters. Namely, the sum of eclipse widths $\Theta_1+\Theta_2$ provide the relative sum of radii $(R_1+R_1)/a$ and the ratio of eclipse depths $\Delta \mathrm{m}_2/\Delta \mathrm{m}_1$ gives the luminosity contrast L_2/L_1. With Keplers' laws and the Stefan-Boltzmann equation, the radii R_1 and R_2 and luminosities L_1 and L_2 of both components are uniquely defined. Today, astronomers measure the mass-radius and mass-luminosity relations of MS stars in detached EBs to accuracies of $\approx$1 - 2% (Torres et al. 2010). Moreover, several primordial pre-MS stars that are still contracting toward their normal MS phase of evolution have been identified in detached EBs (Hillenbrand & White 2004). Their physical properties have been measured, which provide tight constraints for evolutionary tracks of pre-MS stars.

Because the intrinsic luminosities of EBs can be measured from spectroscopy and photometry, they make wonderful standard candles. For example, Pietrzyński et al. (2013) recently measured the physical properties of several detached EBs in the Large Magellanic Cloud (LMC), and derived a distance $d = 50$ kpc to an accuracy of 2%. This measurement provides a crucial rung on the cosmological distance ladder, bridging the gap between between nearby stars measured with parallax and more distant standard candles such as Cepheids and Type Ia supernovae.

Measuring the physical properties of EBs from their photometric light curves to

such high precision requires detailed modeling software. These physical models include the effects of rotational and tidal distortions, limb darkening, gravity darkening, and reflection effects (Wilson & Devinney 1971). The EB photometric light curve models are continuously updated with revised limb darkening coefficients, more accurate stellar atmospheres, and other parameters (Prša & Zwitter 2005).

With the advent of high-cadence and wide-field photometric monitoring surveys, we are now discovering treasure troves of EBs. For example, the *TrES* and *Kepler* surveys identified thousands of EBs in the galactic field (Devor et al. 2008; Prša et al. 2011b). At further distances, the OGLE team discovered tens of thousands of EBs in the galactic bulge and the nearby Magellanic Cloud galaxies (Devor 2005; Graczyk et al. 2011; Pawlak et al. 2013). Early-type stars in the Magellanic Clouds have subsolar metallicities (Korn et al. 2000), and therefore make excellent testbeds for studying the binary statistics of massive stars as a function of metallicity. Chapter 2 of this thesis is dedicated to a comparison of B-type EBs in the Magellanic Clouds and in our Milky Way galaxy.

The discovery of EBs through photometric monitoring surveys is quickly outpacing our ability to obtain follow-up spectra. The photometric light curves alone, however, cannot be generally used to measure all the physical properties of the EB, e.g. the masses M_1 and M_2. For large photometric samples of EBs, other assumptions or constraints are needed. In the past, mass-luminosity and mass-radius MS constraints were utilized to measure M_1 and M_2 of detached MS EBs (Kallrath & Milone 2009). However, MS stars do not follow strict MS relations, but increase in luminosity and radius along the MS. The assumptions of mass-luminosity and mass-radius relations typically lead to large systematic uncertainties of 30% or more in the masses. Devor et al. (2008) therefore

relaxed this MS constraint, and instead fit stellar isochrones to the EB light curves. With the three parameters M_1, M_2, and age τ, they could now account for the spread in the mass-luminosity and mass-radius relations. Devor et al. (2008) fit the photometric light curves for a sample of 773 EBs in the galactic field, and could measure the masses and ages for several of their systems. In general, however, the solutions for M_1, M_2, and τ were highly uncertain and/or degenerate for the majority of EBs in their sample. By adding an extra free parameter, i.e. the age τ, unique solutions for the masses could no longer be recovered.

An additional constraint is therefore needed to accurately measure the physical properties of all EBs in a photometric sample. After much thought, I finally determined the solution. Astronomers have used photometry and spectroscopy of detached EBs to measure their physical properties. These EB measurements, in turn, have been used to constrain the evolutionary tracks of stars and to measure the distance to the LMC. Why not reverse the argument? Given the calibrated evolutionary tracks and the known distance to the LMC, we can measure the physical properties of detached EBs in the LMC based solely on the photmetric light curves. With this extra distance constraint, we can therefore measure M_1, M_2, and τ without spectroscopy. We therefore developed the tools, procedures, and pipeline necessary to fit large samples of EBs in the LMC (discussed in Chapters 3 and 4).

With this pipeline in place, I began to fit the ≈2,200 B-type EBs in the LMC with orbital periods $P = 3$ - 15 days. I was specifically searching for the elusive extreme mass-ratio stellar binaries that do not appear as SB2s but should produce detectable eclipses if oriented edge-on. My pipeline worked on the majority of the EBs, but 22 of the EBs did not seem to converge toward any adequate solutions. These 22 EBs had

very peculiar light curve profiles, and I was ready to throw them out of my sample. I will never forget the sage advice from Rosanne, my Ph.D. advisor. She said you cannot throw systems out of your sample unless you know the genuine physical reason for why you are throwing them out. Even though only ≈1% of the observed EB population shows these unusual light curve features, they may represent an intrinsically larger fraction and therefore play an important role in the binary statistics. So after banging my head against the desk for another day or two, I finally realized what they were: we had serendipitously discovered a new class of nascent EBs with extreme mass ratios. I can honestly say that moment was the most rewarding during my time as a Ph.D. astronomy student. Chapter 3 is dedicated to the discovery of these 22 EBs, which eventually led to a press release.

We continued to use our automated pipeline to analyze the ≈220 B-type EBs in the LMC at intermediate orbital periods $P = 20$ - 50 days. We wanted to test if slightly wider companions have different properties. Most importantly, by probing longer orbital periods, we come closer to measuring the statistics of low-mass companions at intermediate orbital periods, a crucial input parameter for BPS of LMXBs, MSPs, and SNe Ia (see Fig. 1.2). Chapter 4 is dedicated to an analysis of these B-type EBs at intermediate orbital periods.

Finally, although EBs are wonderful astrophysical tools, they do not paint a complete picture. While SB2s and EBs can detect companions at short orbital periods, other methods must be utilized to detect binaries with wide separations. In Chapter 5, we compile more than a dozen samples of early-type binaries identified through a variety of observational techniques. For each sample, we correct for their respective selection effects. For example, EBs are observed only if their orientations are sufficiently edge-on

and if they have deep and wide enough eclipses to be detected given the sensitivity and cadence of the photometric observations. After correcting for the selection effects, we combine all the samples to determine a comprehensive and self-consistent picture of binary star statistics. These statistics provide new insight into the formation of massive binaries. Also, in Chapter 6, I conclude by briefly indicating the implications of these statistics on the predicted rates of SNe Ia and LMXBs.

Chapter 2

The Close Binary Properties of Massive Stars in the Milky Way and Low-Metallicity Magellanic Clouds

This thesis chapter originally appeared in the literature as

M. Moe & R. Di Stefano, *The Astrophysical Journal*, 778, 95, 2013

Abstract

In order to understand the rates and properties of Type Ia and Type Ib/c supernovae, X-ray binaries, gravitational wave sources, and gamma ray bursts as a function of galactic environment and cosmic age, it is imperative that we measure how the close binary properties of O and B-type stars vary with metallicity. We have studied eclipsing binaries with early-B main-sequence primaries in three galaxies with different

metallicities: the Large and Small Magellanic Clouds (LMC and SMC, respectively) as well as the Milky Way (MW). The observed fractions of early-B stars which exhibit deep eclipses $0.25 < \Delta \mathrm{m\,(mag)} < 0.65$ and orbital periods $2 < P\,\mathrm{(days)} < 20$ in the MW, LMC, and SMC span a narrow range of (0.7 - 1.0)%, which is a model independent result. After correcting for geometrical selection effects and incompleteness toward low-mass companions, we find for early-B stars in all three environments: (1) a close binary fraction of $(22 \pm 5)\%$ across orbital periods $2 < P\,\mathrm{(days)} < 20$ and mass ratios $q = M_2/M_1 > 0.1$, (2) an intrinsic orbital period distribution slightly skewed toward shorter periods relative to a distribution that is uniform in $\log P$, (3) a mass-ratio distribution weighted toward low-mass companions, and (4) a small, nearly negligible excess fraction of twins with $q > 0.9$. Our fitted parameters derived for the MW eclipsing binaries match the properties inferred from nearby, early-type spectroscopic binaries, which further validates our results. There are no statistically significant trends with metallicity, demonstrating that the close binary properties of massive stars do not vary across metallicities $-0.7 < \log(Z/\mathrm{Z}_\odot) < 0.0$ beyond the measured uncertainties.

2.1 Introduction

Spectral type O ($M_1 \gtrsim 18\,\mathrm{M}_\odot$) and B ($3\,\mathrm{M}_\odot \lesssim M_1 \lesssim 18\,\mathrm{M}_\odot$) primaries with close binary companions evolve to produce a plethora of astrophysical phenomena, including millisecond pulsars (Lorimer 2008), Type Ia (Wang & Han 2012) and possibly Type Ib/c (Yoon et al. 2010) supernovae, X-ray binaries (Verbunt 1993), Algols (van Rensbergen et al. 2011), short (Nakar 2007) and perhaps long (Izzard et al. 2004) gamma ray bursts, accretion induced collapse (Ivanova & Taam 2004), and gravitational waves

(Schneider et al. 2001). Telescopic surveys dedicated to discovering luminous transients and/or high-energy sources have identified some of these binary star phenomena in low-metallicity host environments such as dwarf and high-redshift galaxies (Kuznetsova et al. 2008; McGowan et al. 2008; Berger 2009; Frederiksen et al. 2012). Recent observations have demonstrated that the rates and properties of certain channels of binary evolution vary with metallicity (Dray 2006; Cooper et al. 2009; Sullivan et al. 2010; Kim et al. 2013). To explain these observed trends, it has been postulated that the physical processes that affect stellar and binary evolution are metallicity dependent (Bellazzini et al. 1995; Kobayashi et al. 1998; Ivanova 2006; Fryer et al. 2007; Kistler et al. 2011). However, the initial conditions of the progenitor main-sequence (MS) binaries may change with metallicity (Machida 2008), which may also account for the observations. In order to distinguish between these two hypotheses, it is imperative that we measure the close binary properties of massive stars at low metallicity.

In the MW, the fraction of primaries which harbor close companions dramatically increases with primary mass (Abt 1983; Raghavan et al. 2010, see also §2.4), reaching ≈70% with orbital periods $P < 3{,}000$ days for massive O-type stars (Sana et al. 2012). Yet the effect of metallicity on the close binary fraction of massive stars has not been robustly measured from observations. This is primarily due to the paucity of short-lived, low-metallicity early-type stars within our own Milky Way (MW), forcing us to explore external galaxies to investigate metallicity dependence. Evans et al. (2006) utilized multi-epoch spectroscopic observations of massive stars in the Large and Small Magellanic Clouds (LMC and SMC, respectively) to derive a lower limit of ≈30% for the close binary fraction. Their cadence was insufficient to fit orbital periods to their radial velocity data for many of their systems, so they were unable to account for

incompleteness. Sana et al. (2013) searched for spectroscopic binaries among O-type stars in the starburst region of the Tarantula Nebula, also known as 30 Doradus, within the LMC. After correcting for observational biases, they computed a binary fraction of ≈50% across orbital periods $0.15 < \log P\,(\text{days}) < 3.5$. This extremely active and dense environment may not be representative of all O-type stars. Moreover, with slightly subsolar abundances of [Fe/H] ≈ [O/H] ≈ −0.2 (Peimbert & Peimbert 2010), 30 Doradus offers little leverage to gauge the effect of metallicity. Finally, Mazeh et al. (2006) utilized observations made during the second phase of the Optical Gravitational Lensing Experiment (OGLE-II) to identify eclipsing binaries with B-type primaries in the LMC. After correcting for geometrical and other selection effects, they estimated that only ≈0.7% of B stars have a companion with orbital periods P = 2 - 10 days, nearly an order of magnitude lower than the value for Milky Way counterparts inferred from spectroscopic radial velocity observations. However, Mazeh et al. (2006) did not account for incompleteness towards low mass secondaries, so it is conceivable that many small companions are hiding by exhibiting shallow eclipses below the threshold of the OGLE-II sensitivity.

In this chapter, we analyze catalogs of eclipsing binaries in the MW, LMC, and SMC to determine the close binary fraction of early-B stars as a function of metallicity. We organize the subsequent sections as follows. In §2.2, we discuss the criteria we developed to compile our samples of eclipsing binaries from various catalogs, and compare the observed properties of the eclipsing systems among the different environments. In §2.3, we utilize sophisticated light curve modeling software and perform detailed Monte Carlo simulations to correct for observational selection effects and incompleteness. In §2.4, we compare our results derived from eclipsing binaries to spectroscopic radial velocity

observations of O and B-type binaries in the MW. We summarize and discuss our conclusions in §2.5.

2.2 The Eclipsing Binary Samples

We utilize catalogs of eclipsing binaries in the MW based on Hipparcos data (Lefèvre et al. 2009), in the LMC identified by OGLE-II (Wyrzykowski et al. 2003) and OGLE-III observations (Graczyk et al. 2011), and in the SMC discovered by the OGLE-II survey (Wyrzykowski et al. 2004). These surveys identified eclipsing systems with varying sensitivity and completeness. In order to make accurate comparisons among these catalogs, we must first apply selection criteria to create a uniform dataset.

First, we select relatively unevolved $M_1 \approx 7\,\mathrm{M}_\odot$ - $18\,\mathrm{M}_\odot$ primaries, corresponding to spectral types ≈B0-B3.5 and luminosity classes ≈III-V. By selecting a narrow range of spectral types and stages of evolution, we can more robustly correct for geometrical selection effects and other observational biases (see §2.3). Because the mass function of early-B stars is strongly skewed toward lower mass objects, the median primary mass in our selected samples is $M_1 = 10\,\mathrm{M}_\odot$ (see §2.3.1).

Second, we restrict our samples to eclipsing binaries with orbital periods $P = 2$ - 20 days. We do not consider shorter period binaries with $P < 2$ days because a large fraction of these systems are contact binaries (EW eclipsing types / W Ursae Majoris variables) that may have substantially evolved from their primordial configurations. Eclipsing binary identification algorithms typically fail to detect MS binaries when the eclipse duration is $\lesssim$5% the total orbital period (Söderhjelm & Dischler 2005). For our

early-B primaries with MS companions, the eclipse widths fall below 4% the total orbital period when the orbital period exceeds $P = 20$ days (see §2.3.1).

Finally, we select eclipsing binaries within a particular range of primary eclipse depths Δm. For spherical MS stars, the maximum eclipse depth possible is Δm = 0.75 mag, corresponding to a twin system with equal mass components observed edge-on at inclination $i = 90^{\rm o}$. In a real stellar population, eclipsing binaries with $\Delta{\rm m} \gtrsim 0.65$ are significantly contaminated by systems which have undergone binary evolution, e.g. Algols (Söderhjelm & Dischler 2005, see their Figure 5), and/or are substantially tidally distorted, so we only consider systems with $\Delta{\rm m} < 0.65$. Because we selected eclipsing binaries with relatively unevolved primaries and $P > 2$ days, most systems with $\Delta{\rm m} < 0.65$ in our samples are not filling their Roche lobes (see also §2.3.1). Depending on the photometric accuracy, the catalogs become less sensitive toward shallow eclipse depths $\Delta{\rm m} \lesssim 0.10$ - 0.25. We consider two subsamples: deep eclipses with $0.25 < \Delta{\rm m} < 0.65$ where all the surveys are sensitive, and an extension that also includes medium eclipse depths with $0.10 < \Delta{\rm m} < 0.65$ where only some of the samples are still complete.

Nearby early-B stars in the MW within ≈2 kpc of our sun cover a narrow range of metallicities centered on solar composition (Gummersbach et al. 1998, [O/H] $= -0.2 \pm 0.2$, [Mg/H] $= 0.0 \pm 0.2$; Daflon & Cunha 2004, [O/H] $= -0.1 \pm 0.2$, [Mg/H] $= -0.1 \pm 0.2$; Lyubimkov et al. 2005, [Mg/H] $= 0.1 \pm 0.2$). Although most catalogs of eclipsing binaries in the MW focus on lower mass, solar-type primaries, Lefèvre et al. (2009) recently classified a list of variable O and early-B stars based on Hipparcos data. They identified $\mathcal{N}_{\rm EB} = 51$ eclipsing binaries with $P = 2$ - 20 days, median Hipparcos magnitudes $\langle {\rm H_P} \rangle < 9.3$, and primaries displaying either spectral types B0-B2 and luminosity classes III-V or spectral types B2.5-B3 and luminosity classes

II-V. From these systems, $\mathcal{N}_{\rm med} = 31$ exhibited eclipse depths $0.10 < \Delta {\rm H_P} < 0.65$, while only $\mathcal{N}_{\rm deep} = 16$ had deep amplitudes $0.25 < \Delta {\rm H_P} < 0.65$. In the Hipparcos database (Perryman et al. 1997), there are $\mathcal{N}_{\rm B} = 1596$ early-B stars which satisfy the same magnitude, spectral type, and luminosity class criteria, where we have included objects without a specifically listed luminosity class but excluded B0-B2 spectral types with a hybrid II-III designation. This results in $\mathcal{F}_{\rm med} = \mathcal{N}_{\rm med}/\mathcal{N}_{\rm B} = (1.94 \pm 0.35)\%$ and $\mathcal{F}_{\rm deep} = \mathcal{N}_{\rm deep}/\mathcal{N}_{\rm B} = (1.00 \pm 0.25)\%$, where the errors derive from Poisson statistics.[1] We summarize these results in Table 2.1.

The LMC provides our first testbed to investigate the effects of metallicity on the frequency of close early-B binaries. Young massive stars and Cepheids, which recently evolved from B-type MS progenitors, have a mean metallicity of $\langle \log({\rm Z/Z_\odot}) \rangle = -0.4$ in this nearby satellite galaxy (Luck et al. 1998, [Fe/H] $= -0.3 \pm 0.2$; Korn et al. 2000, [Fe/H] ≈ -0.4; Rolleston et al. 2002, [O/H] $= -0.3 \pm 0.1$, [Mg/H] $= -0.5 \pm 0.2$; Romaniello et al. 2005, [Fe/H] $= -0.4 \pm 0.2$; Keller & Wood 2006, [Fe/H] $= -0.3 \pm 0.2$), where ${\rm Z_\odot} = 0.015$ (Lodders 2003; Asplund et al. 2009). The LMC has a distance modulus of $\mu = 18.5$, typical reddening of E(V−I) = 0.1, and average extinction of ${\rm A_V} = 0.4$ toward younger stellar environments (Zaritsky 1999; Imara & Blitz 2007; Haschke

[1]Throughout this work, we use $\mathcal{N}$ to represent an absolute *number*, $\mathcal{F}$ for a *fraction*, either observed or intrinsic, $\mathcal{O}$ to represent an *observed* distribution which integrates to the specified fraction, $\mathcal{S}$ for a *simple* approximation to the observed distribution, $\mathcal{M}$ for a detailed *model* distribution based on our Monte Carlo simulations, $\mathcal{U}$ for an intrinsic distribution which describes the *underlying* close binary population, $\mathcal{C}$ for a *correction* factor, $\mathcal{P}$ for the *probability* that a close binary is observed as an eclipsing system, and p for either a *probability* density distribution which integrates to unity or a *probability* statistic from a hypothesis test.

Table 2.1. Eclipsing binary statistics of early-B MS stars in the Milky Way and Magellanic Clouds. The first three columns give the host galaxy, mean metallicity of early-type stars (see text for details), and survey from which the eclipsing binaries were identified. Column 4 lists the total number $\mathcal{N}_{\rm B}$ of relatively unevolved early-B primaries in the samples, while column 5 gives the number $\mathcal{N}_{\rm EB}$ of eclipsing binaries with orbital periods $P = 2\text{-}20$ days. Columns 6 and 7 list the numbers $\mathcal{N}_{\rm med}$ and fractions $\mathcal{F}_{\rm med} = \mathcal{N}_{\rm med}/\mathcal{N}_{\rm B}$ of systems with eclipse depths $\Delta{\rm m} = 0.10\text{-}0.65$ mag and orbital periods $P = 2\text{-}20$ days. Columns 8 and 9 give similar numbers $\mathcal{N}_{\rm deep}$ and fractions $\mathcal{F}_{\rm deep} = \mathcal{N}_{\rm deep}/\mathcal{N}_{\rm B}$, but for those systems displaying deep eclipses $\Delta{\rm m} = 0.25\text{-}0.65$ mag only. Shown in boldface are the cases for which the samples are relatively complete, i.e. when the photometric accuracy of the survey is sensitive to the specified eclipse depths. 1 - Perryman et al. (1997); 2 - Lefèvre et al. (2009); 3 - Udalski et al. (2000); 4 - Wyrzykowski et al. (2003); 5 - Udalski et al. (2008); 6 - Graczyk et al. (2011); 7 - Udalski et al. (1998); 8 - Wyrzykowski et al. (2004).

Galaxy	$\langle\log({\rm Z/Z_\odot})\rangle$	Survey	$\mathcal{N}_{\rm B}$	$\mathcal{N}_{\rm EB}$	$\mathcal{N}_{\rm med}$	$\mathcal{F}_{\rm med}$	$\mathcal{N}_{\rm deep}$	$\mathcal{F}_{\rm deep}$	Refs
MW	0.0	Hipparcos	1,596	51	**31**	**(1.94±0.35)%**	**16**	**(1.00±0.25)%**	1,2
LMC	−0.4	OGLE-II	20,974	308	263	(1.25±0.08)%	**145**	**(0.69±0.06)%**	3,4
LMC	−0.4	OGLE-III	69,616	2,024	**1,301**	**(1.87±0.05)%**	**477**	**(0.69±0.03)%**	5,6
SMC	−0.7	OGLE-II	21,035	298	277	(1.32±0.08)%	**147**	**(0.70±0.06)%**	7,8

et al. 2011; Wagner-Kaiser & Sarajedini 2013). We therefore use ${\rm M_I} = {\rm m_I} - 18.8$ to convert apparent magnitudes to intrinsic absolute magnitudes for the LMC. We select relatively unevolved early-B stars with observed colors ${\rm V-I} < 0.1$ and absolute magnitudes $-3.8 < {\rm M_I} < -1.5$ (Cox 2000; Bertelli et al. 2009, see also §2.3.1).

For the LMC, we compare the regularly monitored OGLE-II fields, which covered 4.6 square degrees in the central portions of the galaxy, to the recent OGLE-III data, which extended an additional 35 square degrees into the periphery. We expect these two populations to be similar since there is no significant metallicity gradient in the LMC (Grocholski et al. 2006; Piatti & Geisler 2013). In the central fields of the OGLE-II LMC photometric catalog (Udalski et al. 2000), $\mathcal{N}_{\rm B}$ = 20,974 stars have $15.0 < {\rm I} < 17.3$ and ${\rm V}-{\rm I} < 0.1$. Wyrzykowski et al. (2003) utilized an automated search algorithm to discover eclipsing binaries in the OGLE-II LMC data, and found $\mathcal{N}_{\rm EB} = 308$ systems which meet our magnitude and color cuts as well as have orbital periods between 2 and 20 days. Of these systems, $\mathcal{N}_{\rm med} = 263$ have primary eclipse depths $0.10 < \Delta{\rm I} < 0.65$, resulting in $\mathcal{F}_{\rm med} = (1.25 \pm 0.08)\%$, while $\mathcal{N}_{\rm deep} = 145$ have $0.25 < \Delta{\rm I} < 0.65$, giving $\mathcal{F}_{\rm deep} = (0.69 \pm 0.06)\%$. In the larger OGLE-III LMC footprint of 35 million objects (Udalski et al. 2008), $\mathcal{N}_{\rm B}$ = 69,616 stars remain after we apply the same magnitude and color cuts. Graczyk et al. (2011) used these observations to identify eclipsing binaries, being careful to exclude non-eclipsing phenomena such as ellipsoidal variables, pulsators, etc. They found $\mathcal{N}_{\rm EB}$ = 2,024 eclipsing binaries with primary eclipse periods P = 2 - 20 days and photometric properties which satisfy our selection criteria. From these eclipsing binaries, $\mathcal{N}_{\rm med}$ = 1,301 have $0.10 < \Delta{\rm I} < 0.65$ and $\mathcal{N}_{\rm deep} = 477$ have $0.25 < \Delta{\rm I} < 0.65$, giving $\mathcal{F}_{\rm med} = (1.87 \pm 0.05)\%$ and $\mathcal{F}_{\rm deep} = (0.69 \pm 0.03)\%$, respectively. We display these LMC results for both the OGLE-II and OGLE-III samples in Table 2.1.

Young B stars and massive Cepheids in the SMC exhibit even lower metallicities of $\langle \log({\rm Z}/{\rm Z}_{\odot}) \rangle = -0.7$ (Luck et al. 1998, [Fe/H] $= -0.7 \pm 0.1$; Korn et al. 2000, [Fe/H] ≈ -0.7; Romaniello et al. 2005, [Fe/H] $= -0.7 \pm 0.1$; Keller & Wood 2006, [Fe/H] $= -0.6 \pm 0.1$), providing even greater leverage to test the effects of metallicities.

Compared to the LMC, the SMC is farther away with $\mu = 19.0$, and experiences similar reddening and extinction of E(V−I) = 0.1 and $A_V = 0.4$ (Zaritsky et al. 2002; Haschke et al. 2012). We therefore use $M_I = m_I - 19.3$ and apply the same color and absolute magnitude cuts that we implemented above for the LMC. There are $\mathcal{N}_B = 21{,}035$ stars with $15.5 < I < 17.8$ and $V-I < 0.1$ in the 2.4 square degree OGLE-II SMC field (Udalski et al. 1998). From these primaries, Wyrzykowski et al. (2004) found $\mathcal{N}_{EB} = 298$ eclipsing binaries with $P = 2$ - 20 days. A total of $\mathcal{N}_{med} = 277$ of these systems have $0.10 < \Delta I < 0.65$, giving $\mathcal{F}_{med} = (1.32 \pm 0.08)\%$, and $\mathcal{N}_{deep} = 147$ have $0.25 < \Delta I < 0.65$, resulting in $\mathcal{F}_{deep} = (0.70 \pm 0.06)\%$. We tabulate these SMC results in Table 2.1.

We first compare the deep eclipsing binary fractions $\mathcal{F}_{deep}$ of the different populations listed in Table 2.1. All four surveys were sensitive to these deep eclipses, so that $\mathcal{F}_{deep}$ should be complete. Remarkably, the three OGLE Magellanic Cloud values match each other within the observational uncertainty of ≈10%. The MW fraction is ≈40% larger, but consistent at the 1.2σ level. The uniformity of $\mathcal{F}_{deep}$ demonstrates that the eclipsing binary fraction of early-B stars does not vary with metallicity beyond the observational uncertainties.

Extending toward medium eclipse depths, the values of $\mathcal{F}_{med}$ in Table 2.1 are not as undeviating. Although the MW and LMC OGLE-III samples match within the uncertainty of ≈20%, the OGLE-II fractions for both the LMC and SMC are statistically lower. We can resolve this discrepancy by investigating the observed primary eclipse depth distributions $\mathcal{O}_{\Delta m}(\Delta m)\,d(\Delta m)$, which we display in Figure 2.1. The distributions are normalized to the total number of early-B stars so that $\mathcal{F}_{deep} = \int_{0.25}^{0.65} \mathcal{O}_{\Delta m}(\Delta m)\,d(\Delta m)$, and the plotted errors $\sigma_{\mathcal{O}_{\Delta m}}(\Delta m)$ derive from Poisson statistics. The OGLE-II LMC and SMC data become incomplete at $\Delta m < 0.25$ due to the lower photometric precision

of the survey, which leads to the underestimation of $\mathcal{F}_{\rm med}$. However, $\mathcal{O}_{\Delta \rm m}$ for all four samples are consistent with each other across the interval for deep eclipses $0.25 < \Delta$m < 0.65, demonstrating again that the close binary properties of early-B stars do not strongly depend on metallicity. Using the large and complete LMC OGLE-III sample for eclipse depths $0.10 < \Delta \rm m < 0.65$, we fit a simple power-law to the eclipse depth distribution. We find $\mathcal{S}_{\Delta \rm m}\,{\rm d}(\Delta {\rm m}) \propto (\Delta {\rm m})^{-1.65 \pm 0.07}\,{\rm d}(\Delta {\rm m})$, which we display as the dashed black line in Figure 2.1. If this distribution extends toward shallower eclipses, then many additional eclipsing systems may be hiding with $\Delta \rm m < 0.1$. We return to our discussion of incompleteness corrections in the next section when we conduct Monte Carlo simulations.

In Figure 2.2, we plot the observed period distributions of eclipsing binaries exhibiting deep eclipses $\mathcal{O}_{\rm deep}(P)\,{\rm d}(\log P)$ for the three OGLE samples (top panel). We also display the observed period distributions of systems with medium through deep eclipses $\mathcal{O}_{\rm med}(P)\,{\rm d}(\log P)$ for the complete MW and LMC OGLE-III populations (bottom panel). Again, we normalize the observed period distributions to the total number of early-B stars so that $\mathcal{F}_{\rm deep} = \int_{\log\ 2}^{\log\ 20} \mathcal{O}_{\rm deep}(P)\,{\rm d}(\log P)$ and $\mathcal{F}_{\rm med} = \int_{\log\ 2}^{\log\ 20} \mathcal{O}_{\rm med}(P)\,{\rm d}(\log P)$. The number of eclipsing binaries dramatically increases toward shorter periods, primarily because of geometrical selection effects. If we ignore limb darkening and tidal distortions, then the probability of eclipses would scale as $\mathcal{P} \propto P^{-2/3}$ based on Kepler's third law. If the binaries were distributed uniformly with respect to $\log P$ according to Öpik's law (Öpik 1924; Abt 1983), we would then expect $\mathcal{S}_{\rm deep}(P)\,{\rm d}(\log P) \propto \mathcal{S}_{\rm med}(P)\,{\rm d}(\log P) \propto P^{-2/3}\,{\rm d}(\log P)$. We display these theoretical curves as the dashed black lines in Figure 2.2, where the normalization is chosen to guide the eye. The distributions are shifted slightly toward shorter periods relative to Öpik's

prediction, especially the OGLE-II SMC data.

Although the $\mathcal{O}_{\rm deep}(P)$ distributions for the OGLE-II and OGLE-III LMC data are consistent with each other, the OGLE-II SMC distribution is discrepantly skewed toward

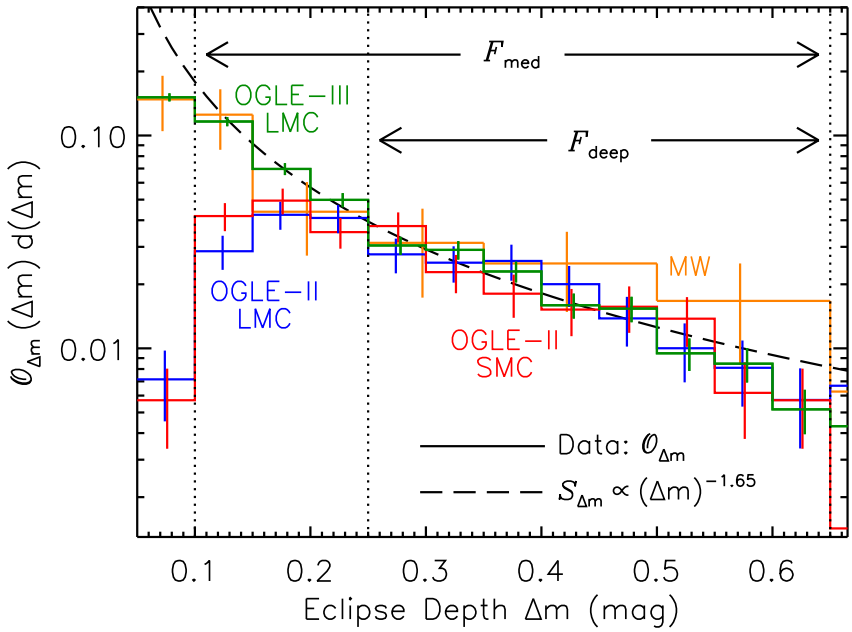

Figure 2.1: The observed primary eclipse depth distribution $\mathcal{O}_{\Delta \rm m}$ with orbital periods $P = 2\text{-}20$ days for early-B stars in the Hipparcos MW (orange), OGLE-II LMC (blue), OGLE-III LMC (green), and OGLE-II SMC (red) samples. The observed slopes and overall normalizations to $\mathcal{F}_{\rm deep} = \int_{0.25}^{0.65} \mathcal{O}_{\Delta \rm m}(\Delta \rm m)\, \rm d(\Delta m) = (0.7\text{-}1.0)\%$ of all four samples are consistent with each other across the interval for deep eclipses $0.25 < \Delta \rm m < 0.65$, demonstrating that the eclipsing binary properties do not substantially change with metallicity. The OGLE-II data for both the LMC and SMC become incomplete toward shallower eclipses $\Delta \rm m \lesssim 0.25$, while the OGLE-III LMC distribution is relatively complete down to $\Delta \rm m = 0.10$ and is well approximated by a simple power-law $\mathcal{S}_{\Delta \rm m}$ (dashed black).

shorter periods. A K-S test between the OGLE-II LMC and SMC unbinned $\mathcal{O}_{\rm deep}(P)$ distributions reveals a probability that they derive from the same parent population of only $p_{\rm KS} = 0.004$. Similarly, the probability of consistency between the OGLE-II SMC and OGLE-III LMC unbinned $\mathcal{O}_{\rm deep}(P)$ data is $p_{\rm KS} = 0.01$. However, the SMC eclipsing binaries are systematically 0.5 magnitudes fainter, so it is conceivable that some long period systems with shallower eclipses and eclipse durations ≈5% of the total orbital period may have remained undetected in this survey (see Söderhjelm & Dischler 2005). In fact, we find that all three OGLE samples are consistent with each other, i.e. $p_{\rm KS} > 0.1$, if we only consider the parameter space of eclipsing binaries with $P = 2$ - 10 days and Δm = 0.30 - 0.65. We investigate this feature with more robust light curve modeling and Monte Carlo calculations in the next section.

2.3 Correction for Selection Effects

We have determined that $\mathcal{F}_{\rm deep} \approx 0.7\%$ for all three OGLE samples of eclipsing binaries in the Magellanic Clouds. The Hipparcos MW value is ≈40% higher, but consistent at the 1.2σ level. Also, both the MW and OGLE-III LMC samples have an observed eclipsing binary fraction with medium eclipse depths of $\mathcal{F}_{\rm med} \approx 1.9\%$.

In order to make a more stringent comparison, we need to convert the observed eclipsing binary fractions into actual close binary fractions $\mathcal{F}_{\rm close}$. We define $\mathcal{F}_{\rm close}$ to be the fraction of systems which have a companion with orbital period 2 days $\leq P \leq$ 20 days and mass ratio $0.1 \leq q \equiv M_{\rm comp}/M_1 \leq 1$. We must therefore correct for geometrical selection effects and incompleteness toward low-mass companions. Our ultimate goal is to utilize the observed properties $\mathcal{O}$ of the eclipsing binary systems, e.g.

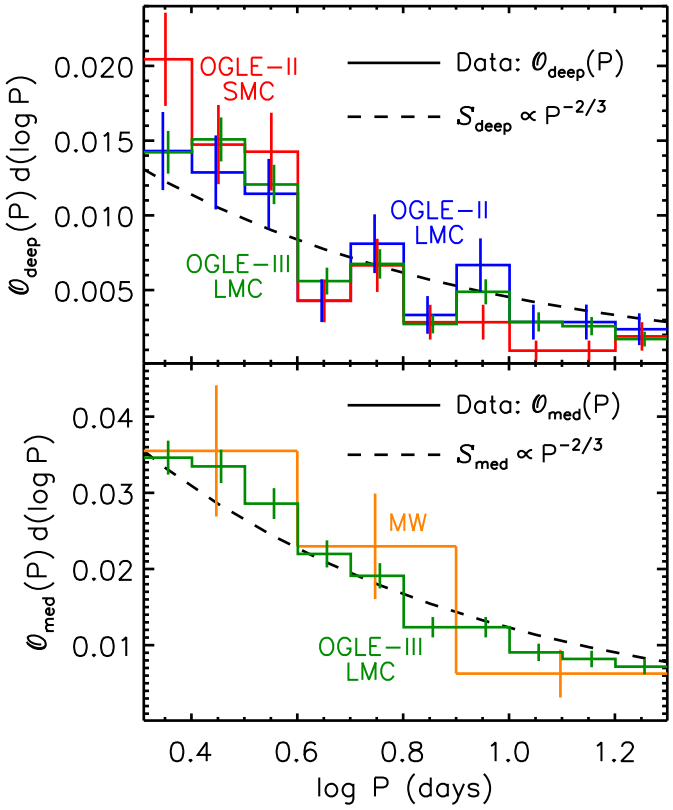

Figure 2.2: The observed orbital period distribution of systems exhibiting deep eclipses $\mathcal{O}_{\rm deep}(P)$ (top panel) for the OGLE-II LMC (blue), OGLE-III LMC (green), and OGLE-II SMC (red) samples, and larger population of medium through deep eclipses $\mathcal{O}_{\rm med}(P)$ (bottom panel) for the complete MW (orange) and OGLE-III LMC (green) samples. The distributions are normalized to the total number of early-B stars so that $\mathcal{F}_{\rm deep} = \int_{\log\ 2}^{\log\ 20} \mathcal{O}_{\rm deep}(P)\,{\rm d}(\log P) \approx 0.7\%$ and $\mathcal{F}_{\rm med} = \int_{\log\ 2}^{\log\ 20} \mathcal{O}_{\rm med}(P)\,{\rm d}(\log P) \approx 1.9\%$. By making simple approximations and assuming close binaries follow Öpik's law, we would expect $\mathcal{S}_{\rm deep}(P)\,{\rm d}(\log P) \propto \mathcal{S}_{\rm med}(P)\,{\rm d}(\log P) \propto P^{-2/3}\,{\rm d}(\log P)$ for the eclipsing binary period distribution (dashed black in both panels). The observed distributions are weighted toward shorter periods compared to Öpik's prediction, especially the OGLE-II SMC sample.

$\mathcal{F}_{\rm deep}$ or $\mathcal{F}_{\rm med}$, $\mathcal{O}_{\rm deep}(P)$ or $\mathcal{O}_{\rm med}(P)$, and $\mathcal{O}_{\Delta \rm m}(\Delta \rm m)$, to derive the underlying properties $\mathcal{U}$ of the close binary population, e.g. $\mathcal{F}_{\rm close}$, intrinsic period distribution $\mathcal{U}_{\rm P}(P)$, and mass-ratio distribution $\mathcal{U}_{\rm q}(q)$. Although the observational biases of eclipsing binaries have been investigated in the literature (e.g. Farinella & Paolicchi 1978; Halbwachs 1981; Söderhjelm & Dischler 2005), we wish to conduct detailed modeling specifically suited to our samples in order to accurately quantify the errors.

For a given binary with primary mass M_1, mass ratio q, age τ, metallicity Z, and orbital period P, there is a certain probability $\mathcal{P}$ that the system has an orientation which produces eclipses. There are even smaller probabilities $\mathcal{P}_{\rm med}$ and $\mathcal{P}_{\rm deep}$ that the system has an eclipse depth Δm which is large enough to be observed in the Hipparcos and OGLE data. We determine these probabilities by first implementing detailed light curve models to compute the eclipse depths Δm of various binary systems as a function of inclination i (§2.3.1). Using a Monte Carlo technique (§2.3.2), we simulate a large population of binaries and synthesize models of the eclipse depth distribution $\mathcal{M}_{\Delta \rm m}(\Delta \rm m)$ and the eclipsing binary period distributions $\mathcal{M}_{\rm deep}(P)$ and $\mathcal{M}_{\rm med}(P)$. We perform thousands of Monte Carlo simulations by making different assumptions regarding the intrinsic period distribution $\mathcal{U}_{\rm P}$ and mass-ratio distribution $\mathcal{U}_{\rm q}$. By minimizing the χ^2 statistic between our Monte Carlo models $\mathcal{M}$ and observed eclipsing binary data $\mathcal{O}$, we can determine the probabilities of observing eclipses $\mathcal{P}_{\rm deep}$ and $\mathcal{P}_{\rm med}$ as well as the underlying binary properties $\mathcal{U}$ for each of our populations (§2.3.3). We then account for Malmquist bias in our magnitude-limited samples (§2.3.4), and present our finalized results for $\mathcal{F}_{\rm close}$ and corrected intrinsic period distribution $\mathcal{U}_{\rm P}$ (§2.3.5).

2.3.1 Light Curve Modeling

To simulate eclipse depths Δm, we use the eclipsing binary light curve modeling software NIGHTFALL[2]. We incorporate many features of this package, including a square-root limb darkening law, tidal distortions, gravity darkening, model stellar atmospheres, and three iterations of mutual irradiation between the two stars. For the majority of close binaries with $P = 2$ - 20 days, tides have partially or completely synchronized the orbits as well as dramatically reduced the eccentricities (Zahn 1977), so we assume synchronous rotation and circular orbits in our models. Magnetic bright spots on the surface of massive stars are expected to produce small 10^{-3} mag variations over short durations of days (Cantiello & Braithwaite 2011). Because OGLE and Hipparcos observed the eclipsing binaries over a much longer timespan of years with less photometric precision, we can ignore the effects of starspots. We compute the NIGHTFALL models without any third light contamination, but consider the effects of triple star systems and stellar blending in the crowded Magellanic Cloud OGLE fields using a statistical method. We now synthesize eclipse depths Δm for the OGLE Magellanic Clouds and Hipparcos MW samples.

Magellanic Clouds

To model the OGLE eclipsing binaries, we utilize the Z=0.004, Y=0.26 stellar tracks from the Padova group (Bertelli et al. 2008, 2009), which correspond to a metallicity between the SMC and LMC mean values. In addition to basic parameters such as radii $R(\tau)$ and photospheric temperatures $T(\tau)$ as a function of stellar age τ, we also extract the surface

[2]http://www.hs.uni-hamburg.de/DE/Ins/Per/Wichmann/Nightfall.html

gravities $g(\tau)$ from the stellar tracks in order to select appropriate model atmospheres in NIGHTFALL. We convert stellar radii to Roche lobe filling factors according to the volume-averaged formula given by Eggleton (1983). Although NIGHTFALL defines the Roche lobe filling factor along the polar axis, it is more appropriate to use the Eggleton (1983) approximation in cases where the star fills a large fraction of its Roche lobe and is therefore distorted along this potential. In any case, the volume-averaged Roche lobe radius is only $\approx 7\%$ larger than the polar Roche lobe radius for systems in our sample, so any systematics due to using the Eggleton (1983) formula as input are small. Based on the numerical calculations performed by Claret (2001) and his comparison to empirical results, we choose an albedo of A = 1.0 for our primary and secondaries hotter than $T >$ 7,500K with radiative envelopes ($M_2 \geq 1.3\,\mathrm{M}_\odot$), and A = 0.75 for low-mass secondaries ($M_2 < 1.3\,\mathrm{M}_\odot$) at lower temperatures with convective atmospheres.

Because we selected the OGLE samples from a narrow range of absolute magnitudes, we can assume that all eclipsing binaries have the same primary mass. If the luminosity of the primary is dominant, then the median absolute magnitude of $M_\mathrm{I} \approx -2.1$ in the OGLE samples corresponds to a primary mass of $M_1 = 12\,\mathrm{M}_\odot$, where we have interpolated the stellar tracks from Bertelli et al. (2009) at half the MS lifetimes as well as utilized bolometric corrections and color indices from Cox (2000). However, if the typical secondary in the observed eclipsing systems increases the brightness by $\Delta\mathrm{M_I} \approx 0.3$ mag (see §2.3.4), then the primary's absolute magnitude of $\mathrm{M_I} \approx -1.8$ corresponds to $M_1 = 10\,\mathrm{M}_\odot$. We therefore adopt $M_1 = 10\,\mathrm{M}_\odot$ for all primaries in our simulations.

We must still consider the systematic error in $\mathcal{F}_\mathrm{close}$ due to this single-mass primary approximation. The sample distributions of absolute magnitudes $\mathrm{M_I}$ have a dispersion of

$\sigma_{\rm M_I} \approx 0.4$ mag, which implies a dispersion in M_1 of ≈25%. According to the mass-radius relation $R \propto M^{0.6}$ and Kepler's law $a \propto M^{1/3}$, then the probability of observing eclipses $\mathcal{P}_{\rm deep} \propto \mathcal{P}_{\rm med} \propto R/a \propto M_1^{0.3}$ due to geometrical selection effects is only weakly dependent on M_1. The systematic error in our derived $\mathcal{F}_{\rm close} = \mathcal{F}_{\rm deep}/\langle\mathcal{P}_{\rm deep}\rangle = \mathcal{F}_{\rm med}/\langle\mathcal{P}_{\rm med}\rangle$ is therefore only a factor of 7% due to the observed dispersion in primary absolute magnitudes $\sigma_{\rm M_I} \approx 0.4$ mag. Similarly, the extinction distributions toward young stars in the Magellanic Clouds have a dispersion of $\sigma_{\rm A_V} \approx 0.3$ mag (Zaritsky 1999; Zaritsky et al. 2002), and the I-band excess distributions from the eclipsing companions have a dispersion of $\sigma_{\Delta\rm M_I} \approx 0.2$ mag (see §2.3.4). These effects contribute additional systematic error factors in $\mathcal{F}_{\rm close}$ of 6% and 4%, respectively. By adding these three sources of uncertainty in quadrature, we find the total systematic error in $\mathcal{F}_{\rm close}$ is only a factor of 10% due to our single-mass primary approximation. In our estimate for $\mathcal{P}_{\rm deep} \propto \mathcal{P}_{\rm med} \propto M_1^{0.3}$, we have assumed the mass-ratio distributions, and therefore the *slopes* of the eclipse depth distributions, do not substantially vary across our narrowly selected interval of primary masses. In fact, for the OGLE-III LMC medium eclipse depth sample, we find $\mathcal{S}_{\Delta\rm m} \propto (\Delta\rm m)^{-1.54\pm0.12}$ for the 563 eclipsing binaries brighter than $M_{\rm I} = -2.3$, and $\mathcal{S}_{\Delta\rm m} \propto (\Delta\rm m)^{-1.74\pm0.11}$ for the 738 systems fainter than $M_{\rm I} = -2.3$. The consistency of these two slopes justifies our approximation, and therefore our assessment of the systematic error in $\mathcal{F}_{\rm close}$ is valid.

Because we restricted our samples to observed colors V−I < 0.1, i.e. $T_1 \gtrsim 10{,}000\,\rm K$ once reddening is taken into account, most primaries are relatively unevolved on the MS. For example, a Z = 0.004, $M_1 = 10\,\rm M_\odot$ primary evolves from $R_1 = 3.3\,\rm R_\odot$, $T_1 = 28{,}000\,\rm K$ on the zero-age MS (luminosity class V) to $R_1 = 8.5\,\rm R_\odot$, $T_1 = 22{,}000\,\rm K$ at the top of the MS by age $\tau_{\rm MS} = 23$ Myr (technically luminosity class III). The star then

rapidly expands and cools, passing from $R_1 = 9.0\,\mathrm{R}_\odot$ to $\mathrm{T}_1 = 10{,}000\,\mathrm{K}$ in $\delta t \approx 30{,}000$ yrs. Considering $\delta t\,/\,\tau_{\mathrm{MS}} \sim 10^{-3}$, the contamination by the few, short-lived bona fide giants with $\tau > \tau_{\mathrm{MS}}$ is negligible.

We calculate the I-band light curve at 1% phase intervals across the orbit, where we include the effects of fractional visibility of surface elements computed by NIGHTFALL. Because the OGLE eclipsing binary catalogs reported eclipse depths in the I-band as the difference between the dimmest and mean out-of-eclipse magnitudes, we set the zero point magnitude in the NIGHTFALL models to the mean value across the phase interval 0.2 - 0.3. We display some example light curves in Figure 2.3. The three panels represent orbital periods of $P = 2$, 6.3, and 20 days, while the colors distinguish various mass ratios $q = M_2/M_1$. We compute the light curves at inclinations $i = 77.3^{\mathrm{o}}$, 84.1^{o}, and 87.3^{o} from left to right so that the projected separations $a_{\mathrm{proj}} \propto P^{2/3}\cos i = \text{constant}$. For spherical stars, the eclipse depths should therefore be identical across these three panels for the same mass ratios. We evaluate these example models at age $\tau = 17$ Myr when the primary reaches an intermediate radius of $R_1 = 5.3\,\mathrm{R}_\odot$.

The left panel of Figure 2.3 with $P = 2$ days corresponds to primaries filling 60-80% of their Roche lobes, depending on the mass ratio. The light curves of these close binaries exhibit pronounced ellipsoidal modulations, while the out-of-eclipse magnitudes of systems at longer orbital periods are relatively constant. In the right panel with $P =$ 20 days, the narrow eclipse widths of 4% are just at the detectability limit ofF eclipsing binary identification algorithms (Söderhjelm & Dischler 2005).

A simple estimate for the eclipse depths can be derived by calculating the bolometric flux in the eclipsed area of the primary assuming spherical stars and no limb darkening.

We compare the NIGHTFALL models to this simple approximation for the maximum eclipse depth (horizontal dotted lines centered on primary eclipses). For $P = 2$ days, the actual eclipse depths determined by NIGHTFALL are generally deeper than the simple approximations because tidal distortions and reflection effects enhance the light curve amplitudes. Alternatively, the NIGHTFALL results for longer period systems at $P = 6.3$ and 20 days are typically shallower than the simple approximations because the actual flux eclipsed along grazing angles is less due to the effect of limb darkening.

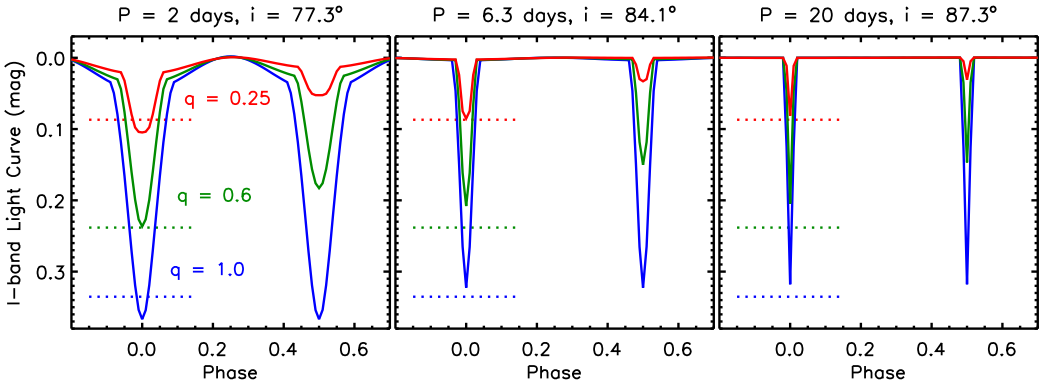

Figure 2.3: Simulated I-band light curves as a function of orbital phase computed by NIGHTFALL for various mass ratios $q = M_2/M_1$ (distinguished by colors). The left, middle, and right panels correspond to orbital periods of $P = 2$, 6.3, and 20 days, respectively, and at the listed inclinations i which satisfy $P^{2/3}\cos i$ = constant. All models are evaluated with primary mass $M_1 = 10\,\mathrm{M}_\odot$ at age $\tau = 17$ Myr when $R_1 = 5.3\,\mathrm{R}_\odot$. We compare the detailed NIGHTFALL light curves to simplistic estimates of the maximum eclipse depths which ignore tidal distortions, limb darkening, and color dependence (horizontal dotted lines centered on primary eclipse). The detailed NIGHTFALL models differ from the simple estimates by 0.00 - 0.04 mag for these systems, but can reach up to 0.16 mag for older, short-period binaries nearly filling their Roche lobes.

Because the OGLE eclipsing binary catalogs exclude ellipsoidal variables that did not exhibit genuine eclipses, we consider only systems with inclinations $i > i_{\rm crit} \equiv \cos^{-1}([R_1 + R_2]/a)$. We use NIGHTFALL to produce a dense grid of eclipse depths $\Delta m(\tau, q, P, i)$ in our parameter space of stellar ages $\tau = [0, \tau_{\rm MS} = 23$ Myr], mass ratios $q = [0.1, 1]$, orbital periods P(days) $= [2, 20]$, and inclinations $i = [i_{\rm crit}, 90^{\rm o}]$. In the three panels of Figure 2.4, we plot our simulated Δm as a function of inclination i for the same three orbital periods, various mass ratios indicated by color, and for the same $\tau = 17$ Myr that gives $R_1 = 5.3\,{\rm R}_\odot$.

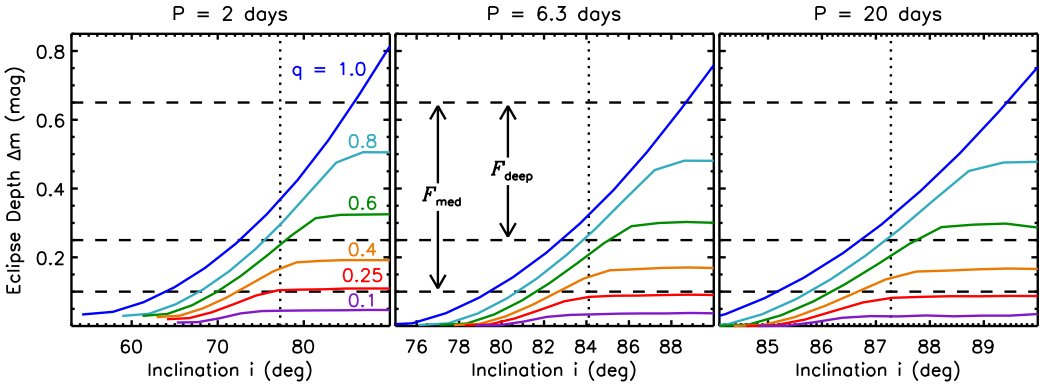

Figure 2.4: Maximum eclipse depths Δm as a function of inclination $i > i_{\rm crit} \equiv \cos^{-1}([R_1 + R_2]/a)$ computed using NIGHTFALL for various mass ratios $q = M_2/M_1$ (distinguished by colors) and three orbital periods (different panels). We compute the models with the same primary mass M_1, age τ, and three orbital periods P as in Figure 2.3, where the vertical dotted lines represent the inclinations of the systems used to display the light curves. We also indicate our adopted definition for deep eclipses and the extension toward medium eclipse depths (horizontal dashed lines). The range of inclinations which produce observable eclipses decreases with increasing P simply due to geometrical selection effects.

The short-period systems in the left panel of Figure 2.4 are significantly affected by tidal distortions. The twin system with $q = 1$ observed edge-on at $i = 90^{\rm o}$ exceeds the maximum eclipse depth limit for spherical stars of $\Delta{\rm m} = 0.75$. Ellipsoidal variables which barely miss eclipses with $i = i_{\rm crit}$ all have light curve amplitudes of $\Delta{\rm m} < 0.05$ for this set of parameters (see where curves terminate at bottom left). For systems which do not fill their Roche lobes, all ellipsoidal variables with $i = i_{\rm crit}$ have amplitudes $\Delta{\rm m} < 0.09$. Granted, some systems with $i > i_{\rm crit}$ may not have strong enough eclipse features to be included in the catalog of eclipsing binaries. Nevertheless, this transition between ellipsoidal variability and genuine eclipses occurs at $\Delta{\rm m} \lesssim 0.1$, so we can be assured that very few eclipsing systems with measured amplitudes $\Delta{\rm m} > 0.1$ have been excluded from the catalogs.

The middle and right panels of Figure 2.4 represent progressively longer orbital periods where tidal distortions and reflection effects become negligible. Note the smaller range of inclinations which produce observable eclipses, simply due to geometrical selection effects. We display with horizontal dashed lines our adopted intervals for deep eclipses and extension toward medium eclipse depths. Assuming the middle panel is most representative of close binaries with $P = 2$ - 20 days, then $i > 85^{\rm o}$ and $q > 0.55$ are required to observe deep eclipses. Given random orientations, the correction factor for geometrical selection effects alone is $\mathcal{C}_{\rm deep,i} \approx 1/\cos(85^{\rm o}) \approx 11$. Assuming a uniform mass-ratio distribution over the interval $q = [0.1, 1.0]$, the correction factor for incompleteness toward low-mass companions alone is $\mathcal{C}_{\rm deep,q} \approx \frac{1-0.1}{1-0.55} \approx 2$. The overall probability of observing a system with a deep eclipse is therefore $\langle \mathcal{P}_{\rm deep} \rangle = (\mathcal{C}_{\rm deep,i} \times \mathcal{C}_{\rm deep,q})^{-1} \approx 0.04$. Similarly, $i > 83^{\rm o}$ and $q > 0.3$ are required to observe eclipses with medium depths, implying $\mathcal{C}_{\rm med,i} \approx 8$, $\mathcal{C}_{\rm med,q} \approx 1.3$, and $\langle \mathcal{P}_{\rm med} \rangle \approx 0.09$. These two

overall probabilities imply similar close binary fractions of $\mathcal{F}_{\rm close} = \mathcal{F}_{\rm deep} \,/\, \langle \mathcal{P}_{\rm deep} \rangle = 0.7\% \,/\, 0.04 \approx 16\%$ and $\mathcal{F}_{\rm close} = \mathcal{F}_{\rm med} \,/\, \langle \mathcal{P}_{\rm med} \rangle = 1.9\% \,/\, 0.09 \approx 20\%$. We obtain more precise values in §2.3.3 by fitting the observed eclipse depth and period distributions to constrain the actual binary properties.

In Figure 2.5, we display simulated eclipse depths from NIGHTFALL similar to Figure 2.4, but for constant $P = 2.9$ days and three different stages of evolution. The left panel corresponds to zero-age MS systems where the primary radius is $R_1 = 3.3\,{\rm R}_\odot$, the middle panel represents an intermediate age binary when $R_1 = 5.3\,{\rm R}_\odot$, and the right panel is for the top of the primary's MS with $R_1 = 8.5\,{\rm R}_\odot$. For young systems, $q = 0.1$ is just at the detectability threshold in our medium eclipse depth samples, which is the primary reason we set the lower limit of our mass-ratio interval to this value. With increasing τ and R_1, the range of inclinations which produce visible eclipses increases due to geometrical selection effects. However, the depths of eclipses for $q \lesssim 0.9$ become smaller because the fractional area of the primary that is eclipsed decreases with increasing primary radius. Therefore, our samples of eclipsing binaries are rather incomplete toward smaller, low-mass companions. For young systems, the probability of observing a low-mass secondary is low, while for older systems the eclipse depths produced by low-mass companions are below the sensitivity of the surveys.

There is a narrow corner of the parameter space with $P \lesssim 2.6$ days and $R_1 \gtrsim 7.0\,{\rm R}_\odot$ where the primary overfills its Roche lobe. We assume that either merging or onset of rapid mass transfer causes these systems to evolve outside the parameter space $0.1 < \Delta{\rm m} < 0.65$. In our Monte Carlo simulations (§2.2.3), we include their contribution toward the close binary fraction, but remove these systems as eclipsing binaries when fitting $\mathcal{O}_{\Delta{\rm m}}(\Delta{\rm m})$ and either $\mathcal{O}_{\rm deep}(P)$ or $\mathcal{O}_{\rm med}(P)$. A $10\,{\rm M}_\odot$ star spends 8% of its MS

evolution with $R_1 > 7.0\,R_\odot$, and (20 - 30)% of the eclipsing binaries in our samples have orbital periods $P < 2.6$ days, depending on the survey. Therefore, the systematic error in our evaluation of the close binary fraction due to these few evolved, close, Roche-lobe filling binaries is only 2%.

For systems which produce eclipse depths $\Delta m > 0.25$ and are not filling their Roche lobes, the root-mean-square deviation between the detailed NIGHTFALL simulations and simple approximations which ignore limb darkening and tidal distortions is $\langle\delta(\Delta m)\rangle$ = 0.05 mag. The difference reaches a maximum value of 0.16 mag for a close period, evolved twin system with $q = 1$ which nearly fills its Roche lobes. Because of these measurable systematics, it is important that we incorporate the NIGHTFALL results instead of relying on the simple estimates.

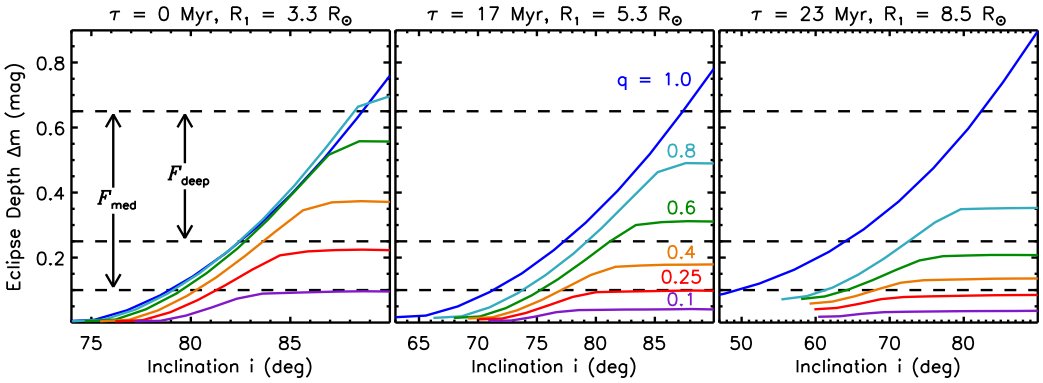

Figure 2.5: Similar to Figure 2.4, but for the same orbital period of $P = 2.9$ days and for three different ages τ on the MS of a $10\,M_\odot$ primary. Note the range of inclinations which produce observable eclipses increases with increasing age, while for $q \lesssim 0.9$ the eclipse depths diminish with age.

Milky Way

We repeat our procedure to model eclipse depths Δm for the Hipparcos MW sample of eclipsing binaries, but with some slight modifications. We still assume all primaries have $M_1 = 10\,\mathrm{M}_\odot$ because the mean spectral type of our sample is B2, but implement the solar metallicity Z=0.017, Y=0.26 tracks from the Padova group (Bertelli et al. 2008, 2009). A solar-metallicity $10\,\mathrm{M}_\odot$ star has a slightly longer lifetime of $\tau_{\rm MS} \approx 25$ Myr, and more importantly is (15 - 25)% larger depending on the stage of evolution. The primary radius is $R_1 = 3.8\,\mathrm{R}_\odot$ on the zero-age MS versus $R_1 = 3.3\,\mathrm{R}_\odot$ for the Z=0.004 model, and reaches $R_1 = 10.5\,\mathrm{R}_\odot$ at the top of the MS compared to $R_1 = 8.5\,\mathrm{R}_\odot$ for the low-metallicity track. For the same close binary properties, we actually expect $\mathcal{F}_{\rm deep}$ in the MW to be 20% higher because the probability of eclipses scales as $\mathcal{P} \propto (R_1 + R_2)$. This radius-metallicity relation diminishes the already small 1.2σ difference between the MW and Magellanic Cloud statistics inferred from $\mathcal{F}_{\rm deep}$. Finally, we evaluate the eclipse depth Δm based on the V-band light curves computed by NIGHTFALL, which closely approximates the Hipparcos passband.

Third Light Contamination

A third light source can have a much larger effect on the observed eclipse depth Δm of an eclipsing binary, depending on the luminosity of the contaminant. We first consider wider companions in triple star systems. About 40% of early-type primaries have a visually resolved companion (Turner et al. 2008; Mason et al. 2009). More importantly, most close binaries, such as our eclipsing systems, are observed to be the inner components of triple star systems (Tokovinin et al. 2006). Specifically, this study found that 96%

of binaries with $P < 3$ days have a wider tertiary companion. Assuming the typical eclipsing secondary increases the brightness by ΔM = 0.3 mag (see §2.3.4), then a tertiary companion with $q = M_3/M_1 > 0.5$ is capable of increasing the system luminosity by $\gtrsim$10%. The wider companions around early-type primaries are observed to be drawn from a mass-ratio distribution weighted toward lower mass, fainter stars (Abt et al. 1990; Preibisch et al. 1999; Duchêne et al. 2001; Shatsky & Tokovinin 2002). These observations find that only (10 - 30)% of wide companions have mass ratios $q > 0.5$. Even if every eclipsing binary has one wider component, we would expect that only ≈20% of tertiaries have large enough luminosities to measurably affect our light curve modeling.

We also consider third light contamination due to stellar blending in the crowded Magellanic Cloud fields. Based on the OGLE photometric catalogs, there are 4.2 million (Udalski et al. 2000), 12 million (Udalski et al. 2008), and 1.5 million (Udalski et al. 1998) systems with $M_I > 1.2$ in the OGLE-II LMC, OGLE-III LMC, and OGLE-II SMC footprints, respectively. The median absolute magnitude of these sources is $M_I \approx 0.4$, which is 10% the I-band luminosity of our median early-B eclipsing binary with $M_I \approx -2.1$. The average space densities of stars with $M_I > 1.2$ are 0.07, 0.03, and 0.05 objects per square arcsecond in the OGLE-II LMC, OGLE-III LMC, and OGLE-II SMC fields, respectively. Given a median seeing of 1.2″-1.3″ during the OGLE observations, we expect only (5 - 12)% of early-B eclipsing binaries to be blended with sources brighter than $M_I = 1.2$. The probability of stellar blending with a background/foreground source is slightly smaller than the probability of contamination in a triple star system, where in both cases we included third light components $\gtrsim$10% the luminosity of the eclipsing system.

Because a sizable fraction of eclipsing binaries are affected by third light

contamination from stellar blending and triples systems, we model the third light sources in the eclipsing binary populations using a statistical method. When we conduct our Monte Carlo simulations in the next section, we synthesize distributions of eclipse depths Δm based on our NIGHTFALL models, but assume that a 20% random subset of eclipsing systems have reduced eclipse depths $\Delta m_{measured} = 0.8\,\Delta m_{true}$. These values approximate the probabilities and representative luminosities of the third light contaminants. By comparing our model fits with and without the third light sources, we can gauge the effect on our derived close binary properties.

2.3.2 Monte Carlo Simulations

The eclipsing binary samples provide the distributions of observed orbital periods and eclipse depths. We would like to use this information to learn as much as possible about the properties of the close binary populations in the different environments. To do this, we use the fact that the eclipse depths $\Delta m(M_1,\, q,\, Z,\, \tau,\, P,\, i)$ are determined by six physical properties of the binary. Based on our single-mass approximation discussed in §2.3.1, we only consider $M_1 = 10 M_\odot$ primaries and propagate the systematic error from this approximation into our finalized results for the close binary fraction. We also evaluate our models for two main metallicity groups: one using the Z=0.004 stellar tracks and I-band eclipse depths to be compared to the three OGLE Magellanic Cloud samples, and one using the Z=0.017 stellar tracks and V-band eclipse depths to be compared to the Hipparcos MW data. The four remaining binary properties τ, i, P, and q are characterized by the distribution functions below, some of which have one or more free parameters $\vec{x}$. To simulate a population of binaries, we use a random number generator

to select systems from these distribution functions. We then conduct a set of Monte Carlo simulations, where each simulation is characterized by a particular combination of model parameters $\vec{x}$.

Because the star formation rates of the Magellanic Clouds (Indu & Subramaniam 2011) and local solar neighborhood in the MW (de la Fuente Marcos & de la Fuente Marcos 2004) have not dramatically changed over the most recent $\tau_{\rm MS} \approx 24$ Myr, we select $10\,{\rm M}_{\odot}$ primaries from a uniform age distribution across the interval $\tau = [0,\, \tau_{\rm MS}]$. The close binary fraction $\mathcal{F}_{\rm close}$ is one of the free parameters $\vec{x}$. For each binary, we assume random orientations and select $\cos\,i$ from a uniform distribution in the range $\cos\,i = [0,\, 1]$. We select an orbital period from the distribution:

$$\mathcal{U}_{\rm P}(P)\,{\rm d}(\log P) = \mathcal{K}_{\rm P}\,P^{\gamma_{\rm P}}\,{\rm d}(\log P) \tag{2.1}$$

across the interval $\log 2 \leq \log P\,({\rm days}) \leq \log 20$. For a given Monte Carlo simulation, we fix the period exponent $\gamma_{\rm P}$, but consider 21 different values in the range $-1.5 \leq \gamma_{\rm P} \leq 0.5$ evaluated at $\Delta\gamma_{\rm P} = 0.1$ intervals when synthesizing different populations of binaries. Note that Öpik's law gives $\gamma_P = 0$. The normalization constant $\mathcal{K}_{\rm P}$ satisfies $\mathcal{F}_{\rm close} = \int_{\log\,2}^{\log\,20} \mathcal{U}_{\rm P}(P)\,{\rm d}(\log\,P)$.

Although the mass-ratio distribution is typically described as a power-law, there is evidence that close binaries harbor an excess fraction of twins with mass ratios approaching unity (Tokovinin 2000; Halbwachs et al. 2003; Lucy 2006; Pinsonneault & Stanek 2006). We therefore implement a two-parameter formalism:

$$\mathcal{U}_{\rm q}(q)\,{\rm d}q = \mathcal{K}_{\rm q}\Big[\frac{1-\mathcal{F}_{\rm twin}}{15}\,e^{\gamma_q}\,q^{\gamma_q} + \mathcal{F}_{\rm twin}\,q^{15}\Big]{\rm d}q \tag{2.2}$$

over the interval $0.1 \leq q \leq 1$. We consider 36 values for the mass-ratio exponent in the range $-2.5 \leq \gamma_{\rm q} \leq 1.0$ evaluated at $\Delta\gamma_{\rm q} = 0.1$ intervals, and 16 values for the excess twin fraction in the range $0 \leq \mathcal{F}_{\rm twin} \leq 0.3$ at $\Delta\mathcal{F}_{\rm twin} = 0.02$ intervals. Again, the normalization constant $\mathcal{K}_{\rm q}$ satisfies $\mathcal{F}_{\rm close} = \int_{0.1}^{1} \mathcal{U}_{\rm q}(q)\,{\rm d}q$. The coefficients in the above equation approximate the relative contribution of the two terms so that the integrated fraction of close binaries in the peak toward unity is $\mathcal{F}_{\rm twin}$ while the total fraction of close binaries in the low-q tail is $1 - \mathcal{F}_{\rm twin}$.

Once we have selected a binary with age τ, inclination i, period P, and mass ratio q, we determine its eclipse depth by interpolating our grid of models $\Delta{\rm m}(\tau,\, i,\, P\; q)$. We simulate 10^6 binaries for each combination of parameters $\gamma_{\rm P}$, $\gamma_{\rm q}$, and $\mathcal{F}_{\rm twin}$, resulting in $21 \times 36 \times 16 = 12{,}096$ sets of Monte Carlo simulations. The fourth free parameter $\mathcal{F}_{\rm close}$ determines the overall normalization, and we consider 71 different values in the range $0.05 \leq \mathcal{F}_{\rm close} \leq 0.4$ evaluated at $\Delta\mathcal{F}_{\rm close} = 0.005$ intervals.

For each combination of parameters $\vec{x} = \{\gamma_{\rm P},\, \gamma_{\rm q},\, \mathcal{F}_{\rm twin},\, \mathcal{F}_{\rm close}\}$, we synthesize our model distributions $\mathcal{M}_{\Delta{\rm m}}(\Delta{\rm m}, \vec{x})$, $\mathcal{M}_{\rm deep}(P,\, \vec{x})$, and $\mathcal{M}_{\rm med}(P,\, \vec{x})$. For our primary results, we have incorporated the detailed NIGHTFALL models where a 20% random subset have eclipse depths reduced by 20% in order to account for third light contamination (§2.3.1). For comparison, we also evaluate the eclipse depths using the NIGHTFALL models without third light contamination as well as using the simple bolometric estimates which ignore tidal distortions and limb darkening.

2.3.3 Fitting the Data

Mass-ratio Distribution $\mathcal{U}_{\rm q}$

We initially fit the observed eclipse depth distribution $\mathcal{O}_{\Delta \rm m}$ only, which primarily constrains the mass-ratio distribution $\mathcal{U}_{\rm q}$ as well as the normalization to $\mathcal{F}_{\rm close}$ according to Eq. 2.2. We determine the best-fit model parameters $\vec{x} = \{\gamma_{\rm P},\, \gamma_{\rm q},\, \mathcal{F}_{\rm twin},\, \mathcal{F}_{\rm close}\}$ by minimizing the $\chi^2_{\Delta \rm m}(\vec{x})$ statistic between the observed eclipse depth distribution $\mathcal{O}_{\Delta \rm m}(\Delta {\rm m})$ and our Monte Carlo models $\mathcal{M}_{\Delta \rm m}(\Delta {\rm m},\, \vec{x})$:

$$\chi^2_{\Delta \rm m}(\vec{x}) = \sum_{k}^{N_{\Delta \rm m}} \Big(\frac{\mathcal{O}_{\Delta \rm m}(\Delta {\rm m}_k) - \mathcal{M}_{\Delta \rm m}(\Delta {\rm m}_k, \vec{x})}{\sigma_{\mathcal{O}_{\Delta \rm m}}(\Delta {\rm m}_k)} \Big)^2 \tag{2.3}$$

We sum over the bins of data displayed in Figure 2.6 that are complete, specifically the $N_{\Delta \rm m} = 8$ bins across $0.25 < \Delta {\rm m\,(mag)} < 0.65$ for the OGLE-II LMC and SMC populations, $N_{\Delta \rm m} = 5$ bins across $0.10 < \Delta {\rm m} < 0.65$ for the MW, and the $N_{\Delta \rm m} = 11$ bins across $0.10 < \Delta {\rm m} < 0.65$ for the OGLE-III LMC sample. In Figure 2.6, we display the best-fit models $\mathcal{M}_{\Delta \rm m}(\Delta {\rm m})$ for each sample, together with the data. Although we have excluded eclipsing binaries with $\Delta {\rm m} > 0.65$ mag, which derive from nearly edge-on twin systems as well at evolved binaries that have filled their Roche lobes, twins are most likely to have grazing trajectories that produce eclipse depths in our selected parameter space (see §2.3.1). For the OGLE Magellanic Cloud samples that have large sample statistics in the interval 0.40 mag $< \Delta {\rm m} < 0.65$ mag, we therefore have sufficient leverage to constrain the excess twin fraction.

The observed eclipse depth distributions can only constrain $\mathcal{F}_{\rm close}$, $\gamma_{\rm q}$, and $\mathcal{F}_{\rm twin}$, which effectively gives $\nu = N_{\Delta \rm m} - 3$ degrees of freedom. We report in Table 2.2 the

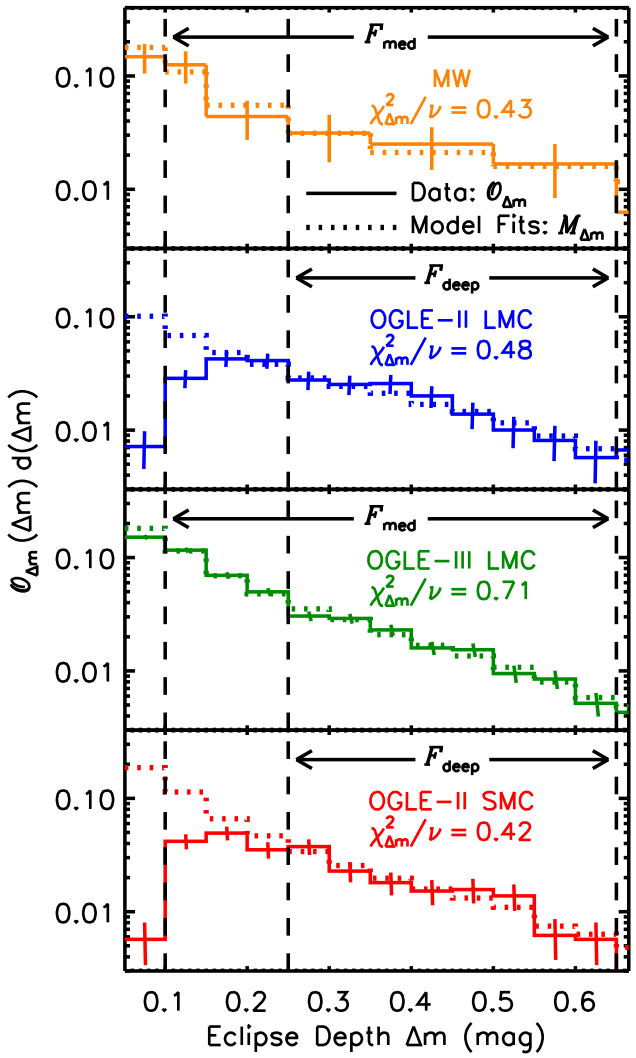

Figure 2.6: The observed primary eclipse depth distributions $\mathcal{O}_{\Delta m}$ (solid) as displayed in Figure 2.1 for Hipparcos MW (orange), OGLE-II LMC (blue), OGLE-III LMC (green), and OGLE-II SMC (red) populations. We determine the best-fit Monte Carlo models $\mathcal{M}_{\Delta m}$ (dotted) by minimizing the $\chi^2_{\Delta m}$ statistic across the $\mathcal{F}_{\rm deep}$ interval for the OGLE-II LMC and SMC data and over the $\mathcal{F}_{\rm med}$ interval for the MW and OGLE-III LMC populations, but we display the full histograms for reference.

Table 2.2. Results of our Monte Carlo simulations and fits to the observed eclipse depth distributions $\mathcal{O}_{\Delta m}$ *only*. For each of the eclipsing binary samples, we list the minimized reduced $\chi^2_{\Delta m}$ statistics, degrees of freedom $\nu = N_{\Delta m} - 3$, probabilities to exceed $\chi^2_{\Delta m}$ given ν, and the mean values and 1σ uncertainties of the three model parameters constrained by $\mathcal{O}_{\Delta m}$.

Sample	$\chi^2_{\Delta m}/\nu$	ν	PTE	$\mathcal{F}_{twin}$	γ_q	$\mathcal{F}_{close}$
MW	0.43	2	0.65	0.16 ± 0.10	-0.9 ± 0.8	0.22 ± 0.06
OGLE-II LMC	0.48	5	0.79	0.10 ± 0.07	-0.6 ± 0.7	0.21 ± 0.08
OGLE-III LMC	0.71	8	0.68	0.04 ± 0.03	-1.0 ± 0.2	0.27 ± 0.05
OGLE-II SMC	0.42	5	0.83	0.08 ± 0.06	-0.9 ± 0.7	0.24 ± 0.08

minimized reduced $\chi^2_{\Delta m}$ statistics, degrees of freedom ν, and probabilities to exceed $\chi^2_{\Delta m}$. We calculate a grid of joint probabilities $p_{\vec{x}}(\vec{x}) \propto e^{-\chi^2_{\Delta m}(\vec{x})/2}$, and then marginalize over the various parameters to calculate the probability density functions $p_{x_i}(x_i)$ for each parameter x_i. In Table 2.2, we list the average values $\mu_{x_i} = \int x_i \, p_{x_i}(x_i) \, dx_i$ and uncertainties $\sigma_{x_i} = [\int (x_i - \mu_{x_i})^2 \, p_{x_i}(x_i) \, dx_i]^{1/2}$ of the three parameters constrained by $\mathcal{O}_{\Delta m}$ for each of the eclipsing binary samples. Some of the parameters are correlated and have asymmetric probability density distributions, so we display two dimensional probability contours $p_{x_i,x_j}(x_i, x_j)$ for some combinations of parameters in Figure 2.7.

The higher quality OGLE-III LMC population, with its larger sample size and completeness down to $\Delta m = 0.10$, best constrains the model parameters. We find a negligible excess fraction of twins $\mathcal{F}_{twin} = (4 \pm 3)\%$, a mass-ratio distribution weighted toward low-mass companions with $\gamma_q = -1.0 \pm 0.2$, and a close binary fraction of $\mathcal{F}_{close} = (27 \pm 5)\%$ (before corrections for Malmquist bias - see §2.3.4). Based on our Monte Carlo simulations, a uniform mass-ratio distribution would have produced $\mathcal{S}_{\Delta m} \, d(\Delta m) \propto$

$(\Delta m)^{-1.0}\,d(\Delta m)$, not as steep as the observed trend $\mathcal{S}_{\Delta m}\,d(\Delta m) \propto (\Delta m)^{-1.65\pm0.07}\,d(\Delta m)$.

The less complete and/or smaller MW, OGLE-II LMC, and OGLE-II SMC samples do not permit precise determinations of γ_q. Nonetheless, the fitted mean values for these three samples span the range $\gamma_q = -0.9$ - -0.6, suggesting these binary populations

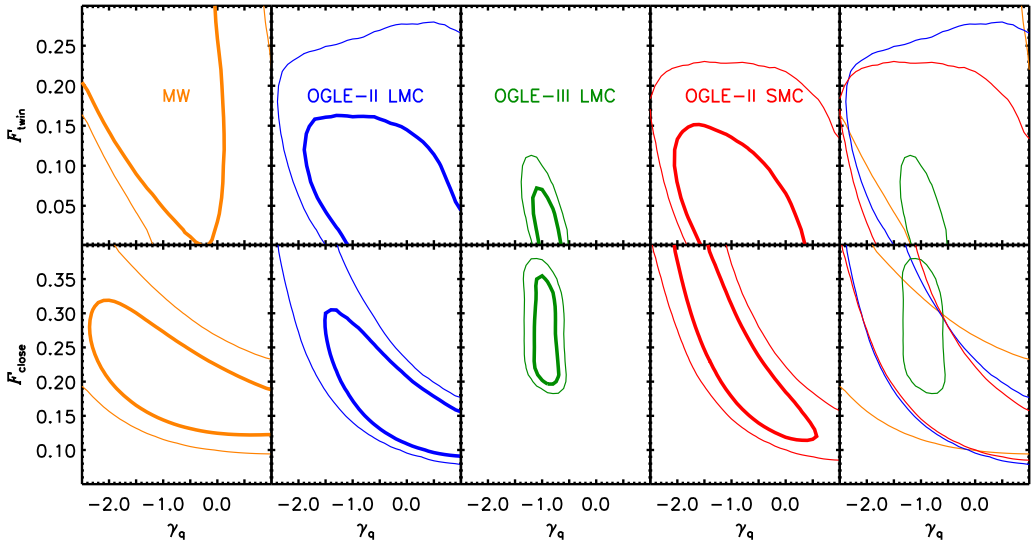

Figure 2.7: Probability contours at the 1σ (thick) and 2σ (thin) confidence levels of model parameter combinations constrained *only* by the observed eclipse depth distributions $\mathcal{O}_{\Delta m}$ for the Hipparcos MW (orange), OGLE-II LMC (blue), OGLE-III LMC (green), and OGLE-II SMC (red) populations. In the top panels, the OGLE-III LMC data clearly demonstrates a distribution weighted toward lower mass secondaries compared to a uniform distribution with $\gamma_q = 0$, and the other populations also favor negative values for the mass-ratio distribution exponent γ_q. For the three OGLE Magellanic Cloud samples, we find a small excess twin population with $q \gtrsim 0.9$ of only $\mathcal{F}_{twin} \approx (4\text{-}10)\%$. In the bottom panels, all four samples are consistent with a close binary fraction of $\mathcal{F}_{close} \approx 25\%$ and a mass-ratio distribution exponent of $\gamma_q \approx -1.0$.

also favor low-mass companions. For these populations, our solutions for the model parameters $\mathcal{F}_{\rm close}$ and $\gamma_{\rm q}$ are anti-correlated (see bottom panels of Figure 2.7). This is because a larger fraction of low-mass secondaries below the threshold of the survey sensitivity implies a higher $\mathcal{F}_{\rm close}$ given the same $\mathcal{F}_{\rm deep}$. All four samples are consistent with a close binary fraction of $\mathcal{F}_{\rm close} \approx 25\%$, slightly higher than our initial estimate of (16 - 20)% in §2.3.1. The precise values will decrease slightly once we correct for Malmquist bias (see §2.3.4).

Even though $\gamma_{\rm q}$ is not well known for the OGLE-II data, we can still constrain the excess twin fraction to be $\mathcal{F}_{\rm twin} \approx (4 - 10)\%$ for all three OGLE Magellanic Cloud samples (see top panels of Figure 2.7). A dominant twin population would have caused the eclipse depth distribution $\mathcal{O}_{\Delta \rm m}$ to flatten or even rise toward the deepest eclipses Δm > 0.4. Instead, the observed eclipse depth distributions for the three OGLE Magellanic Clouds samples continue with the same power-law $\mathcal{S}_{\Delta \rm m} \propto (\Delta {\rm m})^{-1.65}$. Because there are very few eclipsing binaries with $\Delta {\rm m} > 0.4$ in the MW data, we cannot adequately measure $\mathcal{F}_{\rm twin}$ for this population, but see our well-constrained estimate of $\mathcal{F}_{\rm twin} \approx 7\%$ based on spectroscopic observations of early-type stars in the MW (§2.4).

We have reported fitted parameters based on the NIGHTFALL models where a 20% random subset have eclipse depths reduced by 20% to account for third light contamination (§2.3.1). Because shallower eclipses systematically favor lower mass companions, the fitted mass-ratio distributions would have been shifted toward *even lower* values, albeit slightly, had we not considered this effect. Specifically, we find the excess twin fraction would have decreased by $\Delta\mathcal{F}_{\rm twin} = 0.01 - 0.03$ and the mass-ratio distribution exponent would have decreased by $\Delta\gamma_{\rm q} = 0.0 - 0.2$, depending on the sample. The close binary fraction would have changed by a factor of (3 - 6)%, i.e. $\Delta\mathcal{F}_{\rm close} \approx 0.01$,

with no general trend on the direction. Hence, third light contamination only mildly affects the inferred close binary properties.

Probabilities of Observing Eclipses $\mathcal{P}_{\rm deep}(P)$ and $\mathcal{P}_{\rm med}(P)$

The probabilities $\mathcal{P}_{\rm deep}(P)$ and $\mathcal{P}_{\rm med}(P)$ are defined to be the ratios of systems exhibiting deep ($0.25 < \Delta{\rm m} < 0.65$) and medium ($0.10 < \Delta{\rm m} < 0.65$) eclipses, respectively, to the total number of companions with $q > 0.1$ at the designated period. These probabilities obviously decrease with increasing orbital period P due to geometrical selection effects. In addition, $\mathcal{P}_{\rm deep}(P)$ and $\mathcal{P}_{\rm med}(P)$ depend on the metallicity Z, which determines the radial evolution of the stellar components, and also on the underlying mass-ratio distribution $\mathcal{U}_{\rm q}$. Mass-ratio distributions which favor lower-mass, smaller companions result in lower probabilities of observing eclipses because a larger fraction of the systems have eclipse depths below the sensitivity of the surveys. Because we have constrained $\mathcal{U}_{\rm q}$ for each of the four eclipsing binary populations, we have already effectively determined these probabilities from our Monte Carlo simulations. We use these more accurately constrained probabilities when we account for Malmquist bias in §2.3.4 as well as to visualize the corrected period distribution in §2.3.5.

Using our solutions for $\mathcal{U}_{\rm q}$ for each of the four eclipsing binary samples, we display the resulting $\mathcal{P}_{\rm deep}(P)$ and $\mathcal{P}_{\rm med}(P)$ in Figure 2.8. We propagate the fitted errors in $\gamma_{\rm q}$ and $\mathcal{F}_{\rm twin}$, as well as their mutual correlation as displayed in the top panels of Figure 2.7, to determine the uncertainties in the probabilities. For comparison, we calculate $\mathcal{P}_{\rm med}(P)$ and $\mathcal{P}_{\rm deep}(P)$ assuming the low-metallicity $Z = 0.004$ stellar tracks and a uniform mass-ratio distribution $\mathcal{U}_{\rm q}$, i.e. $\gamma_{\rm q} = 0$ and $\mathcal{F}_{\rm twin} = 0$.

In the top panel of Figure 2.8, the probabilities $\mathcal{P}_{\rm deep}$ for the OGLE Magellanic Cloud samples, which all have fitted values of $\gamma_{\rm q}$ that are negative, are systematically lower than the probabilities which assume a uniform mass-ratio distribution. Based on our back-of-the-envelope estimates in §2.3.1 where we assumed a uniform mass-ratio distribution, we determined that the correction factor between $\mathcal{F}_{\rm deep}$ and $\mathcal{F}_{\rm close}$ due to incompleteness toward low-mass companions *alone* was $\mathcal{C}_{\rm deep,q} \approx 2$. The fact that the fitted mass-ratio distributions favor more low-mass companions increases this correction factor to $\mathcal{C}_{\rm deep,q} \approx 3$. Therefore, the overall probability of observing deep eclipses at intermediate periods of $\log P = 0.8$ is $\mathcal{P}_{\rm deep} \approx 0.03$, slightly lower than our estimated average in §2.3.1 of $\langle \mathcal{P}_{\rm deep} \rangle = 0.04$. Finally note the intrinsically small probability of observing deep eclipses at long periods, e.g. only $\mathcal{P}_{\rm deep} \approx 1\%$ of all binaries at $P = 20$ days are detectable as eclipsing systems with $0.25 < \Delta{\rm m} < 0.65$.

In the bottom panel of Figure 2.8, the variations in $\mathcal{P}_{\rm med}$ are significantly smaller. This is because the probability of observing eclipses becomes less dependent on the underlying mass-ratio distribution as the observations become more sensitive to shallower eclipses. Essentially, the correction factor for incompleteness toward low-mass companions alone is only $\mathcal{C}_{\rm med,q} = 1.5$, slightly larger than our original estimate of $\mathcal{C}_{\rm med,q} = 1.3$ in §2.3.1, but still very close to unity. The MW correction factor $\mathcal{C}_{\rm med,i}$ for geometrical selection effects is 20% smaller than the OGLE-III LMC values, and therefore the overall probabilities $\mathcal{P}_{\rm med}$ are 20% larger. This is consistent with our interpretation of the radius-metallicity relation in §2.3.1. Söderhjelm & Dischler (2005) calculated the probabilities of observing solar-metallicity eclipsing binaries with $\Delta{\rm m} > 0.1$ as a function of spectral type and period. Because the fraction of systems with $\Delta{\rm m} > 0.65$ is negligible compared to the fraction with $0.1 < \Delta{\rm m} < 0.65$, we can compare the

Söderhjelm & Dischler (2005) results to our $\mathcal{P}_{\rm med}(P)$. We interpolate the probabilities in their Table A.1 for OB stars with $\langle {\rm M_V} \rangle = -3.04$ and B stars with $\langle {\rm M_V} \rangle = -0.55$ for our sample's median value of ${\rm M_V} \approx -2.3$. The resulting $\mathcal{P}_{\rm med}$, which we display in the bottom panel of Figure 2.8, is consistent with our MW distribution. At $\log P = 0.8$, the OGLE-III LMC value of $\mathcal{P}_{\rm med} = 0.06$ is only slightly lower than the uniform mass-ratio distribution value of $\mathcal{P}_{\rm med} = 0.08$ and our initial estimate in §2.3.1 of $\langle \mathcal{P}_{\rm med} \rangle = 0.09$.

Intrinsic Period Distribution $\mathcal{U}_{\rm P}$

We now fit the observed eclipsing binary period distributions $\mathcal{O}_{\rm deep}(P)$ or $\mathcal{O}_{\rm med}(P)$ only, which constrain the intrinsic period distributions $\mathcal{U}_{\rm P}$ and the normalizations to $\mathcal{F}_{\rm close}$ according to Eq. 2.1. We minimize the $\chi^2_{\rm P}(\vec{x})$ statistics between the measured eclipsing binary period distributions $\mathcal{O}_{\rm deep}(\log P)$ and our Monte Carlo models $\mathcal{M}_{\rm deep}(\log P, \vec{x})$:

$$\chi^2_{\rm P}(\vec{x}) = \sum_{k}^{N_{\rm P}} \Big(\frac{\mathcal{O}_{\rm deep}(\log P_k) - \mathcal{M}_{\rm deep}(\log P_k, \vec{x})}{\sigma_{\mathcal{O}_{\rm deep}}(\log P_k)} \Big)^2 \tag{2.4}$$

We calculate similar statistics for the medium eclipse depth samples. We sum over the logarithmic period bins of data displayed in Figure 2.9, specifically the $N_{\rm P} = 10$ bins of $\mathcal{O}_{\rm deep}(P)$ for the OGLE-II LMC and SMC populations, $N_{\rm P} = 3$ bins of $\mathcal{O}_{\rm med}(P)$ for the MW, and the $N_{\rm P} = 10$ bins of $\mathcal{O}_{\rm med}(P)$ for the OGLE-III LMC sample. The measured period distribution constrains $\gamma_{\rm P}$ and $\mathcal{F}_{\rm close}$, which effectively gives $\nu = N_{\rm P} - 2$ degrees of freedom. As in §2.3.3, we report the $\chi^2_{\rm P}$ statistics and fitted model parameters in Table 2.3 as well as display the two-dimensional probability contour of $\mathcal{F}_{\rm close}$ versus $\gamma_{\rm P}$ in Figure 2.10.

By making simple approximations in §2.2, we showed that all four eclipsing

binary samples were skewed toward shorter periods relative to Öpik's prediction of $\mathcal{S}_{\rm deep}(P)\,{\rm d}(\log P) \propto \mathcal{S}_{\rm med}(P)\,{\rm d}(\log P) \propto P^{-2/3}\,{\rm d}(\log P)$. We confirm this result with our

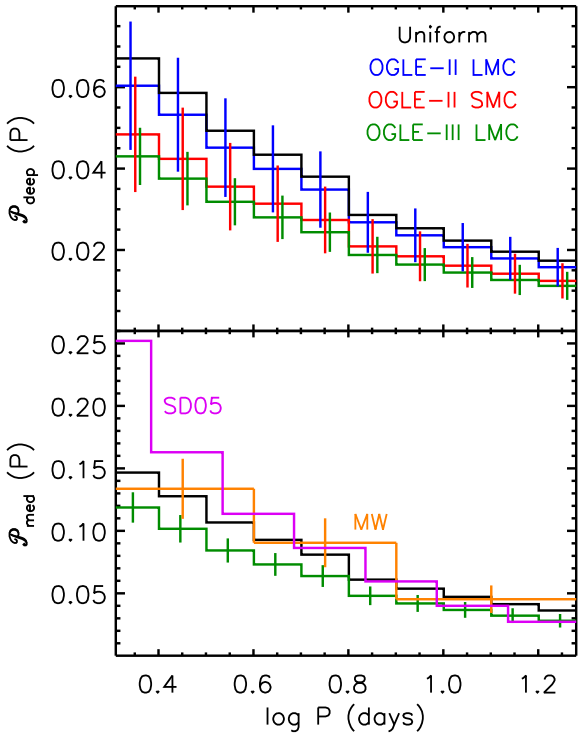

Figure 2.8: The probabilities that a companion with $q > 0.1$ exhibits deep $\mathcal{P}_{\rm deep}$ (top) and medium $\mathcal{P}_{\rm med}$ (bottom) eclipses using our fitted solutions to the overall mass-ratio distribution $\mathcal{U}_{\rm q}$ for the MW (orange), OGLE-II LMC (blue), OGLE-III LMC (green), and OGLE-II SMC (red). We also display $\mathcal{P}_{\rm deep}$ and $\mathcal{P}_{\rm med}$ determined by incorporating the low-metallicity $Z = 0.004$ stellar tracks and assuming a uniform mass-ratio distribution (black). The probabilities $\mathcal{P}_{\rm med}$ based on the Söderhjelm & Dischler (2005) solar-metallicity results (magenta) are consistent with our MW values. The probabilities of observing eclipses decreases with increasing P due to geometrical selection effects, and also decreases with mass-ratio distributions which favor low-mass, smaller companions.

more robust light curve modeling and Monte Carlo simulations, where we find fitted mean values of $\gamma_{\rm P}$ that are negative for all four main samples. However, the OGLE-III LMC

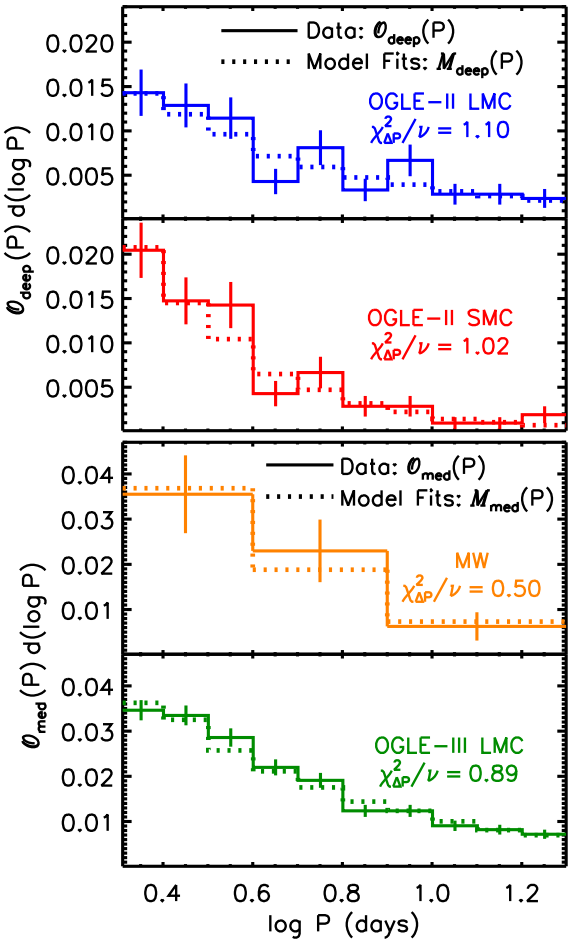

Figure 2.9: The observed eclipsing binary period distributions (solid) for deep eclipses $\mathcal{O}_{\rm deep}(P)$ (top two panels) and extension toward medium eclipse depths $\mathcal{O}_{\rm med}(P)$ (bottom two panels) as displayed in Figure 2.2 for the Hipparcos MW (orange), OGLE-II LMC (blue), OGLE-III LMC (green), and OGLE-II SMC (red) populations. We determine the best-fit Monte Carlo models $\mathcal{M}_{\rm deep}(P)$ and $\mathcal{M}_{\rm med}(P)$ (dotted) by minimizing the $\chi^2_{\rm P}$ statistic across the logarithmic period bins of data.

Table 2.3. Results of our Monte Carlo simulations and fits to the observed eclipsing binary period distributions $\mathcal{O}_{\rm deep}(P)$ or $\mathcal{O}_{\rm med}(P)$ *only*. For each of the eclipsing binary samples, we list whether the deep eclipse $\mathcal{O}_{\rm deep}(P)$ or extension toward medium eclipse depth $\mathcal{O}_{\rm med}(P)$ samples were used to fit the period distribution, minimized reduced $\chi^2_{\rm P}$ statistics, degrees of freedom $\nu = N_{\rm P} - 2$, probabilities to exceed $\chi^2_{\rm P}$ given ν, and the mean values and 1σ uncertainties of the two model parameters constrained by $\mathcal{O}_{\rm deep}(P)$ or $\mathcal{O}_{\rm med}(P)$.

Sample	Eclipse Depths	$\chi^2_{\rm P}/\nu$	ν	PTE	$\gamma_{\rm P}$	$\mathcal{F}_{\rm close}$
MW	Medium & Deep	0.50	1	0.48	-0.4 ± 0.3	0.22 ± 0.06
OGLE-II LMC	Deep	1.10	8	0.36	-0.3 ± 0.2	0.22 ± 0.08
OGLE-III LMC	Medium & Deep	0.89	8	0.53	-0.1 ± 0.2	0.24 ± 0.05
OGLE-II SMC	Deep	1.02	8	0.42	-0.9 ± 0.2	0.21 ± 0.09

value of $\gamma_{\rm P} = -0.1 \pm 0.2$ is still consistent with Öpik's law of $\gamma_{\rm P} = 0$, while the OGLE-II SMC population is significantly skewed toward shorter periods with $\gamma_{\rm P} = -0.9 \pm 0.2$. These two values for $\gamma_{\rm P}$ are discrepant at the 2.4σ level. This is similar to our K-S test in §2.2 between the OGLE-II SMC and OGLE-III LMC unbinned $\mathcal{O}_{\rm deep}(P)$ data, which gave a probability of consistency of $p_{\rm KS} = 0.01$.

As discussed in §2.2, it is possible that long period systems $P > 10$ days with moderate eclipse depths Δm = 0.25 - 0.30 mag have remained undetected in the OGLE-II SMC sample because their members are systematically 0.5 mag fainter. If we only use the OGLE-II SMC data with P = 2 - 10 days and Δm = 0.30 - 0.65 mag to constrain our fit, then we find $\gamma_{\rm P} = -0.7 \pm 0.4$, which is more consistent with the LMC result. In any case, whether the slight discrepancy is intrinsic or due to small systematics, the best-fitting period exponent for the MW of $\gamma_{\rm P} \approx -0.4$ is between the LMC and

SMC values. We confirm this intermediate value based on spectroscopic radial velocity observations of nearby early-type stars (see §2.4). Although there is a strong indication that the SMC period distribution is skewed toward shorter periods compared to the LMC data, there is no clear trend with metallicity. Moreover, the MW, SMC and LMC samples are all mildly consistent, i.e. less than 2σ discrepancy, with the intermediate value of $\gamma_{\rm P} \approx -0.4$.

Close Binary Fraction $\mathcal{F}_{\rm close}$

The close binary fractions $\mathcal{F}_{\rm close}$ are not well constrained by fitting the observed eclipse depth and period distributions separately. For example, the 1σ errors in the close binary fractions from only fitting $\mathcal{O}_{\Delta \rm m}$ were $\delta\mathcal{F}_{\rm close} \approx 0.05$ - 0.08, depending on the sample

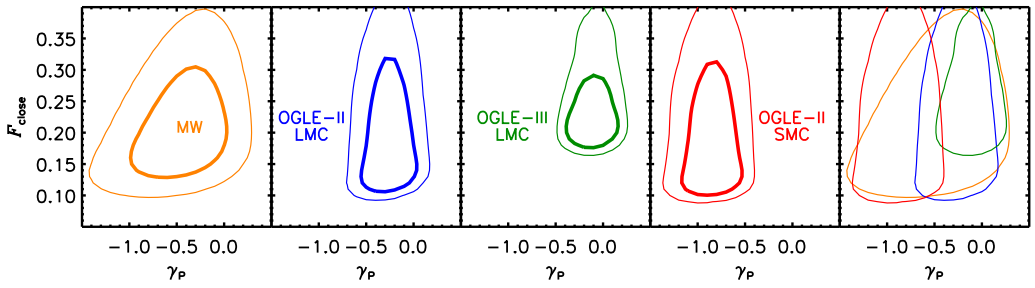

Figure 2.10: Probability contours at the 1σ (thick) and 2σ (thin) confidence levels of $\mathcal{F}_{\rm close}$ versus $\gamma_{\rm P}$ constrained *only* by the observed eclipse depth distributions $\mathcal{O}_{\rm deep}(P)$ or $\mathcal{O}_{\rm med}(P)$ for the Hipparcos MW (orange), OGLE-II LMC (blue), OGLE-III LMC (green), and OGLE-II SMC (red) populations. Although the OGLE-II SMC population favors a distribution that is skewed toward shorter periods while the OGLE-III LMC population is consistent with Öpik's law of $\gamma_{\rm P} = 0$, all four samples are mildly consistent with $\mathcal{F}_{\rm close} \approx 20\%$ and $\gamma_{\rm P} \approx -0.4$.

Table 2.4. Results of our fits to the observed eclipse depth distributions $\mathcal{O}_{\Delta\mathrm{m}}$ *and* observed eclipsing binary period distributions $\mathcal{O}_{\mathrm{deep}}(P)$ or $\mathcal{O}_{\mathrm{med}}(P)$. For each sample, we list whether the deep or extension toward medium eclipse depth samples were used to simultaneously fit the eclipse depth and period distributions. We also report the minimized reduced $\chi^2 = \chi^2_{\Delta\mathrm{m}} + \chi^2_{\mathrm{P}}$ statistics, degrees of freedom $\nu = N_{\Delta\mathrm{m}} + N_{\mathrm{P}} - 4$, probabilities to exceed χ^2 given ν, and the mean values and 1σ uncertainties of the close binary fractions $\mathcal{F}_{\mathrm{close}}$ *before correcting for Malmquist bias and propagating systematic errors.*

Sample	Eclipse Depths	χ^2/ν	ν	PTE	$\mathcal{F}_{\mathrm{close}}$
MW	Medium & Deep	0.44	4	0.76	0.22 ± 0.04
OGLE-II LMC	Deep	0.89	14	0.58	0.21 ± 0.06
OGLE-III LMC	Medium & Deep	1.02	17	0.39	0.28 ± 0.02
OGLE-II SMC	Deep	0.81	14	0.68	0.23 ± 0.06

(see Table 2.2), while the errors from only fitting $\mathcal{O}_{\mathrm{deep}}(P)$ or $\mathcal{O}_{\mathrm{med}}(P)$ were $\delta\mathcal{F}_{\mathrm{close}} \approx 0.05$ - 0.09 (Table 2.3). To measure $\mathcal{F}_{\mathrm{close}}$ most precisely, we now fit $\mathcal{O}_{\Delta\mathrm{m}}$ and either $\mathcal{O}_{\mathrm{deep}}(P)$ or $\mathcal{O}_{\mathrm{med}}(P)$ simultaneously by minimizing $\chi^2 = \chi^2_{\Delta\mathrm{m}} + \chi^2_{\mathrm{P}}$. For each sample, we sum over the same bins of eclipse depths and orbital periods that are complete as reported in §2.3.3. This combined fit gives $\nu = N_{\Delta\mathrm{m}} + N_{\mathrm{P}} - 4$ degrees of freedom since all four model parameters are constrained. In Table 2.4, we report the fitting statistics as well as the means and 1σ uncertainties for $\mathcal{F}_{\mathrm{close}}$ only because this combined method does not alter our previous estimates of γ_{q}, $\mathcal{F}_{\mathrm{twin}}$, and γ_{P}. The χ^2/ν values are all close to unity and the probabilities to exceed are in the 1σ range 0.16 - 0.84, demonstrating our models are sufficient in explaining the data.

In order to fit $\mathcal{O}_{\Delta\mathrm{m}}$ and either $\mathcal{O}_{\mathrm{deep}}(P)$ or $\mathcal{O}_{\mathrm{med}}(P)$ simultaneously, we have assumed

Δm and P are independent so that $p \propto e^{-\chi^2_{\Delta\mathrm{m}}/2} \times e^{-\chi^2_{\mathrm{P}}/2} = e^{-(\chi^2_{\Delta\mathrm{m}}+\chi^2_{\mathrm{P}})/2} = e^{-\chi^2/2}$. For all four samples of eclipsing binaries, the Spearman rank correlation coefficients between Δm and P are rather small at $|\rho| < 0.15$ across the eclipse depth intervals which are complete. These small coefficients justify our procedure for fitting the eclipsing binary period and eclipse depth distributions together in order to better constrain $\mathcal{F}_{\mathrm{close}}$. Moreover, the probability of observing medium eclipses $\mathcal{P}_{\mathrm{med}}(P)$ determined in §2.3.3 only marginally depends on the underlying mass-ratio distribution $\mathcal{U}_{\mathrm{q}}$. Therefore, any trend between mass-ratios and orbital periods will not affect the fitted close binary fractions beyond the quantified errors.

If we had used simple prescriptions for eclipse depths instead of the detailed NIGHTFALL light curve models, our fitted values for $\mathcal{F}_{\mathrm{close}}$ would have been a factor of (10 - 20)% different, i.e. $\Delta\mathcal{F}_{\mathrm{close}} \approx 0.02$ - 0.04 depending on the sample with no general trend on the direction. This would have been a dominant source of error, especially for the OGLE-III LMC data, so it was imperative that we implemented the more precise NIGHTFALL simulations. Before we comment further on our measurements of $\mathcal{F}_{\mathrm{close}}$ in the different environments, we must first correct for Malmquist bias.

2.3.4 Malmquist Bias

Milky Way

Unresolved binaries, including eclipsing systems, are systematically brighter than their single star counterparts. For a magnitude-limited sample within our MW, more luminous binaries are probed over a larger volume than their single star counterparts, which causes the binary fraction to be artificially enhanced. This classical Malmquist bias is

sometimes referred to as the Öpik (1923) or Branch (1976) effect in the context of binary stars.

Of the $\mathcal{N}_{\rm med} = 31$ eclipsing binaries in our medium eclipse depth MW sample with $\langle {\rm H_P} \rangle < 9.3$, only four systems are fainter than $\langle {\rm H_P} \rangle > 8.8$ (Lefèvre et al. 2009). One of these systems, V2126 Cyg, has a moderate magnitude of $\langle {\rm H_P} \rangle = 9.0$ and shallow eclipse depth of $\Delta {\rm H_P} = 0.13$. This small eclipse depth indicates a faint, low-mass companion, although the less likely scenario of a grazing eclipse with a more massive secondary is also feasible. The remaining three systems, IT Lib, LN Mus, and TU Mon, all have fainter system magnitudes $\langle {\rm H_P} \rangle > 9.1$ and deeper eclipses $\Delta {\rm H_P} > 0.18$, suggesting that their primaries alone do not fall within our magnitude limit of $\langle {\rm H_P} \rangle < 9.3$. If we remove this excess number of $\mathcal{N}_{\rm ex} = 3\text{-}4$ eclipsing binaries from both our eclipsing binary sample $\mathcal{N}_{\rm med}$ as well as from the total number of systems $\mathcal{N}_{\rm B}$, then the eclipsing binary fraction with medium eclipse depths $\mathcal{F}_{\rm med} = \mathcal{N}_{\rm med}/\mathcal{N}_{\rm B}$ would decrease by a factor of $\approx$11%, i.e. $\Delta \mathcal{F}_{\rm med} \approx -0.002$.

However, we must also remove from the denominator $\mathcal{N}_{\rm B}$ *other* binaries with luminous secondaries which have primaries that fall below our magnitude limit. These include close binaries that remain undetected because they have orientations which do not produce observable eclipses. Based on the correction factor $\mathcal{C}_{\rm med,i} = 9 \pm 2$ for geometrical selection effects alone for the MW sample (see §2.3.3), then we expect a total of $\mathcal{N}_{\rm med} \times \mathcal{C}_{\rm med,i} \approx 30$ binaries with $P = 2\text{-}20$ days that should be removed from $\mathcal{N}_{\rm B}$.

Additional systems that contaminate $\mathcal{N}_{\rm B}$ consist of binaries with luminous secondaries outside of our period range of $P = 2\text{-}20$ days. To estimate their contribution toward Malmquist bias, we calculate the ratio $\mathcal{R}_{\rm P}$ between the frequency of massive

secondaries across all orbital periods to the frequency of massive secondaries with $P =$ 2 - 20 days. Spectroscopic observations of O and B type stars in the MW reveal 0.16 - 0.31 companions with $q > 0.1$ per decade of orbital period at $\log P \approx 0.8$ (Garmany et al. 1980; Levato et al. 1987; Abt et al. 1990; Sana et al. 2012, see also §2.4). At longer orbital periods of $\log P \approx 6.5$, photometric observations of visually resolved binaries give a lower value of ≈ 0.10 - 0.16 companions with $q \gtrsim 0.1$ per decade of orbital period (Duchêne et al. 2001; Shatsky & Tokovinin 2002; Turner et al. 2008; Mason et al. 2009). Using these two points to anchor the slope of the period distribution, we integrate from $\log P = 0.1$ to the widest, stable orbits of $\log P \approx 8.5$. We find there are 6.4 ± 1.3 as many total companions as there are binaries with $P = 2$ - 20 days. However, longer period binaries with $P > 20$ days may have a mass-ratio distribution that differs from our sample at shorter orbital periods. For example, Abt et al. (1990) and Duchêne et al. (2001) suggest random pairings of the initial mass function for wide binaries so that $\gamma_{\rm q} \approx -2.3$, the distribution of Preibisch et al. (1999) indicates a more moderate value of $\gamma_{\rm q} \approx -1.5$, while Shatsky & Tokovinin (2002) gives $\gamma_{\rm q} \approx -0.5$ for visually resolved binaries, which is consistent with the values inferred from our close eclipsing binary samples of $\gamma_{\rm q} \approx -1.0$ - -0.6. Assuming $\gamma_{\rm q} = -1.5 \pm 0.5$ for binaries outside our period range, then there are 2.3 ± 1.1 times fewer binaries with $q > 0.6$ relative to the mass-ratio distribution constrained for our close eclipsing binaries. Since we are primarily concerned with massive secondaries which contribute toward Malmquist bias, then $\mathcal{R}_{\rm P} \approx (6.4 \pm 1.3)/(2.3 \pm 1.1) = 2.8 \pm 1.4$.

The eclipsing binary fraction for the MW sample after correcting for classical Malmquist bias is then:

$$\mathcal{F}_{\rm med} = \frac{\mathcal{N}_{\rm med} - \mathcal{N}_{\rm ex}}{\mathcal{N}_{\rm B} - \mathcal{N}_{\rm ex}\mathcal{C}_{\rm med,i}\mathcal{R}_{\rm P}} = (1.83 \pm 0.38)\% \tag{2.5}$$

where we propagated the uncertainties in $\mathcal{C}_{\rm med,i}$ and $\mathcal{R}_{\rm P}$ as well as the Poisson errors in $\mathcal{N}_{\rm med}$ and $\mathcal{N}_{\rm ex}$. Note that removing non-eclipsing binaries with luminous secondaries that remain undetected mitigates the effects of Malmquist bias. Specifically, we find the reduction factor to be $\mathcal{C}_{\rm Malm} = 0.94 \pm 0.05$ instead of the factor of $\mathcal{C}_{\rm Malm} = 0.89$ determined above when we only removed $\mathcal{N}_{\rm ex}$ eclipsing systems. Although these two competing effects in the numerator and denominator of the above relation have been discussed in the literature (e.g. Bouy et al. 2003), the removal of binaries with luminous secondaries which remain undetected is typically neglected. The inferred close binary fraction for the MW will also decrease by a factor of $\mathcal{C}_{\rm Malm} = 0.94$, so that the corrected value is only slightly lower at $\mathcal{F}_{\rm close} = 21\%$ (see §2.3.5).

Magellanic Clouds

In the case of the Magellanic Clouds at fixed, known distances, classical Malmquist bias does not apply. Nonetheless, our absolute magnitude interval of $\overline{\rm M}_{\rm I} = [-3.8, -1.3]$ contain binaries with primaries which are lower in intrinsic luminosity and stellar mass relative to single stars in the same magnitude range. Some binaries in our sample have primaries that are fainter than our magnitude limit of $\rm M_I = -1.3$, while some systems have primaries in the range we want to consider but are pushed beyond $\rm M_I = -3.8$ because of the excess light added by the secondary. Since the number of primaries dramatically increases with decreasing stellar mass and luminosity, the net effect is that the binary fractions are biased toward larger values. Hence, our statistics are affected

by Malmquist bias of the second kind because two classes of objects, e.g. binaries and single stars, are surveyed to a certain depth down their respective luminosity functions (Teerikorpi 1997; Butkevich et al. 2005).

For example, Mazeh et al. (2006) used OGLE-II data of the LMC to identify 938 eclipsing binaries on the MS with apparent magnitudes $17 < \mathrm{I} < 19$ and periods $2 < P$ (days) < 10. Instead of normalizing these eclipsing binaries to the total number of $\approx$330,000 MS systems with $17 < \mathrm{I} < 19$, they assumed the average eclipsing binary was $\langle \Delta \mathrm{M_I} \rangle = 0.5$ mag brighter than the primary component alone, and therefore normalized to the $\approx$700,000 MS systems with $17.5 < \mathrm{I} < 19.5$. Their correction for Malmquist bias of the second kind lowered the inferred close binary fraction by a factor of 2.1, i.e. $\mathcal{C}_{\rm Malm} = 0.48$.

Instead of adding systems below our lower magnitude limit as done by Mazeh et al. (2006), we remove binaries with luminous secondaries within our magnitude interval $\overline{\mathrm{M}}_\mathrm{I} = [-3.8, -1.3]$ as described above for the MW. To determine the average fraction $\langle \delta \mathcal{F}_\mathrm{I} \rangle$ of eclipsing binaries that should be removed from our Magellanic Cloud samples, we use the OGLE photometric catalogs (Udalski et al. 1998, 2000, 2008) to compute the observed fractional decrease $\delta \mathcal{F}_\mathrm{I}$ in the total number of MS systems as a function of incremental I-band magnitude $\Delta \mathrm{M_I}$. Quantitatively:

$$\delta \mathcal{F}_\mathrm{I}(\Delta \mathrm{M_I}) = 1 - \frac{\mathcal{N}(\overline{\mathrm{M}}_\mathrm{I} - \Delta \mathrm{M_I})}{\mathcal{N}(\overline{\mathrm{M}}_\mathrm{I})} \tag{2.6}$$

where $\mathcal{N}(\overline{\mathrm{M}}_\mathrm{I}) = \mathcal{N}_\mathrm{B}$ is our original total number of MS systems and $\mathcal{N}(\overline{\mathrm{M}}_\mathrm{I} - \Delta \mathrm{M_I})$ is the number of systems with colors $\mathrm{V}-\mathrm{I} < 0.1$ in the interval $\mathrm{M_I} = [-3.8, -1.3 - \Delta \mathrm{M_I}]$. We display $\delta \mathcal{F}_\mathrm{I}$ in the top panel of Figure 2.11 for the three OGLE Magellanic Cloud

samples. We only show the fractional decreases $\delta\mathcal{F}_{\rm I}$ across the interval $0 < \Delta{\rm M_I} < 0.75$ because binary companions can only contribute a luminosity excess in this range. The three distributions of $\delta\mathcal{F}_{\rm I}$ are similar among the three populations due to the consistency of the stellar mass function in the different environments. The total number of systems is approximately halved, i.e. $\delta\mathcal{F}_{\rm I} = 0.5$, at $\Delta{\rm M_I} \approx 0.5$, consistent with the result of Mazeh et al. (2006).

Instead of assuming an average value for the magnitude difference $\langle\Delta{\rm M_I}\rangle = 0.5$ mag between a single star and eclipsing binary with the same primary, we use the OGLE eclipsing binary data and our Monte Carlo simulations to model an I-band excess probability distribution $p_{\rm I}\left(\Delta{\rm M_I}\right){\rm d}(\Delta{\rm M_I})$. Using the best-fit models for each of the three OGLE samples, we synthesize distributions of secondary masses which produce observable eclipses, i.e. systems with eclipse depths $0.25 < \Delta{\rm m} < 0.65$ for our deep samples and $0.1 < \Delta{\rm m} < 0.65$ for our extension toward medium eclipse depths (OGLE-III LMC only). We then use the stellar tracks of Bertelli et al. (2009) as well as color indices and bolometric corrections of Cox (2000) to convert the distribution of secondary masses that produce observable eclipses into a distribution of secondary absolute magnitudes in the I-band. We can then easily determine the system luminosity, the luminosity of the primary alone, and the I-band excess $\Delta{\rm M_I}$ between the two for each eclipsing binary. In the bottom panel of Figure 2.11, we display our results for the I-band excess probability distribution $p_{\rm I}\left(\Delta{\rm M_I}\right){\rm d}(\Delta{\rm M_I})$, which is normalized so that the distribution integrates to unity.

The I-band excess probability distributions $p_{\rm I}$ for the three OGLE samples exhibiting deep eclipses are all quite similar. This is because they have similar eclipse depth distributions $\mathcal{O}_{\Delta{\rm m}}$, and therefore similar mass-ratio distributions $\mathcal{U}_{\rm q}$. Very few low-mass,

low-luminosity secondaries with $\Delta M_I < 0.1$ mag are capable of producing deep eclipses with $0.25 < \Delta m < 0.65$. However, many of these faint secondaries are included in the

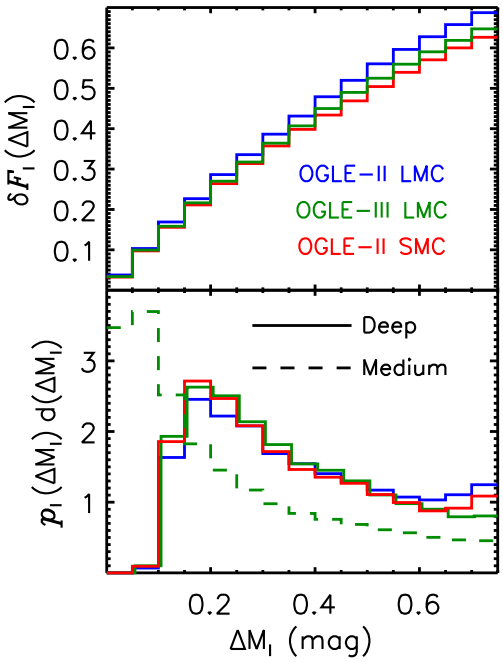

Figure 2.11: Top panel: the observed fractional decrease $\delta\mathcal{F}_I$ in the total number of MS systems as a function of incremental I-band magnitude ΔM_I for the OGLE-II LMC (blue), OGLE-III LMC (green), and OGLE-II SMC (red) samples. Bottom panel: based on our best-fit Monte Carlo simulations, the modeled I-band excess probability distributions $p_I\,(\Delta M_I)\,d(\Delta M_I)$ of binaries exhibiting deep (solid) and medium (dashed) eclipses due to increased luminosity from the companion. In order to correct for Malmquist bias of the second kind, we determine the average fraction $\langle\delta\mathcal{F}_I\rangle$ of eclipsing binaries that should be removed from our samples according to $\langle\delta\mathcal{F}_I\rangle = \int \delta\mathcal{F}_I(\Delta M_I)\,p_I(\Delta M_I)\,d(\Delta M_I)$.

OGLE-III LMC medium eclipse depth sample. The median I-band excess is only $\langle \Delta M_I \rangle = 0.35$ and $\langle \Delta M_I \rangle = 0.20$ mag for the deep and medium samples, respectively, which are lower than the value of $\langle \Delta M_I \rangle = 0.5$ used by Mazeh et al. (2006). Note that these values of $\langle \Delta M \rangle = 0.2$ - 0.5 mag are the reason we excluded the $\mathcal{N}_{ex} = 3$ - 4 eclipsing binaries in the MW sample (§2.3.4) that were within 0.2 - 0.5 mag of our magnitude limit of $\langle H_P \rangle = 9.3$.

We can now compute the average fraction $\langle \delta\mathcal{F}_I \rangle$ of eclipsing binaries that should be removed from our samples by weighting $\delta\mathcal{F}_I$ with the I-band excess probability distribution, i.e. $\langle \delta\mathcal{F}_I \rangle = \int \delta\mathcal{F}_I(\Delta M_I)\, p_I(\Delta M_I)\, d(\Delta M_I)$. We find $\langle \delta\mathcal{F}_I \rangle = 0.38 \pm 0.11$ and $\langle \delta\mathcal{F}_I \rangle = 0.35 \pm 0.10$ for the OGLE-II LMC and SMC deep eclipse samples, respectively, and $\langle \delta\mathcal{F}_I \rangle = 0.23 \pm 0.08$ for the OGLE-III LMC medium eclipse sample. These values are lower than the estimate of $\langle \delta\mathcal{F}_I \rangle = 0.52$ by Mazeh et al. (2006) because the modeled I-band excess probability distributions are weighted more toward fainter companions.

Instead of only removing this average fraction $\langle \delta\mathcal{F}_I \rangle$ of eclipsing binaries, i.e. assuming $\mathcal{C}_{Malm} = 1 - \langle \delta\mathcal{F}_I \rangle$, we must also account for the other binaries with luminous secondaries outside our parameter space of eclipse depths and orbital periods. Using a similar format as in Eq. 2.5, we derive:

$$\mathcal{C}_{Malm} = \frac{1 - \langle \delta\mathcal{F}_I \rangle}{1 - \mathcal{F}_{med} \langle \delta\mathcal{F}_I \rangle \mathcal{C}_{med,i} \mathcal{R}_P} \tag{2.7}$$

where $\mathcal{F}_{med} = 1.87\%$ is the uncorrected eclipsing binary fraction in Table 2.1 and $\mathcal{C}_{med,i} = 11 \pm 2$ is the correction factor for geometrical selection effects alone (see §2.3.3) for the OGLE-III LMC medium sample, and $\mathcal{R}_P = 2.8 \pm 1.4$ has the same definition as in §2.3.4. We calculate similar values for the OGLE-II LMC and SMC deep eclipse samples, where

$\mathcal{F}_{\rm deep} = 0.70\%$ and $\mathcal{C}_{\rm deep,i} = 14 \pm 3$. We find the overall correction factors for Malmquist bias of the second kind to be $\mathcal{C}_{\rm Malm} = 0.73 \pm 0.16$, 0.91 ± 0.12, and 0.76 ± 0.15 for the OGLE-II LMC, OGLE-III LMC, and OGLE-II SMC samples respectively. Because the OGLE-III LMC survey was sensitive to shallow eclipses that systematically favored low-luminosity companions with $\langle \Delta {\rm M_I} \rangle \approx 0.2$ mag, the correction for Malmquist bias for this population is nearly negligible.

2.3.5 Corrected Results

We have implemented detailed NIGHTFALL light curve models (§2.3.1) and computed thousands of Monte Carlo simulations (§2.3.2) in order to correct for geometrical selection effects and incompleteness toward low-mass companions. By fitting the observed eclipsing binary distributions using various methods, we have derived the underlying intrinsic binary properties for the MW, LMC, and SMC (§2.3.3). Because our eclipsing binary samples are magnitude limited and therefore subject to Malmquist bias, we have determined accurate reduction factors (§2.3.4) by incorporating the observed stellar luminosity functions, modeling the I-band excess probability distributions, and accounting for other binaries outside our parameter space of eclipsing systems. We have also quantified many sources of systematic errors in our analysis, including the single-mass primary approximation (factor of 8% uncertainty for the MW and 10% for the Magellanic Cloud samples, i.e. $\delta \mathcal{F}_{\rm close} \approx 0.02$), the contribution of the few giants and evolved primaries filling their Roche lobes (factor of 3%), the conversion of Roche-lobe filling factors (factor of 7%), effects of eccentric orbits (factor of 2%), third light contamination due to triple systems and stellar blending (factor of 6%), and the

Table 2.5. For the four different eclipsing binary samples, we list the corrected fractions of early-B stars with companions $q > 0.1$ at orbital periods $P = 2$ - 20 days after accounting for geometrical selection effects, incompleteness toward low-mass companions, Malmquist bias, and systematic errors.

	MW	OGLE-II LMC	OGLE-III LMC	OGLE-II SMC
$\mathcal{F}_{\rm close}$	$(21 \pm 5)\%$	$(16 \pm 6)\%$	$(25 \pm 4)\%$	$(17 \pm 6)\%$

uncertainties in the Malmquist bias reduction factors (factors of 5 - 16%, depending on the sample). Assuming Gaussian uncertainties, we add these systematic errors in quadrature and propagate the total factor of (14-21)% systematic uncertainty, i.e. $\delta\mathcal{F}_{\rm close} \approx 0.03$ - 0.04 depending on the sample, into our evaluations of the close binary fraction.

Based on our χ^2 fits, correction for Malmquist bias, and propagation of systematic errors, our finalized results for $\mathcal{F}_{\rm close}$ are 0.21 ± 0.05, 0.16 ± 0.06, 0.25 ± 0.04, and 0.17 ± 0.06 for the MW, OGLE-II LMC, OGLE-III LMC, and OGLE-II SMC populations, respectively. We list these corrected values in Table 2.5. All of the close binary fractions $\mathcal{F}_{\rm close}$ are consistent with each other at the 1.2σ level. The fact that all four environments have $\mathcal{F}_{\rm close} = (16$ - $25)\%$ demonstrates that the close binary fraction does not substantially vary across metallicities $\log(Z/{\rm Z}_\odot) \approx -0.7$ - 0.0.

Instead of inferring the intrinsic period distributions $\mathcal{U}_{\rm P}$ from our fitted model parameters $\gamma_{\rm P}$ and $\mathcal{F}_{\rm close}$, we can also visualize the distributions based on the observed eclipsing binary period distributions (see §2.2) and our modeled probabilities of observing eclipses (see §2.3.3). For the OGLE-II LMC and SMC samples, we use $\mathcal{U}_{\rm P}(P)\,{\rm d}(\log P) = [\mathcal{O}_{\rm deep}(P)\,{\rm d}(\log P)\,/\,\mathcal{P}_{\rm deep}(P)] \times C_{\rm Malm}$, where $C_{\rm Malm} \approx 0.75$ is the slight correction factor for Malmquist bias (§2.3.4). Similarly, we use $\mathcal{U}_{\rm P}(P)\,{\rm d}(\log P)$

$= [\mathcal{O}_{\rm med}(P)\,{\rm d}(\log P)\,/\,\mathcal{P}_{\rm med}(P)]\times C_{\rm Malm}$, where $C_{\rm Malm} = 0.91$ for the OGLE-III LMC population and $C_{\rm Malm} = 0.94$ for the MW. We present the results in Figure 2.12, where we have propagated in quadrature the errors from each of the three terms in the relations for $\mathcal{U}_{\rm P}(P)$.

At short periods $P = 2\text{-}4$ days, the populations have $\mathcal{U}_{\rm P} \approx 0.2\text{-}0.3$ companions with $q > 0.1$ per full decade of period. At longer periods $P = 10\text{-}20$ days, the values

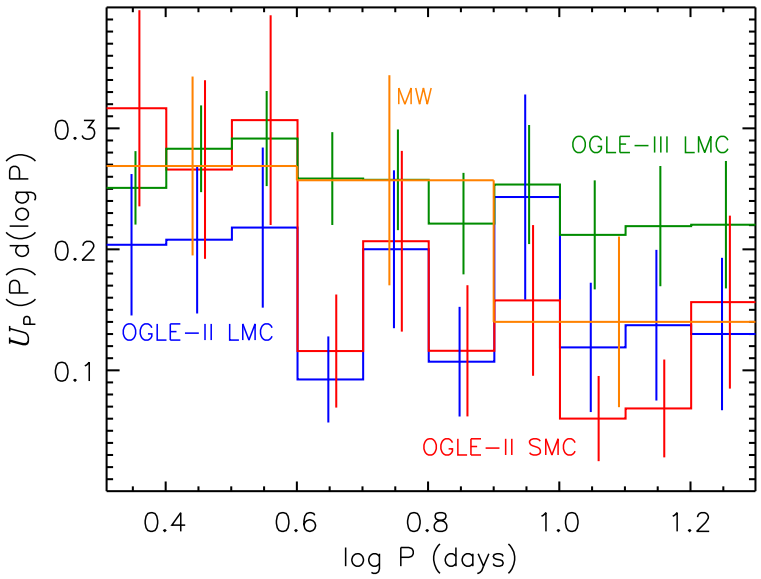

Figure 2.12: The corrected intrinsic period distribution $\mathcal{U}_{\rm P}$, i.e. the frequency of companions with $q > 0.1$ per full decade of period, for the MW (orange), OGLE-II LMC (blue), OGLE-III LMC (green), and OGLE-II SMC (red) populations. All the distributions favor a period distribution that decreases slightly with increasing period, even after correcting for geometrical selection effects. The small range in the integrated fractions $\mathcal{F}_{\rm close} = \int \mathcal{U}_{\rm P}\,{\rm d}(\log P) = (16\text{-}25)\%$ attests to the uniformity of the early-B close binary fraction.

are slightly lower at $\mathcal{U}_{\rm P} \approx 0.1$ - 0.2. Even after correcting for geometrical selection effects and incompleteness toward low-mass companions, the general trend is that $\mathcal{U}_{\rm P}$ decreases with increasing P across the interval $0.3 < \log P < 1.3$. This is consistent with our $\chi^2_{\rm P}$ fits which favored negative $\gamma_{\rm P}$, i.e. distributions skewed toward shorter periods compared to Öpik's law of $\gamma_{\rm P} = 0$. The integrated fractions cover a narrow range $\mathcal{F}_{\rm close} = \int \mathcal{U}_{\rm P}\, {\rm d}(\log P) = 0.16$ - 0.25, again demonstrating the close binary fraction does not change with metallicity.

2.4 Comparison to Spectroscopic Binaries in the MW

We have utilized the Lefèvre et al. (2009) catalog of eclipsing binaries based on Hipparcos data to constrain the close binary properties of early-B primaries in the MW (summarized in Table 2.6). We now wish to compare these properties to spectroscopic observations of early-type stars in the MW. This will demonstrate consistency between the eclipsing and spectroscopic methods of inferring the close binary parameters. As with eclipsing systems, observations of spectroscopic binaries are biased toward systems with edge-on orientations and massive secondaries. For each of the following spectroscopic samples, we must consider their sensitivity and completeness toward low-mass companions so that we can accurately compare $\mathcal{F}_{\rm close}$.

In the spectroscopic survey of 78 B-type stars in the Sco-Cen association, Levato et al. (1987) found 15 systems with $P = 2$ - 20 days. Their sample was complete to velocity semi-amplitudes of $K \gtrsim 15$ km s^{-1}. Assuming a typical primary mass of

Table 2.6. Milky Way comparison of our fitted binary properties for early-type stars based on spectroscopic radial velocity observations to our analysis of Hipparcos MW eclipsing binaries. The close binary fraction, i.e. the fraction of systems which have a companion with orbital period $P = 2\text{-}20$ days and mass ratio $q > 0.1$, nearly doubles between late-B and O spectral type primaries. Other parameters are fairly consistent with a negligible excess twin fraction $\mathcal{F}_{\rm twin} \approx 7\%$, a mass-ratio distribution weighted toward low-mass companions with $\gamma_{\rm q} \approx -0.9$, and a period distribution with $\gamma_{\rm P} \approx -0.3$ that is slightly skewed toward shorter periods relative to Öpik's law.

Spec. Type	Method	$\mathcal{F}_{\rm twin}$	$\gamma_{\rm q}$	$\gamma_{\rm P}$	$\mathcal{F}_{\rm close}$	Sample Reference
Late-B	Spectroscopic	0.06 ± 0.03	-1.2 ± 0.4	-0.3 ± 0.4	0.16 ± 0.06	Levato et al. (1987)
Early-B					0.22 ± 0.07	
Early-B	Eclipsing	0.16 ± 0.10	-0.9 ± 0.8	-0.4 ± 0.3	0.21 ± 0.05	Lefèvre et al. (2009)
Early-B	Spectroscopic	0.06 ± 0.05	-0.9 ± 0.4	0.2 ± 0.5	0.23 ± 0.06	Abt et al. (1990)
O	Spectroscopic	0.08 ± 0.06	-0.2 ± 0.5	-0.5 ± 0.3	0.31 ± 0.07	Sana et al. (2012)

$M_1 \approx 5\,{\rm M}_\odot$ for a mid B-type star, a representative inclination of $i \approx 50^{\rm o}$, and their mean orbital period of $P \approx 6$ days, then the corresponding sensitivity is coincidentally $q \approx 0.10$. Since we do not need to correct for incompleteness down to $q = 0.1$, the close binary fraction is $\mathcal{F}_{\rm close} = 15\,/\,78 = (19 \pm 5)\%$. If we divide the sample into late-type ($\geq$ B5) and early-type ($\leq$ B4) groups, then the close binary fractions would be $\mathcal{F}_{\rm close} = (16 \pm 6)\%$ and $(22 \pm 7)\%$, respectively.

Using these $\mathcal{N} = 15$ systems in the Levato et al. (1987) catalog, we fit the orbital period distribution $\mathcal{U}_{\rm P}$ based on the theoretical parametrization in Eq. 2.1. To constrain $\gamma_{\rm P}$, we maximize the likelihood function ${\rm L}(\gamma_{\rm P}) = \prod_{k=1}^{\mathcal{N}} \mathcal{U}_{\rm P}(P_k|\gamma_{\rm P})\,{\rm d}(\log P)$, where we ensure $\mathcal{U}_{\rm P}$ integrates to unity in this instance. We repeat this procedure $\mathcal{N}$ times

with delete-one jackknife resamplings of the data to quantify the error. We find $\gamma_{\rm P} = -0.3 \pm 0.4$, i.e. a distribution slightly skewed toward shorter periods but still consistent with Öpik's law.

We also use these 15 systems to estimate a statistical mass-ratio distribution $\mathcal{U}_{\rm q}$. For the three double-lined spectroscopic binaries with well-defined orbits, we determine q simply from the ratio of the observed velocity semi-amplitudes. For the remaining 12 systems, primarily single-lined spectroscopic binaries, we determine the primary mass M_1 from the spectral type, assume a random inclination in the interval $i = 10^{\rm o}$ - $80^{\rm o}$ for each system k, and then utilize the listed mass function $f(M)$ to estimate a statistical mass-ratio q_k. Using our parametrization in Eq. 2.2, we then maximize the likelihood function $\mathrm{L}(\gamma_{\rm q},\, \mathcal{F}_{\rm twin}) = \prod_{k=1}^{\mathcal{N}} \mathcal{U}_{\rm q}(q_k|\gamma_{\rm q}, \mathcal{F}_{\rm twin})\, {\rm d}q$, where we only include systems with statistical mass-ratios in the interval $q_k = 0.1$ - 1.0. To quantify the error, we repeat this process $\mathcal{N}$ times with delete-one jackknife resamplings of the data, where we evaluate each of the systems without a dynamical mass ratio at a different random inclination. We find a mass-ratio distribution weighted toward low-mass companions with $\gamma_{\rm q} = -1.2 \pm 0.4$, and a small excess twin fraction of $\mathcal{F}_{\rm twin} = 0.06 \pm 0.03$. We report these results in Table 2.6.

In the magnitude-limited sample of early-B stars, Abt et al. (1990) corrected for classical Malmquist bias and found 16 out of 109 systems to be spectroscopic binaries with $P = 2$ - 20 days. They were only sensitive down to velocity semi-amplitudes of $K \gtrsim 20$ km s^{-1}, but reported incompleteness factors down to $M_2 \approx 0.7\,{\rm M}_\odot$ of $I \approx 1.4$ for $P = 0.36$ - 3.6 days and $I \approx 1.8$ for $P = 3.6$ - 36 days. Given their nominal primary mass of $M_1 \approx 8\,{\rm M}_\odot$, we adopt an intermediate incompleteness factor of $I = 1.6$ to correct down to $q \approx 0.1$ for our systems of interest with $P = 2$ - 20 days. This results in a

close binary fraction of $\mathcal{F}_{\rm close} = 16 \times 1.6 \,/\, 109 = (23 \pm 6)\%$, consistent with the early-B subsample result we derived from the Levato et al. (1987) data.

We determine the period distribution $\mathcal{U}_{\rm P}$ and mass-ratio distribution $\mathcal{U}_{\rm q}$ for the Abt et al. (1990) survey using two methods. First, we fit the 16 observed systems using the same procedure utilized above for the Levato et al. (1987) sample. We find $\gamma_{\rm P} = 0.1 \pm 0.4$, $\gamma_{\rm q} = -0.8 \pm 0.3$, and $\mathcal{F}_{\rm twin} = 0.07 \pm 0.04$. Second, we use the values in Table 2.6 of Abt et al. (1990), which have been corrected for incompleteness. They estimate there to be ≈ 5.7 systems with $P = 1.7$ - 3.6 days, i.e. ≈ 17.5 systems per decade of period at $\log P \approx 0.4$, and ≈ 34.4 systems with $P = 3.6$ - 36 days, i.e. 34.4 systems per decade of period at $\log P \approx 1.1$. These two data points imply a slope of $\gamma_P = 0.3$. We then utilize their four bins of secondary masses for the 40.1 systems with $P < 36$ days. Minimizing the χ^2 statistic between the four bins of data and our two-parameter formalism $\mathcal{U}_{\rm q}$, we find $\gamma_{\rm q} \approx -1.0$ and $\mathcal{F}_{\rm twin} = 0.05$. We adopt the average of the two methods so that $\gamma_{\rm P} = 0.2 \pm 0.5$, $\gamma_{\rm q} = -0.9 \pm 0.4$, and $\mathcal{F}_{\rm twin} = 0.06 \pm 0.05$ (see Table 2.6).

Based on spectroscopic observations of 71 O-type stars in various open clusters, Sana et al. (2012) found 21 systems with orbital periods $P = 2$ - 20 days. After they corrected down to $q = 0.1$, they estimated there to be only ≈ 1 additional system that escaped their detection in this period range. This results in a close binary fraction of $\mathcal{F}_{\rm close} = (31 \pm 7)\%$, which is slightly higher than the B-type results.

We fit the period and mass-ratio distributions for these 21 systems using the same method as for the Levato et al. (1987) sample. We find $\gamma_P = -0.5 \pm 0.3$, which is consistent with their result of $\mathcal{U}_{\rm P} \propto (\log P)^{-0.55 \pm 0.22} \, {\rm d}(\log P)$ for all their spectroscopic binaries (note slightly different parametrization). We also find $\gamma_{\rm q} = -0.2 \pm 0.5$ and

$\mathcal{F}_{\rm twin} = 0.08 \pm 0.06$, consistent with their fit of $\gamma_{\rm q} = \kappa = -0.1 \pm 0.6$ to all the systems in their sample. This result for the mass-ratio distribution is fairly robust because 18 of the 21 systems were double-lined spectroscopic binaries with dynamical mass ratios. However, the formal error bar on the derived $\gamma_{\rm q}$ is quite large, so that the fit is still consistent with the lower values of γ_q measured for the previous populations.

We compare the close binary parameters for the three spectroscopic samples and the Hipparcos eclipsing binary sample in Table 2.6. The only clear trend is an increasing close binary fraction with primary mass so that $\mathcal{F}_{\rm close}$ nearly doubles between late-B and O type stars. Assigning $\langle M_1 \rangle = 4\,{\rm M}_\odot$, $10\,{\rm M}_\odot$, and $25\,{\rm M}_\odot$ to late-B, early-B, and O spectral types, respectively, the Pearson correlation coefficient of $\log M_1$ versus $\log \mathcal{F}_{\rm close}$ for the five data points in Table 2.6 is $r = 0.99$. This highly significant correlation implies that M_1 and $\mathcal{F}_{\rm close}$ are related via a simple power-law, which we find to be $\mathcal{F}_{\rm close} = 0.22(M_1/10{\rm M}_\odot)^{0.4}$. All of the populations are consistent with a small twin fraction $\mathcal{F}_{\rm twin} \approx 7\%$, mass-ratio distribution that favors low-mass companions with $\gamma_{\rm q} \approx -0.9$, and a period distribution with $\gamma_{\rm P} \approx -0.3$ that is skewed toward shorter periods compared to Öpik's law. The fact that all the derived binary properties derived from the eclipsing and spectroscopic binary samples are in agreement is testament to the robustness of our eclipsing binary models and the validity of $\mathcal{F}_{\rm close}$ reported for the different environments in §2.3.

2.5 Discussion

2.5.1 Summary

We have analyzed four different samples of eclipsing binaries with early-B primaries: one in the MW with $\langle \log(Z/\mathrm{Z}_\odot) \rangle = 0.0$, two in the LMC with $\langle \log(Z/\mathrm{Z}_\odot) \rangle = -0.4$, and one in the SMC with $\langle \log(Z/\mathrm{Z}_\odot) \rangle = -0.7$. The fractions of early-B stars which exhibit deep eclipses $0.25 < \Delta\mathrm{m\,(mag)} < 0.65$ with orbital periods $2 < P\,(\mathrm{days}) < 20$ span a narrow range of $\mathcal{F}_{\mathrm{deep}} = (0.7\text{-}1.0)\%$ among all four populations (Table 2.1). The OGLE-II LMC and SMC observations become incomplete toward shallower eclipses, while the OGLE-III LMC and Hipparcos MW observations are complete to $\Delta\mathrm{m} = 0.1$. For these latter two surveys, $\mathcal{F}_{\mathrm{med}} = 1.9\%$ of early-B stars exhibit eclipses $0.1 < \Delta\mathrm{m} < 0.65$ with $P = 2\text{-}20$ days (Table 2.1). The consistency of these results are model independent, demonstrating that the eclipsing binary fractions do not vary with metallicity.

All four samples have similar eclipse depth distributions $\mathcal{O}_{\Delta\mathrm{m}}$ across the intervals over which their respective surveys are complete (Figure 2.1). Based on the larger and more complete OGLE-III LMC sample, we find a simple power-law fit $\mathcal{S}_{\Delta\mathrm{m}}\,\mathrm{d}(\Delta\mathrm{m}) \propto (\Delta\mathrm{m})^{-1.65\,\pm\,0.07}\,\mathrm{d}(\Delta\mathrm{m})$, which is significantly steeper than the distribution $\mathcal{S}_{\Delta\mathrm{m}}\,\mathrm{d}(\Delta\mathrm{m}) \propto (\Delta\mathrm{m})^{-1.0}\,\mathrm{d}(\Delta\mathrm{m})$ we would expect if the companions were selected from a uniform mass-ratio distribution. All four samples also have observed period distributions $\mathcal{O}_{\mathrm{deep}}(P)$ or $\mathcal{O}_{\mathrm{med}}(P)$ that are slightly skewed toward shorter periods relative to Öpik's prediction of $\mathcal{S}_{\mathrm{deep}}(P)\,\mathrm{d}(\log P) \propto \mathcal{S}_{\mathrm{med}}(P)\,\mathrm{d}(\log P) \propto P^{-2/3}\,\mathrm{d}(\log P)$ (Figure 2.2). The OGLE-II SMC distribution is especially weighted toward shorter periods, but this sample may be slightly incomplete for modest eclipse depths $\Delta\mathrm{m} = 0.25\text{-}0.30$ mag and longer

orbital periods $P = 10\text{-}20$ days. It would be worthwhile to examine this feature once an OGLE-III SMC eclipsing binary catalog becomes available.

In order to correct for geometrical selection effects and incompleteness toward low-mass companions, we employed detailed NIGHTFALL light curve models and performed thousands of Monte Carlo simulations for various binary populations. By minimizing the χ^2 statistics between the observed distributions $\mathcal{O}$ and our models $\mathcal{M}$, we were able to constrain the underlying properties $\mathcal{U}$ of the close binaries in each of our samples. In our models, we considered a multitude of systematic effects including tidal distortions, mutual irradiation, limb darkening, stellar evolution and Roche lobe filling, third light contamination due to stellar blending and triple star systems, eccentric orbits, uncertainties in dust extinction, and Malmquist bias.

The four fitted model parameters $\gamma_{\rm q}$, $\mathcal{F}_{\rm twin}$, $\gamma_{\rm P}$, and $\mathcal{F}_{\rm close}$ for all four eclipsing binary samples are fairly consistent with each other. The mean mass-ratio exponents span $\gamma_{\rm q} = -1.0\text{-}-0.6$ for the four samples (Table 2.2 and Figure 2.7), suggesting the mass-ratio distribution $\mathcal{U}_{\rm q} \propto q^{\gamma_{\rm q}}\,{\rm d}q$ is weighted toward lower mass companions relative to a uniform distribution with $\gamma_{\rm q} = 0$. An excess of twins with $q > 0.9$ comprise a small fraction $\mathcal{F}_{\rm twin} = (4\text{-}16)\%$ of all companions with $q > 0.1$ (Table 2.2 and Figure 2.7). The period distributions are slightly skewed toward shorter periods relative to Öpik's law, giving $\gamma_{\rm P} = -0.9\text{-}-0.1$ in the relation $\mathcal{U}_{\rm P} \propto P^{\gamma_{\rm P}}\,{\rm d}(\log P)$ (Table 2.3 and Figures 2.10 & 2.12). Finally, the close binary fractions with $q > 0.1$ and $P = 2\text{-}20$ days span a narrow range of $\mathcal{F}_{\rm close} = (16\text{-}25)\%$ (Table 2.5 and Figure 2.12). None of these parameters exhibited a trend with metallicity, signifying that the close binary properties do not vary with metallicity across the interval $-0.7 < \log(Z/{\rm Z}_\odot) < 0.0$.

We emphasize that these model parameters are only valid for $q > 0.1$ and $P = 2\text{-}20$ days, and should not be extrapolated toward lower mass companions or longer orbital periods. Moreover, these quantities represent the mean values in our parameter space because we have assumed the mass-ratio distribution $\mathcal{U}_{\rm q}$ is independent of the orbital period P. The large OGLE-III LMC medium eclipse depth sample exhibits a statistically significant trend between P and Δm, and we will investigate this feature in more detail in a future study. Nevertheless, all four samples of eclipsing binaries exhibited weak or no correlations between P and Δm with Spearman rank coefficients $|\rho| < 0.15$. In addition, the probabilities of observing medium eclipses $\mathcal{P}_{\rm med}(P)$ are relatively independent of the underlying mass-ratio distribution $\mathcal{U}_{\rm q}$ (see §2.3.3). The close binary fraction $\mathcal{F}_{\rm close}$ for the OGLE-III LMC population will therefore not vary beyond the cited errors, even when we consider a period-dependent mass-ratio distribution.

2.5.2 Comparison with Previous Studies

In §2.4, we examined three samples of spectroscopic binaries in the MW with early-type primaries (Levato et al. 1987; Abt et al. 1990; Sana et al. 2012). These observations demonstrated that the close binary fraction increased by nearly a factor of two between late-B type primaries with $\mathcal{F}_{\rm close} \approx 16\%$ and O-type primaries with $\mathcal{F}_{\rm close} \approx 31\%$. The three samples were consistent with a negligible excess twin fraction $\mathcal{F}_{\rm twin} \approx 7\%$, a mass-ratio distribution weighted toward low-mass companions with $\gamma_{\rm q} \approx -0.9$, and a period distribution with $\gamma_{\rm P} \approx -0.3$ that is slightly skewed toward shorter periods relative to Öpik's law. The only outlier beyond the 1σ level was the overall mass-ratio distribution of the Sana et al. (2012) sample, which we fitted to have $\gamma_{\rm q} = -0.2 \pm 0.5$.

More recently, however, Sana et al. (2013) found a lower value and tighter constraint of $\gamma_q = \kappa = -1.0 \pm 0.4$ based on spectroscopic observations of O-type stars in 30 Doradus, which is even more consistent with our mean value. The fact that the close binary fractions and properties inferred from spectroscopic binaries match the parameters derived from our eclipsing binary samples is testament to the robustness of our models.

There may indeed be a narrow peak of twins in the mass-ratio distribution so that $\mathcal{U}_{\rm q}(q \approx 1)$ is several times the value of $\mathcal{U}_{\rm q}(q \approx 0.8)$. However, this twin contribution represents a small fraction of the total population of secondaries in the entire interval $0.1 < q < 1$. Based on a sample of 21 detached eclipsing binaries in the SMC with massive primaries, $P < 5$ days, and well-determined spectroscopic orbits, Pinsonneault & Stanek (2006) estimated a modest excess twin fraction of $\mathcal{F}_{\rm twin} = 20\text{-}25\%$. However, they assumed their underlying uniform mass-ratio distribution could be extrapolated below their detection limit of $q \approx 0.55$, so they expected relatively few systems below their survey sensitivity. If instead the low-q tail was replaced with our fitted mean value of $\gamma_{\rm q} = -1.0\text{--}0.6$, depending on the sample, then the twin fraction would be reduced to $\mathcal{F}_{\rm twin} = (5\text{-}10)\%$, which is consistent with our results. Because we find the overall mass-ratio distribution to be weighted toward lower masses with $\gamma_{\rm q} \approx -0.9$, the relative contribution of twin systems with $q \gtrsim 0.9$ is small compared to all secondaries across the interval $0.1 < q < 1$.

Mazeh et al. (2006) used OGLE-II LMC eclipsing binary data to derive a close binary fraction of 0.7%. Our value of $\mathcal{F}_{\rm close} = (16 \pm 6)\%$ for this population is a factor of ≈20 higher for four reasons. First, Mazeh et al. (2006) only included systems with orbital periods $P = 2\text{-}10$ days while we extended our sample to include orbital periods up to $P = 20$ days. Assuming Öpik's law, we would expect our close binary fraction to

be 40% higher, a minor contribution to the overall discrepancy. Second, our samples contained early-B primaries with $-3.8 < \mathrm{M_I} < -1.3$ while Mazeh et al. (2006) considered late-B stars with $-1.8 < \mathrm{M_I} < 0.2$. The close binary fraction rapidly increases with primary mass (see §2.4), so that $\mathcal{F}_{\rm close}$ for early-B stars is ≈1.5 times the late-B value. Third, although Mazeh et al. (2006) accounted for geometrical selection effects, they did not correct for incompleteness toward small, low-mass secondaries. The increase in the eclipsing binary fraction from $\mathcal{F}_{\rm deep} = 0.7\%$ to $\mathcal{F}_{\rm med} = 1.9\%$ already suggests that the increased sensitivity of the OGLE-III survey could find three times more eclipsing systems. In §2.3.3, we showed that correcting for mass-ratio incompleteness *alone* increased the inferred close binary fraction by a factor of $\mathcal{C}_{\rm deep,q} \approx 3$. Finally, our reduction in $\mathcal{F}_{\rm close}$ due to Malmquist bias of the second kind by a factor of $\mathcal{C}_{\rm Malm} = 0.73$ is a not as severe as the factor of $\mathcal{C}_{\rm Malm} = 0.48$ implemented by Mazeh et al. (2006). This is partially because the average luminosity of the eclipsing companions was fainter than the $\langle \Delta \mathrm{M_I} \rangle = 0.5$ mag I-band excess assumed by Mazeh et al. (2006), but also because we accounted for other binaries with luminous secondaries outside our eclipsing binary parameter space of eclipse depths and orbital periods.

2.5.3 Conclusions

Weighting our four samples of eclipsing binaries and the three samples of spectroscopic binaries, we find the best overall model parameters to be $\mathcal{F}_{\rm twin} = 0.07 \pm 0.05$, $\gamma_{\rm q} = -0.9 \pm 0.3$, and $\gamma_{\rm P} = -0.3 \pm 0.3$. The close binary fraction increases with primary mass according to $\mathcal{F}_{\rm close} = (0.22 \pm 0.05)(M_1 \,/\, 10\mathrm{M}_\odot)^{0.4}$. None of these properties exhibited statistically significant trends with metallicity across the interval $-0.7 < \log(Z/\mathrm{Z}_\odot) < 0.0$,

demonstrating the close binary properties of massive stars are fairly independent of metallicity. Any observed variations in the rates or properties of massive star or binary evolution within this metallicity range must derive from metallicity-dependent stellar physical processes, and not on the initial conditions of the MS binaries themselves.

Chapter 3

A New Class of Nascent Eclipsing Binaries with Extreme Mass Ratios

This thesis chapter originally appeared in the literature as

M. Moe & R. Di Stefano, *The Astrophysical Journal*, 801, 113, 2015

Abstract

Early B-type main-sequence (MS) stars ($M_1 \approx 5\text{-}16\,M_\odot$) with closely orbiting low-mass stellar companions ($q = M_2/M_1 < 0.25$) can evolve to produce Type Ia supernovae, low-mass X-ray binaries, and millisecond pulsars. However, the formation mechanism and intrinsic frequency of such close extreme mass-ratio binaries have been debated, especially considering none have hitherto been detected. Utilizing observations of the Large Magellanic Cloud galaxy conducted by the Optical Gravitational Lensing Experiment, we have discovered a new class of eclipsing binaries in which a luminous

B-type MS star irradiates a closely orbiting low-mass pre-MS companion that has not yet fully formed. The primordial pre-MS companions have large radii and discernibly reflect much of the light they intercept from the B-type MS primaries ($\Delta I_{\rm refl} \approx 0.02$ - 0.14 mag). For the 18 definitive MS + pre-MS eclipsing binaries in our sample with good model fits to the observed light curves, we measure short orbital periods $P = 3.0$ - 8.5 days, young ages $\tau \approx 0.6$ - $8\,{\rm Myr}$, and small secondary masses $M_2 \approx 0.8$ - $2.4\,{\rm M}_\odot$ ($q \approx 0.07$ - 0.36). The majority of these nascent eclipsing binaries are still associated with stellar nurseries, e.g. the system with the deepest eclipse $\Delta I_1 = 2.8$ mag and youngest age $\tau = 0.6 \pm 0.4$ Myr is embedded in the bright H II region 30 Doradus. After correcting for selection effects, we find that $(2.0 \pm 0.6)\%$ of B-type MS stars have companions with short orbital periods $P = 3.0$ - 8.5 days and extreme mass ratios $q \approx 0.06$ - 0.25. This is $\approx$10 times greater than that observed for solar-type MS primaries. We discuss how these new eclipsing binaries provide invaluable insights, diagnostics, and challenges for the formation and evolution of stars, binaries, and H II regions.

3.1 Introduction

Close binaries with orbital periods $P \lesssim 10^3$ days are ubiquitous (Abt 1983; Duquennoy & Mayor 1991; Kobulnicky & Fryer 2007; Raghavan et al. 2010; Sana et al. 2012; Duchêne & Kraus 2013) and are the progenitors of a variety of astrophysical phenomena (Paczyński 1971; Iben & Tutukov 1987; Verbunt 1993; Phinney & Kulkarni 1994; Taam & Sandquist 2000). Nonetheless, a close stellar companion cannot easily form in situ (see Mathieu 1994 and Tohline 2002 for observational and theoretical reviews, respectively). Instead, the companion most likely fragments from the natal gas cloud or circumstellar

disk at initially wider orbital separations (Bate & Bonnell 1997; Kratter & Matzner 2006). Various migration hypotheses have been proposed for how the orbit decays to shorter periods (Bate et al. 2002; Bonnell & Bate 2005). These formation scenarios produce mostly close binaries with components of comparable mass because a low-mass companion either accretes additional mass from the disk, merges with the primary, remains at wide separations, or is dynamically ejected from the system.

Close binaries with extreme mass ratios most likely require an alternative formation mechanism. For example, a low-mass companion can be tidally captured into a closer orbit (Press & Teukolsky 1977; Bally & Zinnecker 2005; Moeckel & Bally 2007), possibly with the assistance of gravitational perturbations from a third star (Kiseleva et al. 1998; Naoz & Fabrycky 2014). Indeed, a significant fraction of close binaries are orbited by an outer tertiary (Tokovinin et al. 2006), suggesting the third star may play a role in the dynamical formation of the system. It is fair to say that the mutual formation and coevolution between massive stars and close companions are not yet fully understood. It has even been proposed that massive stars formed primarily via mergers of close binaries instead of through gas accretion from the circumstellar disk (Bonnell & Bate 2005; Bally & Zinnecker 2005). A complete census of close companions to massive stars must be conducted in order to determine the dominant formation mechanism of close binaries and massive stars as well as to reliably predict the production rates of certain channels of binary evolution.

It is extremely difficult, however, to detect faint low-mass companions that are closely orbiting massive luminous primaries. B-type main-sequence (MS) stars with low-mass secondaries have been photometrically resolved at extremely wide orbital separations $a \gtrsim 50$ AU, i.e. long orbital periods $P \gtrsim 10^5$ days (Abt et al. 1990; Shatsky

& Tokovinin 2002). Some of these resolved low-mass companions are still pre-MS stars that can emit X-rays (Hubrig et al. 2001; Stelzer et al. 2003). Late B-type MS stars detected at X-ray wavelengths most likely have unresolved low-mass pre-MS companions at $a \lesssim 50$ AU (Evans et al. 2011). However, the precise orbital periods of these putative X-ray emitting companions have not yet been determined. These unresolved binaries may have short orbital periods $P < 10^3$ days and may eventually experience substantial mass transfer and/or common envelope evolution as the primary evolves off the MS. Alternatively, the binaries could have intermediate orbital periods $P = 10^3$ - 10^5 days and could therefore avoid Roche-lobe overflow.

Multi-epoch radial velocity observations of double-lined spectroscopic binaries (SB2s) can provide the orbital periods P and velocity semi-amplitudes K_1 and K_2. Hence, the mass ratio $q \equiv M_2/M_1 = K_1/K_2$ of an SB2 can be directly measured dynamically. However, SB2s with MS components can only reveal companions that are comparable in luminosity, and therefore mass, to the primary star. SB2s with early-type primaries, known orbital periods, and dynamically measured masses all have moderate mass ratios $q > 0.25$ (Wolff 1978; Levato et al. 1987; Abt et al. 1990; Sana et al. 2012). Gullikson & Dodson-Robinson (2013) combined multiple high-resolution spectra of early-type stars in order to substantially increase the signal-to-noise. By implementing this novel technique, they detected SB2s with larger luminosity contrasts and therefore smaller mass ratios $q \approx 0.1$ - 0.2. Although Gullikson & Dodson-Robinson (2013) found a few candidates, stacking multiple spectra from random epochs in order to increase the signal-to-noise does not relay the orbital period of the binary. Similar to the case above of late-B primaries with unresolved, X-ray emitting companions, these SB2s with indeterminable periods may have wide orbital separations.

Close faint companions to B-type MS primaries can induce small radial velocity variations, and these reflex motions have been observed with multi-epoch spectroscopy (Wolff 1978; Levato et al. 1987; Abt et al. 1990). Although the orbital periods of these single-lined spectroscopic binaries (SB1s) can be measured, they have only lower limits for their mass ratios because the inclinations are not known. Nonetheless, an average inclination or a distribution of inclinations can be assumed for a population of SB1s in order to recover a statistical mass-ratio distribution (Mazeh & Goldberg 1992). For SB1s with solar-type MS primaries $M_1 \approx 1\,\mathrm{M}_\odot$, the companions are almost certainly low-mass M-dwarfs (Duquennoy & Mayor 1991; Mazeh et al. 1992b; Grether & Lineweaver 2006; Raghavan et al. 2010). For early-type MS primaries $M_1 \approx 10\,\mathrm{M}_\odot$, however, SB1s can either contain $M_2 \approx 0.5\text{-}3\,\mathrm{M}_\odot$ K-A type stellar companions or $M_2 \approx 0.5\text{-}3\,\mathrm{M}_\odot$ stellar remnants such as white dwarfs, neutron stars, or black holes (Wolff 1978; Garmany et al. 1980). Wolff (1978) even suggests that most SB1s with late-B MS primaries contain white dwarf companions, and therefore the fraction of unevolved low-mass stellar companions to B-type MS stars is rather small. Unfortunately, there is at present no easy and systematic method for distinguishing between these two possibilities for all SB1s in a statistical sample. Because early-type SB1s may be contaminated by evolved stellar remnants, it is prudent to only consider binaries where the nature of the secondaries are reliably known. In addition to discovering close unevolved low-mass companions to B-type MS stars, we must also utilize a different observational technique for easily identifying such systems from current and future telescopic surveys.

Fortunately, extensive visual monitoring of one of our satellite galaxies, the Large Magellanic Cloud (LMC), conducted by the third phase of the Optical Gravitational Lensing Experiment (OGLE-III) has yielded a vast database primed for the identification

and analysis of such binaries (Udalski et al. 2008; Graczyk et al. 2011). OGLE-III surveyed 35 million stars in the LMC over seven years, typically obtaining ≈470 near-infrared I and ≈45 visual V photometric measurements per star (Udalski et al. 2008). Moreover, Graczyk et al. (2011) utilized a semi-automated routine to identify more than 26,000 eclipsing binaries in the OGLE-III LMC database. They cataloged basic observed parameters of the eclipsing binaries such as orbital periods P and primary eclipse depths ΔI_1, but the intrinsic physical properties of the eclipsing binaries still need to be quantified.

We previously showed that B-type MS stars with low-mass zero-age MS companions $q \approx 0.1$ - 0.2 can produce shallow eclipses $\Delta I_1 \approx 0.1$ - 0.2 mag if the inclinations are sufficiently close to edge-on (see Fig. 3.5 in Moe & Di Stefano 2013). Indeed, the OGLE-III LMC survey is sensitive to such shallow eclipses, so we expect B-type MS stars with low-mass companions to be hiding in the OGLE-III LMC eclipsing binary catalog. We therefore began to systematically measure the physical properties of the eclipsing binaries in hopes of identifying such extreme mass-ratio binaries.

While investigating the light curves of eclipsing binaries in the OGLE-III LMC database, we serendipitously discovered an unusual subset that displayed sinusoidal profiles between narrow eclipses (prototype shown in Fig. 3.1). We soon realized the sinusoidal variations are caused by the reflection of light received by a large, low-mass, *pre-MS* companion from the hot B-type MS primary. The present study is dedicated to a full multi-stage analysis of this new class of eclipsing binaries. In §3.2, we present our selection criteria for identifying "reflecting" eclipsing binaries with B-type MS stars and low-mass pre-MS companions. We then measure the physical properties of these systems by fitting eclipsing binary models to the observed light curves (§3.3). We also

examine observed correlations among various properties of our nascent eclipsing binaries, including their associations with star-forming H II regions (§3.4). In §3.5, we correct for selection effects in order to determine the intrinsic frequency of close, low-mass companions to B-type MS stars. In §3.6, we discuss the implications of these eclipsing binaries in the context of binary star formation and evolution. Finally, we summarize our main results and conclusions (§3.7).

3.2 A New Class of Eclipsing Binaries

3.2.1 Selection Criteria and Analytic Models

The OGLE-III LMC photometric database (Udalski et al. 2008) lists the mean magnitudes $\langle I \rangle$, colors $\langle V - I \rangle$, and positions for each of the 35 million stars in their survey. Throughout this work, we adopt a distance $d = 50$ kpc to the LMC (Pietrzyński et al. 2013). We also incorporate stellar parameters such as temperature-dependent bolometric corrections $\mathrm{BC}(T_{\mathrm{eff}})$ and intrinsic color indices $(V - I)_{\mathrm{o}}\,(T_{\mathrm{eff}})$ from Pecaut & Mamajek (2013). Based on these parameters, we select the $\mathcal{N}_{\mathrm{B}} \approx 174{,}000$ systems from the OGLE-III LMC catalog with mean magnitudes $16.0 < \langle I \rangle < 18.0$ and colors $-0.25 < \langle V - I \rangle < 0.20$ that correspond to luminosities and surface temperatures, respectively, of B-type MS stars.

The OGLE-III LMC eclipsing binary catalog (Graczyk et al. 2011) provides the time t, photometric magnitude I or V, and photometric error σ_{phot} for the $\mathcal{N}_I \approx 470$ and $\mathcal{N}_V \approx 45$ measurements of each eclipsing binary. It also gives general properties of each eclipsing binary such as the orbital period P (in days) and epoch of primary eclipse

minimum t_o (Julian Date − 2450000). The orbital phase simply derives from folding the time of each measurement with the orbital period:

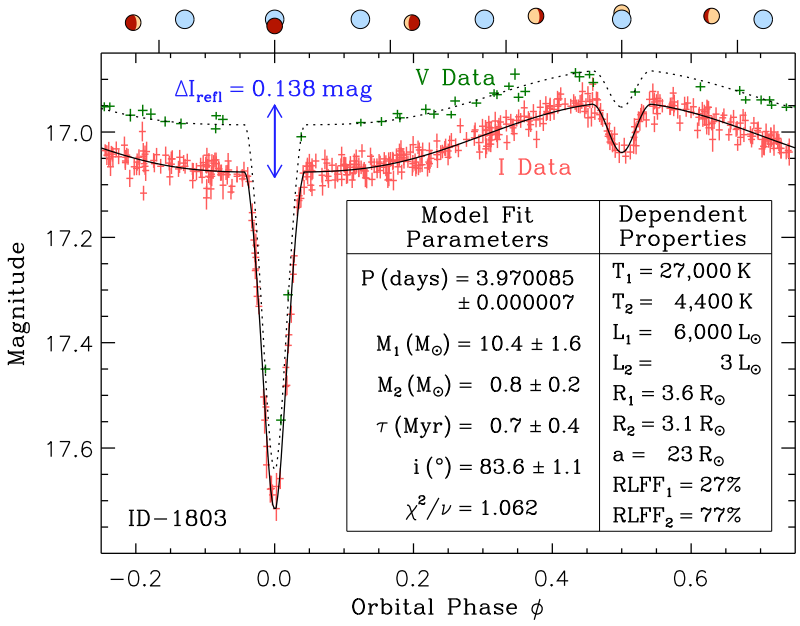

Figure 3.1: One of the 22 OGLE-III LMC eclipsing binary light curves with a B-type MS primary and low-mass pre-MS companion. We fit a detailed *physical* model (black; see §3.3 for details) to the V-band data (green) and I-band data (red). The large reflection effect amplitude $\Delta I_{\rm refl}$ (blue) is used to identify such systems (see §3.2). Above is a to-scale schematic diagram of the binary at the orbital phases indicated by the tick marks. The narrow eclipses dictate a detached binary configuration with Roche-lobe fill-factors $RLFF < 80\%$, which indicate both components are effectively evolving along their respective single-star sequences. The inset tables show the main parameters constrained by the physical model fit (left), and the dependent properties (right) derived by using the model parameters in combination with Kepler's laws and stellar evolutionary tracks. Note the extreme mass ratio $q = M_2/M_1 = 0.07$, young age, and how the primary B-type MS star is significantly hotter and more luminous than the pre-MS secondary.

$$\phi(t) = \frac{(t - t_{\rm o}) \bmod P}{P}. \tag{3.1}$$

We analyze the 2,206 OGLE-III LMC eclipsing binaries that have orbital periods $P =$ 3 - 15 days and satisfy our magnitude and color criteria. Such an immense sample of close companions to B-type MS stars is two orders of magnitude larger than previous spectroscopic binary surveys (Wolff 1978; Levato et al. 1987; Abt et al. 1990).

To automatically and robustly identify "reflecting" eclipsing binaries, we fit an analytic model of Gaussians and sinusoids to the I-band light curves for each of the 2,206 eclipsing binaries in our full sample. The parameters are as follows. The average magnitude $\langle I \rangle$ is the total I-band magnitude of both stars if they did not exhibit eclipses or reflection effects. The primary and secondary eclipse depths are ΔI_1 and ΔI_2, and the primary and secondary eclipse widths are Θ_1 and Θ_2, respectively. The phase of the secondary eclipse Φ_2 provides a lower limit to the eccentricity of the orbit (Kallrath & Milone 2009):

$$e \geq e_{\rm min} = |e \cos(\omega)| = \pi |\Phi_2 - 1/2|/2, \tag{3.2}$$

where ω is the argument of periastron. Finally, $\Delta I_{\rm refl}$ is the full amplitude of the reflection effect, which unlike eclipses, leads to an increase in brightness. With these definitions, we model the I-band light curves in terms of Gaussians and sinusoids:

$$I_{\rm GS}(\phi) = \langle I \rangle + \Delta I_1 \Big[\exp\Big(\frac{-\phi^2}{2\Theta_1^2} \Big) + \exp\Big(\frac{-(\phi-1)^2}{2\Theta_1^2} \Big) \Big] + \Delta I_2 \exp\Big(\frac{-(\phi-\Phi_2)^2}{2\Theta_2^2} \Big) - \frac{\Delta I_{\rm refl}}{2} \Big[\cos\big(2\pi [\phi - 1/2] \big) + 1 \Big]. \quad (3.3)$$

The photometric errors $\sigma_{\rm phot}$ provided in the catalog systematically underestimate the true rms dispersion outside of eclipse by (5 - 20)% (see Fig. 3.2). This is especially true for the brightest systems $\langle I \rangle \approx 16.0$ - 16.5 where the photometric errors $\sigma_{\rm phot} \approx 0.008$ mag are small. We separately fit 3$^{\rm rd}$ degree polynomials across the out-of-eclipse intervals $3\Theta_1 < \phi < \Phi_2 - 3\Theta_2$ and $\Phi_2 + 3\Theta_2 < \phi < 1 - 3\Theta_1$ for the eclipsing binaries with at least 50 data points across these intervals. We then measure the rms dispersion $\sigma_{\rm rms}$ of the residuals resulting from these fits. To rectify the differences between the catalog and actual errors, we multiply each of the photometric uncertainties by a correction factor f_σ:

$$\sigma_{\rm corr}(t) = \sigma_{\rm phot}(t) f_\sigma, \quad (3.4)$$

where f_σ increases toward brighter systems:

$$f_\sigma(I) = 1.05 + 0.15 \times 10^{(16.0-I)/2}. \quad (3.5)$$

The source of this systematic error could partially be due to intrinsic variations in the luminosities of B-type MS stars at the 0.5% level. In any case, the corrected total errors $\sigma_{\rm corr}$ follow the measured rms errors $\sigma_{\rm rms}$ quite well (Fig. 3.2). We implement these corrected errors $\sigma_{\rm corr}$ in our analytic light curve models below.

Even after accounting for the systematic error correction factor f_σ, a few of the photometric measurements are clear outliers. We therefore clip up to $\mathcal{N}_c \leq 2$ measurements per light curve that deviate more than 4σ from our best-fit model. To be conservative, we only eliminate up to two data points to ensure we did not remove any intrinsic signals. Our analytic model has nine parameters (seven explicitly written in Eq. 3.3 as well as our own fitted values of P and t_o according to Eq. 3.1), which provide $\nu = \mathcal{N}_I - \mathcal{N}_c - 9$ degrees of freedom.

For the 2,206 eclipsing binaries, we use an automated Levenberg-Marquardt technique to minimize the χ^2_{GS} statistic between the light curves and analytic models. We also calculate the covariance matrix and standard 1σ statistical uncertainties for our

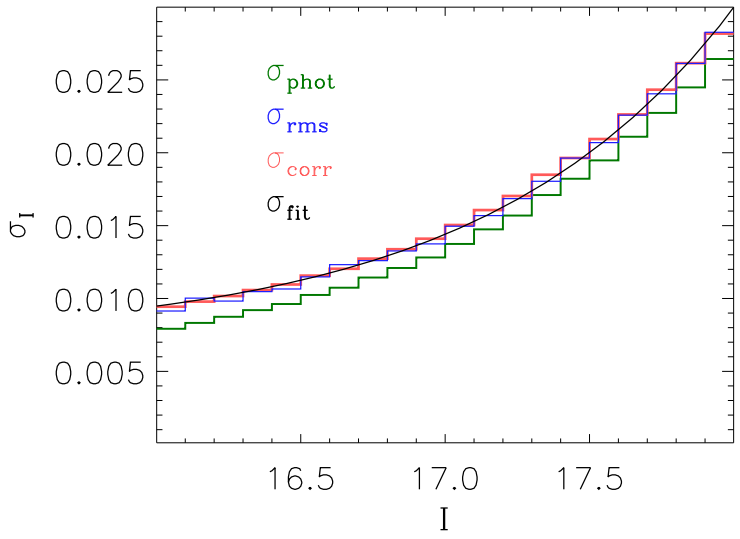

Figure 3.2: For each interval of I-band magnitudes, we compare the median values of the photometric errors σ_{phot} reported in the OGLE-III LMC eclipsing binary catalog (green), the intrinsic rms variations σ_{rms} outside of eclipse (blue), and the total corrected errors σ_{corr} (red). We also display a fit σ_{fit} (black) to the total errors.

nine fitted parameters. We visually inspect the solutions for all systems with $\chi^2_{\rm GS}/\nu > 1.5$ to ensure the parameters converged to the best possible values. For the few models that automatically converged to a local non-global minimum, we adjusted the initial fit parameters and reiterated the Levenberg-Marquardt technique to determine the lowest $\chi^2_{\rm GS}/\nu$ value possible.

Our analytic model of Gaussians and sinusoids does not adequately describe some of the eclipsing binaries, which can lead to large values of $\chi^2_{\rm GS}/\nu = 2\text{-}5$. For example, some of our systems with nearly edge-on orientations exhibit flat-bottomed eclipses, and therefore a simple Gaussian does not precisely match the observed eclipse profile. In addition, our analytic model cannot reproduce light curves with extreme ellipsoidal modulations, i.e. systems with tidally deformed and oblate stars. Nonetheless, our analytic model captures the basic light curve parameters of eclipse depths, eclipse widths, eclipse phases, and amplitude of the reflection effect. These parameters are sufficient in allowing us to distinguish different classes of eclipsing binaries.

To identify eclipsing binaries with reflection effects and well-defined eclipses, we impose the following selection criteria. We require the reflection effect amplitude to be $\Delta I_{\rm refl} > 0.015$ mag and its 1σ uncertainty to be <20% of its value. We stipulate that the 1σ uncertainties in the eclipse depths ΔI_1 and ΔI_2 and eclipse widths Θ_1 and Θ_2 are <25% their respective values. We discard eclipsing binaries with wide eclipses $\Theta_{\rm max} = \max(\Theta_1, \Theta_2) > 0.05$, which removes most systems that have filled their Roche lobes, e.g. semi-detached and contact binaries. Eclipsing binaries with shallow eclipse depths can remain undetected given the sensitivity and cadence of the OGLE-III LMC observations. We therefore keep only systems with total light curve amplitudes:

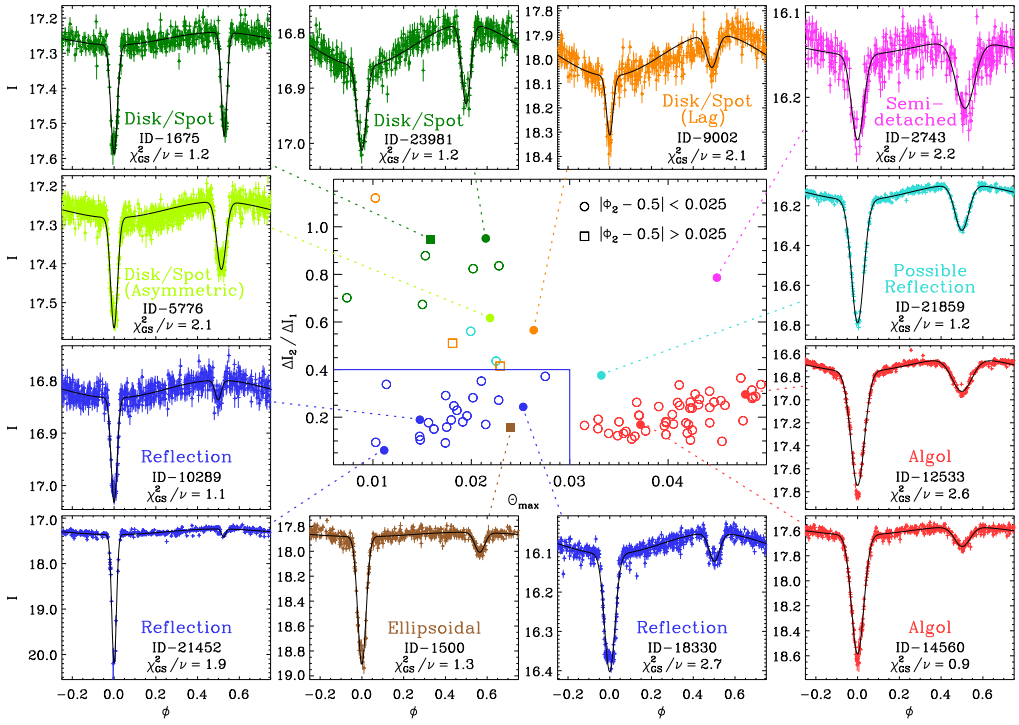

Figure 3.3: Outside panels: Example light curves of the various eclipsing binary populations and the best *analytic* fits of Gaussians and sinusoids. Center panel: Ratio of eclipse depths $\Delta I_2/\Delta I_1$ versus maximum eclipse width $\Theta_{\rm max} = \max(\Theta_1, \Theta_2)$ for the 90 eclipsing binaries with B-type MS primaries, $P = 3$ - 15 days, $\Delta I_{\rm refl} > 0.015$ mag, and $\Theta_{\rm max} < 0.05$. Eclipsing binaries with components of comparable luminosity are toward the top and those with a component that fills or nearly fills its Roche lobe are toward the right. We also distinguish systems with eccentric orbits $e > e_{\rm min} > 0.04$ (square symbols) from those that most likely have nearly circular orbits (circles) based on the observed orbital phase of the secondary eclipse Φ_2. Dotted lines and filled symbols match each light curve to the corresponding system in the central panel. The 22 eclipsing binaries exhibiting genuine reflection effects (blue) have nearly circular orbits and form a distinct population toward the bottom left with $\Theta_{\rm max} < 0.03$ and $\Delta I_2/\Delta I_1 < 0.4$ (blue solid lines).

$$\Delta I = \Delta I_1 + \Delta I_{\rm refl} \geq 10^{0.2(\langle I \rangle - 16.0)} \times 0.08\,{\rm mag} \tag{3.6}$$

to ensure our sample is complete in our selected parameter space (see detection limits in Fig. 3.3 of Graczyk et al. 2011).

3.2.2 Results

We find 90 eclipsing binaries that satisfy these initial selection criteria (see Fig. 3.3). In this subsample, there is one semi-detached binary (magenta system in Fig. 3.3) and 51 Algols, i.e. evolved semi-detached eclipsing binaries that have inverted their mass ratios via stable mass transfer (red population in Fig. 3.3). These evolved eclipsing binaries have wide eclipses $0.031 < \Theta_{\rm max} < 0.050$ that dictate at least one of the binary components fills their Roche lobe. Previous studies of eclipsing binaries in the LMC have noted this Algol population by identifying systems with wide eclipses and large temperature contrasts (Mazeh et al. 2006; Prša et al. 2008).

The remaining 38 objects that satisfy our initial selection criteria have intriguing light curves. We list their catalog properties and analytic light curve parameters in Table 3.1. All but one of these eclipsing binaries have $\Theta_{\rm max} < 0.028$, which indicate a detached configuration. In the following, we use the measured analytic parameters of these 38 systems to understand their physical properties as well as to distinguish various classes of eclipsing binaries.

MS + Pre-MS "Reflecting" Eclipsing Binaries

with Extreme Mass Ratios

Of the 38 unusual eclipsing binaries, we discover that 22 systems form a distinct population with definitive reflection effects $\Delta I_{\rm refl} > 0.015$ mag, narrow eclipses $\Theta_{\rm max} < 0.03$, relatively shallow secondary eclipses $\Delta I_2/\Delta I_1 < 0.4$, and nearly circular orbits according to Φ_2 and Eq. 3.2 (blue systems in Fig. 3.3). These 22 eclipsing binaries have short orbital periods $P = 3.0$ - 8.5 days, large reflection effect amplitudes $\Delta I_{\rm refl} = 0.017$ - 0.138 mag, and moderate to deep primary eclipses $\Delta I_1 = 0.09$ - 2.8 mag.

The reflection effects and primary eclipse depths can be so prominent only if the companions are comparable in size to but substantially cooler than the B-type MS primaries. The companions cannot be normal MS stars since cooler MS stars are also considerably smaller. We can eliminate the alternative that the companions are evolved cool subgiants in an Algol binary because such large subgiants fill their Roche lobes and produce markedly wider eclipses. We therefore conclude that the companions in our 22 systems are cool medium-sized low-mass pre-MS stars that have not yet fully formed.

We can observe these nascent B-type MS + low-mass pre-MS eclipsing binaries at such a special time in their evolution because low-mass companions $q \lesssim 0.25$ contract considerably more slowly during their pre-MS phase of formation. See §3.3, where we more thoroughly analyze the physical properties of these systems by fitting detailed physical light curve models. Our 22 eclipsing binaries with pronounced reflection effects therefore constitute a new class of detached MS + pre-MS close binaries with extreme mass ratios. These systems also represent the first unambiguous identification of B-type MS stars with closely orbiting low-mass stellar companions.

In addition to the selection effects discussed in §3.1, the difficulty in detecting low-mass eclipsing companions to B-type MS stars partially stems from the small number of nearby B-type MS stars in our Milky Way galaxy. Quantitatively, there are only ≈6,000 B-type stars with robust parallactic distances $d < 500\,\mathrm{pc}$ (Perryman et al. 1997). This is a factor of ≈30 times smaller than the number of B-type MS stars $\mathcal{N}_{\mathrm{B}} \approx 174{,}000$ in our OGLE-III LMC sample. It is therefore not surprising that we have not yet observed in the Milky Way the precise counterparts to our reflecting eclipsing binaries with B-type MS primaries and low-mass pre-MS companions.

Other Intriguing Light Curves

We now discuss the remaining 16 unusual systems in our OGLE-III LMC sample. The properties of these 16 eclipsing binaries are not fully understood, and may potentially have important implications for the evolution of close binaries. However, they have distinctly different light curve parameters and physical characteristics than those in our 22 reflecting MS + pre-MS eclipsing binaries. A detailed study of these 16 unusual systems is therefore not in the scope of the present study. We only summarize the observed properties of these 16 systems to illustrate the uniqueness of our nascent eclipsing binaries.

The 12 eclipsing binaries in the top left of Fig. 3.3 have deep secondary eclipses and large out-of-eclipse variations that are not necessarily symmetric with respect to the eclipses. The lack of symmetry dictates that the variations cannot be solely due to reflection effects. Moreover, the deeper secondary eclipses in these systems indicate excess light from a hot spot and/or accretion disk. Similar systems exist in our Milky Way

Table 3.1. Analytic model parameters of 38 eclipsing binaries with intriguing light curves.

Catalog Properties			Analytic Model Parameters											
ID	$\langle V-I\rangle$	$\mathcal{N}_I$	P	t_o	$\langle I\rangle$	ΔI_1	Θ_1	Φ_2	ΔI_2	Θ_2	$\Delta I_{\rm refl}$	$\mathcal{N}_c$	$\chi^2_{\rm GS}/\nu$	Type
1500	0.17	440	6.025412	3563.908	17.883	1.023	0.0201	0.565	0.160	0.0240	0.035	1	1.29	Ellipsoidal
1675	0.04	465	8.697351	3568.781	17.277	0.310	0.0159	0.528	0.294	0.0136	0.037	1	1.21	Disk/Spot
1803	−0.07	460	3.970086	3572.117	17.090	0.637	0.0162	0.501	0.096	0.0156	0.138	1	1.55	Reflection
1965	−0.09	440	3.175248	3570.628	17.221	0.197	0.0219	0.497	0.073	0.0275	0.017	2	1.10	Reflection
2139	−0.16	477	8.462510	3576.045	16.507	0.328	0.0103	0.502	0.031	0.0089	0.033	2	1.28	Reflection
3972	0.06	448	3.396033	3565.053	17.882	0.263	0.0170	0.496	0.148	0.0199	0.023	2	4.14	Possible Reflection
5205	−0.04	456	4.164725	3564.819	16.682	0.162	0.0225	0.499	0.071	0.0221	0.044	1	1.22	Possible Reflection
5377	−0.11	447	3.276364	3563.150	17.346	0.165	0.0178	0.502	0.047	0.0202	0.020	1	1.18	Reflection
5776	−0.03	856	4.715550	3564.833	17.282	0.283	0.0166	0.514	0.174	0.0219	0.042	2	2.06	Disk/Spot (Asym.)
5898	−0.05	439	5.323879	3567.545	16.752	0.834	0.0212	0.501	0.141	0.0215	0.098	1	1.13	Reflection
6630	−0.02	410	3.105571	3563.821	17.104	0.164	0.0205	0.497	0.058	0.0210	0.019	1	1.16	Reflection
7419	0.13	421	4.255889	3563.579	16.502	0.185	0.0180	0.497	0.035	0.0135	0.037	2	1.11	Reflection
7842	−0.05	477	3.781798	3565.825	17.966	1.725	0.0148	0.498	0.181	0.0148	0.083	1	1.24	Reflection
9002	0.04	424	3.578291	3568.696	18.069	0.243	0.0156	0.490	0.137	0.0263	0.173	2	2.08	Disk/Spot (Lag)
9642	0.11	782	3.913360	3565.613	17.933	0.699	0.0174	0.502	0.064	0.0143	0.050	1	1.23	Reflection
10289	−0.09	557	4.642567	3566.031	16.833	0.199	0.0144	0.499	0.038	0.0148	0.034	1	1.09	Reflection
10941	−0.02	559	4.079727	3563.840	17.585	0.154	0.0211	0.401	0.064	0.0229	0.041	2	1.26	Disk/Spot (Lag)
11731	−0.04	477	5.661823	3544.866	16.837	0.059	0.0181	0.529	0.030	0.0169	0.065	1	1.65	Disk/Spot (Lag)
11787	−0.03	493	3.305829	3542.971	17.757	0.487	0.0202	0.500	0.401	0.0201	0.024	0	1.09	Disk/Spot
12528	0.03	476	8.187359	3537.820	17.749	0.240	0.0153	0.498	0.211	0.0153	0.019	2	1.15	Disk/Spot
13194	0.05	493	11.535650	3557.945	17.826	0.234	0.0079	0.498	0.262	0.0103	0.048	2	1.36	Disk/Spot (Lag)
13721	−0.10	428	3.122558	3558.192	17.818	0.420	0.0169	0.500	0.096	0.0185	0.025	1	1.01	Reflection
15306	−0.03	537	12.654262	3580.455	17.955	0.612	0.0068	0.501	0.430	0.0074	0.058	2	0.92	Disk/Spot
15761	−0.11	223	5.310911	3581.568	16.530	0.850	0.0147	0.504	0.101	0.0142	0.108	2	2.86	Reflection
15792	−0.11	600	4.317022	3566.098	16.721	0.231	0.0140	0.500	0.041	0.0156	0.039	2	1.63	Reflection
16828	−0.16	606	3.675697	3572.011	16.618	0.109	0.0174	0.502	0.032	0.0146	0.018	2	1.26	Reflection
17217	−0.12	592	5.354795	3576.802	16.543	0.098	0.0114	0.490	0.033	0.0096	0.022	2	1.24	Reflection
17387	−0.17	605	4.772926	3567.419	16.157	0.094	0.0219	0.499	0.026	0.0228	0.017	0	1.15	Reflection
17695	0.01	473	3.096068	3567.092	17.343	0.176	0.0208	0.501	0.148	0.0228	0.019	2	0.92	Disk/Spot
18330	−0.01	599	3.252913	3561.424	16.104	0.297	0.0253	0.502	0.073	0.0252	0.056	2	2.75	Reflection
18419	−0.13	599	4.118145	3564.319	16.741	0.545	0.0158	0.485	0.086	0.0175	0.059	2	1.83	Reflection
19186	0.01	473	5.652474	3567.458	17.701	0.278	0.0130	0.500	0.187	0.0150	0.019	1	0.94	Disk/Spot
21025	−0.10	435	4.543290	3581.225	16.777	0.134	0.0182	0.491	0.033	0.0138	0.025	1	0.97	Reflection
21452	0.17	377	8.178958	3541.898	17.362	2.824	0.0111	0.525	0.172	0.0098	0.124	2	1.86	Reflection
21641	0.05	436	3.092424	3572.506	16.741	0.405	0.0191	0.500	0.073	0.0191	0.062	1	0.76	Reflection
21859	0.00	428	3.154536	3571.735	16.172	0.617	0.0296	0.499	0.232	0.0332	0.080	1	1.23	Possible Reflection
21975	0.13	437	3.021139	3571.601	16.208	0.139	0.0196	0.500	0.029	0.0160	0.030	0	1.11	Reflection
23981	0.09	435	5.720508	3579.130	16.861	0.152	0.0215	0.499	0.144	0.0213	0.076	0	1.17	Disk/Spot

such as V11 in the old open cluster NGC 6791 (de Marchi et al. 2007), T-And0-00920 in the galactic field (Devor et al. 2008), and SRa01a_34263 in the young open cluster NGC 2264 (Klagyivik et al. 2013). Quantitatively, these 12 eclipsing binaries with luminous

disks and/or hot spots have $\Delta I_2/\Delta I_1 > 0.4$, while our 22 systems with low-luminosity pre-MS companions have $\Delta I_2/\Delta I_1 < 0.4$.

Our 22 eclipsing binaries with pre-MS companions have nearly circular orbits with $|\Phi_2 - 1/2| \leq 0.025$, as expected from tidal damping even earlier in their pre-MS phase of evolution (Zahn & Bouchet 1989a). One peculiar eclipsing binary, ID-1500 (brown system in Fig. 3.3), satisfies our selection criteria of $\Theta_{\rm max} < 0.03$ and $\Delta I_2/\Delta I_1 < 0.4$, but has a moderately eccentric orbit of $e > e_{\rm min}(\Phi_2 = 0.565) = 0.10$ according to Eq. 3.2. This eclipsing binary has a deep primary eclipse $\Delta I_1 = 1.0$ mag that stipulates the binary components cannot both be normal MS stars. However, the light curve of ID-1500 peaks at $\phi \approx 0.8$, i.e. $\phi \approx -0.2$ as folded in Fig. 3.3, suggesting the out-of-eclipse variations are due to ellipsoidal modulations in an eccentric orbit instead of reflection effects. Specifically, periastron in this system probably occurs near $\phi \approx -0.2$, at which point the stars are tidally deformed into oblate ellipsoids and the perceived flux is increased. We attempt to fit a detailed physical model (see §3.3) to this system assuming the companion is a pre-MS star, but our fit is rather poor with $\chi^2/\nu = 1.7$. Moreover, our physical model converges toward an unrealistic solution with $q \approx 0.5$. Whether the out-of-eclipse variations in this system are due to reflection effects or are entirely because of ellipsoidal modulations, the removal of this one system does not affect our investigation of low-mass $q < 0.25$ companions to B-type MS stars.

We find three additional eclipsing binaries that may display reflection effects with a pre-MS companion, but lie just outside of our selected parameter space (cyan systems in Fig. 3.3). ID-21859 has a broad eclipse $\Theta_{\rm max} = 0.033$, but has eclipse depth properties that separate it from the observed Algol population. ID-3972 and ID-5205 have slightly deeper secondary eclipses $\Delta I_2/\Delta I_1 \approx 0.5$, but exhibit symmetric light curve profiles with

no immediate indications of disks and/or hot spots. In our Monte Carlo simulations (§3.5), we implement the same selection criteria utilized here, and so we do not include these three systems in our statistical sample. Moreover, the observed population of eclipsing binaries with genuine reflection effects are concentrated near $\Theta_{\rm max} \approx 0.018$ and $\Delta I_2/\Delta I_1 \approx 0.2$. Increasing distance from this center according to our adopted metric increases the likelihood that the system is not a MS + pre-MS eclipsing binary. Our 22 eclipsing binaries that exhibit pronounced reflection effects $\Delta I_{\rm refl} > 0.015$ mag with pre-MS companions at $P = 3.0$ - 8.5 days have $\Theta_{\rm max} \leq 0.03$, which cleanly differentiates them from Algols and contact binaries that fill their Roche lobes, $\Delta I_2/\Delta I_1 \leq 0.4$, which distinguishes them from systems with luminous disks and/or hot spots, and $|\Phi_2 - 1/2| \leq 0.025$, which separates them from systems that show ellipsoidal modulations in an eccentric orbit (Fig. 3.3). We emphasize that these criteria are rather effective in selecting systems with low-mass pre-MS companions while simultaneously minimizing contamination from other types of eclipsing binaries.

3.2.3 Comparison to Previously Known Classes

Irradiated Binaries

Other classes of detached binaries can exhibit intense irradiation effects, but there are key differences that distinguish our 22 systems. Namely, our 22 eclipsing binaries contain a hot MS primary with a cool pre-MS companion, while most previously known reflecting eclipsing binaries contain a hot evolved remnant with a cool MS companion (Bond 2000; Lee et al. 2009). For example, eclipsing binaries with subdwarf B-type (sdB) primaries and M-dwarf companions, sometimes called HW Vir eclipsing binaries

after the prototype, have similar reflection effect amplitudes and light curve properties (Lee et al. 2009; Barlow et al. 2013; Pietrukowicz et al. 2013). However, HW Vir systems differ from our systems in three fundamental parameters. First, the sdB primaries in HW Vir eclipsing binaries are intrinsically ∼100 times less luminous than B-type MS stars, and would therefore not be detectable in the LMC given the sensitivity of the OGLE-III survey. Second, HW Vir eclipsing binaries have shorter orbital periods $P \lesssim 0.5$ days than our 22 systems with $P = 3.0$ - 8.5 days. This is because the sdB primaries and M-type MS secondaries are smaller and less luminous than our B-type MS primaries and pre-MS companions, and therefore must be closer together to produce observable reflection effects. Finally, HW Vir systems are evolved binaries and associated with old stellar populations, while our 22 nascent eclipsing binaries are situated in or near star-forming H II regions (see §3.4).

As another example, binaries in which a MS star orbits the hot central star of a planetary nebula can pass through a very brief interval $\lesssim$10,000 yrs when reflection effects are detectable, although eclipses are generally not observed (Bond 2000). Such systems could have satisfied our magnitude and color criteria, but these binaries are typically at shorter periods $P < 3$ days than we have selected (Miszalski et al. 2009). Moreover, we cross-referenced the positions of our 22 systems with catalogs of planetary nebulae (Reid & Parker 2010) and emission-line point sources (Howarth 2013) in the LMC, and do not find any matches. Our nascent B-type MS + pre-MS eclipsing binaries clearly exhibit a phenomenologically different type of reflection effect than those observed in evolved binaries with stellar remnants.

Pre-MS Binaries

Although there is a rich literature regarding pre-MS binaries (see Hillenbrand & White 2004 and review by Mathieu 1994), only a few close MS + pre-MS binaries have been identified. For example, photometric and spectroscopic observations of the eclipsing binaries EK Cep (Popper 1987), AR Aur (Nordstrom & Johansen 1994), TY CrA (Casey et al. 1998), and RS Cha (Alecian et al. 2007) have demonstrated the primaries are close to the zero-age MS while the secondaries are still contracting on the pre-MS. However, these systems have late-B/A-type MS primaries ($M_1 \approx 1.9$ - $3.2\,M_\odot$), components of comparable mass ($q \approx 0.5$ - 1.0), and temperature contrasts ($T_2/T_1 \approx 0.4$ - 0.9) that are too small to produce detectable reflection effects. Morales-Calderón et al. (2012) identified ISOY J0535-447 as a young pre-MS eclipsing binary with an extreme mass ratio $q \approx 0.06$, but with a low-mass $M_1 \approx 0.8\,M_\odot$ early-K primary.

The only similar analog of a B-type MS primary with a closely orbiting low-mass pre-MS companion is the eclipsing binary BM Orionis (Hall & Garrison 1969; Palla & Stahler 2001; Windemuth et al. 2013), although the nature of its secondary has been debated and has even been suggested to be a black hole (Wilson 1972). Located in the heart of the Orion Nebula, BM Ori exhibits broad eclipses with noticeable undulations in the eclipse shoulders. These features indicate the companion nearly fills its Roche lobe and is still accreting from the surrounding disk. If BM Ori contains an accreting pre-MS companion, then it could be a precursor to our 22 eclipsing binaries that show no evidence for an accretion disk. Indeed, BM Ori is extremely young with an age $\tau \lesssim 0.1$ Myr estimated from pre-MS contraction timescales (Palla & Stahler 2001) and the dynamics of the inner region of the Orion Nebula (O'Dell et al. 2009). Meanwhile,

the disk photoevaporation timescale around Herbig Be pre-MS stars with $M_1 \approx 3\text{-}8\,M_\odot$ is ≈0.3 Myr (Alonso-Albi et al. 2009). It is therefore not unexpected that BM Ori at $\tau < 0.1$ Myr still has a disk. Alternatively, our 22 systems no longer have a noticeable accretion disk in the photometric light curves, and so must be older than $\tau \gtrsim 0.3$ Myr (see also §3.3.3).

If BM Ori was placed in the LMC and observed by the OGLE-III survey, it would not be contained in our sample for three reasons. First, BM Ori contains an extremely young and reddened mid-B MS primary with $M_1 \approx 6\,M_\odot$, $\langle V-I \rangle \approx 0.8$, and $\langle I \rangle \approx 8.8$ at the distance $d \approx 400$ pc to the Orion Nebula (Windemuth et al. 2013). It would be rather faint at $\langle I \rangle \approx 19.3$ if located at the distance $d = 50$ kpc to the LMC, and therefore below our photometric selection limit. Second, even if we extended our search toward fainter systems, the reflection effect amplitude in BM Ori is too small to be observed given the sensitivity of the OGLE-III LMC observations. Finally, the secondary eclipse is extremely shallow with undulations in the eclipse shoulders. We could not measure well-defined secondary eclipse parameters according to our analytic model. In addition to being at a fundamentally different stage of evolution, i.e. still accreting from a disk, BM Ori has clearly different photometric light curve properties than those of our 22 eclipsing binaries.

Finally, BM Ori has a modest mass ratio $q = 0.31$. In contrast, the majority of our reflecting eclipsing binaries have extreme mass ratios $q < 0.25$ (see below), as indicated by their more luminous, massive primaries and larger reflection effect amplitudes. Our reflecting eclipsing binaries represent the first detection of B-type MS stars with close extreme mass-ratio companions where the orbital periods and the nature of the companions are reliably known.

3.3 Physical Properties

3.3.1 Overview of Methodology

The component masses in eclipsing binaries are typically measured dynamically via spectral radial velocity variations. However, our eclipsing binaries in the LMC are relatively faint $16 < \langle I \rangle < 18$ and typically embedded in H II regions (§3.4) that would contaminate the stellar spectra with nebular emission lines. Moreover, B-type MS stars experience slight atmospheric variations and rotate so rapidly that their spectral absorption lines are generally broadened by $v_{\rm surface} \approx 100$ - 250 km s^{-1} (Abt et al. 2002; Levato & Grosso 2013). There is a small population of slowly rotating B-type MS stars with $v_{\rm surface} \approx 50$ km s^{-1}, and Abt et al. (2002) and Levato & Grosso (2013) suggest these systems may by tidally synchronized with closely orbiting low-mass companions. Indeed, our reflecting eclipsing binaries may partially explain the origins of B-type MS slow rotators. In any case, it would be quite observationally expensive to detect small velocity semi-amplitudes $K_1 \approx 25\,(q/0.1)$ km s^{-1} induced by closely orbiting low-mass companions for all 22 eclipsing binaries in our statistical sample. In the future, we plan to obtain multi-epoch spectra for a small subset of our MS + pre-MS eclipsing binaries. To analyze all 22 systems, however, we must currently utilize a different technique of inferring the physical properties based solely on the observed photometric light curves.

Fortunately, we have two additional constraints that allow us to estimate the masses of the binary components from the observed eclipse properties. First, our eclipsing binaries are detached from their Roche lobes, as demonstrated by their narrow eclipses, and therefore the primary and secondary are each effectively evolving along their

respective single-star sequences (see §3.3.4 for further justification of this expectation and a discussion of systematic uncertainties). Given an age τ and masses M_1 and M_2, we can interpolate stellar radii R_1 and R_2, photospheric temperatures T_1 and T_2, and luminosities L_1 and L_2 from theoretical stellar evolutionary tracks. We can then use empirical bolometric corrections and color indices to map the physical properties of the eclipsing binaries into observed magnitudes and colors. Devor & Charbonneau (2006) and Devor et al. (2008) employed a similar technique of estimating ages and masses of galactic eclipsing binaries by incorporating stellar isochrones into their photometric light curve modeling. Their algorithm worked for a small subset of systems. In general, however, the parameters τ, M_1, and M_2 were generally degenerate, not unique, and/or not constrained.

This brings us to our second constraint. Unlike the sample of galactic eclipsing binaries studied by Devor et al. (2008), we know the distances to our 22 eclipsing binaries in the LMC. This extra distance constraint fully eliminates the degeneracy and allows us to calculate unique solutions for the physical properties of the eclipsing binaries. The deductions of the physical parameters progress as follows. The measured mean magnitude $\langle I \rangle$ and color $\langle V - I \rangle$, along with the distance, bolometric corrections, and color indices, mainly provide the luminosity L_1 of the B-type MS primary and the amount of dust reddening $E(V - I)$, respectively. From MS stellar evolutionary tracks, we can estimate the mass M_1 and radius R_1 of a young B-type MS star with luminosity L_1. The amplitude of the reflection effect $\Delta I_{\rm refl}$ is an indicator of T_2/T_1 and R_2/R_1 as discussed in §3.2, but also depends on the albedo of the secondary A_2. The sum of eclipse widths $\Theta_1 + \Theta_2$ determines the sum of the relative radii $(R_1 + R_2)/a$, the ratio of eclipse depths $\Delta I_2/\Delta I_1$ gives the luminosity contrast L_2/L_1, and the magnitude of the primary

eclipse depth ΔI_1 provides the inclination i. Since we already know M_1, R_1 and L_1, we can infer R_2 and L_2 directly from the observed light curve parameters. Finally, according to pre-MS evolutionary tracks, the radius R_2 and luminosity L_2 of the pre-MS secondary uniquely corresponds to its age τ and mass M_2. In our full procedure (see below), we calculate each of these parameters simultaneously in a self-consistent manner. We also consider various sources of systematic errors in our measured light curve parameters as well as stellar evolutionary tracks. Nonetheless, the steps discussed above illustrate how we can estimate the physical properties of detached, unevolved, eclipsing binaries with known distances using only the photometric light curves.

3.3.2 Physical Model Fits

In our eclipsing binary models, we have eight physical parameters: orbital period P, epoch of primary eclipse minimum $t_{\rm o}$, primary mass M_1, secondary mass M_2, age τ, inclination i, albedo of the secondary A_2, and amount of dust extinction A_I toward the system. B-type MS stars in the LMC have slightly subsolar metallicities $\log(Z/{\rm Z}_\odot) \approx -0.4$ (Korn et al. 2000), where ${\rm Z}_\odot \approx 0.015$. We therefore incorporate the Padova Z=0.008, Y=0.26 stellar evolutionary tracks to describe the MS evolution (Bertelli et al. 2009), and the Pisa Z=0.008, Y=0.265, $\alpha = 1.68$, X_D=2×10^{-5} tracks to model the pre-MS evolution (Tognelli et al. 2011). The physical properties of the binary components, e.g. radii R_1 and R_2, surface temperatures T_1 and T_2, luminosities L_1 and L_2, and surface gravities g_1 and g_2, are then interpolated from these stellar tracks according to the model parameters M_1, M_2, and τ. We use updated, temperature-dependent color indices and bolometric corrections (Pecaut & Mamajek 2013) to transform the intrinsic luminosities

and temperatures of both binary components into combined absolute magnitudes M_I and M_V. We adopt the dust reddening law of $E(V-I) = 0.7A_I$ (Cardelli et al. 1989; Fitzpatrick 1999; Ngeow & Kanbur 2005) and LMC distance modulus of $\mu = 18.5$ (Pietrzyński et al. 2013) to then calculate the observed magnitudes $\langle I \rangle = M_I + \mu + A_I$ and $\langle V \rangle = M_V + \mu + 1.7A_I$.

We primarily utilize the eclipsing binary modeling software NIGHTFALL[1] to synthesize I-band and V-band light curves. We implement a square-root limb darkening law with the default limb-darkening coefficients, the default gravity brightening coefficients, model atmospheres according to the surface gravities of the binary components, fractional visibility of surface elements, three iterations of reflection effects, and the default albedo of $A_1 = 1.0$ for the hot B-type MS primaries.

Given the sensitivity of the OGLE-III data, the 19 eclipsing binaries with $|\Phi_2 - 1/2| < 0.01$ and $\Theta_1 \approx \Theta_2$ have $e < 0.02$ (see Eqn. 3.2 and Kallrath & Milone 2009). For these 19 systems, we assume circular orbits in our physical models. The three systems (ID-17217, ID-18419, and ID-21452) in slightly eccentric orbits with $0.010 \leq |\Phi_2 - 1/2| \leq 0.025$ have longer orbital periods where tidal effects are not as significant. The eclipse widths $\Theta_1 \approx \Theta_2$ are also comparable to each other in these three eclipsing binaries, dictating the eccentricities $0.02 < e < 0.08$ are small. Because the orbits are so close to circular, we cannot easily break the degeneracy between the eccentricity e and the argument of periastron ω. For these three systems, we impose $e = e_{\rm min}/\langle \cos(\omega) \rangle = 1.6\, e_{\rm min}$ according to Eqn. 3.2, where we have assumed a uniform probability distribution for ω. Adjusting the eccentricities to values within $e_{\rm min} < e < 2.2 e_{\rm min}$ do not change the fitted model

[1] http://www.hs.uni-hamburg.de/DE/Ins/Per/Wichmann/Nightfall.html

parameters beyond the uncertainties. For ID-21452, which has $\Phi_2 > 0.5$, we assume $\omega = 50^{\rm o}$. For ID-17217 and ID-18419, which have $\phi_2 < 0.5$, we adopt $\omega = 230^{\rm o}$. Changing the argument of periastron to the opposite angle, e.g. $\omega = 310^{\rm o}$ for ID-21452 or $\omega = 130^{\rm o}$ for ID-17217 and ID-18419, has a negligible effect on the other model parameters considering the eccentricities are so small.

Since tides have fully or nearly circularized the orbits, the rotation rates of the pre-MS companions with large convective envelopes are expected to be tidally synchronized with the orbital periods (Zahn & Bouchet 1989a). For example, a $1.5\,{\rm M}_\odot$ pre-MS star with age $\tau = 1$ Myr in a $P = 4$ day orbit with a $10\,{\rm M}_\odot$ B-type MS star has rapid synchronization and spin-orbit alignment timescales of $\lesssim 0.01$ Myr (Hut 1981; Belczynski et al. 2008). Meanwhile, the circularization timescale is orders of magnitude longer at ≈ 2 Myr, which is still only a small fraction of the secondary's pre-MS lifetime of ≈ 10 Myr. Hence, it is not surprising that all of our eclipsing binaries with $P < 4$ days have been circularized, while three systems with $P > 4$ days are in slightly eccentric orbits with $e \approx 0.03$ - 0.06.

B-type MS stars have radiative envelopes, and so tidal damping is not as efficient. Although the B-type MS primaries may spin independently from the orbital periods, we assume for simplicity that they are also tidally locked with the orbit (see also discussion of B-type MS slow rotators in §3.3.1). B-type MS stars become oblate only if they rotate close to their break-up speed or nearly fill their Roche lobes (Ekström et al. 2008b). Fortunately, young B-type MS stars typically rotate more slowly than their break-up speed (Abt et al. 2002; Ekström et al. 2008b; Levato & Grosso 2013), and the B-type MS primaries in our eclipsing binaries are well-detached from their Roche lobes. Even if the B-type MS primaries are not already synchronized with the orbit, their true shapes

will differ only slightly from our model assumptions. For example, a B-type MS primary that quickly spins at $v_{\rm surface} = 300$ km s^{-1} will have an equatorial radius that is only 6% larger than its polar radius (Ekström et al. 2008b).

We show in Fig. 3.4 the reflection effect amplitude $\Delta I_{\rm refl}$ for three secondary masses $M_2 = 1$, 2, and 3 $M_\odot$ based on our NIGHTFALL models and adopted evolutionary tracks. For these sequences, we fix the other parameters at representative values of $M_1 = 10\,M_\odot$, $P = 4$ days, $i = 90^{\rm o}$, and $A_2 = 0.7$. The observable pre-MS duration of the $3\,M_\odot$ companion is only $\sim$2% the MS lifetime of the primary. Hence, the majority of our eclipsing binaries that display reflection effects must have $q < 0.3$ because the likelihood of observing a pre-MS + MS binary at larger q is very low. The radii of MS companions with $q < 0.15$ are too small to produce detectable eclipses given the cadence and sensitivity of the OGLE-III observations. We can therefore observe extreme mass-ratio eclipsing binaries only when the companion is large and still contracting on the pre-MS.

The correction factor $f_\sigma(I)$ for the photometric errors we calculated in §3.2.1 can differ between systems, even if they have the same magnitude. We therefore do not use the simple relation in Eq. 3.5 in our physical models. Instead, we calculate the correction factors between the catalog photometric errors and intrinsic rms scatter for each of our 22 eclipsing binaries individually. To achieve this, we separately fit 3$^{\rm rd}$ degree polynomials across the out-of-eclipse intervals $0.05 < \phi < 0.45$ and $0.55 < \phi < 0.95$ for each of the I-band and V-band light curves. We remove all residuals that exceed 4σ, measure the rms dispersions of the remaining residuals, and then calculate the correction factors $f_{\sigma,I}$ and $f_{\sigma,V}$ between the catalog photometric errors and the measured rms scatter. For some light curves, there are too few data points to accurately measure the

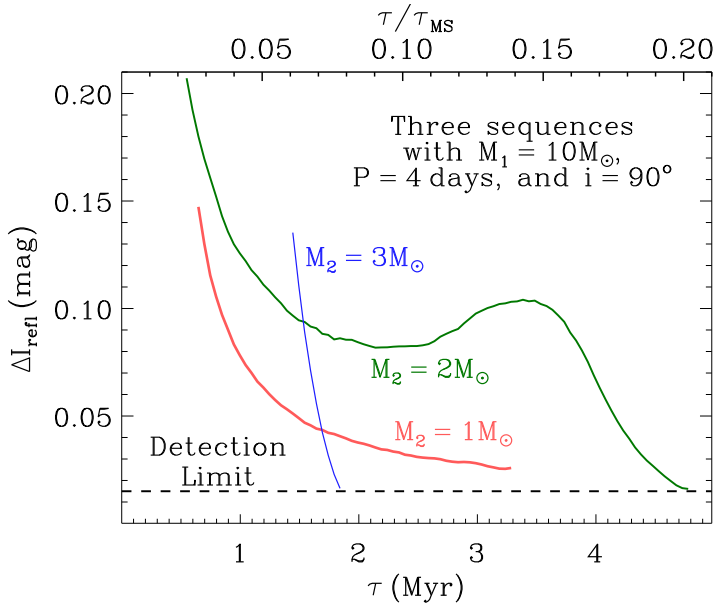

Figure 3.4: Reflection effect amplitude $\Delta I_{\rm refl}$ as a function of age τ for three secondary masses M_2. Above is time in units of the MS lifetime $\tau_{\rm MS} = 24\,{\rm Myr}$ of the *primary* B-type MS star. We show only the portions of the evolution where the light curve properties satisfy our selection criteria. At early times $\tau \lesssim (0.02\text{-}0.06)\,\tau_{\rm MS}$, the companions have Roche-lobe fill-factors $RLFF_2 \gtrsim 80\%$ and are difficult to distinguish from large, evolved subgiants. At later times $\tau \gtrsim (0.1\text{-}0.2)\,\tau_{\rm MS}$, the secondary becomes substantially smaller as it approaches its own MS phase of evolution. Not only do the reflection effects fall below the detection limit of $\Delta I_{\rm refl} = 0.015$ mag (dashed line), but the eclipse depths can also diminish below the sensitivity of the OGLE-III LMC observations. Extreme mass-ratio binaries $q \lesssim 0.15$ (red) produce observable eclipses only when the companions are on the early pre-MS phase of evolution. Binaries at moderate mass ratios $q \gtrsim 0.3$ (blue) spend only $\lesssim$2% of the primary's evolution in such a MS + pre-MS combination. The nonmonotonic behavior in $\Delta I_{\rm refl}$ for the $M_2 = 2{\rm M}_\odot$ sequence (green) is due to the complex pre-MS evolution of stars with $M > 1.4{\rm M}_\odot$.

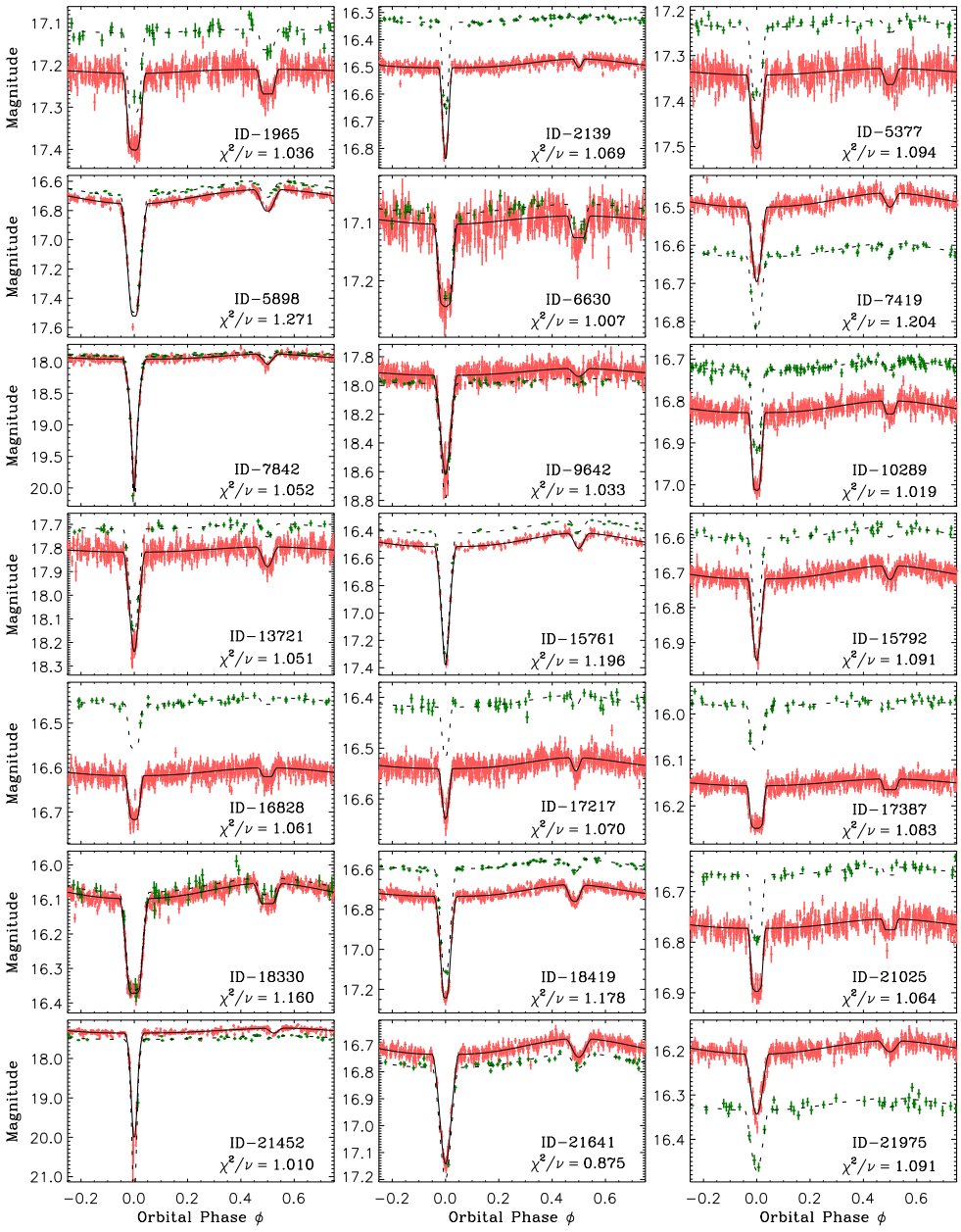

Figure 3.5: As shown in Fig. 3.1 for the prototype ID-1803, we compare the physical model fits to the the observed light curves for the remaining 21 eclipsing binaries with B-type MS primaries and irradiated pre-MS companions. We present the physical fit parameters and statistics for all 22 systems in Tables 3.2-3.3.

Table 3.2. Best-fit model parameters and statistics for 22 eclipsing binaries with reflection effects. The uncertainties reported in parenthesis, which include systematic uncertainties, are not necessarily symmetric around the best-fit model values.

	Physical Model Properties								Fit Statistics							
ID	P (days)	t_o (JD-2450000)	M_1 ($M_\odot$)	M_2 ($M_\odot$)	τ (Myr)	i (^{o})	A_2 (%)	A_I (mag)	$\mathcal{N}_I$	$\mathcal{N}_{c,I}$	$f_{\sigma,I}$	$\mathcal{N}_V$	$\mathcal{N}_{c,V}$	$f_{\sigma,V}$	χ^2/ν	PTE
1803	3.970085 (7)	3572.1174 (9)	10.4 (1.6)	0.8 (0.2)	0.7 (0.4)	83.6 (1.1)	97 (17)	0.32 (4)	460	1	1.17	41	0	1.21	1.062	0.167
1965	3.175265 (9)	3570.6285 (17)	7.7 (1.2)	1.9 (0.3)	15 (4)	89.8 (1.5)	100 (28)	0.22 (3)	440	2	1.09	45	0	1.50	1.036	0.283
2139	8.462504 (21)	3576.0465 (23)	12.7 (2.0)	1.9 (0.4)	0.9 (0.5)	84.0 (1.3)	29 (15)	0.23 (3)	477	2	1.19	70	1	1.16	1.069	0.132
5377	3.276373 (10)	3563.1493 (19)	7.4 (1.2)	1.2 (0.2)	14 (5)	84.8 (1.6)	68 (22)	0.19 (3)	447	1	1.11	43	0	1.08	1.094	0.075
5898	5.323855 (13)	3567.5433 (17)	7.7 (1.5)	3.8 (0.8)	0.8 (0.4)	83.5 (1.5)	86 (25)	0.07 (3)	439	1	1.30	44	2	1.25	1.271	<0.001
6630	3.105556 (9)	3563.8238 (16)	8.3 (1.3)	1.5 (0.2)	13 (4)	86.5 (1.3)	100 (27)	0.34 (4)	410	1	1.12	40	0	1.05	1.007	0.450
7419	4.255885 (9)	3563.5793 (14)	13.7 (2.4)	1.7 (0.3)	5.2 (1.5)	81.1 (2.1)	61 (21)	0.66 (7)	421	2	1.12	40	0	1.10	1.204	0.002
7842	3.781792 (8)	3565.8256 (10)	6.0 (0.9)	2.0 (0.3)	2.6 (0.8)	88.5 (0.8)	60 (16)	0.17 (3)	477	1	1.13	72	0	1.08	1.052	0.197
9642	3.913363 (9)	3565.6120 (14)	6.4 (1.0)	2.3 (0.4)	1.7 (0.5)	81.2 (1.4)	29 (19)	0.29 (4)	782	1	1.16	40	1	1.05	1.033	0.249
10289	4.642579 (11)	3566.0280 (15)	11.2 (1.8)	0.8 (0.2)	2.5 (0.7)	86.9 (0.9)	100 (18)	0.32 (4)	557	1	1.07	115	0	1.05	1.019	0.357
13721	3.122554 (11)	3558.1903 (16)	6.2 (1.0)	1.5 (0.3)	8 (2)	83.3 (2.0)	37 (16)	0.14 (3)	428	1	1.05	40	0	1.05	1.051	0.214
15761	5.310910 (12)	3581.5694 (14)	12.6 (2.4)	2.3 (0.4)	1.9 (0.5)	85.4 (1.1)	78 (17)	0.30 (4)	223	0	1.74	21	0	1.37	1.196	0.021
15792	4.317015 (9)	3566.0986 (15)	11.5 (1.8)	1.6 (0.3)	2.8 (1.0)	83.3 (1.7)	69 (22)	0.30 (4)	600	1	1.35	40	0	1.41	1.091	0.056
16828	3.675702 (10)	3572.0106 (17)	10.8 (1.7)	1.0 (0.2)	7 (2)	83.7 (2.0)	100 (23)	0.23 (3)	606	3	1.18	47	0	1.05	1.061	0.137
17217[a]	5.354787 (20)	3576.8028 (26)	11.3 (1.8)	1.7 (0.4)	7 (3)	81.6 (2.1)	100 (31)	0.28 (5)	592	3	1.18	47	0	1.37	1.070	0.109
17387	4.772901 (14)	3567.4122 (24)	12.4 (2.0)	1.2 (0.2)	8 (2)	89.6 (1.5)	100 (22)	0.23 (4)	605	1	1.17	47	1	1.34	1.083	0.071
18330	3.252921 (8)	3561.4274 (17)	14.6 (2.5)	1.6 (0.3)	5.6 (1.5)	89.5 (1.6)	100 (19)	0.46 (6)	599	2	1.48	46	0	3.04	1.160	0.003
18419[b]	4.118151 (8)	3564.3203 (12)	11.6 (2.0)	1.5 (0.3)	1.6 (0.5)	88.0 (1.1)	78 (17)	0.27 (4)	599	1	1.28	70	0	1.18	1.178	0.001
21025	4.543312 (13)	3581.2269 (22)	10.7 (1.7)	1.0 (0.3)	6 (2)	88.5 (1.6)	100 (26)	0.31 (4)	435	1	1.05	45	0	1.05	1.064	0.165
21452[c]	8.178961 (19)	3541.8978 (22)	10.1 (1.6)	2.4 (0.7)	0.6 (0.4)	89.3 (2.2)	67 (17)	0.61 (7)	337	1	1.43	40	0	1.88	1.010	0.436
21641	3.092426 (7)	3572.5059 (18)	12.7 (2.0)	1.9 (0.3)	2.6 (1.0)	82.8 (1.6)	51 (19)	0.54 (6)	436	1	1.05	45	0	1.05	0.875	0.976
21975	3.021141 (9)	3571.6002 (19)	16.0 (2.6)	1.7 (0.3)	4.0 (1.4)	77.9 (2.3)	36 (21)	0.68 (8)	437	1	1.16	42	0	1.72	1.091	0.084

(a): modeled with $e = 0.03$ and $\omega = 230^o$; (b): $e = 0.04$ and $\omega = 230^o$; (c): $e = 0.06$ and $\omega = 50^o$; the other 19 systems have circular orbits.

correction factors, so we impose a minimum value of 1.05 for $f_{\sigma,I}$ and $f_{\sigma,V}$. For each of our 22 eclipsing binaries, we multiply the catalog photometric errors by their respective correction factors $f_{\sigma,I}$ and $f_{\sigma,V}$ when we fit our physical models.

To constrain the eight parameters in our physical models, we fit NIGHTFALL synthetic light curves to the I-band and V-band data simultaneously. As in §3.2, we use a Levenberg-Marquardt method to minimize the χ^2 statistic between the light curves and physical models. We clip up to $\mathcal{N}_{c,I} + \mathcal{N}_{c,V} \leq 3$ data points that deviate more than 4σ from our best-fit model. Since we fit both the I-band and V-band together, there are $\nu = \mathcal{N}_I + \mathcal{N}_V - \mathcal{N}_{c,I} - \mathcal{N}_{c,V} - 8$ degrees of freedom. We compare the observed light

Table 3.3. Dependent physical properties derived by using main model parameters in Table 3.2 in combination with Kepler's laws and stellar evolutionary tracks. The representative uncertainties are 15% or 0.03, which ever is larger, in the mass ratios q and relative ages $\tau/\tau_{\rm MS}$, 10% in orbital separation a, radii R_1 and R_2, and Roche-lobe fill factors $RLFF_1$ and $RLFF_2$, 8% in temperatures T_1 and T_2, 40% in luminosities L_1 and L_2, and 0.1 mag in absolute magnitudes M_I and M_V.

ID	q	$\tau/\tau_{\rm MS}$	a ($R_\odot$)	R_1 ($R_\odot$)	R_2 ($R_\odot$)	$RLFF_1$	$RLFF_2$	T_1 (K)	T_2 (K)	L_1 ($L_\odot$)	L_2 ($L_\odot$)	M_I	M_V
1803	0.07	0.03	23	3.6	3.1	0.27	0.77	27,000	4,400	6,000	3	−1.7	−2.1
1965	0.24	0.35	19	3.6	1.4	0.39	0.29	23,000	9,900	3,000	17	−1.5	−1.7
2139	0.15	0.05	43	4.2	3.7	0.19	0.39	29,000	5,200	12,000	9	−2.2	−2.5
5377	0.16	0.33	19	3.5	1.2	0.36	0.30	22,000	6,100	3,000	2.2	−1.3	−1.6
5898	0.49	0.02	29	3.0	6.3	0.25	0.73	24,000	8,400	2,500	180	−1.8	−1.9
6630	0.18	0.41	19	3.9	1.3	0.41	0.31	23,000	7,800	4,000	6	−1.7	−2.0
7419	0.12	0.35	28	5.1	2.6	0.35	0.47	30,000	6,200	18,000	9	−2.7	−3.0
7842	0.33	0.04	20	2.7	2.9	0.29	0.53	21,000	5,700	1,200	8	−0.7	−0.9
9642	0.36	0.03	21	2.7	3.7	0.29	0.63	21,000	5,800	1,400	14	−0.9	−1.0
10289	0.07	0.13	27	4.0	1.5	0.26	0.34	28,000	4,300	9,000	0.7	−2.0	−2.3
13721	0.25	0.13	18	2.8	2.0	0.34	0.46	20,000	7,200	1,300	10	−0.8	−1.0
15761	0.18	0.12	32	4.3	4.0	0.27	0.56	29,000	6,100	12,000	20	−2.3	−2.6
15792	0.14	0.15	26	4.1	2.1	0.30	0.38	28,000	5,200	9,000	3	−2.1	−2.4
16828	0.09	0.33	23	4.4	1.2	0.34	0.30	27,000	4,500	9,000	0.6	−2.1	−2.4
17217	0.15	0.34	30	4.5	2.1	0.29	0.33	27,000	7,800	10,000	15	−2.2	−2.5
17387	0.09	0.48	28	5.2	1.4	0.33	0.26	28,000	5,300	15,000	1.4	−2.6	−2.9
18330	0.11	0.42	23	5.5	2.5	0.43	0.54	30,000	6,200	23,000	8	−2.9	−3.2
18419	0.13	0.08	25	4.0	2.4	0.31	0.48	28,000	5,000	9,000	3	−2.0	−2.4
21025	0.09	0.28	26	4.2	1.3	0.29	0.27	27,000	4,600	8,000	0.7	−2.0	−2.4
21452	0.24	0.02	40	3.6	5.2	0.20	0.58	27,000	5,200	6,000	17	−1.8	−2.0
21641	0.15	0.16	22	4.4	2.7	0.39	0.58	29,000	5,600	13,000	6	−2.3	−2.6
21975	0.11	0.34	23	5.5	2.5	0.44	0.56	32,000	5,800	28,000	6	−3.0	−3.3

curves to our best physical model fits in Fig. 3.1 (for our prototype ID-1803) and Fig. 3.5 (for the remaining 21 reflecting eclipsing binaries). We present the fit parameters and statistics in Table 3.2, and other physical properties in Table 3.3.

3.3.3 Results

For 21 of our 22 eclipsing binaries, our models have good fit statistics $\chi^2/\nu = 0.87$ - 1.20. The one remaining eclipsing binary, ID-5898, has a poor fit with $\chi^2/\nu = 1.27$, i.e. a

probability to exceed χ^2 of $PTE < 0.001$, most likely caused by third light contamination. We discuss third light contamination and other systematic uncertainties in §3.3.4.

For the 21 eclipsing binaries with good fit statistics, we measure primary masses $M_1 = 6\text{-}16\,\mathrm{M}_\odot$ appropriate for early B-type MS stars, low-mass secondaries $M_2 = 0.8\text{-}2.4\,\mathrm{M}_\odot$ ($q = 0.07\text{-}0.36$), young ages $\tau = 0.6\text{-}15$ Myr, nearly edge-on inclinations $i = 78^\mathrm{o}\text{-}90^\mathrm{o}$, secondary albedos $A_2 = (30\text{-}100)\%$, and moderate to large dust extinctions $A_I = 0.14\text{-}0.68$ mag. The B-type MS primaries have relative ages τ/τ_MS that span from 2% up to 50% their MS lifetimes. The fits confirm these eclipsing binaries with narrow eclipses are in detached configurations with Roche-lobe fill-factors $RLFF_1 = 0.2\text{-}0.4$ and $RLFF_2 = 0.3\text{-}0.8$. Given the orbital separations $a = 20\text{-}40\,\mathrm{R}_\odot$, these fill-factors correspond to physical radii $R_1 = 2.7\text{-}5.5\,\mathrm{R}_\odot$ and $R_2 = 1.2\text{-}5.2\,\mathrm{R}_\odot$. Finally, as expected for eclipsing binaries that exhibit substantial reflection effects, we find comparable radii $R_2/R_1 = 0.3\text{-}1.4$ but extreme contrasts in temperature $T_2/T_1 = 0.15\text{-}0.43$ and luminosity $L_2/L_1 \approx 10^{-4}\text{-}10^{-2}$.

Considering B-type MS stars span a narrow range of temperatures T_1 and radii R_1, the temperatures T_2 and radii R_2 of the companions are more accurately and robustly measured than their masses M_2 or ages τ. In Fig. 3.6, we compare the locations of the pre-MS companions on a Hertzsprung-Russell diagram to the theoretical Pisa evolutionary tracks (Tognelli et al. 2011). ID-5898 is biased toward larger L_2 most likely due to third light contamination (see below). ID-1965, ID-5377, and ID-6630 have small reflection effect amplitudes $\Delta I_\mathrm{refl} = 0.017\text{-}0.20$ mag just above our detection limit of 0.015 mag (see Fig. 3.5 and Table 3.1). These three systems also have shallow, flat-bottomed eclipses $\Delta I_1 \approx 0.2$ mag that dictate full non-grazing eclipse trajectories and ratio of radii $R_2/R_1 \approx 0.3\text{-}0.4$. The companions in these three eclipsing binaries

are therefore small, warm, late pre-MS or zero-age MS stars with relatively older ages $\tau \approx 13$ - 15 Myr (Table 3.2). Nonetheless, these three systems still have small secondary masses $M_2 = 1.2$ - $1.9\,M_\odot$ ($q = 0.16$ - 0.24), so we keep these eclipsing binaries in our statistical sample.

The remaining 18 systems have deeper eclipses and/or larger reflection effect amplitudes, which dictate the companions are larger and/or cooler. The secondaries in these 18 eclipsing binaries are inconsistent with zero-age MS stars (Fig. 3.6), but instead must be primordial pre-MS stars with young ages $\tau = 0.6$ - 8 Myr and small masses $M_2 = 0.8$ - $2.4\,M_\odot$. The majority of these companions have developed a radiative core and are evolving with nearly constant R_2 on the Henyey track (Siess et al. 2000; Tognelli et al. 2011). A few secondaries are still fully convective and contracting on the Hyashi phase of the pre-MS. According to our adopted pre-MS evolutionary tracks (Tognelli et al. 2011), eleven of our pre-MS secondaries have not yet initiated stable nuclear burning in their cores but are powered completely by gravitational energy.

3.3.4 Systematic Uncertainties

The one system with a poor model fit, i.e. ID-5898, converges toward a solution with a high-mass secondary $M_2 = 3.8\,M_\odot$ ($q = 0.49$), young age $\tau \approx 0.8$ Myr, and small dust extinction $A_I = 0.07$. We find four reasons to suspect this system suffers from contamination with a third light source, most likely a hot late-B/early-A tertiary companion. First, the amplitude of the reflection effect in ID-5898 appears to be color dependent with $\Delta I_{\rm refl} = 0.10$ mag and $\Delta V_{\rm refl} = 0.07$ mag (see Fig. 3.5). The decrease in $\Delta V_{\rm refl}$ is most likely caused by stellar blending with a third light source that is relatively

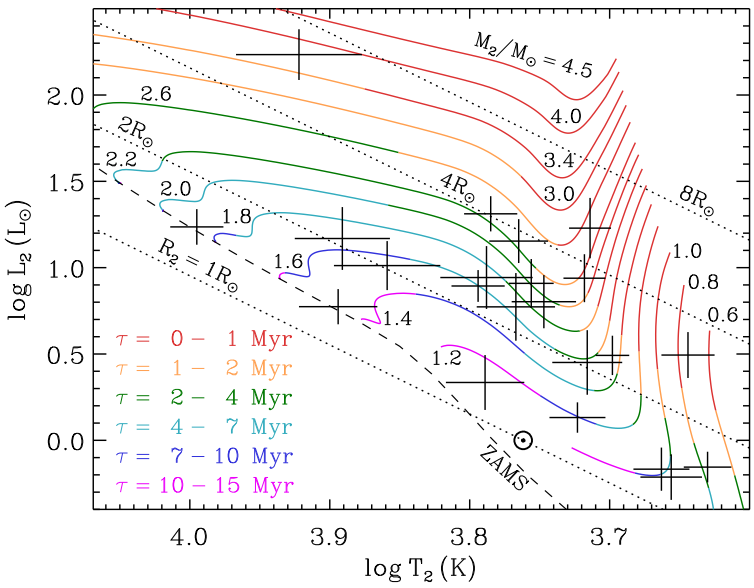

Figure 3.6: Hertzsprung-Russell diagram of the companions in our 22 eclipsing binaries. We compare the dependent model properties T_2 and L_2 to the Pisa pre-MS tracks (Tognelli et al. 2011) used to constrain the parameters of the observed systems. We display evolutionary tracks for secondary masses $M_2 = 0.6$ - $4.5\,\mathrm{M}_\odot$, where the colors indicate the ages of the pre-MS stars. We also show lines of constant radius (dotted) and the zero-age MS (dashed). ID-5898, which has the worst model fit statistic $\chi^2/\nu = 1.27$ and is probably contaminated by a third light source, is toward the top left. The three systems to the bottom left (ID-1965, ID-5377, and ID-6630) have small reflection effect amplitudes ΔI_{refl} = 0.017 - 0.20 mag, shallow eclipses $\Delta I_1 = 0.2$ mag, and companions that are consistent with the zero-age MS. The remaining 18 eclipsing binaries have companions that are larger and/or cooler and therefore definitively pre-MS stars. The observed systems cluster on the Henyey track near $T_2 \approx 6{,}000\,\mathrm{K}$ and $L_2 \approx 10\,\mathrm{L}_\odot$, which corresponds well to where large pre-MS stars with $R_2 \approx 2$ - $4\,\mathrm{R}_\odot$ are longest lived and therefore have the highest probability of producing detectable reflection effects.

hot and brighter in the V-band. Second, the measured dust extinction $A_I = 0.07$ is smaller than that compared to dust reddening estimates of young stars along similar lines-of-sight (Zaritsky et al. 2004, see also below). Third light contamination from a hot source would artificially shift the observed color toward the blue and bias our dust reddening measurement toward smaller values. Third, extra light would diminish the primary eclipse depth ΔI_1. This would mainly lead to an underestimation of the inclination i, but may also cause us to overestimate L_2, R_2, and M_2. Considering the other 21 companions have $L_2 \lesssim 20\,\mathrm{L}_\odot$, $R_2 \lesssim 5.2\,\mathrm{R}_\odot$, and $M_2 \lesssim 2.4\,\mathrm{M}_\odot$, the measurements of $L_2 \approx 180\,\mathrm{L}_\odot$, $R_2 \approx 6.3\,\mathrm{R}_\odot$, and $M_2 \approx 3.8\,\mathrm{M}_\odot$ for ID-5898 are clear outliers and indicative of third light contamination. Finally, because third light contamination can bias our light curve solution to larger L_2 and R_2, our measured τ is also shifted toward younger ages. Of the four eclipsing binaries in our sample with age estimates $\tau \lesssim 1$ Myr, only ID-5898 is not embedded in a bright and/or compact H II region (see §3.4).

Considering the above, we remove ID-5898 when discussing correlations (§3.4) and the intrinsic binary fraction (§3.5). Nonetheless, ID-5898 is phenomenologically similar to the other 21 eclipsing binaries in our sample, and it most likely contains a low-mass pre-MS companion. We therefore still include this system in our total sample of 22 reflecting eclipsing binaries. We are simply unable to accurately constrain the physical properties of this system because of systematic effects most likely caused by third light contamination. Even if ID-5898 has a true mass ratio $q < 0.25$, the addition of this one object to the 19 measured systems with $q = 0.07$ - 0.25 would have a negligible effect on our statistics.

For each of our 22 eclipsing binaries, we calculate the covariance matrix and

measurement uncertainties in our eight physical model parameters. However, most of our measured physical properties are dominated by systematic errors. In the following, we quantify the magnitudes and directions of various sources of systematic errors:

1. Bolometric corrections. For our hot B-type MS primaries, the bolometric corrections are large and typically uncertain by 0.2 - 0.3 mag (Pecaut & Mamajek 2013). This dictates the primary luminosities L_1 are uncertain by at least ≈20 - 30%, and therefore the inferred primary masses M_1 have systematic uncertainties of at least ≈10%. However, if we were to systematically overestimate or underestimate M_1, we would also bias our inferred M_2 in the same direction. This is because the measured ratio of eclipse depths $\Delta I_2/\Delta I_1$ mainly determines the luminosity contrast L_2/L_1 and therefore the mass ratio $q = M_2/M_1$. Hence, our measured mass ratios q are relatively insensitive to the uncertainties in the bolometric corrections.

2. Color indices. Given a surface temperature T_2, the intrinsic colors $(V - I)_o$ of hot B-type MS stars are uncertain by ≈0.02 mag (Pecaut & Mamajek 2013). The zero-point calibrations in the measured OGLE-III LMC colors are also uncertainty by ≈0.01 - 0.02 mag (Udalski et al. 2008). Our measured dust extinctions A_I therefore have a minimum systematic error of ≈0.03 mag.

3. Dust reddening law. The coefficient in our adopted dust reddening law $E(V - I) = 0.7A_I$ has a systematic error of ∼10% (Cardelli et al. 1989; Fitzpatrick 1999; Ngeow & Kanbur 2005). The inferred dust extinctions A_I are also uncertain by this factor.

4. Evolutionary tracks. Given a luminosity L_1 of the primary B-type MS star, the primary masses are uncertain by ≈10% according to the stellar evolutionary tracks (Dotter et al. 2008; Bertelli et al. 2009). Rotating models of young B-type MS stars

are only 4% cooler than their non-rotating counterparts (Ekström et al. 2008a). This implies a 5% systematic uncertainty in the masses of the B-type MS stars due to the uncertainty in the rotation rates. For the pre-MS companions in our eclipsing binaries, we compare pre-MS models based on four different calculations (Siess et al. 2000; Dotter et al. 2008; di Criscienzo et al. 2009; Tognelli et al. 2011). For ages $\tau \gtrsim 1$ Myr and masses $M_2 > 1.3$, all pre-MS evolutionary tracks agree fairly well with typical errors of ≈15% in mass and ≈25% in age. At younger ages and lower masses, the systematic uncertainties increase to $\delta\tau \approx 0.3$ Myr and $\delta M_2 \approx 0.2 M_\odot$.

5. Irradiation effects. The luminosity received by the pre-MS companion from the B-type MS star is comparable to the intrinsic luminosity of the pre-MS star itself. This may cause the companion to enlarge, especially if it has a convective envelope and the albedo is measurably less than unity. This effect has been studied in the context of low-mass X-ray binaries in which a hot accretion disk around a compact object irradiates a cool, low-mass donor (Podsiadlowski 1991; Ritter et al. 2000). If the irradiation effects are on one side, as they are in X-ray binaries as well as in our eclipsing binaries, then the radius of the companion increases by only ≈5% (Ritter et al. 2000). Instead of becoming stored in the interior of the star, the intercepted energy quickly diffuses laterally to the unirradiated side and subsequently lost via radiation. This ≈5% systematic effect in radius is smaller than the uncertainties due to the evolutionary tracks discussed above. Most importantly, irradiation effects would shift the pre-MS companions toward larger radii and luminosities, so that we would have overestimated, not underestimated, their masses. Our conclusion that the companions in our eclipsing binaries are low-mass pre-MS stars is therefore not affected by irradiation effects.

6. Zero-point age calibration. Although our eclipsing binaries are detached from their Roche lobes and are currently evolving relatively independently from each other, they most likely experienced prior coevolution. In particular, the two components probably competed for accretion in the same circumbinary disk (Bate et al. 2002). Isolated T Tauri pre-MS stars with masses $\approx 1\text{-}3\,M_\odot$ still have thick circumstellar disks at ages $\tau \approx 0.5\text{-}5$ Myr (Hartmann 2009). There is no evidence for circumstellar disks in the photometric light curves of our 22 eclipsing binaries in the LMC as we observe in nearby BM Orionis (Windemuth et al. 2013, see §3.2). The absence of circumstellar disks in our eclipsing binaries demonstrates that the pre-MS companions formed differently than they would have in isolation. Nonetheless, most of the mass of a solar-type star is accreted at very early stages $\tau \lesssim 0.2$ Myr (Hartmann 2009). Moreover, the theoretical evolutionary tracks (Siess et al. 2000; Dotter et al. 2008; di Criscienzo et al. 2009; Tognelli et al. 2011) assume pre-MS stars evolve with constant mass, which better describe our low-mass pre-MS companions without disks than isolated low-mass pre-MS stars with disks.

   The time of initial pre-MS contraction and observability, sometimes called the birthline (Palla & Stahler 1990), can differ by 0.2 Myr between components in the same binary system (Stassun et al. 2008). Fortunately, the initial contraction phases are extremely rapid, and so the zero-point age calibration is uncertain by at most $\approx$0.4 Myr (see also fourth item in this list). Finally, we measured the ages τ and masses M_2 of the *companions* according to their properties T_2 and R_2 (Fig. 3.6). We inferred these companion properties from T_1, R_1, and the light curve characteristics. Because T_1 and R_1 of the B-type MS primaries evolve much more slowly than T_2 and R_2 of the low-mass pre-MS companions, then our models are not too sensitive to

the age of the primary. Even if the primary was slightly older or younger than the companion, we would still measure the same age τ and mass M_2 for the secondary. In short, the current properties of our pre-MS companions with ages $\tau > 0.6$ Myr are primarily dictated by their masses, with little dependence on the presence of a disk, prior coevolution at $\tau \lesssim 0.4$ Myr, or age of the primary.

7. Eclipsing binary models. For the same physical parameters, we compare our best-fit models produced by NIGHTFALL with light curves generated by the eclipsing binary software PHOEBE (Prša & Zwitter 2005). We find only slight differences, typically caused by the different treatment of limb-darkening and albedo between the two packages.

8. Third light contamination. Our measured physical properties can deviate beyond the calculated uncertainties if the photometric light curves include a third light source that is brighter than $\gtrsim$10% the luminosity of the B-type MS primary. In Moe & Di Stefano (2013), we measured the spatial density of bright stars, typically giants, in the LMC. We determined the probability that a luminous B-type MS eclipsing binary is blended with such a bright foreground or background star is only $\approx$5%. Most close binaries are orbited by an outer tertiary component (Tokovinin et al. 2006), but wide companions are weighted toward small mass ratios (Abt et al. 1990; Shatsky & Tokovinin 2002). Hence, the probability that our eclipsing binaries are orbited by a bright, massive late-B/early-A tertiary component is only $\approx$10% (Moe & Di Stefano 2013). Given our sample of 22 reflecting eclipsing binaries, we expect only one to be blended with a background or foreground cool giant, and possibly two to contain a hot luminous tertiary companion. ID-5898 probably experiences the latter of these two types of third light contamination. In addition, our model for

ID-7419 results in a moderately poor fit statistic $\chi^2/\nu = 1.20$, low inclination $i \approx 81^{\rm o}$, and large dust extinction $A_I \approx 0.7$ mag. ID-7419 is most likely contaminated with a cool foreground or background giant. Third light contamination causes us to overestimate, not underestimate, the secondary masses M_2, and typically results in larger χ^2/ν statistics. Most importantly, third light contamination affects only two to three individual systems in our sample, not our entire population like the previously discussed sources of systemic errors.

Based on the above, we add in quadrature to our statistical measurement uncertainties the following systematic errors. M_1: 15% relative error; M_2: 15% relative error or absolute error of $0.2\,{\rm M}_\odot$, whichever is larger; τ: 25% or 0.4 Myr, whichever is larger; and A_I: 10% or 0.03 mag, whichever is larger. We propagate these systematic uncertainties in M_1, M_2, τ, and A_I into the other model parameters P, $t_{\rm o}$, i, and A_2 according to the covariance matrix. In Table 3.2, the values in parenthesis represent the total uncertainties, including systematic errors, in the final decimal places of our eight model parameters. Note that we list the best-fit model parameters in Table 3.2, and so the reported uncertainties are not necessarily symmetric around the best-fit values. The uncertainties in P and $t_{\rm o}$ primarily derive from the observed light curves with little contribution from the systematic errors. The uncertainties in the secondary albedos A_2 are quite large, but the other physical properties are relatively independent of this parameter. Typical errors in the mass ratios q and relative ages $\tau/\tau_{\rm MS}$ are 15% or 0.03, whichever is larger. The uncertainties in the luminosities L_1 and L_2 are $\approx$40%, which are primarily due to the systematic uncertainties in the bolometric corrections discussed above. Given the precisely measured orbital periods and the uncertainties in the masses and evolutionary tracks, the uncertainties in the orbital separations a, radii R_1 and R_2,

and Roche-lobe fill-factors $RLFF_1$ and $RLFF_2$ are ≈10% according to Kepler's third law. Finally, given the uncertainties in the radii and luminosities, the representative errors in the temperatures T_1 and T_2 are ≈8% according to the Stefan-Boltzmann law.

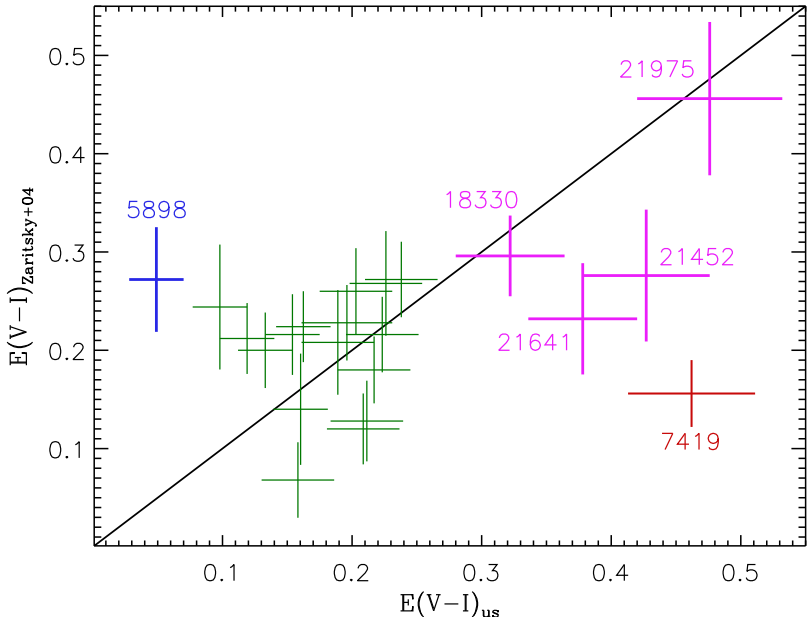

Figure 3.7: Comparison of our fitted dust reddening measurements to values obtained by Zaritsky et al. (2004) of hot young stars along similar lines-of-sight to our 22 nascent eclipsing binaries. The majority of systems (green) are only slightly reddened with $E(V-I) \approx 0.1$ - 0.3. The four highly reddened eclipsing binaries (magenta) with $E(V-I) \approx 0.3$ - 0.5 are in the eastern portions of the LMC and embedded in bright, dusty H II regions, e.g. ID-21452 is in 30 Doradus. The two systems that deviate more than 3σ from the Zaritsky et al. (2004) measurements, ID-5989 (blue) and ID-7419 (red), happen to be the two eclipsing binaries with the poorest model fits to the observed light curves, $\chi^2/\nu = 1.27$ and $\chi^2/\nu = 1.20$, respectively. This indicates third light contamination dominates the systematic errors in these two systems, while the other 20 eclipsing binaries are relatively free from third light contamination.

Although the systematic errors dominate our total uncertainties, our conclusions that 19 of our eclipsing binaries with reflection effects have small mass ratios $q \lesssim 0.25$ and young ages $\tau \lesssim 15$ Myr are robust.

As a consistency check, we compare our fitted dust reddening measurements $E(V-I) = 0.7A_I$ to the Zaritsky et al. (2004) LMC dust reddening maps. Specifically, we compile the Zaritsky et al. (2004) A_V values toward hot, young LMC stars within one arcminute of each of our 22 eclipsing binaries. We typically find ≈10 - 25 such systems in their database that are this close to our eclipsing binaries. For each area, we calculate the mean extinction and standard deviation of the mean extinction. We convert these V-band extinction values into dust reddenings $E(V-I) = 0.41A_V$ using are adopted reddening law. Finally, we add in quadrature to the measurement uncertainties a systematic error of 0.03 mag (see second item in list above). In Fig. 3.7, we compare our values and uncertainties for $E(V-I)$ to those we compiled from Zaritsky et al. (2004). Only ID-5989 and ID-7419, which have the largest χ^2/ν statistics most likely caused by third light contamination, have dust reddening measurement that are discrepant with the Zaritsky et al. (2004) values. As discussed above, third light contamination will bias our dust reddening measurements toward larger or smaller values, depending on the color of the third light source. For the remaining 20 of our eclipsing binaries, the two dust reddening estimates are in agreement, which demonstrates the reliability of our eclipsing binary models.

3.4 Association with H II Regions

Because our eclipsing binaries with reflection effects contain pre-MS companions, they should be systematically younger than their non-reflecting counterparts. To test this prediction, we check for correlations between the coordinates of the eclipsing binaries and positions of star-forming H II regions in the LMC. In Table 3.4, we list various properties of our 22 eclipsing binaries, including their identification numbers and coordinates from the OGLE-III LMC eclipsing binary catalog (Graczyk et al. 2011). To perform our statistical analysis below, we utilize the coordinates, sizes, and position angles of the 1,164 H II regions in the Bica et al. (1999) catalog designated as class NA or NC, i.e. stellar associations and clusters, respectively, clearly related to emission nebulae. We report in Table 3.4 the properties of the H II regions with which 20 of our reflecting eclipsing binaries are associated. This includes the projected offset r (in pc) between the eclipsing binaries and the centers of the H II regions, the physical radii $\langle r \rangle_{\rm H\,II}$ (in pc) of the H II regions, and the H II region catalog identification numbers and names from Bica et al. (1999). We define the mean physical radius to be $\langle r \rangle_{\rm H\,II} = \sqrt{A \times B}/2$, where A and B are the major and minor axes provided by Bica et al. (1999) projected at the distance $d = 50$ kpc to the LMC.

In Fig. 3.8, we show the coordinates of the 2,206 B-type MS eclipsing binaries in our full sample, and the 22 systems that exhibit reflection effects with large, pre-MS companions. In the background of Fig. 3.8, we display an image of the LMC taken from the Magellanic Cloud Emission Line Survey (Smith et al. 2005), where the star-forming H II regions are clearly visible. Based on the Bica et al. (1999) catalog, only 16% of normal B-type MS eclipsing binaries have projected distances $r < 30\,$pc from the

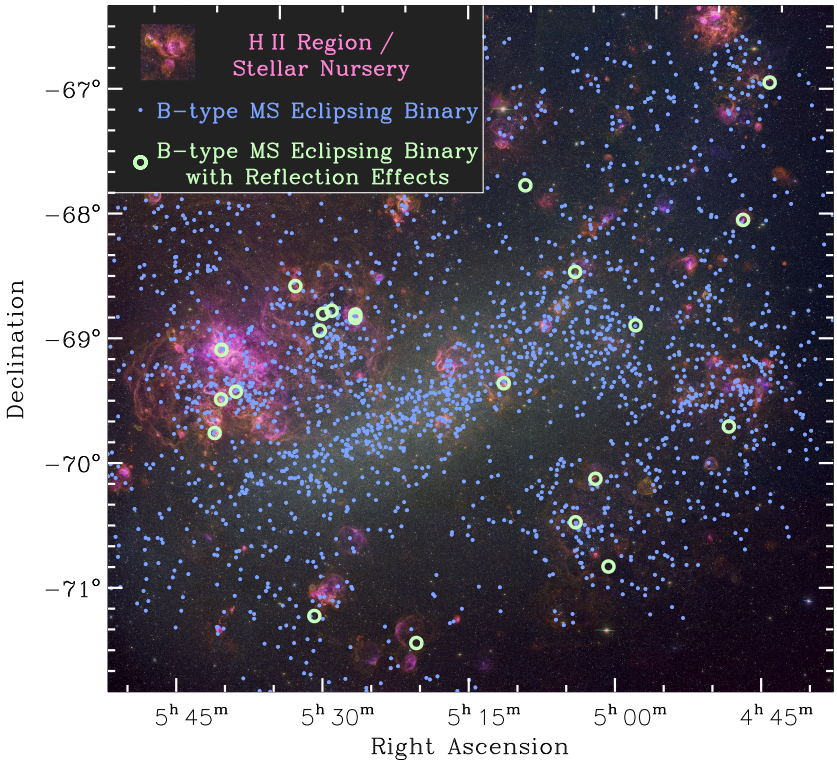

Figure 3.8: The positions of the 2,206 eclipsing binaries with B-type MS primaries and orbital periods P = 3 - 15 days (blue dots) and the subset of 22 systems that exhibit pronounced reflection effects with pre-MS companions (green circles) superimposed on a narrow-band color image of the LMC taken from the Magellanic Cloud Emission Line Survey (Smith et al. 2005). The largest concentration of normal B-type MS eclipsing binaries is in the central bar of the LMC, while those displaying reflection effects typically reside in star-forming H II regions. Relative to their non-reflecting counterparts, the positions of our 22 reflecting eclipsing binaries are correlated with the positions of H II regions at the 4.1σ confidence level. This demonstrates our 22 eclipsing binaries that exhibit reflection effects are systematically younger, which reinforces our conclusion that they contain low-mass pre-MS secondaries.

Table 3.4. Coordinates and properties of the 22 eclipsing binaries with reflection effects, and their association with H II regions.

ID	RA (J2000)	DE (J2000)	ΔI_1	$\Delta I_{\rm refl}$	τ (Myr)	r (pc)	$\langle r \rangle_{\rm H\,II}$ (pc)	H II ID	H II Name
1803	4h 51m 58.23s	$-66^{\rm o}$ 57′ 00.0″	0.64	0.138	0.7	25	8	351	NGC1714 in Shapley-VI
1965	4h 52m 34.89s	$-69^{\rm o}$ 42′ 24.7″	0.20	0.017	15	140	400	470	SGshell-LMC7
2139	4h 53m 05.17s	$-68^{\rm o}$ 03′ 03.4″	0.33	0.033	0.9	3	6	418	HDE268680 in NGC1736
5377	5h 01m 44.99s	$-68^{\rm o}$ 53′ 43.2″	0.17	0.020	14				
5898	5h 02m 58.72s	$-70^{\rm o}$ 49′ 44.7″	0.83	0.098	0.8	380	400	1172	Shapley-VIII
6630	5h 04m 39.43s	$-70^{\rm o}$ 07′ 33.3″	0.16	0.019	13	19	26	1331	BSDL552 in LMC-DEM68
7419	5h 06m 21.44s	$-70^{\rm o}$ 28′ 27.5″	0.19	0.037	5.2	290	400	1172	Shapley-VIII
7842	5h 07m 17.97s	$-68^{\rm o}$ 28′ 03.8″	1.73	0.083	2.6	5	16	1572	BSDL657 in LMC-DEM76
9642	5h 11m 46.29s	$-67^{\rm o}$ 46′ 25.1″	0.70	0.050	1.7				
10289	5h 13m 23.92s	$-69^{\rm o}$ 21′ 37.3″	0.20	0.034	2.5	6	11	2124	NGC1876 in SL320
13721	5h 21m 51.38s	$-71^{\rm o}$ 26′ 31.5″	0.42	0.025	8	80	120	3018	LMC-DEM164 in SGshell-LMC9
15761	5h 26m 35.54s	$-68^{\rm o}$ 48′ 35.7″	0.85	0.108	1.9	5	3	3598	LMC-N144B in SL476
15792	5h 26m 37.37s	$-68^{\rm o}$ 50′ 09.2″	0.23	0.039	2.8	17	11	3635	NGC1970 in SL476
16828	5h 28m 40.41s	$-68^{\rm o}$ 46′ 42.8″	0.11	0.018	7	170	200	3759	Shapley-II in SGshell-LMC3
17217	5h 29m 27.69s	$-68^{\rm o}$ 48′ 09.9″	0.10	0.022	7	180	200	3759	Shapley-II in SGshell-LMC3
17387	5h 29m 49.28s	$-68^{\rm o}$ 56′ 17.6″	0.09	0.017	8	150	200	3759	Shapley-II in SGshell-LMC3
18330	5h 31m 44.95s	$-68^{\rm o}$ 34′ 52.5″	0.30	0.056	5.6	11	11	4256	BSDL2159 in LMC-DEM227
18419	5h 31m 55.78s	$-71^{\rm o}$ 13′ 32.0″	0.55	0.059	1.6	30	4	4389	LMC-N206D in SGshell-LMC9
21025	5h 37m 45.75s	$-69^{\rm o}$ 25′ 38.8″	0.13	0.025	6	48	56	5056	LMC-DEM261 in LH96
21452	5h 38m 43.99s	$-69^{\rm o}$ 05′ 29.6″	2.82	0.124	0.6	8	26	5112	30 Doradus in NGC2070
21641	5h 39m 10.90s	$-69^{\rm o}$ 29′ 20.2″	0.41	0.062	2.6	12	27	5140	NGC2074 in LMC-N158
21975	5h 40m 03.86s	$-69^{\rm o}$ 45′ 32.3″	0.14	0.030	4.0	5	10	5252	NGC2084e in LMC-N159

centers of H II regions. In contrast, 13 of our 22 systems with reflection effects, i.e. $(59 \pm 10\%)$, are situated this close to such stellar nurseries. These values differ at the 4.1σ significance level, demonstrating that B-type MS eclipsing binaries with reflection effects are dramatically younger.

Similarly, only 4.8% of B-type MS eclipsing binaries are located in centrally condensed H II regions with mean physical radii $\langle r \rangle_{\rm H\,II} = 3$ - 30 pc. Meanwhile, 10 of the 22 systems with reflection effects, i.e. $(45 \pm 11)\%$, are embedded in such star-forming environments. In addition, 10 of the remaining 12 reflecting eclipsing binaries are associated with extended, more diffuse H II regions with $\langle r \rangle_{\rm H\,II} > 30$ pc. These statistics demonstrate that our B-type MS eclipsing binaries with reflection effects are relatively young with ages $\tau \approx 1$ - 8 Myr that are comparable to the lifetimes of H II regions.

Only 2 of our 22 eclipsing binaries with reflection effects do not appear to be associated with an H II region. One of these systems, ID-5377, is relatively old at $\tau = 14 \pm 5$ Myr (Table 3.4), and so it is not unexpected that it is relatively remote from a site of active star formation. In contrast, the other eclipsing binary that is not in an H II region, ID-9642, is relatively young at $\tau = 1.7 \pm 0.5$ Myr. We speculate that this eclipsing binary with a B-type MS primary may have formed in relative isolation without nearby O-type stars to ionize the surrounding gas (see de Wit et al. 2004; Parker & Goodwin 2007). As another possibility, the young ID-9642 may be embedded in a compact H II region with $\langle r \rangle_{\rm H\,II} \lesssim 1$ pc that is below the resolution limit of ground-based surveys and therefore not in the Bica et al. (1999) catalog. In any case, the fact that 20 our our 22 eclipsing binaries are associated with H II regions reinforces our conclusion that the majority of the companions are young, low-mass, pre-MS stars.

The positions of our 22 eclipsing binaries and their associations with H II regions also corroborate the reliability of our eclipsing binary models. For example, ID-15761 and ID-15792 are both associated with the same H II region SL476. For these two systems, we derived ages $\tau = 1.9 \pm 0.5$ Myr and $\tau = 2.8 \pm 1.0$ Myr, respectively, that are consistent with each other, and dust extinctions $A_I = 0.30 \pm 0.04$ mag that match each other. Similarly, ID-16828, ID-17217, and ID-17387 are all in the large diffuse H II region Shapley-II with $\langle r \rangle_{\rm H\,II} \approx 200$ pc. These three eclipsing binaries have slightly older ages $\tau \approx 7$ - 8 Myr and consistently smaller dust extinctions $A_I \approx 0.23$ - 0.28 mag. Our youngest three eclipsing binaries with reliable age estimates $\tau \lesssim 1$ Myr, i.e. ID-1803, ID-2139, and ID-21452, are all associated with centrally condensed H II regions with $\langle r \rangle_{\rm H\,II} \lesssim 30$ pc. Alternatively, our three oldest systems with $\tau \approx 13$ - 15 Myr and companions close to the zero-age MS, i.e. ID-1965, ID-5377, and ID-6630, are either not associated with

star-forming environments or are in relatively large and/or diffuse H II regions.

We now examine these correlations between eclipsing binary parameters and the properties of the H II regions in which they reside in a more statistical manner. In Table 3.4, we list the observed primary eclipse depths ΔI_1 and reflection effect amplitudes $\Delta I_{\rm refl}$ from Table 3.1, and the modeled ages τ from Table 3.2. The uncertainties in the primary eclipse depths are dominated by systematic errors $\delta\Delta I_1 \approx 0.01$ mag, except for the two systems with the deepest eclipses that have $\Delta I_1 = 1.73 \pm 0.05$ mag (ID-7842) and $\Delta I_1 = 2.82 \pm 0.14$ mag (ID-21452). The uncertainties in the reflection effect amplitudes are $\delta\Delta I_{\rm refl} \approx 0.003$ mag, and the uncertainties in the ages τ are as those reported in Table 3.2.

In Fig. 3.9, we compare the eclipsing binary properties listed in Table 3.4, where we have excluded ID-5898 which is most likely biased toward shallower eclipses and younger ages due to third light contamination. The empirical properties of primary eclipse depth ΔI_1 and reflection effect amplitude $\Delta I_{\rm refl}$ are positively correlated (Spearman rank correlation coefficient $\rho = 0.85$) at a statistically significant level (probability of no correlation $p = 2{\times}10^{-6}$). This is because both ΔI_1 and $\Delta I_{\rm refl}$ are inextricably linked to the radius R_2 of the pre-MS companion. The age τ is anti-correlated with both ΔI_1 and $\Delta I_{\rm refl}$ ($\rho = -0.70$ and $\rho = -0.83$, respectively) because older pre-MS stars are systematically smaller. Although still statistically significant ($p = 3{\times}10^{-6}$ - $4{\times}10^{-4}$), these correlations are not as strong because the radius of a pre-MS star also depends on its mass in addition to its age.

The three properties ΔI_1, $\Delta I_{\rm refl}$, and τ of the eclipsing binaries are all significantly correlated with the mean physical radii $\langle r \rangle_{\rm H\,II}$ of the H II regions with which they are

associated. Namely, younger eclipsing binaries with deeper primary eclipses and larger reflection effect amplitudes are typically embedded in bright and/or condensed H II regions. These correlations are statistically significant ($p = 5\times10^{-4}$ - 0.01), but the mapping between the eclipsing binary properties and the radii of the H II regions are not one-to-one ($|\rho| \approx 0.6$ - 0.7). For example, ID-21452, which happens to be our youngest system ($\tau = 0.6 \pm 0.4$ Myr) with the deepest eclipse ($\Delta I_1 \approx 2.8$ mag), resides in the famous, bright, large H II region 30 Doradus (also known as the Tarantula Nebula; RA $\approx 5^{\rm h}39^{\rm m}$ and DE $\approx -69.1^{\rm o}$ in Fig. 3.8). Such large, bright H II regions can host multiple episodes of star formation (Crowther 2013). Specifically, 30 Doradus contains an older population of stars with $\tau = 20$ - 25 Myr, which is consistent with its larger size, and a more recent generation that is $\tau \lesssim 1$ - 2 Myr old, which is consistent with the age derived for ID-21452 (Massey & Hunter 1998; Grebel & Chu 2000).

The properties of our nascent eclipsing binaries provide powerful diagnostics for the long-term evolution of H II regions. Namely, the mean expansion velocity $\langle v \rangle_{\rm H\,II} = \langle \langle r \rangle_{\rm H\,II} / \tau \rangle$ of H II regions derives from the slope of the observed correlation in the bottom right panel of Fig. 3.9. For the 12 bright and centrally condensed H II regions with $\langle r \rangle_{\rm H\,II} = 3$ - 30 pc, we find a mean expansion velocity of $\langle v \rangle_{\rm H\,II} = 8 \pm 3$ km s^{-1}. This is consistent with both observed and theoretical estimates of $\langle v \rangle_{\rm H\,II} \approx 10$ km s^{-1} during the subsonic expansion phase of H II regions when $\tau \approx 0.01$ - 5 Myr (Yorke 1986; Cichowolski et al. 2009). For the seven large and diffuse H II regions with $\langle r \rangle_{\rm H\,II} > 30$ pc, we calculate $\langle v \rangle_{\rm H\,II} = 29 \pm 8$ km s^{-1}. This coincides with the observed range of expansion velocities $v \approx 15$ - 45 km s^{-1} in giant H II shell-like regions within nearby galaxies (Chu & Kennicutt 1994; Tomita et al. 1998). Our ability to measure the ages of several eclipsing binaries to accuracies of ≈25% give tight constraints for the dynamical evolution of the H II regions

in which they formed.

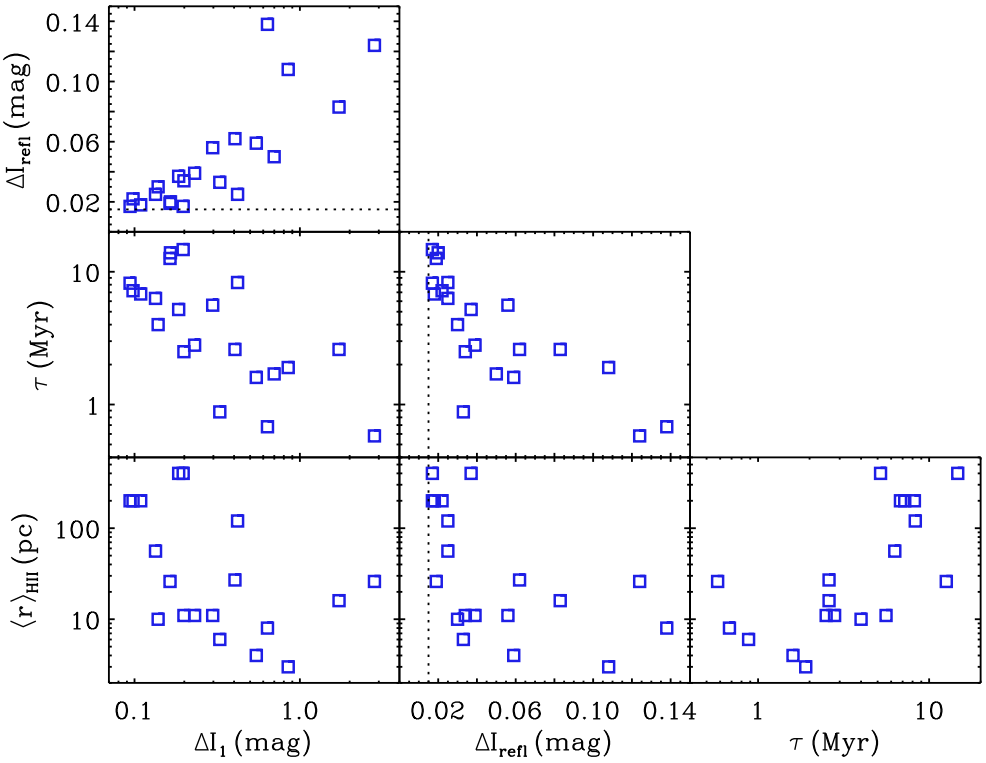

Figure 3.9: Properties of eclipsing binaries and H II regions. The reflection effect amplitudes $\Delta I_{\rm refl}$, primary eclipse depths ΔI_1, ages τ, and physical radii of the H II regions $\langle r \rangle_{\rm H\,II}$ in which the eclipsing binaries reside are all correlated with each other at a statistically significant level. Our eclipsing binaries provide powerful diagnostics and constraints for the dynamical evolution and expansion velocities $\langle v \rangle_{\rm H\,II} \approx 10$ - 30 km s^{-1} of H II regions. See text for details and a discussion of uncertainties.

3.5 The Intrinsic Close Binary Statistics

In the following, we determine the intrinsic fraction F of B-type MS stars that have close low-mass companions. We utilize the properties and statistics of our nascent eclipsing binaries, and so we must correct for geometrical and evolutionary selection effects in our magnitude-limited sample. To achieve this, we estimate the probability density functions (§3.5.1) for the eight parameters in §3.3 that describe our physical models. With these distributions, we calculate the probability of observing reflection effects using two approaches: a simple estimate (§3.5.2) and a detailed Monte Carlo simulation (§3.5.3 - 3.5.4).

3.5.1 Probability Density Functions

The distribution of dust extinction toward B-type MS stars in the LMC peaks at $A_V \approx 0.4$ mag, i.e. $A_I \approx 0.2$ mag according to our adopted reddening law, with a long tail toward larger values (Zaritsky 1999; Zaritsky et al. 2004). To match these observations, we utilize a beta probability distribution to model the extinction distribution in the I-band:

$$p_{A_I} = 30 A_I (1 - A_I)^4 \quad \text{for } 0 < A_I < 1, \tag{3.7}$$

where A_I is in magnitudes. The measured dust extinctions A_I of our 22 reflecting eclipsing binaries are also consistent with this distribution (see Table 3.2 and Fig. 3.7).

To quantify the probability density functions for M_1 and τ, we estimate the initial mass function (IMF) and recent star-formation history (SFH) within the OGLE-III

footprint of the LMC. We consider a single power-law IMF for massive primaries:

$$dN = kM_1^{-\alpha}dM_1 \quad \text{for } 3\,M_\odot < M_1 < 30\,M_\odot \tag{3.8}$$

where the normalization constant k and IMF slope α are free parameters. Note that α = 2.35 corresponds to the standard Salpeter value. We model the relative SFH of the LMC for ages $0\,\mathrm{Myr} < \tau < 320\,\mathrm{Myr}$, where $\tau = 320\,\mathrm{Myr}$ is the MS lifetime of the lowest mass primaries $M_1 = 3\,\mathrm{M}_\odot$ we have considered. We set the relative star-formation rate during recent times $0\,\mathrm{Myr} < \tau < 10\,\mathrm{Myr}$ to unity, and consider five free parameters A-E to describe the SFH at earlier epochs:

$$SFH(\tau) = \begin{cases} 1 & \text{for } \ 0\,\mathrm{Myr} \le \tau < \ 10\,\mathrm{Myr} \\ A & \text{for } 10\,\mathrm{Myr} \le \tau < \ 20\,\mathrm{Myr} \\ B & \text{for } 20\,\mathrm{Myr} \le \tau < \ 40\,\mathrm{Myr} \\ C & \text{for } 40\,\mathrm{Myr} \le \tau < \ 80\,\mathrm{Myr} \\ D & \text{for } 80\,\mathrm{Myr} \le \tau < 160\,\mathrm{Myr} \\ E & \text{for } 160\,\mathrm{Myr} \le \tau < 320\,\mathrm{Myr} \end{cases} \tag{3.9}$$

To measure the IMF and SFH model parameters, we utilize the observed present-day luminosity function of MS stars in the OGLE-III LMC database (Udalski et al. 2008). In Fig. 3.10, we show the observed magnitude distribution across $15.0 < \langle I \rangle < 18.0$ for early-type MS systems with $-0.25 < \langle V - I \rangle < 0.20$. We have extended our magnitude range to include brighter, short-lived O-type primaries to better constrain the more recent SFH within the OGLE-III LMC footprint.

To account for systematic errors caused by unresolved binary stars in the OGLE-III LMC database, we consider two models. For Model 1, we assume all stars are single, and so the magnitude $\langle I \rangle$ and color $\langle V - I \rangle$ of a system is simply determined by M_1, τ, and A_I according to our adopted stellar tracks. For Model 2, we assess the bias in the luminosity distribution due to companions $q \gtrsim 0.7$ that are comparable in mass and luminosity to the primary. This bias in the luminosity distribution of binary stars was first discussed by Öpik (1923), and we have previously investigated this Öpik effect in the context of stellar populations in extragalactic environments (Moe & Di Stefano 2013). In short, we must approximate the total fraction of B-type MS stars with companions $q \gtrsim 0.7$ across all orbital periods that can measurably affect the luminosity of the system. For Model 2, we therefore assume a 100% total binary star fraction and an overall mass-ratio distribution $p_q \propto q^{-0.4}\, dq$ across $0.05 < q < 1.0$, which is consistent with current observations of B-type MS stars (Kobulnicky & Fryer 2007; Kouwenhoven et al. 2007; Rizzuto et al. 2013). The companion star fraction may exceed 100% for B-type MS stars, but this is most likely at the expense of increasing the number of low-mass tertiaries that are not easily detectable. Hence, the fraction of B-type MS primaries that have luminous companions $q \gtrsim 0.7$ is robust at (23 ± 10)%.

By implementing a Monte Carlo technique, we generate a population of stars (Model 1) or binaries (Model 2) using our adopted evolutionary stellar tracks and models for the IMF, SFH, and dust extinction distribution. To constrain the IMF and SFH model parameters, we minimize the χ^2 statistic between the observed and simulated present-day $\langle I \rangle$ distributions (see Fig. 3.10). For both models, we measure a primary star IMF that is consistent with the Salpeter value. We also find that the star-formation rate has been relatively constant over the past ≈ 20 Myr, but was $\approx$40% the present-day value at

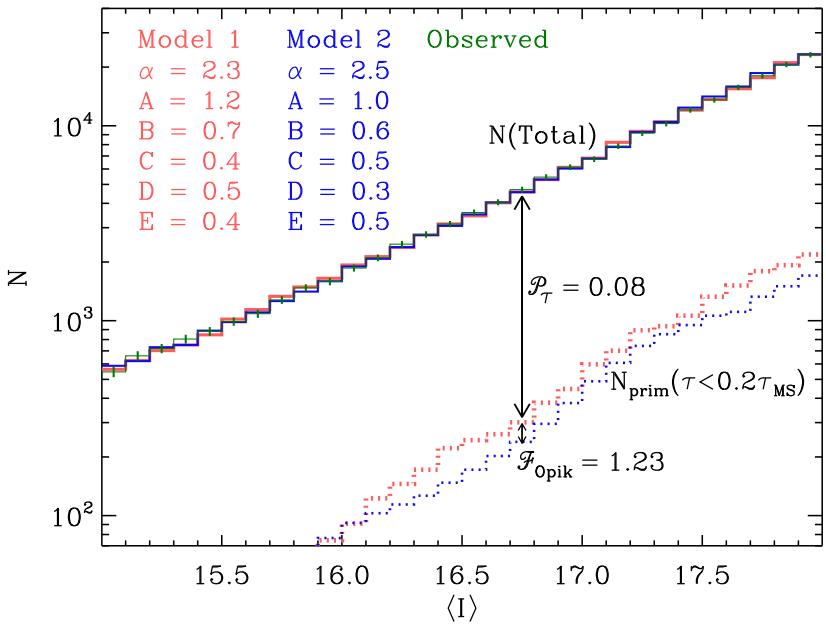

Figure 3.10: Present-day luminosity function of MS stars in the LMC. We compare the $\langle I \rangle$ distribution of MS systems with $-0.25 < \langle V - I \rangle < 0.20$ in the OGLE-III LMC database (green) to simulated models assuming all systems are single stars (Model 1 - red) or binaries (Model 2 - blue). We find similar fit parameters between these two models for the slope α of the IMF and relative rates A - E of star formation. For our simulated stellar populations, we also display the predicted number of primaries with ages that are <20% their MS lifetimes (dotted). In a magnitude-limited sample, only $\mathcal{P}_\tau \approx 8\%$ of systems are young enough to have pre-MS companions that are capable of producing detectable reflection effects. In a population of binaries that contain companions $q \gtrsim 0.7$ that are comparable in mass and luminosity to the primary, the total luminosity function is biased toward these bright binaries according to the Öpik effect. Hence, there are *fewer* total primaries by a factor of $\mathcal{F}_{\rm Opik} = 1.23 \pm 0.10$.

earlier epochs $\tau > 80$ Myr. This is consistent with other measurements of the SFH in the LMC (Harris & Zaritsky 2009; Indu & Subramaniam 2011). The uncertainties in the overall binary properties have little influence on our derived slope of the IMF or the relative SFH. We therefore adopt parameters between our two models, namely $\alpha = 2.4$, $A = 1.1$, $B = 0.7$, $C = 0.5$, and D=E=0.4.

Only the normalization constant between our single and binary star populations significantly differ. For our binary population, we measure ≈20% fewer systems due to the Öpik effect. We also find 20% more total mass in our binary population because the average binary contains ≈1.4 times the mass of the primary, i.e. $\langle q \rangle \approx 0.4$. When we generate synthetic eclipsing binary light curves (§3.5.3), we simulate only systems that are similar to our 22 observed eclipsing binaries. Quantitatively, we generate only B-type MS stars with low-mass companions $q = 0.06$ - 0.40 at short orbital periods $P = 3.0$ - 8.5 days. We therefore need to correct for the luminosity bias of $q \gtrsim 0.7$ companions. Because the observed luminosity distribution is biased toward these binaries with equally bright components, the distribution is biased *against* single stars as well as binaries with faint, low-mass companions $q \lesssim 0.7$. We therefore multiply our calculated intrinsic fraction F of low-mass companions by a correction factor of $\mathcal{F}_{\rm Opik} = 1.23 \pm 0.10$ to account for this Öpik effect.

The probability density functions for the remaining physical model parameters are easier to quantify. We assume random epochs of primary eclipse minima $t_{\rm o}$. We also assume random orbital orientations so that $\cos(i) = [0, 1]$ is uniformly distributed on this interval. We select secondary albedos from a uniform distribution across the interval $A_2 = [0.3, 1.0]$, which encompasses the range of observed albedos in our eclipsing binaries with reflection effects (see Table 3.3). Although the average albedo of this

distribution $\langle A_2 \rangle = 0.65$ is slightly lower than the observed average $\langle A_2 \rangle \approx 0.71$, the latter is a posterior average and companions with higher albedos are more likely to be detected. Also, the albedo A_2 may be dependent on the effective temperature T_2 (Claret 2001), but small correlations between model parameters are second-order effects in our overall calculations. We assume log P is uniformly distributed across the interval $P = 3.0$ - 8.5 days, which is consistent with observations of binaries with B-type MS primaries (Abt et al. 1990; Kobulnicky & Fryer 2007; Kouwenhoven et al. 2007). Reasonable deviations from this distribution have little effect on our statistics, especially considering we are examining such a narrow window of orbital periods. Finally, in order to calculate the detectability of reflection effects as a function of mass ratio, we consider four logarithmic $d\log q = 0.2$ intervals across the total range log $q = -1.2$ - -0.4, i.e. $q = 0.06$ - 0.40. In our detailed Monte Carlo simulations, we treat each of these four mass-ratio bins independently, and select log q from a uniform distribution within each interval. Again, the precise distribution of mass ratios within each narrowly divided bin is inconsequential to our overall uncertainties.

3.5.2 Simple Estimate

Before we utilize a Monte Carlo technique to generate synthetic light curves for a population of eclipsing binaries, we first perform a simple calculation. Using the measured properties of our 22 eclipsing binaries, we estimate the probability $\mathcal{P}_{\rm refl}$ that a B-type MS primary and low-mass companion have the necessary configuration to produce observable eclipses and reflection effects. In this simple estimate, we do not account for all eight physical model parameters outlined above. Instead, we consider

only the following three main selection effects.

First, eclipsing binaries must have nearly edge-on orientations so that the eclipses are deep enough to be observed given the sensitivity of the OGLE-III LMC observations. The observed eclipsing binaries with reflection effects in our sample generally have $i \gtrsim 80^{\rm o}$ (Table 3.2). This implies the probability of having sufficiently edge-on inclinations is $\mathcal{P}_i \approx \cos(80^{\rm o}) \approx 0.17$.

Second, the observed eclipsing binaries generally have short orbital periods. This is not only due to geometrical selection effects, but also because irradiation effects quickly diminish with orbital separation. The majority of our systems have $P = 3.0$ - 5.5 days, implying $\mathcal{P}_P \approx (\log 5.5 - \log 3.0)/(\log 8.5 - \log 3.0) \approx 0.6$ if the intrinsic distribution of orbital periods is uniform in $\log P$.

Finally, our reflecting eclipsing binaries must be young enough so that the companion is still on the pre-MS, but bright enough to be contained in our magnitude-limited sample. A B-type MS primary can have a pre-MS companion only if the age of the binary τ is a certain fraction of the primary's MS lifetime $\tau_{\rm MS}$. For moderate mass ratios $q \approx 0.25$, the ages must be $\tau \lesssim 0.1\ \tau_{\rm MS}$. For binaries with extreme mass ratios $q \approx 0.15$, close orbits $P = 3$ - 4 days, and bright massive primaries $M_1 = 12$ - $16\ {\rm M}_\odot$, we can discern reflection effects up to $\tau \approx 0.5\,\tau_{\rm MS}$ (Table 3.3, Fig. 3.4, and left panel of Fig. 3.11). For our simple estimation purposes, we adopt an average criterion that the binary must have an age $\tau < 0.2\,\tau_{\rm MS}$ in order for the companion to be a pre-MS star. One may initially assume that the probability of observing such a young binary is $\mathcal{P}_\tau = 0.2$, but this is not the case for our magnitude-limited sample. By incorporating our simulated stellar populations used to quantify the SFH and IMF above, we display in Fig. 3.10 the number

of systems with primaries that have ages $\tau < 0.2\ \tau_{\rm MS}$ for each magnitude bin. The true probability that a system has such a young age is $\mathcal{P}_\tau = \mathcal{N}(\tau < 0.2\tau_{\rm MS})/\mathcal{N}({\rm total}) \approx 0.08$, which is a factor of 2 - 3 times lower than the crude estimate of $\mathcal{P}_\tau = 0.2$. Late-B MS primaries with $M_1 \approx 3$ - 6 $M_\odot$ can have observed magnitudes $\langle I \rangle < 18.0$ only if they are older and more luminous on the upper MS. Alternatively, in order to see a system with $\tau < 0.2\tau_{\rm MS}$ and $\langle I \rangle < 18.0$, the primary must be rather massive with $M_1 \gtrsim 6\,M_\odot$. Note that all of our observed eclipsing binaries with reflection effects have early B-type MS primaries with $M_1 \gtrsim 6\,M_\odot$. Because the IMF is significantly weighted toward lower-mass primaries, our magnitude-limited sample is dominated by late-B primaries that are systematically older on the upper MS. This is the reason why the probability of observing a young system with $\tau < 0.2\,\tau_{\rm MS}$ in our magnitude-limited sample is only $\mathcal{P}_\tau \approx 0.08$.

Putting these three factors together, then the probability of observing reflection effects is $\mathcal{P}_{\rm refl} = \mathcal{P}_i\,\mathcal{P}_\tau\,\mathcal{P}_P \approx 0.8\%$. In our actual sample, we selected $\mathcal{N}_{\rm B} = 174{,}000$ B-type MS stars from the OGLE-III LMC survey. From this population, we observed $\mathcal{N}_{\rm obs} = 19$ eclipsing binaries that exhibit reflection effects with $q = 0.06$ - 0.25 companions and $P = 3.0$ - 8.5 days. After accounting for the correction factor $\mathcal{F}_{\rm Opik} = 1.23$ due to the Öpik effect, then the intrinsic fraction of B-type MS stars with low-mass $q = 0.06$ - 0.25 companions and short orbital periods $P = 3.0$ - 8.5 days is $F = (\mathcal{N}_{\rm obs}\,\mathcal{F}_{\rm Opik})\,/\,(\mathcal{N}_{\rm B}\,\mathcal{P}_{\rm refl}) \approx (19 \times 1.23)\,/\,(174{,}000 \times 0.008) \approx 1.7\%$. This is only an approximation as we need to quantify $\mathcal{P}_{\rm refl}$ as a function of q in a more robust manner. Nonetheless, this simple analysis separates the individual selection effects and illustrates the difficulty in detecting young, low-mass pre-MS companions that eclipse B-type MS stars.

3.5.3 Detailed Monte Carlo Simulation

We now perform a more detailed Monte Carlo simulation by synthesizing NIGHTFALL light curves for a population of eclipsing binaries. Using our probability density functions,

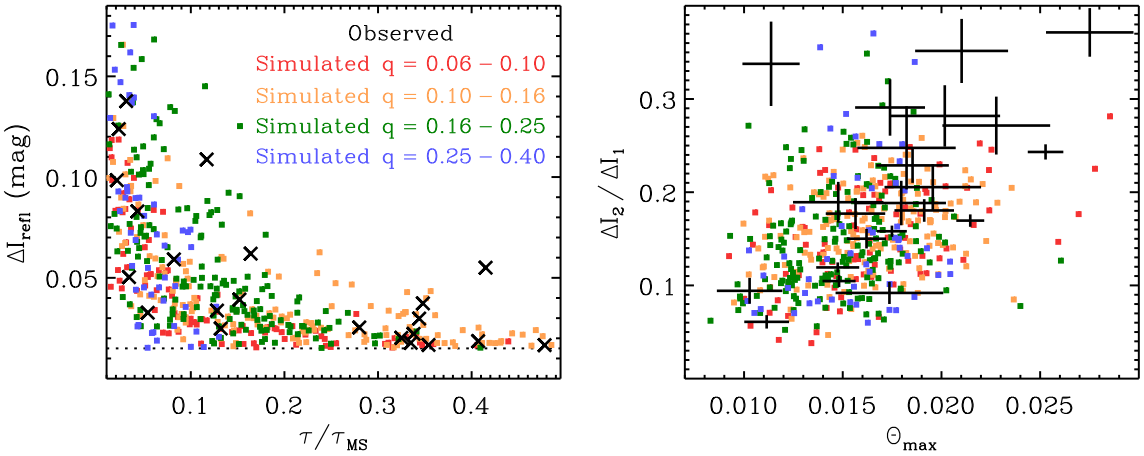

Figure 3.11: We compare the properties of the 22 observed eclipsing binaries (black) to the 468 simulated systems (color) with B-type MS primaries, low-mass $q = 0.06$ - 0.40 pre-MS companions, and pronounced reflection effects as listed in Table 3.5. Left panel: The anti-correlation between the reflection effect amplitude and the age relative to the MS lifetime of the primary is similar to the trend seen in the middle panel of Fig 3.9. Binaries with moderate mass ratios $q = 0.25$ - 0.40 (blue) can have pre-MS companions only at extremely young ages $\tau \lesssim 0.1\ \tau_{\rm MS}$, while lower-mass companions can have pre-MS evolutions that last up to ≈50% the MS lifetime of the primary. Right panel: Identical parameter space used in Fig. 3.3 to identify our systems and differentiate them from other classes of eclipsing binaries. Our simulated systems correspond well to the observed population. We can therefore easily identify eclipsing binaries with B-type MS primaries and low-mass pre-MS companions at $P = 3.0$ - 8.5 days by selecting systems with reflection effect amplitudes $\Delta I_{\rm refl} > 0.015$ mag, maximum eclipse widths $\Theta_{\rm max} < 0.03$, and ratios of eclipse depths $\Delta I_2/\Delta I_1 < 0.4$.

we select a binary with a primary mass M_1, mass ratio q, age τ, and dust extinction A_I. Based on our adopted evolutionary stellar tracks, we then determine the observed magnitude $\langle I \rangle$ and color $\langle V - I \rangle$ of the binary. If the magnitudes and colors do not satisfy our photometric selection criteria, we generate a new binary. Otherwise, we count its contribution toward our statistics of binaries with B-type MS primaries. For each of the four mass-ratio bins, we simulate $\mathcal{N}_{\rm sim} = 2{\times}10^4$ binaries that satisfy our magnitude and color criteria and therefore have B-type MS primaries.

For each of these binaries, we then select P, t_o, i, and A_2 according to their respective probability density functions. To be detectable as a detached, closely orbiting eclipsing binary, the system must be old enough so that the pre-MS companion neither fills its Roche lobe nor accretes from a thick circumstellar disk (see §3.2). Based on our observed systems (Table 3.2), we therefore require the companion Roche-lobe fill-factor to be $RLFF_2 < 80\%$ and the age $\tau > 0.5$ Myr. If these criteria are satisfied, we synthesize an eclipsing binary light curve with NIGHTFALL as in §3.3.2 according to our eight randomly generated physical model parameters. We note that we have implicitly assumed that the orbital periods of binaries do not significantly change between $\tau = 0.5$ Myr and the time $\tau \approx \tau_{\rm MS} \approx 25$ Myr until the primary fills its Roche lobe. It is possible, however, that subsequent dynamical interactions with a tertiary can harden the orbit of the inner binary (Kiseleva et al. 1998; Naoz & Fabrycky 2014). This may bring additional systems into our parameter space $P = 3.0$ - 8.5 days after the secondary has contracted into a MS star. Hence, we can only measure the fraction of B-type MS stars with close, low-mass companions at 0.5 Myr $\lesssim \tau \lesssim 0.4\ \tau_{\rm MS} \approx 10$ Myr. The binary fraction at earlier or later epochs may be different.

We now ensure our synthesized light curve matches the cadence and precision of

the OGLE-III LMC observations. We therefore interpolate our theoretical NIGHTFALL eclipsing binary light curve at $\mathcal{N}_I = 470$ randomly selected orbital phases. Obviously, the total photometric errors increase toward fainter systems. We relate the I-band photometric error to the I-band magnitude according to the following:

$$\sigma_{\rm fit}(I) = \left[1 + 10^{(I-17.0)/2}\right] \times 0.0072\,{\rm mag}. \tag{3.10}$$

This simple formula fits the observed rms scatter in the eclipsing binary light curves as discussed in §3.2.1 (see black curve in Fig. 3.2). For each I-band value in our synthesized light curve, we add random Gaussian noise according to Eq. 3.10.

We then fit our analytic model of Gaussians and sinusoids (Eq. 3.3) to this simulated I-band light curve by implementing the same Levenberg-Marquardt technique in §3.2.1. To ensure automated and fast convergence toward the true solution, we choose initial model parameters motivated by the properties of the eclipsing binary. For example, because we only synthesize eclipsing binaries with circular orbits in our Monte Carlo simulations, we select $\Phi_2 = 0.5$ as the initial estimates in our analytic models. In this manner, for each synthetic eclipsing binary generated by NIGHTFALL, we measure the analytic model parameters, e.g. ΔI_1, Θ_1, $\Delta I_{\rm refl}$, etc., and their respective errors.

To be considered an eclipsing binary with observable reflection effects, we impose the same selection criteria as in §3.2. The reflection effect amplitude must be $\Delta I_{\rm refl} > 0.015$ mag with a 1σ error that is <20% the actual value. We require the uncertainties in the eclipse depths ΔI_1 and ΔI_2 and eclipse widths Θ_1 and Θ_2 to be <25% their respective values. The full light curve amplitude $\Delta I = \Delta I_1 + \Delta I_{\rm refl}$ must be deep enough to be detectable by the OGLE-III LMC survey according to Eq. 3.6. Finally, the

maximum eclipse width $\Theta_{\rm max} < 0.03$ and ratio of eclipse depths $\Delta I_2/\Delta I_1 < 0.4$ need to satisfy our selected parameter space as shown in Fig. 3.3. If the synthetic light curve satisfies all these properties, then it contributes toward the number $\mathcal{N}_{\rm refl}$ of eclipsing binaries with reflection effects.

3.5.4 Results

We generated a total of $4 \times \mathcal{N}_{\rm sim} = 8{\times}10^4$ eclipsing binaries with B-type MS primaries, low-mass companions $q = 0.06$ - 0.40, and magnitudes and colors that satisfy our photometric selection criteria. Of these simulated systems, only $\mathcal{N}_{\rm refl} = 468$ eclipsing binaries have the necessary ages and orientations to produce detectable reflection effects and eclipses. We compare the properties of these $\mathcal{N}_{\rm refl} = 468$ eclipsing binaries from our Monte Carlo simulations to our 22 observed systems in Fig. 3.11. In the left panel, we can see that larger reflection effect amplitudes dictate younger relative ages $\tau/\tau_{\rm MS}$ for both the observed and simulated populations. The only system that noticeably deviates from this trend is ID-18330, which has a moderate reflection effect $\Delta I_{\rm refl} = 0.056$ and older relative age $\tau/\tau_{\rm MS} = 0.42$. We note that ID-18330 has a large intrinsic V-band scatter $f_{\sigma,V} = 3.0$ and a modest fit statistic $\chi^2/\nu = 1.16$, so that the systematic error in our measured age for this system is larger than usual. In any case, ID-18330 is relatively bright $\langle I \rangle = 16.1$, which requires a massive primary $M_1 \approx 15\,{\rm M}_\odot$. Hence, ID-18330 has a large relative age $\tau/\tau_{\rm MS} = 0.42$ mainly because the massive primary is short-lived with $\tau_{\rm MS} \approx 13\,{\rm Myr}$. We therefore expect the majority of eclipsing binaries with $\tau/\tau_{\rm MS} > 0.2$ to have $\Delta I_{\rm refl} < 0.04$ mag, while only the few systems with short-lived, massive primaries $M_1 \gtrsim 14\,{\rm M}_\odot$ can have $\Delta I_{\rm refl} \approx 0.04$ - 0.06 mag at these older relative ages.

In the right panel of Fig. 3.11, we compare the maximum eclipse depths $\Theta_{\rm max}$ versus the ratio of eclipse depths $\Delta I_2/\Delta I_1$ for our 468 simulated and 22 observed eclipsing binaries. Both the observed and simulated systems cluster near $\Theta_{\rm max} = 0.017$ and $\Delta I_2/\Delta I_1 = 0.2$. As discussed in §3.2, the pre-MS companions are detached from their Roche lobes and have low luminosities, which require $\Theta_{\rm max} < 0.3$ and $\Delta I_2/\Delta I_1 < 0.4$, respectively. Only the three systems at the top with $0.3 < \Delta I_2/\Delta I_1 < 0.4$ are marginally discrepant with the simulated population. Two of these, ID-1965 and ID-6630, have reflection effect amplitudes $\Delta I_{\rm refl} = 0.017$ - 0.019 mag just above our detection limit of $\Delta I_{\rm refl} = 0.015$ mag and companion properties that are consistent with the zero-age MS (see Fig. 3.6). If we had assumed a detection limit of $\Delta I_{\rm refl} = 0.012$ mag in our Monte Carlo simulations, we would have synthesized an additional ≈15% of reflecting eclipsing binaries. The majority of these additional systems would have occupied the upper-right portion in the right panel of Fig. 3.11, consistent with ID-1965 and ID-6630. The other eclipsing binary, ID-17217, that is slightly discrepant with the simulated population has a slightly asymmetric light curve profile between eclipses (see Fig. 3.5). This asymmetry is most likely due to an eccentric orbit, as indicated by the phase of the secondary eclipse $\Phi_2 = 0.490$. However, the slight asymmetry could also be caused by a disk or hot spot, similar to other systems we observed with $\Delta I_2/\Delta I_1 > 0.4$ (see Fig. 3.3). Even if this one system is a contaminant in our sample, it has a negligible effect on our statistics. Most importantly, the 19 observed eclipsing binaries with $\Delta I_2/\Delta I_1 < 0.3$ match the simulated population and clearly have young, low-mass companions.

We present the statistics of our Monte Carlo simulations in Table 3.5. For each of our four mass-ratio intervals, we report the number $\mathcal{N}_{\rm obs}$ of observed systems in our sample, the number $\mathcal{N}_{\rm refl}$ of simulated systems that exhibit reflection effects, the

probability of observing reflection effects $\mathcal{P}_{\rm refl} = \mathcal{N}_{\rm refl}/\mathcal{N}_{\rm sim}$ where $\mathcal{N}_{\rm sim} = 2{\times}10^4$, and the intrinsic binary fraction $F = (\mathcal{N}_{\rm obs}\,\mathcal{F}_{\rm Opik})\,/\,(\mathcal{N}_{\rm B}\,\mathcal{P}_{\rm refl})$ where $\mathcal{F}_{\rm Opik} = 1.23$ and $\mathcal{N}_{\rm B}$ = 174,000. As expected, $\mathcal{P}_{\rm refl} \approx 0.8\%$ is largest for systems with $q = 0.10$ - 0.25. The probability $\mathcal{P}_{\rm refl} \approx 0.3\%$ quickly diminishes toward larger mass ratios because the pre-MS timescales of more massive companions are markedly shorter. Even though lower mass companions $q = 0.06$ - 0.10 have longer pre-MS evolutions, the probability $\mathcal{P}_{\rm refl} \approx 0.5\%$ of observing eclipses and reflection effects is low because the radii of the companions are systematically smaller (see Figs. 3.4 and 3.6).

In the bottom row of Table 3.5, we combine the statistics for our three smallest mass-ratio bins. For our observed sample of 19 eclipsing binaries in this interval, the relative error from Poisson statistics is 23%. We expect a systematic error of 15% due to uncertainties in our light curve modeling. For example, the few systems with $q =$ 0.20 - 0.25 could easily shift toward solutions with $q > 0.25$ outside our defined interval of extreme mass ratios. We also estimate a 10% systematic error due to third light contamination and the possibility of mimics in our sample. For example, ID-5898 may have $q < 0.25$ and should therefore be added to our statistics (see §3.3), while ID-17217 may host a disk and/or hot spot and therefore should be removed from our statistics (see above). Finally, the correction factor $\mathcal{F}_{\rm Opik}$ due to the Öpik effect is uncertain by 10%. We add all these sources of error in quadrature, and find the total relative error in our binary statistics is ≈30%. Therefore, $F = (2.0 \pm 0.6)\%$ of young B-type MS stars have low-mass companions $q = 0.06$ - 0.25 with short orbital periods $P = 3.0$ - 8.5 days. This result from our detailed Monte Carlo simulation is consistent with our simple estimate of $F \approx 1.7\%$. The selection effects are therefore well understood and the probability of observing reflection effects is robust.

Table 3.5. Results of Monte Carlo simulation.

$\log q$	q	$\mathcal{N}_{\rm obs}$	$\mathcal{N}_{\rm refl}$	$\mathcal{P}_{\rm refl}$ (%)	F (%)
-1.2 - -1.0	0.06 - 0.10	5	92	0.46	0.77 ± 0.34
-1.0 - -0.8	0.10 - 0.16	8	156	0.78	0.73 ± 0.26
-0.8 - -0.6	0.16 - 0.25	6	167	0.84	0.51 ± 0.21
-0.6 - -0.4	0.25 - 0.40	2	53	0.26	0.53 ± 0.37
-1.2 - -0.6	**0.06 - 0.25**	**19**	**415**	**0.69**	$\mathbf{2.0 \pm 0.6}$

3.6 Discussion

3.6.1 Binary Statistics

The close binary fraction of MS stars has long been understood to increase with primary mass (Abt 1983; Duquennoy & Mayor 1991; Raghavan et al. 2010; Sana et al. 2012; Duchêne & Kraus 2013). This correlation between the close binary fraction and spectral type has been primarily based on observations of moderate mass-ratio companions with $q \gtrsim 0.25$. In Fig. 3.12, we show the binary star fraction across orbital periods $P = 3.0$ - 8.5 days as a function of mass ratio q for solar-type primaries (Grether & Lineweaver 2006), B-type primaries (Wolff 1978; Levato et al. 1987; Abt et al. 1990), and O-type primaries (Sana et al. 2012). About 1.0% of solar-type stars have companions with moderate mass ratios $q > 0.25$ and short orbital periods $P = 3.0$ - 8.5 days. This increases to $\approx 3.8\%$ for B-type MS stars, and up to $\approx 14\%$ for O-type stars. Hence, the close binary fraction at moderate mass ratios $q > 0.25$ increases by a factor of ≈ 4 between $M_1 \approx 1\,{\rm M}_\odot$ solar-type primaries and $M_1 \approx 10\,{\rm M}_\odot$ B-type MS primaries.

As discussed in §3.1, SB1s with early-type MS primaries may have companions that are evolved stellar remnants (Wolff 1978; Garmany et al. 1980). We can therefore

not reliably infer the frequency of extreme mass-ratio stellar companions from early-type spectroscopic binaries. The companions in our reflecting eclipsing binaries are unambiguously low-mass, unevolved, pre-MS stars. After correcting for geometrical and evolutionary selection effects (§3.5), we found that $(2.0 \pm 0.6)\%$ of young B-type MS stars have companions with $q = 0.06$ - 0.25 and $P = 3.0$ - 8.5 days. Considering 3.8% of B-type MS stars have companions with $q > 0.25$ across the same period range, then extreme mass-ratio companions $q = 0.06$ - 0.25 constitute one-third of close stellar companions to B-type MS stars. This result indicates the majority of SB1s with B-type MS primaries contain low-mass stellar companions. This is in disagreement with Wolff (1978), who suggested SB1s with late-B MS primaries most likely contain white dwarf companions.

For solar-type MS primaries $M_1 \approx 1\,\mathrm{M}_\odot$, low-mass companions $M_2 \approx 0.1$ - $0.2\,\mathrm{M}_\odot$ are almost certainly low-mass M-dwarfs (Duquennoy & Mayor 1991; Halbwachs et al. 2000). In a sample of 2,001 spectroscopic binaries with solar-type MS primaries (Grether & Lineweaver 2006), only 4 (0.2%) had companions with $P = 3.0$ - 8.5 days and $q \approx 0.08$ - 0.25. We found that $(2.0 \pm 0.6)\%$ of B-type MS stars have stellar companions across the same mass-ratio and period interval, which is a factor of $\approx$10 times larger (Fig. 3.12). The frequency of close, extreme-mass ratio companions increases with primary mass even more dramatically than the overall close binary fraction.

We can also interpret this trend according to differences in the intrinsic mass-ratio probability distribution p_q. The mass-ratio distribution is typically described by a power-law $p_q \propto q^\gamma\, dq$. For close companions to solar-type MS stars, the mass-ratio distribution across $0.08 < q < 1.0$ is close to uniform, i.e. $\gamma = 0.1 \pm 0.2$ (Grether & Lineweaver 2006; Raghavan et al. 2010). By combining the statistics of eclipsing binaries and SB2s with B-type MS primaries, we measure $\gamma = -0.7 \pm 0.3$ across the broad interval

$0.07 < q < 1.0$ (Fig. 3.12). This is consistent with our previous measurement of $\gamma =$

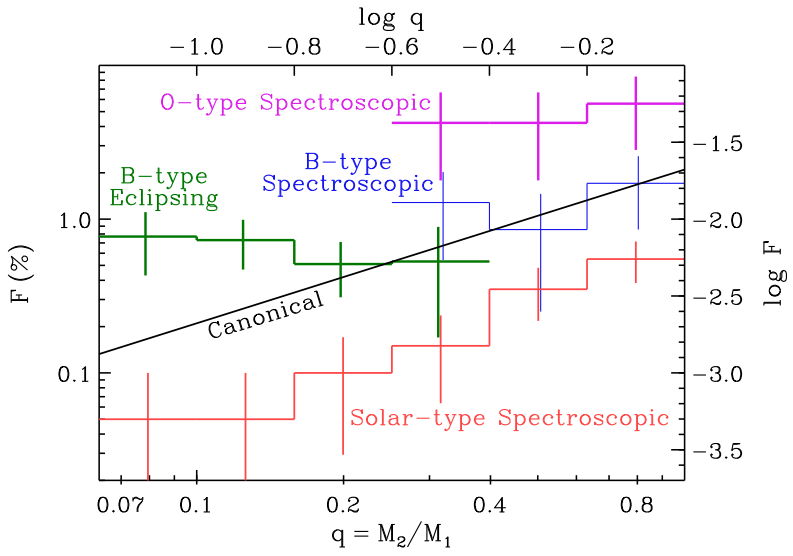

Figure 3.12: The fraction F of MS primaries that have stellar companions with orbital periods $P = 3.0$ - 8.5 days divided into $d\log q = 0.2$ intervals. In a spectroscopic survey of 71 O-type stars (magenta; Sana et al. 2012) and combined sample of 234 B-type stars (blue; Wolff 1978; Levato et al. 1987; Abt et al. 1990), 10 (14%) and 9 (3.8%), respectively, were identified as double-lined spectroscopic binaries in our period range with dynamically measured mass ratios $q > 0.25$. Utilizing eclipsing binaries is the only way of accurately measuring the intrinsic frequency of low-mass unevolved stellar companions to B-type MS stars (green). In a survey of 2,001 solar-type primaries (Grether & Lineweaver 2006), only 25 (1.2%) were found to be spectroscopic binaries in our period range with mass functions that indicate a stellar secondary companion with $q > 0.08$ (red). Population synthesis studies of close binaries canonically assume a uniform mass-ratio distribution (Kiel & Hurley 2006; Ruiter et al. 2011; Claeys et al. 2014), i.e. flat in *linear* q, according to $dF = 0.1\, dq\, d\log P$ (black).

-0.8 ± 0.3 in Moe & Di Stefano (2013) for close companions ($P = 2$ - 20 days) to B-type MS stars. In Moe & Di Stefano (2013), however, we used only the primary eclipse depth distribution of eclipsing binaries to recover the intrinsic mass-ratio distribution. In the present study, we have directly measured the physical properties of companions with extreme mass ratios $q = 0.07$ - 0.25. Not only does the close binary fraction increase with primary mass, but the mass-ratio distribution also becomes weighted toward smaller values (see also Duchêne & Kraus 2013, and references therein).

3.6.2 Binary Formation

The dearth of short-period, low-mass companions to solar-type MS stars has been investigated in previous spectroscopic binary surveys (Duquennoy & Mayor 1991; Halbwachs et al. 2003; Raghavan et al. 2010). In fact, there appears to be a complete absence of close $q \approx 0.02$ - 0.08 companions to solar-type MS stars, commonly known as the brown dwarf desert (Halbwachs et al. 2000; Grether & Lineweaver 2006). This is most likely because such low-mass companions would have migrated inward during their formation in the circumstellar disk and subsequently merged with the primary (Armitage & Bonnell 2002). For luminous and massive B-type MS primaries, however, the circumstellar disk quickly photoevaporates within $\tau \lesssim 0.3$ Myr (Alonso-Albi et al. 2009). Moreover, B-type MS stars with $q \approx 0.1$ companions have ≈10 times more mass and orbital angular momenta than their solar-type counterparts. Our nascent eclipsing binaries demonstrate that the rapid disk photoevaporation timescales and larger orbital angular momenta of more massive binaries can allow an extreme mass-ratio system to stabilize into a short orbit without necessarily merging.

As discussed in §3.1, there is a body of work indicating that components in close binaries coevolved via fragmentation and competitive accretion in the circumbinary disk (Bate & Bonnell 1997; Bate et al. 2002; Bonnell & Bate 2005; Kratter & Matzner 2006). Coevolution preferentially leads to binary component masses that are correlated. The rapid disk photoevaporation timescales around more massive stars suggest competitive accretion may be less significant. It is therefore plausible that less efficient competitive accretion in early-type systems can naturally produce close binaries with extreme mass ratios. This would be consistent with the measured mass-ratio distribution of close early-type binaries, which favors extreme mass ratios more readily than that observed for solar-type binaries.

It is also possible that extreme mass-ratio binaries require a different formation mechanism. The low-mass pre-MS companions in our eclipsing binaries are quite large with moderate Roche-lobe fill-factors $30\% < RLFF_2 < 80\%$. Tidal dissipation of orbital energy and angular momentum in a pre-MS star with a large convective envelope is orders of magnitude more efficient than in a MS star (Zahn & Bouchet 1989a). Binary formation via tidal capture of low-mass companions may be substantially more efficient than previously realized (Press & Teukolsky 1977; Moeckel & Bally 2007) if one accounts for the long pre-MS timescales of the low-mass secondaries. Additionally, the pre-MS companions may have been captured with the assistance of dynamical perturbations from an outer tertiary via Kozai cycles and tidal friction (Kiseleva et al. 1998; Naoz & Fabrycky 2014). In any case, future formation models of massive stars and close binaries must readily produce these kinds of systems on rapid timescales.

3.6.3 Binary Evolution

Given the short orbital periods $P < 10$ days of our 22 systems, we expect these binaries will eventually coalesce as the primary evolves off the MS. Low-mass X-ray binaries and millisecond pulsars that form in the galactic field (Kalogera & Webbink 1998; Kiel & Hurley 2006) as well as Type Ia supernovae that explode in elliptical galaxies (Whelan & Iben 1973; Ruiter et al. 2011) can derive from B-type MS primaries with low-mass companions $q \approx 0.1$ - 0.3 at slightly longer orbital periods $P \approx 10^2$ - 10^3 days. These binary population synthesis studies canonically assume a uniform mass-ratio distribution, i.e. $\gamma = 0$, normalized to 0.1 companions per primary per decade of orbital period (Fig. 3.12). We have shown that low-mass companions $q < 0.25$ to B-type MS stars at short orbital periods $P < 10$ days not only survive, but are found in abundance and constitute one-third of such close companions (i.e., $\gamma \approx -0.7$).

Photometrically resolved companions to early-type MS stars with $P \gtrsim 10^5$ days are generally weighted toward even smaller mass ratios (Preibisch et al. 1999; Shatsky & Tokovinin 2002; Peter et al. 2012). These wide companions to early-type stars may have formed relatively independently from the primaries, and may therefore have a mass-ratio distribution exponent $\gamma = -2.35$ that is consistent with random pairings from a Salpeter IMF (Abt et al. 1990; Duchêne et al. 2001).

If we interpolate between these two regimes, then we may expect low-mass companions to early-type stars to be plentiful at moderate orbital periods. Hence, there may be more progenitors of low-mass X-ray binaries, millisecond pulsars, and Type Ia supernovae than originally assumed. We intend to confirm this conjecture by investigating the properties of massive binaries at intermediate orbital separations.

Specifically, we are in the process of characterizing OGLE-III LMC eclipsing binaries with B-type MS primaries and $P > 20$ days (Moe et al., in prep.).

3.7 Summary

1. *New Class of Eclipsing Binaries.* We analyzed the light curves of 2,206 systems in the OGLE-III LMC eclipsing binary catalog (Graczyk et al. 2011) with B-type MS primaries and orbital periods $P = 3$ - 15 days (§3.2.1). We discovered a subset of 22 detached eclipsing binaries with short orbital periods ($P = 3.0$ - 8.5 days) that exhibit substantial reflection effects ($\Delta I_{\rm refl} = 0.017$ - 0.138 mag) and moderate to deep primary eclipses ($\Delta I_1 = 0.09$ - 2.8 mag). Because such deep eclipses and prominent reflection effects require the secondaries to be comparable in size to the primaries ($R_2/R_1 > 0.3$) but markedly cooler ($T_2/T_1 < 0.4$), we concluded the companions in these 22 eclipsing binaries are large, cool, low-mass pre-MS stars (§3.2.2).

   Similar irradiation effects have been observed in evolved binaries that contain a hot, low-luminosity, compact remnant in an extremely short orbit ($P \lesssim 1$ day) with a late-type MS companion (§3.2.3). Previous observations of young MS + pre-MS eclipsing binaries have been limited to large mass ratios $q \gtrsim 0.5$, low-mass primaries $M_1 \lesssim 3\,{\rm M}_\odot$, and/or systems that are still accreting from a circumbinary disk (§3.2.3). Hence, our 22 eclipsing binaries constitute a new class of nascent eclipsing binaries in which a detached, non-accreting, low-mass pre-MS companion discernibly reflects much of the light it intercepts from the B-type MS primary. We have not yet observed the precise counterparts to these systems in our own Milky Way galaxy, primarily because our sample of continuously monitored $\mathcal{N}_{\rm B} = 174{,}000$ B-type MS stars in the

OGLE-III LMC dataset (Udalski et al. 2008) is two orders of magnitude larger than previous surveys.

2. *Physical Model Fits.* For detached eclipsing binaries with MS primaries and known distances, we can utilize stellar evolutionary tracks to estimate the ages τ and component masses M_1 and M_2 based solely on the observed photometric light curves (§3.3.1 - 3.3.2). For the 18 definitive MS + pre-MS eclipsing binaries, we measured primary masses $M_1 = 6$ - $16\,M_\odot$, secondary masses $M_2 = 0.8$ - $2.4\,M_\odot$ ($q = 0.07$ - 0.36), and ages $\tau = 0.6$ - 8 Myr (§3.3.3). We investigated multiple sources of systemic uncertainties and performed various consistency checks (§3.3.4). Our conclusions that the majority of our reflecting eclipsing binaries have pre-MS companions with extreme mass ratios $q < 0.25$ and young ages $\tau < 8$ Myr are robust.

3. *Association with H II Regions.* Relative to our total sample of 2,206 B-type MS eclipsing binaries, the coordinates of our 22 reflecting eclipsing binaries are correlated with the positions of star-forming H II regions at the 4.1σ significance level (§3.3.4). In addition, our youngest eclipsing binaries with deeper eclipses and larger reflection effect amplitudes are more likely to be associated with bright and/or compact H II regions. These statistics and correlations: (1) reinforce our conclusions that our reflecting eclipsing binaries contain young, low-mass, pre-MS companions, (2) demonstrate the reliability of our eclipsing binary models, and (3) provide powerful diagnostics for the expansion velocities $\langle v \rangle_{\rm H\,II} \approx 10$ - 30 km s^{-1} and long-term dynamical evolution of H II regions.

4. *Intrinsic Close Binary Statistics.* We performed detailed Monte Carlo simulations to generate synthetic light curves for a large population of eclipsing binaries

(§3.5.1 - 3.5.3). Only $\mathcal{P}_{\rm refl} \approx 0.7\%$ of B-type MS stars with low-mass companions have the necessary ages and orientations to produce detectable eclipses and reflection effects (§3.5.4). Hence, $F = (2.0 \pm 0.6)\%$ of B-type MS stars have companions with extreme mass ratios $q = 0.06$ - 0.25 and short orbital periods $P = 3.0$ - 8.5 days. This is ≈10 times larger than that observed around solar-type MS stars in the same period and mass-ratio interval (§3.6.1). Our analysis represents the first direct measurement for the fraction of B-type MS stars with close, low-mass, non-degenerate stellar companions.

5. *Implications for Binary Formation.* The lack of close extreme mass-ratio companions to solar-type MS stars, commonly known as the brown dwarf desert, is probably because such companions migrated inward at the time of formation in the circumbinary disk and merged with the primary (Armitage & Bonnell 2002). Because massive binaries have rapid disk photoevaporation timescales and larger orbital angular momenta, our extreme mass-ratio eclipsing binaries could therefore stabilize into short orbits without merging (§3.6.2). Close binaries with extreme mass ratios may have formed either through: (1) less efficient competitive accretion in the circumbinary disk (Bate & Bonnell 1997), (2) tidal capture while the secondary is still a large, convective pre-MS star (Press & Teukolsky 1977; Moeckel & Bally 2007), and/or (3) Kozai cycles with a tertiary component and subsequent tidal friction between the inner B-type MS + low-mass pre-MS inner binary (Kiseleva et al. 1998).

6. *Implications for Binary Evolution.* B-type MS stars with closely orbiting low-mass companions $q = 0.1$ - 0.3 can evolve to produce Type Ia supernovae, low-mass X-ray binaries, and millisecond pulsars (Kiel & Hurley 2006; Ruiter et al. 2011). We find more close, low-mass companions to B-type MS stars than is typically assumed in

binary population synthesis (§3.6.3). If this result holds at slightly longer orbital periods, we anticipate more progenitors of Type Ia supernovae and low-mass X-ray binaries than originally predicted.

Chapter 4

Early-type Eclipsing Binaries with Intermediate Orbital Periods

This thesis chapter has recently been accepted as

M. Moe & R. Di Stefano, *The Astrophysical Journal*, 2015

Abstract

We analyze 221 eclipsing binaries (EBs) in the Large Magellanic Cloud with B-type main-sequence (MS) primaries ($M_1 \approx 4$ - 14 $M_\odot$) and orbital periods $P = 20$ - 50 days that were photometrically monitored by the Optical Gravitational Lensing Experiment. We utilize our three-stage automated pipeline to (1) classify all 221 EBs, (2) fit physical models to the light curves of 130 detached well-defined EBs from which unique parameters can be determined, and (3) recover the intrinsic binary statistics by correcting for selection effects. We uncover two statistically significant trends with age. First, younger

EBs tend to reside in dustier environments with larger photometric extinctions, an empirical relation that can be implemented when modeling stellar populations. Second, younger EBs generally have large eccentricities. This demonstrates that massive binaries at moderate orbital periods are born with a Maxwellian "thermal" orbital velocity distribution, which indicates they formed via dynamical interactions. In addition, the age-eccentricity anticorrelation provides a direct constraint for tidal evolution in highly eccentric binaries containing hot MS stars with radiative envelopes. The intrinsic fraction of B-type MS stars with stellar companions $q = M_2/M_1 > 0.2$ and orbital periods $P = 20\text{-}50$ days is $(7 \pm 2)\%$. We find early-type binaries at $P = 20\text{-}50$ days are weighted significantly toward small mass ratios $q \approx 0.2\text{-}0.3$, which is different than the results from previous observations of closer binaries with $P < 20$ days. This indicates that early-type binaries at slightly wider orbital separations have experienced substantially less competitive accretion and coevolution during their formation in the circumbinary disk.

4.1 Introduction

It has long been understood that the main-sequence (MS) binary star fraction increases with primary mass (Abt 1983; Duquennoy & Mayor 1991; Fischer & Marcy 1992; Raghavan et al. 2010; Duchêne & Kraus 2013, etc.). Indeed, most massive stars with $M_1 > 10\,\mathrm{M}_\odot$ will interact with a stellar companion before they explode as core-collapse supernovae (Sana et al. 2012). Throughout the decades, there have been significant advances in the detection of close and wide companions to massive stars (Wolff 1978; Garmany et al. 1980; Levato et al. 1987; Abt et al. 1990; Shatsky & Tokovinin 2002;

Kouwenhoven et al. 2007; Sana et al. 2012; Rizzuto et al. 2013; Kobulnicky et al. 2014). However, the intrinsic properties of binary companions to early-type primaries, e.g. their eccentricity and mass-ratio distributions, remain elusive at intermediate orbital periods. The major goal of this work is to help fill this particular portion of the parameter space.

Eclipsing binaries (EBs) offer a key to the accurate measurement of the binary properties of early-type stars. Large photometric surveys, such as the third phase of the Optical Gravitational Lensing Experiment (OGLE-III), have discovered tens of thousands of EBs (Graczyk et al. 2011; Pietrukowicz et al. 2013). These populations of EBs are orders of magnitude larger than previous binary samples. Despite the geometrical selection effects, we can still achieve large sample statistics to reliably infer the intrinsic binary fraction and properties at intermediate orbital periods. We emphasize that EBs can probe a unique portion of the binary parameter space unavailable to other observational techniques.

In Moe & Di Stefano (2013, hereafter Paper I), we incorporated OGLE catalogs of EBs in the Large and Small Magellanic Clouds (LMC and SMC, respectively) as well as Hipparcos observations of EBs in the Milky Way. We compared the close binary properties ($P < 20$ days) of early-B MS primaries in the three different galaxies. The Milky Way and SMC EB samples are too small to warrant an analysis of period-dependent binary properties. The OGLE-III LMC EB catalog (Graczyk et al. 2011), on the other hand, contains ≈ 5 - 40 times more systems, is relatively complete toward shallow eclipse depths, and includes the full I-band and V-band light curves.

In Moe & Di Stefano (2015a, hereafter Paper II), we developed a three-stage automated pipeline to analyze EBs with short orbital periods in the OGLE-III LMC

database. This pipeline (1) classifies EBs according to their light curve characteristics, (2) measures the intrinsic physical properties of detached EBs, e.g. ages and component masses, based on the observed radii and temperatures, and (3) recovers the intrinsic binary statistics by correcting for selection effects.

In the present study, we utilize EBs in the OGLE-III LMC database to measure the binary fraction, mass-ratio distribution, and eccentricity distribution of B-type MS stars with intermediate orbital periods $P = 20$ - 50 days. We organize the rest of this paper as follows. In §4.2, we define our selection criteria for identifying EBs with B-type MS primaries, intermediate orbital periods, and well-defined eclipse parameters. We next describe an automated procedure we developed to fit detailed physical models to the observed EB light curves, and we present our results for the physical properties of the individual EBs (§4.3). In §4.4, we explain the observed trends in the measured EB parameters, paying special attention to the empirical age-extinction and age-eccentricity anticorrelations. We then perform Monte Carlo simulations to quantify selection effects, and present our results for the corrected binary statistics (§4.5). We summarize our main results and conclusions in §4.6.

4.2 EB Selection and Classification (Stage I)

In Paper II, we developed a three-stage automated pipeline to fully analyze short-period EBs in the OGLE-III LMC database. In the present study, we adapt our routine to identify intermediate-period EBs with well-defined light curves (Stage I - this section), measure their physical properties (Stage II - §4.3), and correct for selection effects (Stage III - §4.5). EBs with intermediate orbital periods exhibit two major differences

that must be considered. First, the eclipse widths Θ_1 and Θ_2, which are expressed as a fraction of the orbital period P, become narrower with increasing orbital separation. Given the average number $\langle \mathcal{N}_I \rangle \approx 470$ of I-band measurements in the OGLE-III LMC survey (Graczyk et al. 2011), the light curves are not sufficiently sampled if either of the eclipse widths $\Theta < \langle \mathcal{N}_I \rangle^{-1} \approx 0.0021$ are too narrow. EBs with small MS components and long orbital periods $P \gtrsim 50$ days have narrow eclipses $\Theta \lesssim 0.002$, and are therefore not Nyquist sampled. This subsampling leads to detection incompleteness, issues with aliasing, and the inability to fully characterize their intrinsic physical properties. Hence, it is the finite cadence of the OGLE-III observations, *not* geometrical selection effects, that limits our present study of EBs to $P = 20$ - 50 days (see also Söderhjelm & Dischler 2005).

Second, the majority of early-type EBs at $P > 20$ days are in eccentric orbits. We must therefore adapt our physical models to simultaneously fit the eccentricity e and argument of periastron ω (§4.3). In addition, it is possible for an eccentric binary to have a certain combination of eccentricity, periastron angle, and inclination that is sufficiently offset from edge-on (e.g., $i \lesssim 86^{\rm o}$) so that there is only one eclipse per orbit. Indeed, there are many EBs with single eclipses in the OGLE-III LMC database (see below). Unfortunately, we cannot measure the physical properties of these systems. We therefore remove single-eclipse EBs from our well-defined sample, and we account for their removal when we correct for selection effects (see §4.5). In the following, we review our methods from Paper II, where we pay special attention to the nuances of EBs with intermediate orbital periods.

In this study, we select the $\mathcal{N}_{\rm B} \approx 96{,}000$ systems in the OGLE-III LMC catalog (Udalski et al. 2008) with mean magnitudes $16.0 < \langle I \rangle < 17.6$ and observed colors

$-0.25 < \langle V-I \rangle < 0.20$. Given the distance modulus $\mu = 18.5$ to the LMC (Pietrzyński et al. 2013) and typical dust reddenings $E(V-I) \approx 0.1$ - 0.3 mag toward hot young stars in the LMC (Zaritsky et al. 2004), these stars have luminosities and surface temperatures that correspond to B-type MS primaries. From this sample, we analyze the 221 systems that were identified as EBs with orbital periods $P = 20$ - 50 days (Graczyk et al. 2011). In Table 4.1, we list the OGLE-III LMC EB identification numbers, observed colors $\langle V-I \rangle$, and numbers of I-band measurements $\mathcal{N}_I$ for each of these 221 EBs.

As in Paper II, we measure the intrinsic rms scatter in the I-band light curve outside of eclipses for each EB. We then calculate the correction factor $f_{\sigma,I} \geq 1.0$, i.e. the ratio between the actual rms scatter and photometric uncertainties reported in the catalog. For each I-band measurement in an EB light curve, we multiply the listed photometric uncertainties by the correction factor $f_{\sigma,I}$ to determine the corrected uncertainties.

We classify EBs based on an analytic light curve model of two Gaussians with eight total free parameters. The orbital phase $0 \leq \phi < 1$ is determined by the time of observation and two model parameters: the orbital period P (in days) and epoch of primary eclipse minimum $t_{\rm o}$ (Julian date − 2450000). The six remaining analytic model parameters are the average I-band magnitude outside of eclipses $\langle I \rangle$, primary and secondary eclipse depths ΔI_1 and ΔI_2, primary and secondary eclipse widths Θ_1 and Θ_2, and the phase of secondary eclipse Φ_2. The analytic model of Gaussians is:

$$I_{\rm G}(\phi) = \langle I \rangle + \Delta I_1 \Big[\exp\Big(\frac{-\phi^2}{2\Theta_1^2} \Big) + \exp\Big(\frac{-(\phi-1)^2}{2\Theta_1^2} \Big) \Big] + \Delta I_2 \exp\Big(\frac{-(\phi-\Phi_2)^2}{2\Theta_2^2} \Big) \tag{4.1}$$

We fit this analytic model to each EB I-band light curve. Specifically, we utilize an automated Levenberg-Marquardt algorithm (MPFIT, Markwardt 2009) to minimize the $\chi^2_{\rm G}$ statistic. The MPFIT routine provides robust best-fit solutions and measurement uncertainties for the eight analytic model parameters. Some of the photometric measurements are clear outliers, so we clip up to $\mathcal{N}_{\rm c} \leq 2$ data points per light curve that exceed 4σ from the model. This results in $\nu = \mathcal{N}_I - \mathcal{N}_{\rm c} - 8$ degrees of freedom. For each EB, we report in Table 4.1 the eight fitted analytic model parameters and the fit statistics. Excluding the few EBs that exhibit variability or are evolved Roche-lobe filling systems (see below), the goodness-of-fit statistics $\chi^2_{\rm G}/\nu = 0.87$ - 1.16 indicate the analytic models can adequately describe the EB light curves.

We can measure the physical properties of EBs based solely on the observed photometric light curves (see §4.3) only if: (1) the binary components are detached from their Roche lobes, (2) the light curves have two well-defined eclipses, and (3) there is no superimposed variability. To be considered well-defined, we require that the 1σ uncertainties in the measured eclipse depths ΔI_1 and ΔI_2 and eclipse widths Θ_1 and Θ_2 are $<$20% their respective values. These criteria are not satisfied for 91 of the 221 EBs due to a variety of reasons, which we discuss below:

(A) No Secondary Eclipse. For 16 of our EBs, there is no evidence for a secondary eclipse. These EBs may have secondary eclipses that are too shallow and below the sensitivity of the OGLE-III LMC survey, or have eclipse widths that are too narrow and therefore not detected given the cadence of the observations. Most likely, the EBs have a certain combination of e, ω, and i as discussed above so that there is only one eclipse per orbit. We list these 16 systems in Category 1 of Table 4.1, and we show an example in panel A of Fig. 4.1.

(B) Uncertain. For 32 EBs, both eclipses are observed but one or more of their measured properties are uncertain by more than 20%. This is because one of the eclipses

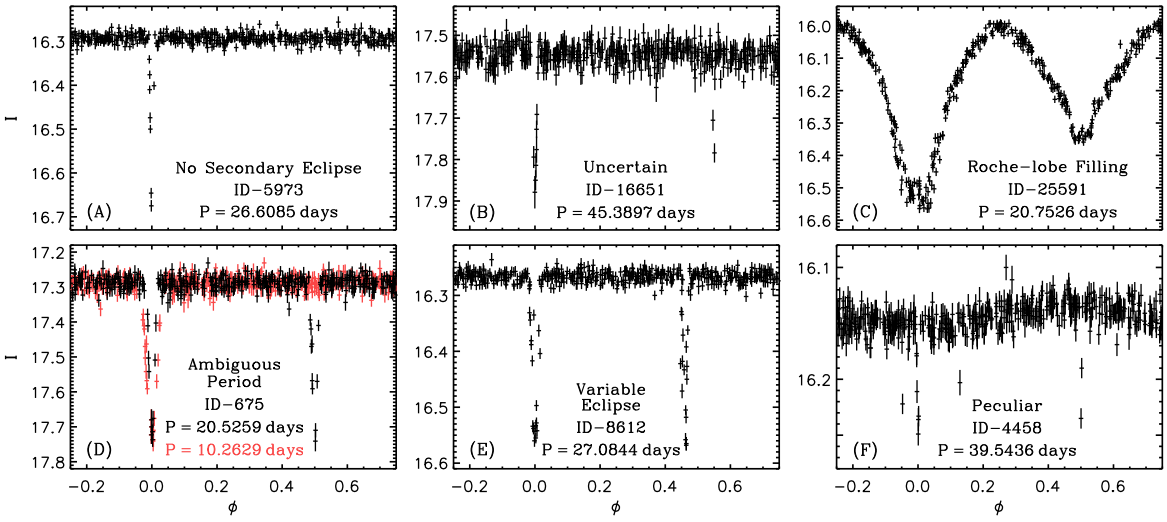

Figure 4.1: Six examples of the 91 EBs that have properties that are uncertain, variable, peculiar, etc., which leaves 130 EBs in our well-defined sample. Panel A: one of 16 EBs that does not have a visible secondary eclipse. Panel B: one of 32 EBs that show both eclipses but where one of them is too narrow and/or too shallow to be accurately measured. Panel C: one of the three EBs with wide eclipses that demonstrate one or both components fill their Roche lobes. Panel D: one of the 23 EBs with an ambiguous orbital period. Using the catalog orbital periods (black), these systems have nearly identical eclipses separated by almost precisely 50% in orbital phase. The more plausible scenario is that these EBs have half the listed orbital periods (red) and therefore exhibit one eclipse per orbit such as the example shown in panel A. Panel E: one of the 15 EBs that exhibit variability. Three of these systems are intrinsic variables. The other 12, such as the displayed example, show changes in the eclipse properties most likely caused by orbital motion with a tertiary companion. Panel F: one of the two EBs with peculiar light curve properties.

is too shallow and/or too narrow. We group these 32 systems in Category 2 of Table 4.1. In panel B of Fig. 4.1, we display an example of a long-period $P \approx 45$ day EB with a secondary eclipse at $\Phi_2 \approx 0.55$ that is too narrow to be accurately measured.

(C) Roche-lobe filling. Three EBs have wide eclipses such that one or both components of the binary must be filling their Roche lobes. We list these three systems in Category 3 of Table 4.1, and we show an example in panel C of Fig. 4.1.

(D) Ambiguous Periods. The orbital periods of 23 of our EBs are ambiguous. These 23 EBs can either have twin components $q \approx 1.0$ in nearly circular orbits $e \approx 0.0$ or have half the listed orbital periods and exhibit only one eclipse per very eccentric orbit. Using the orbital periods listed in the OGLE-III LMC catalog, these EBs have primary and secondary eclipses that are nearly identical and separated by almost precisely 50% in orbital phase. Quantitatively, we identify these systems to have values of and uncertainties in eclipse depths, widths, and phases that satisfy:

$$|\Delta I_1 - \Delta I_2| \leq 3\left[(\sigma_{\Delta I_1})^2 + (\sigma_{\Delta I_2})^2\right]^{1/2} \tag{4.2a}$$

$$|\Theta_1 - \Theta_2| \leq 3\left[(\sigma_{\Theta_1})^2 + (\sigma_{\Theta_2})^2\right]^{1/2} \tag{4.2b}$$

$$|\Phi_2 - 1/2| \leq 3\sigma_{\Phi_2} \tag{4.2c}$$

Given the sensitivity of the data, the observed properties imply the 23 systems have large mass ratios $q \gtrsim 0.9$ with extremely small eccentricities $e \lesssim 0.05$ (see §4.3). However, none of the EBs in our sample have eclipse depths that satisfy Eqn. 4.2a ($q \gtrsim 0.9$) with secondary eclipse phases $3\sigma_{\Phi_2} < |\Phi_2 - 1/2| \leq 10\sigma_{\Phi_2}$ ($e \approx 0.05$ - 0.10). Similarly, there is only one EB that satisfies Eqn. 4.2c ($e \lesssim 0.05$) with primary and secondary eclipse

depths that are discrepant at the (3 - 10)σ level ($q \approx 0.8$ - 0.9). Hence, there are no twin systems in slightly eccentric orbits, and there is only one moderate-mass companion in a nearly circular orbit. The prevalence of 23 twin systems in nearly circular orbits at these moderate orbital periods is therefore highly unlikely. If there is indeed an excess of twins in circular orbits relative to twins in eccentric orbits, our study does not include them. We expect only a few of the 23 EBs that appear to be twins in circular orbits to have the listed orbital periods. The majority of these EBs more likely have orbital periods that are half their listed values, and would therefore exhibit only one eclipse per orbit similar to the systems discussed in (A) above. In panel D of Fig. 4.1, we show one example where we fold the photometric data with the listed orbital period (in black) and the more plausible scenario that the binary has half the catalog orbital period (in red). We list these 23 EBs in Category 4 of Table 4.1. We further motivate the removal of these 23 systems in §4.4 when we show the intrinsic frequency of $q > 0.6$ companions with $e < 0.2$ is relatively sparse.

(E) Superimposed Variability. Fifteen of the EBs exhibit superimposed variability. Three of these systems are intrinsic variables, two of which (ID-7651 and ID-22929) were already listed as such in the OGLE-III LMC EB catalog. The intrinsic variability is readily apparent in the unfolded light curves. Moreover, the measured intrinsic scatter outside of eclipses is substantially higher than the photometric errors, e.g. $f_{\sigma,I} \approx 2.8$ for ID-3414. We note that a few additional systems with $f_{\sigma,I} \approx 1.5$ - 1.9 may exhibit low-amplitude variations $\delta I < 0.01$ mag, but these variations are sufficiently small so as to not to interfere with the light curve modeling. We list the three systems that exhibit definitive intrinsic variability in Category 5 of Table 4.1. The other 12 EBs exhibit variability in the eclipses themselves, only one of which (ID-17017) was identified as

such in the OGLE-III LMC catalog. For these systems, it is possible that more than two bad data points occur near the eclipse. More likely, these 12 EBs display changes in the eclipse depths and/or eclipse phases during the seven years of observations. Apsidal motion due to tidal and relativistic effects are negligible on timescales $dt \approx 7$ yrs at these wide orbital separations. Such evolution in the eclipse parameters are most likely caused by orbital motion with a tertiary component (Rappaport et al. 2013). We group these 12 EBs in Category 6 of Table 4.1, and we display an example in panel E of Fig. 4.1.

(F) Peculiar. Finally, two EBs have peculiar light curves. ID-343 exhibits a pronounced peak in the folded light curve at $\phi = 0.8$ between eclipses. This peak may be caused by ellipsoidal modulation in an extremely eccentric orbit. ID-4458, which is shown in panel F of Fig. 4.1, displays a sinusoidal variation between two eclipses of comparable depth. ID-4458 may contain a hot spot and/or disk, and is similar to the green systems in the top left corner of Fig. 3 in Paper II. We list these two systems in Category 7 of Table 4.1.

After removing these 91 systems, our well-defined sample contains 130 EBs. We list these 130 systems in Category 8 of Table 4.1. When necessary, we switch the primary and secondary eclipses to ensure $\Delta I_1 > \Delta I_2$ in our well-defined sample. If the epoch of primary eclipse minimum t_o substantially changed from the catalog value in order to satisfy this criterion, we place an asterisk next to our value of t_o in Table 4.1.

The 130 EBs in our well-defined sample have uncertainties in eclipse depths ΔI_1 and ΔI_2 and eclipse widths Θ_1 and Θ_2 that are $\lesssim$20% their respective values. The uncertainties in the Gaussian analytic fit parameters have been used only to determine which EBs have detectable and measurable eclipse properties. These uncertainties

propagate into our Monte Carlo simulations when we calculate the fraction of binaries that produce detectable eclipses (see §4.5). The uncertainties in the Gaussian analytic fit parameters are *not* utilized to calculate the uncertainties in the physical properties of the EBs. Instead, we implement detailed light curve models to measure the values of and uncertainties in the physical model properties, which we now discuss.

Table 4.1: Analytic model parameters that describe the basic light curve features for the 221 EBs with OGLE-III LMC catalog properties $16.0 < \langle I \rangle < 17.6$, $-0.25 < \langle V - I \rangle < 0.20$, and $P = 20$ - 50 days. Based on the measured analytic model parameters, we divide the total sample into eight categories: (1) EBs without secondary eclipses, (2) EBs with uncertain eclipse parameters, (3) Roche-lobe filling EBs, (4) EBs with ambiguous orbital periods, (5) intrinsic variables, (6) EBs with variable eclipses, (7) peculiar EBs, and (8) detached well-defined EBs. For each category, we list the OGLE-III LMC catalog properties (Graczyk et al. 2011) including the identification number, mean color $\langle V - I \rangle$, and number $\mathcal{N}_I$ of I-band measurements. We then list the eight best-fit analytic model parameters: orbital period P (days), epoch of primary eclipse minimum t_o (Julian date $-$ 2450000), mean magnitude $\langle I \rangle$, primary and secondary eclipse depths ΔI_1 and ΔI_2 (mag), orbital phase of secondary eclipse Φ_2, and eclipse widths Θ_1 and Θ_2 (fraction of the orbital period). Finally, we list the fit statistics, including the correction factor $f_{\sigma,I}$ in the photometric errors, number $\mathcal{N}_c$ of clipped data points, and goodness-of-fit statistic χ^2_G/ν.

Category 1: list of 16 EBs without visible secondary eclipses. These EBs most likely have a certain combination of e, ω, and i so there is only one eclipse per orbit.

Catalog Properties			Analytic Model Parameters								Fit Statistics		
ID	$\langle V-I \rangle$	$\mathcal{N}_I$	P	t_o	$\langle I \rangle$	ΔI_1	ΔI_2	Φ_2	Θ_1	Θ_2	$f_{\sigma,I}$	$\mathcal{N}_c$	χ^2_G/ν
316	0.01	211	24.9947	3538.528	17.34	0.22	-	-	0.0074	-	1.00	0	1.01
2164	−0.04	440	43.0029	3569.803	17.34	0.40	-	-	0.0029	-	1.09	1	1.01
3091	−0.08	424	27.4499	3602.602	17.14	0.21	-	-	0.0054	-	1.14	0	1.09
4652	0.02	445	23.7441	3572.959	16.61	0.10	-	-	0.0040	-	1.06	2	1.03
5548	−0.13	466	23.5235	3585.619	17.23	0.33	-	-	0.0027	-	1.09	0	1.02
5704	−0.12	421	25.2059	3566.122	16.25	0.18	-	-	0.0044	-	1.20	0	1.04
5973	−0.05	468	26.6085	3635.421	16.29	0.42	-	-	0.0039	-	1.20	0	1.08
9850	0.03	422	37.3082	3634.111	17.39	0.49	-	-	0.0025	-	1.11	1	1.03
12084	−0.03	477	29.8000	3588.434	16.90	0.18	-	-	0.0037	-	1.15	0	1.02
12913	−0.08	493	25.2768	3589.836	16.08	0.09	-	-	0.0050	-	1.23	0	1.04
13991	−0.02	449	30.6988	3592.784	17.16	0.41	-	-	0.0029	-	1.08	2	1.02
17232	−0.03	454	26.9222	3639.974	16.24	0.12	-	-	0.0023	-	1.37	2	1.07
21007	−0.04	367	33.7279	3600.454	16.40	0.09	-	-	0.0097	-	1.14	1	1.04
22467	−0.14	437	20.2896	3593.730	16.46	0.14	-	-	0.0028	-	1.06	0	1.03
23086	0.08	434	25.0090	3608.833	17.30	0.21	-	-	0.0017	-	1.09	0	1.02
25112	−0.04	391	39.9125	3581.880	16.07	0.09	-	-	0.0083	-	1.49	0	1.04

Category 2: list of 32 EBs with uncertain eclipse parameters. These EBs generally have eclipses that are too narrow ($\Theta \lesssim 0.003$) and/or too shallow ($\Delta I \lesssim 0.15$ mag) to be accurately measured.

Catalog Properties			Analytic Model Parameters								Fit Statistics		
ID	$\langle V-I \rangle$	$\mathcal{N}_I$	P	t_o	$\langle I \rangle$	ΔI_1	ΔI_2	Φ_2	Θ_1	Θ_2	$f_{\sigma,I}$	$\mathcal{N}_c$	χ^2_G/ν
219	0.01	405	49.9100	3626.670	17.53	0.42	0.56	0.390	0.0090	0.0011	1.00	1	0.99
1450	0.11	465	28.5096	3573.275	17.52	0.38	0.17	0.426	0.0045	0.0048	1.17	0	1.01
1924	0.06	464	31.0128	3607.649	16.89	0.25	0.09	0.651	0.0053	0.0070	1.15	0	1.00
2539	−0.06	457	38.1274	3585.424	17.07	0.14	0.13	0.756	0.0033	0.0021	1.03	1	1.02
2843	−0.05	440	26.0647	3599.963	17.57	0.17	0.46	0.746	0.0096	0.0013	1.07	0	0.98
3492	0.06	457	20.8220	3598.229	17.58	0.48	0.09	0.769	0.0033	0.0074	1.15	0	1.02
3745	0.03	225	26.5908	3575.121	17.58	0.41	0.53	0.527	0.0094	0.0015	1.11	0	1.08
4095	−0.05	432	33.9572	3615.866	17.39	0.19	0.15	0.936	0.0061	0.0022	1.14	2	1.00
4396	−0.03	358	25.3069	3598.022	17.14	0.14	0.09	0.542	0.0060	0.0059	1.20	1	1.10
5257	−0.02	463	35.1506	3575.663	17.29	0.16	0.07	0.472	0.0044	0.0036	1.05	2	0.99
6494	−0.12	421	45.3346	3623.790	16.96	0.18	0.14	0.606	0.0030	0.0017	1.25	0	1.01
7832	−0.07	476	26.6117	3613.760	17.35	0.12	0.06	0.468	0.0059	0.0016	1.05	0	1.02
7954	−0.05	435	27.1161	3606.847	17.25	0.20	0.32	0.709	0.0044	0.0030	1.11	1	1.00
8824	0.01	437	37.6744	3617.323	17.56	0.18	0.18	0.277	0.0052	0.0037	1.14	1	1.06
10248	−0.14	557	43.9229	3633.148	16.36	0.35	0.72	0.258	0.0047	0.0005	1.49	2	1.00
11655	−0.02	477	30.0005	3595.741	16.29	0.10	0.07	0.431	0.0056	0.0150	1.23	0	1.00
12065	−0.08	459	29.0408	3563.836	16.81	0.20	0.21	0.806	0.0048	0.0025	1.09	1	1.06
12202	−0.17	477	41.4788	3572.545	16.76	0.35	0.45	0.217	0.0048	0.0013	1.11	2	1.03
12696	−0.09	457	40.3637	3587.966	16.76	0.14	0.05	0.373	0.0050	0.0033	1.46	1	1.02
13076	−0.08	493	33.6509	3637.571	16.01	0.06	0.03	0.436	0.0036	0.0023	1.07	1	1.01
14307	0.01	540	22.3483	3601.494	17.58	0.12	0.23	0.290	0.0055	0.0041	1.00	1	1.01
16651	−0.10	449	45.3897	3684.769	17.54	0.34	0.69	0.549	0.0045	0.0015	1.06	0	1.02
16922	0.02	580	41.6338	3670.541	17.58	0.13	0.30	0.186	0.0037	0.0018	1.22	2	1.00
17204	−0.01	473	31.9060	3650.939	17.60	0.23	0.07	0.566	0.0032	0.0028	1.06	0	1.00
17262	−0.14	626	33.8546	3650.508	16.50	0.34	0.19	0.499	0.0014	0.0016	1.30	2	1.02
17957	−0.11	626	47.9194	3623.161	17.23	0.19	0.05	0.492	0.0030	0.0050	1.15	2	1.07
18800	0.03	470	22.0031	3582.822	17.47	0.26	0.17	0.325	0.0044	0.0050	1.10	0	1.02
20667	0.10	417	35.3260	3627.664	17.54	0.36	0.60	0.498	0.0022	0.0014	1.05	1	0.97
22464	−0.08	437	20.7824	3575.419	17.38	0.30	0.10	0.499	0.0034	0.0036	1.00	2	0.99
22512	0.08	437	25.1642	3588.758	17.41	0.22	0.25	0.484	0.0091	0.0440	1.31	0	0.99
22853	−0.10	430	23.4011	3637.436	16.94	0.19	0.06	0.398	0.0020	0.0049	1.12	1	1.02
23330	−0.02	414	43.4464	3616.771	16.94	0.26	0.35	0.529	0.0035	0.0029	1.28	0	1.01

Table 4.1 (cont.):

Category 3: list of 3 Roche-lobe filling EBs, as demonstrated by their wide eclipses $\Theta > 0.06$.

Catalog Properties			Analytic Model Parameters								Fit Statistics		
ID	$\langle V-I\rangle$	$\mathcal{N}_I$	P	t_o	$\langle I\rangle$	ΔI_1	ΔI_2	Φ_2	Θ_1	Θ_2	$f_{\sigma,I}$	$\mathcal{N}_c$	χ^2_G/ν
3864	−0.09	473	26.6937	3602.081	16.41	0.02	0.02	0.497	0.0640	0.0670	1.13	2	0.89
16199	−0.04	460	46.3408	3632.722	17.18	0.08	0.08	0.496	0.0609	0.0668	1.00	0	1.22
25591	0.18	423	20.7526	3588.389	16.01	0.52	0.31	0.503	0.0777	0.0856	1.41	2	3.61

Category 4: list of 23 EBs with ambiguous orbital periods. These systems have $\Delta I_1 \approx \Delta I_2$, $\Phi_2 \approx 0.5$, and $\Theta_1 \approx \Theta_2$ given the listed orbital periods. The majority of these EBs most likely have half the listed orbital periods, and therefore exhibit only one eclipse per orbit such as the systems listed in Category 1.

Catalog Properties			Analytic Model Parameters								Fit Statistics		
ID	$\langle V-I\rangle$	$\mathcal{N}_I$	P	t_o	$\langle I\rangle$	ΔI_1	ΔI_2	Φ_2	Θ_1	Θ_2	$f_{\sigma,I}$	$\mathcal{N}_c$	χ^2_G/ν
675	0.08	442	20.5259	3584.169	17.29	0.44	0.47	0.500	0.0079	0.0071	1.08	0	1.05
885	−0.04	456	23.5967	3564.996	17.31	0.33	0.33	0.500	0.0028	0.0027	1.15	0	1.01
1478	0.14	460	32.0021	3628.807	17.09	0.14	0.14	0.501	0.0020	0.0026	1.24	1	1.03
8321	0.00	467	34.8297	3643.253	17.12	0.11	0.11	0.502	0.0031	0.0025	1.05	2	1.02
8376	0.01	468	36.9128	3638.843	17.33	0.31	0.23	0.500	0.0025	0.0029	1.15	0	1.00
9146	−0.04	559	21.1796	3606.499	17.40	0.25	0.25	0.500	0.0023	0.0021	1.11	0	1.00
11930	−0.24	477	42.0006	3542.808	16.06	0.21	0.20	0.500	0.0012	0.0013	1.26	1	1.03
11931	0.06	493	24.6953	3569.815	16.67	0.27	0.29	0.500	0.0050	0.0048	1.11	0	1.05
14753	−0.01	600	22.4059	3580.305	17.41	0.29	0.30	0.500	0.0023	0.0024	1.16	1	1.02
15309	0.06	566	44.9548	3621.008	16.54	0.18	0.18	0.501	0.0029	0.0019	1.29	0	1.00
17257	−0.03	626	30.1341	3586.993	16.48	0.30	0.28	0.500	0.0016	0.0019	1.19	2	1.00
17407	−0.06	626	25.8992	3612.024	16.92	0.11	0.12	0.499	0.0053	0.0048	1.24	2	1.08
17715	−0.07	626	35.5355	3616.239	16.73	0.13	0.13	0.499	0.0022	0.0024	1.32	1	1.03
18138	0.12	601	42.9000	3599.789	16.92	0.39	0.38	0.500	0.0024	0.0024	1.23	0	1.03
19309	−0.09	612	32.1801	3593.017	16.13	0.08	0.09	0.500	0.0015	0.0018	1.34	0	1.01
19582	−0.11	473	20.0314	3608.284	16.59	0.08	0.10	0.498	0.0024	0.0026	1.15	1	1.03
19612	−0.01	605	20.8496	3616.468	17.14	0.46	0.41	0.500	0.0026	0.0029	1.18	0	1.03
19651	−0.06	473	26.4068	3598.679	16.83	0.25	0.19	0.499	0.0026	0.0034	1.20	1	0.99
20441	0.08	437	23.5402	3608.235	17.21	0.12	0.13	0.498	0.0042	0.0051	1.00	0	0.98
20661	0.07	436	20.5829	3618.710	17.41	0.15	0.13	0.499	0.0036	0.0045	1.16	0	0.99
21273	0.04	213	20.7646	3598.007	16.77	0.21	0.25	0.499	0.0031	0.0037	1.07	0	1.02
21477	−0.02	436	23.3476	3602.139	17.52	0.27	0.23	0.499	0.0044	0.0035	1.00	2	0.97
24604	−0.02	840	38.0192	3591.216	17.04	0.21	0.17	0.500	0.0028	0.0033	1.34	0	0.99

Category 5: list of 3 EBs that are intrinsic variables, as indicated by their large rms scatter $f_{\sigma,I} \gtrsim 1.6$.

Catalog Properties			Analytic Model Parameters								Fit Statistics		
ID	$\langle V-I\rangle$	$\mathcal{N}_I$	P	t_o	$\langle I\rangle$	ΔI_1	ΔI_2	Φ_2	Θ_1	Θ_2	$f_{\sigma,I}$	$\mathcal{N}_c$	χ^2_G/ν
3414	−0.12	479	38.9097	3607.475	17.02	0.40	0.50	0.897	0.0041	0.0021	2.78	0	1.02
7651	−0.01	435	34.8819	3595.802	16.64	0.14	0.12	0.267	0.0075	0.0038	2.25	0	0.99
22929	−0.06	764	26.4805	3597.217	16.63	0.26	0.22	0.772	0.0068	0.0064	1.56	2	1.06

Category 6: list of 12 EBs with variable eclipses. These EBs either have more than $\mathcal{N}_c > 2$ bad data points near the eclipses or, more likely, exhibit variations in the eclipse parameters due to orbital motion with a tertiary companion.

Catalog Properties			Analytic Model Parameters								Fit Statistics		
ID	$\langle V-I\rangle$	$\mathcal{N}_I$	P	t_o	$\langle I\rangle$	ΔI_1	ΔI_2	Φ_2	Θ_1	Θ_2	$f_{\sigma,I}$	$\mathcal{N}_c$	χ^2_G/ν
3112	−0.12	456	20.8143	3569.074	16.96	0.23	0.33	0.498	0.0023	0.0012	1.07	2	1.16
3233	−0.10	476	32.8948	3573.927	16.66	0.15	0.11	0.272	0.0039	0.0038	1.34	2	1.02
7992	0.16	858	49.8658	3624.125	16.75	0.21	0.09	0.477	0.0052	0.0005	1.35	2	1.06
8612	0.02	476	27.0844	3607.949	16.27	0.30	0.26	0.462	0.0079	0.0054	1.08	2	2.82
12973	−0.07	605	30.8419	3590.014	16.69	0.20	0.15	0.511	0.0045	0.0060	1.30	2	1.63
12987	0.02	493	25.9121	3584.179	17.41	0.18	0.13	0.363	0.0034	0.0065	1.03	2	1.08
14083	0.01	577	29.9824	3583.922	17.51	0.19	0.20	0.657	0.0054	0.0045	1.31	2	1.03
17017	−0.10	606	25.7548	3637.727	16.29	0.12	0.11	0.519	0.0041	0.0007	1.20	2	1.10
18037	0.00	433	31.5140	3563.204	17.00	0.45	0.36	0.573	0.0047	0.0063	1.06	2	1.46
19353	0.02	437	22.2690	3587.215	17.14	0.27	0.34	0.448	0.0077	0.0058	1.01	2	1.24
20313	0.04	369	27.7087	3602.991	16.40	0.37	0.59	0.496	0.0012	0.0031	1.30	2	1.38
23350	0.07	402	28.3841	3623.853	17.40	0.46	0.63	0.369	0.0029	0.0011	1.25	2	1.10

Category 7: list of 2 peculiar EBs that exhibit variations between eclipses.

Catalog Properties			Analytic Model Parameters								Fit Statistics		
ID	$\langle V-I\rangle$	$\mathcal{N}_I$	P	t_o	$\langle I\rangle$	ΔI_1	ΔI_2	Φ_2	Θ_1	Θ_2	$f_{\sigma,I}$	$\mathcal{N}_c$	χ^2_G/ν
343	0.13	437	33.5508	3572.393	17.35	0.27	0.17	0.694	0.0124	0.0087	1.30	1	1.03
4458	−0.07	445	39.5436	3581.850	16.14	0.11	0.22	0.501	0.0029	0.0007	1.14	2	1.41

Table 4.1 (cont.):

Category 8: list of 130 detached EBs with well-defined eclipse parameters.

Catalog Properties			Analytic Model Parameters								Fit Statistics		
ID	$\langle V-I\rangle$	$\mathcal{N}_I$	P	t_o	$\langle I\rangle$	ΔI_1	ΔI_2	Φ_2	Θ_1	Θ_2	$f_{\sigma,I}$	$\mathcal{N}_c$	χ^2_G/ν
91	0.06	411	24.8099	3619.170	16.80	0.45	0.32	0.459	0.0080	0.0114	1.28	0	1.02
170	−0.03	426	26.3720	3566.276	17.10	0.38	0.10	0.155	0.0036	0.0066	1.18	0	1.05
784	0.00	444	44.1196	3633.801	16.72	0.50	0.45	0.115	0.0026	0.0035	1.18	2	1.02
866	0.06	424	28.0132	3598.047*	16.47	0.63	0.49	0.496	0.0046	0.0101	1.46	0	1.04
1056	0.01	444	30.6713	3647.862*	17.40	0.34	0.15	0.503	0.0037	0.0065	1.11	0	1.04
1530	0.06	465	42.1989	3632.166	17.42	0.21	0.14	0.655	0.0044	0.0033	1.09	2	1.02
1968	0.13	911	44.8940	3627.360	17.33	0.25	0.18	0.437	0.0035	0.0038	1.33	0	1.01
2142	0.01	457	27.7692	3595.213	16.57	0.27	0.19	0.162	0.0047	0.0050	1.23	0	1.05
2277	0.01	465	36.5936	3616.509	17.08	0.35	0.29	0.473	0.0039	0.0041	1.32	2	1.00
2708	0.04	465	44.5975	3633.684	17.48	0.38	0.36	0.422	0.0066	0.0031	1.13	1	1.03
2780	−0.12	446	27.0438	3628.748*	17.03	0.53	0.48	0.375	0.0024	0.0088	1.00	0	1.02
3082	−0.06	876	45.5327	3589.237	16.71	0.12	0.06	0.710	0.0024	0.0024	1.38	2	1.00
3177	−0.12	434	20.2216	3585.258	16.70	0.19	0.06	0.455	0.0045	0.0106	1.13	1	1.04
3388	−0.08	448	44.9697	3588.586*	16.53	0.56	0.39	0.168	0.0019	0.0049	1.29	1	1.00
3557	0.00	412	23.8734	3592.035	17.03	0.27	0.12	0.478	0.0048	0.0062	1.46	1	1.01
4031	−0.10	448	32.5105	3577.358	16.46	0.41	0.22	0.821	0.0045	0.0035	1.31	0	1.04
4399	0.03	447	22.9067	3624.060*	16.76	0.14	0.12	0.644	0.0068	0.0074	1.03	2	1.03
4419	0.07	434	42.0950	3575.980	16.09	0.49	0.44	0.415	0.0032	0.0046	1.33	1	1.02
4721	−0.05	456	21.8793	3592.692	17.05	0.21	0.16	0.511	0.0059	0.0073	1.03	2	1.06
4737	0.07	440	31.5717	3612.900*	17.51	0.35	0.29	0.644	0.0036	0.0080	1.09	1	1.00
4804	−0.02	429	23.0375	3601.271	16.23	0.14	0.08	0.463	0.0046	0.0048	1.34	1	1.00
4837	−0.02	445	26.8055	3608.319*	17.56	0.35	0.33	0.576	0.0050	0.0043	1.11	2	1.01
5145	0.00	445	47.6341	3684.851	17.55	0.15	0.12	0.173	0.0036	0.0033	1.05	0	1.00
5153	−0.04	456	24.4530	3582.856*	16.28	0.23	0.21	0.829	0.0039	0.0031	1.09	1	1.02
5195	−0.06	445	39.4245	3564.482	17.19	0.20	0.13	0.439	0.0064	0.0047	1.12	2	1.06
5492	−0.04	429	32.9664	3602.498	16.27	0.36	0.15	0.280	0.0042	0.0085	1.31	1	1.03
5965	−0.05	439	20.3374	3616.353	17.54	0.39	0.22	0.684	0.0041	0.0059	1.29	2	1.02
6187	0.00	477	29.8706	3612.492*	16.91	0.11	0.10	0.537	0.0042	0.0085	1.11	1	1.08
6555	−0.02	477	29.0548	3591.351	17.19	0.57	0.54	0.657	0.0071	0.0038	1.16	1	1.00
6996	−0.04	476	29.9285	3596.250*	16.54	0.50	0.49	0.445	0.0041	0.0096	1.05	2	1.05
7380	0.02	468	31.4810	3597.756*	17.23	0.25	0.17	0.564	0.0036	0.0045	1.13	2	1.00
7560	−0.01	418	26.7461	3611.788*	16.49	0.28	0.24	0.575	0.0036	0.0032	1.21	2	1.09
7565	0.13	477	29.0955	3601.070	17.45	0.19	0.17	0.667	0.0103	0.0051	1.08	0	1.01
7935	−0.01	404	24.0615	3609.910	17.39	0.32	0.22	0.449	0.0045	0.0051	1.13	1	1.05
7975	−0.05	477	20.1226	3615.517*	16.86	0.11	0.06	0.607	0.0031	0.0072	1.11	2	1.03
8543	0.00	451	25.3380	3621.313	17.07	0.41	0.35	0.414	0.0067	0.0057	1.68	1	1.05
8559	−0.06	468	42.2643	3631.168*	17.54	0.63	0.48	0.239	0.0019	0.0045	1.13	2	1.04
8783	0.08	458	48.7243	3622.458	17.44	0.21	0.12	0.170	0.0041	0.0041	1.02	1	1.06
8903	−0.05	463	25.6605	3637.923*	16.49	0.22	0.22	0.593	0.0049	0.0050	1.89	1	0.99
8993	−0.09	891	29.4599	3599.445*	17.11	0.56	0.41	0.617	0.0024	0.0073	1.03	2	0.99
9159	0.05	466	48.1575	3695.306	17.34	0.39	0.36	0.622	0.0038	0.0054	1.16	0	1.00
9386	−0.07	559	29.8063	3619.572*	16.61	0.40	0.19	0.682	0.0030	0.0062	1.21	1	1.00
9429	0.11	476	20.6681	3605.574*	17.15	0.11	0.08	0.532	0.0075	0.0126	1.02	1	1.08
9441	0.05	476	20.8997	3596.643	17.45	0.26	0.11	0.432	0.0058	0.0075	1.09	0	1.00
9953	−0.10	490	45.5783	3729.995*	17.05	0.25	0.22	0.140	0.0025	0.0032	1.12	2	1.05
10096	0.05	431	35.2251	3628.920	17.58	0.28	0.20	0.317	0.0049	0.0060	1.20	1	1.01
10422	−0.11	612	21.1694	3586.720*	16.91	0.29	0.26	0.841	0.0032	0.0045	1.26	1	1.02
10575	−0.05	559	29.1436	3592.083	17.14	0.24	0.12	0.546	0.0057	0.0049	1.04	2	1.04
10953	−0.12	616	42.2762	3610.382	16.31	0.14	0.08	0.265	0.0059	0.0044	1.34	1	1.08
11252	−0.04	490	22.2402	3592.677	17.19	0.59	0.56	0.496	0.0067	0.0052	1.15	1	1.02
11299	0.07	1049	39.5635	3584.911*	17.22	0.49	0.45	0.214	0.0055	0.0063	1.29	1	1.01
11526	−0.01	477	49.2837	3595.345	16.67	0.20	0.19	0.418	0.0035	0.0041	1.13	0	1.09
11538	−0.17	477	33.7813	3600.922*	16.28	0.56	0.17	0.504	0.0017	0.0092	1.18	2	1.02
11636	0.08	474	31.1510	3579.485	17.59	0.26	0.24	0.612	0.0054	0.0069	1.13	1	1.09
11907	−0.04	440	45.4195	3629.747	17.20	0.28	0.22	0.589	0.0031	0.0047	1.17	0	1.00
12170	−0.04	452	29.1744	3586.509	17.60	0.43	0.33	0.439	0.0060	0.0045	1.09	0	1.01
12179	−0.01	477	25.1020	3555.863*	16.84	0.31	0.30	0.485	0.0032	0.0098	1.14	0	0.99
12384	0.12	476	25.1786	3591.906	17.12	0.10	0.09	0.251	0.0116	0.0096	1.14	2	1.08
12454	−0.14	476	30.1523	3591.689	17.01	0.20	0.16	0.649	0.0043	0.0029	1.11	2	1.04
12832	−0.08	493	20.1668	3551.653*	16.37	0.10	0.09	0.425	0.0047	0.0049	1.30	0	1.04
13177	−0.01	477	40.5158	3542.700	17.11	0.32	0.17	0.813	0.0034	0.0058	1.17	2	1.00
13260	0.00	450	24.2957	3593.162	17.21	0.29	0.27	0.447	0.0095	0.0066	1.07	0	1.16
13390	0.10	477	35.7858	3571.607	17.59	0.35	0.24	0.630	0.0026	0.0057	1.15	1	1.01
13418	−0.11	465	26.9111	3587.289*	16.94	0.57	0.46	0.907	0.0025	0.0040	1.10	0	1.03
13441	−0.04	493	30.6531	3593.354	17.26	0.22	0.17	0.618	0.0042	0.0044	1.24	1	1.03

*Epoch of primary eclipse minimum t_o appropriately adjusted to ensure $\Delta I_1 > \Delta I_2$.

Table 4.1 (cont.):

Category 8 (cont.): list of 130 detached EBs with well-defined eclipse parameters.

Catalog Properties			Analytic Model Parameters								Fit Statistics		
ID	$\langle V-I\rangle$	$\mathcal{N}_I$	P	t_o	$\langle I\rangle$	ΔI_1	ΔI_2	Φ_2	Θ_1	Θ_2	$f_{\sigma,I}$	$\mathcal{N}_c$	χ^2_G/ν
13482	−0.08	493	21.5789	3548.902*	17.32	0.46	0.43	0.659	0.0050	0.0058	1.10	2	0.99
13491	0.10	477	21.3014	3578.036*	16.82	0.31	0.30	0.510	0.0069	0.0069	1.10	2	1.07
13726	0.10	493	20.9344	3554.051	17.37	0.29	0.07	0.679	0.0050	0.0069	1.13	2	1.03
13867	−0.02	831	21.7457	3604.874	17.33	0.33	0.21	0.493	0.0047	0.0051	1.65	1	1.00
14171	−0.02	457	21.7291	3621.792	16.95	0.21	0.05	0.528	0.0043	0.0051	1.05	2	1.02
14360	0.00	540	30.2612	3651.363*	16.20	0.15	0.13	0.595	0.0038	0.0072	1.00	1	0.99
14895	0.06	506	34.4641	3574.345*	17.33	0.60	0.57	0.186	0.0040	0.0034	1.31	0	1.01
15235	−0.10	726	28.9500	3553.091*	17.17	0.33	0.27	0.317	0.0045	0.0047	1.08	2	1.05
15244	0.07	446	21.8435	3622.895	17.41	0.45	0.27	0.299	0.0064	0.0071	1.02	2	1.02
15380	−0.09	325	27.6171	3624.679*	16.79	0.17	0.12	0.802	0.0028	0.0045	1.09	0	1.05
15788	−0.06	600	29.0140	3561.929*	17.04	0.18	0.17	0.246	0.0031	0.0033	1.27	2	1.04
15979	−0.12	449	28.1428	3635.572	16.27	0.22	0.20	0.637	0.0077	0.0032	1.09	1	1.08
16026	0.00	449	30.8480	3566.099	16.40	0.56	0.43	0.661	0.0038	0.0103	1.00	0	0.87
16126	0.02	600	22.2111	3609.525	17.49	0.34	0.20	0.234	0.0038	0.0075	1.58	1	0.99
16350	−0.10	599	30.9801	3603.346*	17.09	0.47	0.31	0.746	0.0027	0.0046	1.16	0	1.02
16399	0.01	456	39.1458	3653.057*	17.45	0.51	0.28	0.849	0.0020	0.0039	1.00	0	1.00
16418	0.03	482	20.4164	3586.945	17.08	0.12	0.06	0.619	0.0070	0.0079	1.05	0	1.03
16711	−0.13	449	26.5576	3632.458*	16.25	0.35	0.25	0.833	0.0027	0.0056	1.02	1	1.04
16964	−0.10	606	23.5422	3603.149	16.44	0.22	0.05	0.846	0.0031	0.0052	1.08	0	1.03
17067	−0.14	581	28.1151	3592.517	16.57	0.19	0.09	0.666	0.0033	0.0070	1.24	0	1.02
17316	−0.14	986	26.7747	3611.392	16.68	0.27	0.27	0.775	0.0056	0.0027	1.00	2	1.00
17361	0.03	472	20.9318	3562.002	17.48	0.36	0.30	0.551	0.0111	0.0065	1.00	0	0.98
17539	0.06	473	23.9094	3562.789*	17.51	0.36	0.24	0.471	0.0053	0.0082	1.04	2	0.99
17569	−0.08	626	22.2019	3591.019	16.91	0.29	0.23	0.523	0.0049	0.0035	1.18	2	1.12
17750	−0.11	473	20.7086	3586.855	16.98	0.13	0.06	0.750	0.0066	0.0072	1.10	1	1.01
17784	−0.09	626	25.2613	3575.400	17.11	0.17	0.12	0.280	0.0038	0.0031	1.28	1	1.01
17822	0.07	437	44.2706	3641.930	16.75	0.13	0.12	0.579	0.0072	0.0048	1.09	1	1.01
18237	−0.10	588	20.3285	3616.375	16.03	0.17	0.14	0.481	0.0105	0.0092	1.63	1	1.14
18582	0.02	441	41.9856	3608.318*	16.60	0.29	0.25	0.539	0.0047	0.0065	1.09	2	1.06
18659	0.04	456	21.4449	3594.435	17.14	0.28	0.27	0.665	0.0079	0.0048	1.19	1	1.03
18813	0.11	605	39.6989	3627.894*	16.92	0.53	0.44	0.498	0.0041	0.0078	1.22	0	1.02
18824	−0.08	626	33.5726	3576.478	16.54	0.21	0.08	0.439	0.0044	0.0064	1.13	1	1.03
18839	−0.04	473	48.2133	3619.336*	17.28	0.25	0.24	0.269	0.0037	0.0036	1.00	1	0.91
18859	0.00	435	24.5592	3624.022	17.01	0.55	0.35	0.505	0.0038	0.0096	1.08	0	1.00
18869	−0.08	572	42.5786	3628.587	16.90	0.15	0.08	0.648	0.0039	0.0023	1.17	0	1.00
19083	0.02	601	22.2719	3600.521	16.85	0.21	0.08	0.517	0.0062	0.0062	1.26	2	1.09
19230	0.04	473	37.4005	3569.116	16.89	0.10	0.08	0.280	0.0040	0.0041	1.03	0	0.98
19792	−0.10	912	29.6438	3640.465	16.00	0.10	0.07	0.519	0.0047	0.0042	1.52	0	1.01
19840	0.02	625	30.9709	3617.985	16.15	0.12	0.03	0.449	0.0080	0.0046	1.26	1	1.04
20309	−0.02	428	48.2396	3694.899	17.60	0.48	0.43	0.443	0.0034	0.0039	1.00	0	1.01
20459	−0.14	436	30.7408	3642.410*	17.22	0.48	0.24	0.590	0.0033	0.0039	1.06	2	1.02
20522	0.07	423	27.2575	3619.621	17.40	0.19	0.16	0.457	0.0058	0.0073	1.14	1	1.06
20590	0.06	428	40.0925	3618.364*	17.32	0.17	0.16	0.563	0.0063	0.0058	1.07	0	1.11
20646	0.04	437	26.0462	3620.172	16.91	0.18	0.17	0.656	0.0068	0.0066	1.09	0	1.02
20746	0.08	436	28.3719	3614.200*	16.69	0.57	0.50	0.575	0.0045	0.0090	1.03	0	1.02
21059	0.07	428	25.7904	3611.136*	17.56	0.24	0.19	0.674	0.0043	0.0046	1.06	0	0.98
21518	0.02	433	21.4601	3629.580	17.10	0.41	0.34	0.443	0.0074	0.0077	1.05	2	1.08
21621	0.04	444	38.5314	3576.469*	17.20	0.51	0.37	0.341	0.0032	0.0075	1.00	2	0.96
21881	0.04	428	21.0056	3588.139*	16.80	0.28	0.18	0.354	0.0050	0.0073	1.10	0	1.05
22082	−0.06	436	33.1149	3586.199	16.76	0.20	0.08	0.341	0.0056	0.0027	1.08	0	1.04
22553	0.01	419	22.8430	3598.817	17.31	0.41	0.29	0.804	0.0042	0.0061	1.00	2	0.96
22691	0.00	434	31.8865	3579.266*	16.89	0.53	0.21	0.235	0.0018	0.0068	1.26	0	0.98
22713	−0.09	437	33.3752	3617.549	17.00	0.12	0.09	0.679	0.0037	0.0035	1.11	1	1.02
22764	0.00	428	29.7044	3572.606*	16.63	0.60	0.53	0.155	0.0026	0.0050	1.13	0	1.03
23088	0.09	424	22.4312	3598.919	17.43	0.20	0.11	0.495	0.0065	0.0070	1.09	0	1.07
23101	0.08	427	46.3819	3616.728*	16.79	0.59	0.22	0.196	0.0014	0.0094	1.02	1	1.06
23368	0.03	426	22.9011	3629.347*	17.29	0.25	0.20	0.646	0.0037	0.0056	1.00	1	0.99
23773	0.06	428	35.2308	3570.982*	16.75	0.45	0.35	0.372	0.0040	0.0055	1.17	0	1.08
24195	0.13	423	36.6221	3639.504	17.33	0.12	0.08	0.235	0.0041	0.0047	1.05	0	1.02
24580	−0.06	844	31.1688	3608.707	16.50	0.18	0.17	0.456	0.0043	0.0027	1.19	1	1.01
24818	−0.04	711	21.5495	3586.096	17.54	0.43	0.43	0.778	0.0050	0.0027	1.18	0	1.02
24858	0.13	397	45.0560	3623.442	17.14	0.18	0.14	0.937	0.0029	0.0033	1.03	1	1.03
25297	0.04	451	34.3872	3647.584	17.44	0.29	0.28	0.225	0.0053	0.0055	1.05	0	1.03
25578	−0.11	423	21.7054	3582.818	16.08	0.54	0.44	0.298	0.0060	0.0097	1.34	2	1.01
26109	−0.04	422	34.5497	3622.492	16.55	0.57	0.54	0.864	0.0035	0.0041	1.17	1	0.99

*Epoch of primary eclipse minimum t_o appropriately adjusted to ensure $\Delta I_1 > \Delta I_2$.

4.3 Physical Models (Stage II)

4.3.1 Algorithm

The physical properties of EBs are routinely measured by fitting detailed models to the observational data (Wilson & Devinney 1971; Prša & Zwitter 2005; Devor & Charbonneau 2006; Kallrath & Milone 2009). Normally, spectroscopic radial velocity observations are required to dynamically measure the component masses M_1 and M_2. In the modern era of wide-field photometric surveys, the discovery of EBs is quickly outpacing our ability to obtain follow-up spectra (Devor et al. 2008; Prša et al. 2011b,a). For large EB samples, the physical properties must be inferred based solely on the photometric light curves. MS constraints (Prša & Zwitter 2005; Kallrath & Milone 2009) and isochrone fitting (Devor & Charbonneau 2006) have helped ascertain EB properties from the photometric data. In general, however, these methods lead to large systematic uncertainties and/or solutions that are highly degenerate.

In Paper II, we developed a technique that uniquely and accurately characterizes the intrinsic physical properties of *detached EBs with known distances* using only the photometric data. The distances to EBs in the LMC are known. In fact, we have already utilized the observed magnitudes $\langle I \rangle$ and colors $\langle V - I \rangle$ to select EBs with B-type MS primaries. For detached EBs with MS primaries, both components are effectively evolving along their respective single-star evolutionary sequences. The photospheric properties of the stellar components, e.g. effective temperatures T_1 and T_2, radii R_1 and R_2, and luminosities L_1 and L_2, therefore depend entirely on the age τ and component masses M_1 and M_2. The systematic uncertainties in the evolutionary tracks are relatively

small, e.g. ≈15% uncertainties in the masses and ≈30% uncertainties in the ages (see Paper II and §4.3.3 for further justification and a full assessment of the uncertainties). We can therefore measure the component masses M_1 and M_2 and ages τ of detached EBs with known distances based solely on the observed light curve features (Fig. 4.2).

In our physical models, detached EBs with B-type MS primaries can be uniquely described by nine independent properties. These nine physical model parameters are the orbital period P, epoch of primary eclipse minimum t_o, primary mass M_1, secondary mass M_2, age τ, inclination i, eccentricity e, argument of periastron ω, and I-band dust

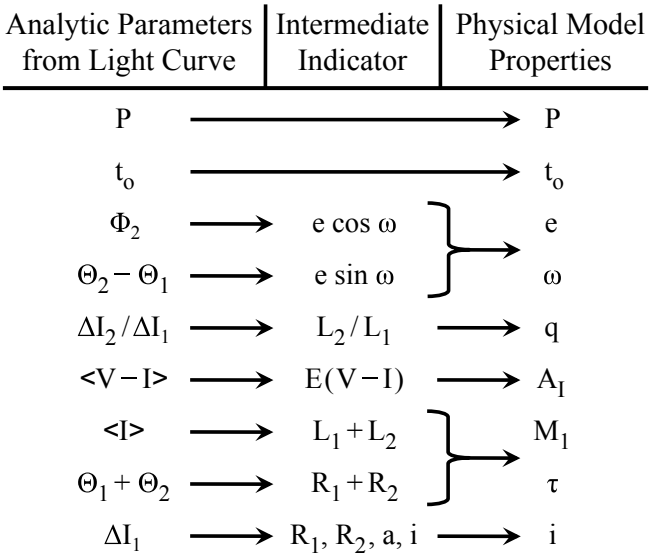

Figure 4.2: For detached EBs with known distances and MS primaries, the nine observed photometric light curve parameters (left) provide unique solutions for the nine independent intrinsic physical properties of the system (right). Other properties of the binary, e.g. stellar radii R_1 and R_2 and luminosities L_1 and L_2, are utilized as intermediate indicators (middle), but depend entirely on the independent properties M_1, $q = M_2/M_1$, and τ according to stellar evolutionary tracks.

extinction A_I. Given the age τ and component masses M_1 and M_2 of the binary, we interpolate the radii R_1 and R_2, surface gravities g_1 and g_2, effective temperatures T_1 and T_2, and luminosities L_1 and L_2 from pre-MS and MS stellar evolutionary tracks with metallicity $Z = 0.008$ (Tognelli et al. 2011; Bertelli et al. 2009). We then use the LMC distance modulus $\mu = 18.5$ (Pietrzyński et al. 2013), dust reddening law $E(V - I) = 0.7A_I$ (Cardelli et al. 1989; Fitzpatrick 1999; Ngeow & Kanbur 2005), and temperature-dependent color indices and bolometric corrections (Pecaut & Mamajek 2013) to transform the intrinsic properties of the binary into observed magnitudes and colors. Our physical model parameter space (M_1, M_2, τ, etc.) of EBs with detached configurations, pre-MS/MS evolutionary constraints, and known distances is quite different than the typical EB parameter space (T_2/T_1, $(R_1+R_2)/a$, etc.) where the distances and evolutionary status of the components are unknown (e.g. Devor & Charbonneau 2006; Prša et al. 2011b).

Using the physical properties of a binary, e.g., P, M_1, M_2, R_1, R_2, T_1, T_2, e, ω, etc., we synthesize photometric light curves with the EB modeling package NIGHTFALL[1]. We use the same NIGHTFALL model options adopted in Paper II, e.g. a square-root limb darkening law, default gravity darkening coefficients, model atmospheres, etc., except for three notable distinctions. First, we do not assume circular orbits for our EBs at longer orbital periods, but instead solve for both the eccentricity e and periastron angle ω. Second, we set the albedo of the secondary to $A_2 = 0.7$ and implement one iteration of reflection effects. Considering reflection effects are minuscule for our wider EBs in this study, different treatments of reflection have negligible effects on the synthesized light

[1]http://www.hs.uni-hamburg.de/DE/Ins/Per/Wichmann/Nightfall.html

curves. Finally, we simulate an EB light curve at 1,000 uniformly-spaced discrete orbital phases to ensure narrow eclipses are sufficiently sampled.

Most of our EBs with intermediate orbital periods have eccentric orbits and narrow eclipses. NIGHTFALL and all other EB software packages that account for tidal effects are computationally expensive for eccentric binaries. This is because the three-dimensional photospheric surfaces of the stars need to be recalculated at each of the 1,000 discretely sampled orbital phases. We therefore adapt our algorithm from Paper II to guarantee fast, automated convergence. Namely, we choose initial values for our nine physical model properties that are sufficiently close to the true values to ensure χ^2 minimization converges quickly to the global solution. The major goal of our algorithm is to synthesize light curves with NIGHTFALL as few times as possible. Our routine can easily be adapted for any population of detached EBs with known distances, and can be used in combination with any EB light curve modeling software.

We decompose our algorithm into three steps.[2] In Step 1, we select initial values for our nine physical model properties based on the observed light curve features quantified in §4.2. In Step 2, we make small adjustments in the physical model properties until the analytic model parameters of the synthesized light curve matches those of the observed light curve. In Step 3, we utilize a Levenberg-Marquardt technique, as done in Paper II, to minimize the χ^2 statistic between the observed and simulated light curves. We elaborate on these three steps below. To help illustrate this procedure, we display in

[2]The three steps discussed in this section are not to be confused with the three full stages of our automated pipeline, which classifies EBs (Stage I - §4.2), fits physical models to the light curves (Stage II - §4.3), and corrects for selection effects (Stage III - §4.5). The three steps regarding physical models are all included in Stage II.

Fig. 4.3 the light curve of an example EB, ID-2142, and the solutions at the end of each of these three steps.

Step 1. We use the eight analytic model parameters (P, t_o, $\langle I \rangle$, ΔI_1, Θ_1, Φ_2, ΔI_2, Θ_2) and observed color $\langle V - I \rangle$ from Table 4.1 to estimate initial solutions for the nine physical model properties. In Fig. 4.2, we show how the nine observed light curve features can be used to approximate the nine physical properties of the binary. We select the physical parameters P and t_o to match the analytic model values. We then estimate e and ω according to the observed phase of the secondary eclipse and the difference in eclipse widths (Kallrath & Milone 2009, Eqn. 3.1.24 and 3.1.26, see our Fig. 4.2):

$$e \cos \omega \approx \frac{\pi}{2}(\Phi_2 - 1/2) \tag{4.3a}$$

$$e \sin \omega \approx \frac{\Theta_2 - \Theta_1}{\Theta_2 + \Theta_1} \tag{4.3b}$$

In this study, $\omega = 90^o$ if periastron coincides with the observed primary eclipse. For our example ID-2142, $\Theta_1 \approx \Theta_2$ and $\Phi_2 \approx 0.16$, indicating $\omega \approx 180^o$ and $e \approx 0.5$ - 0.6.

The intrinsic colors of B-type MS stars span a narrow interval $-0.3 \lesssim \langle V - I \rangle_o \lesssim -0.1$ (Pecaut & Mamajek 2013). We therefore initially assume the intrinsic color of an EB to be:

$$\langle V - I \rangle_o \approx -0.22 + 0.08(\langle I \rangle - 17) \tag{4.4}$$

where we have accounted for the fact that more luminous B-type MS stars tend to be more massive, hotter, and bluer. The dust extinction A_I is simply estimated from the

observed color $\langle V-I\rangle$ and our adopted dust reddening law $E(V-I) = \langle V-I\rangle - \langle V-I\rangle_{\rm o} = 0.7A_I$ (see Fig. 4.2).

We then use the eclipse depths ΔI_1 and ΔI_2 to approximate the mass ratio $q = M_2/M_1$. For a MS + MS binary in a circular orbit, the ratio of eclipse depths $\Delta I_2/\Delta I_1$ provides an accurate indicator of the luminosity contrast L_2/L_1 (Fig. 4.2). This luminosity contrast can then be used to infer the mass ratio q according to a MS mass-luminosity relation (see Fig. 3 in Paper I). For eccentric orbits, however, the eclipse depth ratio can be modified because the projected distances during primary and secondary eclipses can be different. Nonetheless, deeper eclipses still suggest larger mass ratios. For example, $\Delta I_2 > 0.4$ mag requires $q > 0.7$, regardless of the eccentricity or whether the secondary is a MS or pre-MS star. We use a linear combination of these methods to estimate the mass ratio:

$$q \approx 0.6\Delta I_1 + 0.5\Delta I_2 + 0.5\frac{\Delta I_2}{\Delta I_1} \tag{4.5}$$

where the eclipse depths are in magnitudes.

We next use the observed mean magnitude $\langle I\rangle$ and sum of eclipse widths $\Theta_1 + \Theta_2$ to simultaneously measure the primary mass M_1 and age τ. Assuming non-grazing eclipses and standard limb darkening coefficients, the sum of eclipse widths $\Theta_1 + \Theta_2$ directly provides the relative sum of the radii $(R_1+R_2)/a$. Our EBs occupy a narrow range of magnitudes $16.0 < \langle I\rangle < 17.6$ and therefore span a small interval of total masses $M = M_1 + M_2$. The orbital separation $a \propto P^{2/3}M^{1/3}$ therefore derives mainly from the known period P. We can now use $\Theta_1 + \Theta_2$ and P to determine R_1+R_2. For EBs with B-type MS primaries, we find the following approximation:

$$R_1 + R_2 \approx 7\,\mathrm{R}_\odot \frac{\Theta_1 + \Theta_2}{0.01} \Big(\frac{P}{30\,\mathrm{days}} \Big)^{2/3} \tag{4.6}$$

Given our estimates for q and A_I above, we interpolate the stellar evolutionary tracks to determine the primary mass M_1 and age τ that reproduce the sum of the radii $R_1 + R_2$ according to Eqn. 4.6 and the observed combined magnitude $\langle I \rangle$. Although $\langle I \rangle$ and $\Theta_1 + \Theta_2$ both depend on M_1 and τ, they are sufficiently non-degenerate so that we can calculate a unique solution. Namely, the primary mass M_1 largely dictates the luminosity and therefore the observed magnitude $\langle I \rangle$, while the age τ primarily determines the radii $R_1 + R_2$ and therefore the observed eclipse widths $\Theta_1 + \Theta_2$ (see Fig. 4.2).

Finally, we select an inclination i that approximately reproduces the observed primary eclipse depth ΔI_1 (Fig. 4.2). From our estimates of M_1, $M_2 = q\,M_1$, and τ, we interpolate the radii R_1 and R_2 and effective temperatures T_1 and T_2 from stellar evolutionary tracks. In this step only, we ignore limb darkening and colors of the two stars, and instead assume the stars are uniformly illuminated grey disks (see Paper I). We assume the surface brightnesses of the disks are proportional to the stellar temperatures, i.e. the Rayleigh-Jeans law, because we are observing at relatively long wavelengths in the near-infrared I-band. Using these approximations, we calculate the eclipsed area A_o of the primary at the time of primary eclipse t_o based on the observed primary eclipse depth:

$$\Delta I_1 \approx -2.5 \log \Big(1 - \frac{A_\mathrm{o} T_1}{\pi (R_1^2 T_1 + R_2^2 T_2)} \Big) \tag{4.7}$$

Given the eclipsed area A_o and stellar radii R_1 and R_2, we then determine the projected distance d_o between the two stars at t_o. The actual physical separation at primary eclipse

is already known via (Kallrath & Milone 2009, Eqn. 3.1.36 evaluated at geometric phase $\theta = 0^{\rm o}$):

$$r_{\rm o} = a\,\frac{1-e^2}{1+e\sin\omega} \tag{4.8}$$

where a derives from our estimates of M_1, M_2, and P according to Kepler's third law, and e and ω are approximated from Eq. 4.3. Hence, the inclination simply derives from $\cos i = d_{\rm o}/r_{\rm o}$. We limit our initial approximation of the inclination to the interval $i = 86.5^{\rm o}$ - $89.5^{\rm o}$.

We now have initial estimates for the nine physical model properties. We emphasize that Eqns. 4.3 - 4.7 are simple approximations, and that the true values of e, ω, A_I, M_1, M_2, τ, and i may substantially differ from the initial values estimated here. We simply use these estimates as initial parameters in our fitting routine in order to minimize the number of iterations and accelerate convergence toward the final solution (see below and §4.3.2).

In the top panel of Fig. 4.3, we compare the I-band and V-band light curves of ID-2142 to a simulated NIGHTFALL model using the values of the nine physical model properties at the end of Step 1. The model matches key features of the observed light curve, but there are three noticeable differences. First, the simulated phase of the secondary eclipse does not match the observations; recall that Eqn. 4.3 is an approximation. Second, the simulated color is bluer than the observed $\langle V-I\rangle$, indicating we underestimated the dust reddening A_I in our initial step. Finally, the simulated eclipses are slightly deeper than the observed because the more accurate NIGHTFALL model accounts for limb darkening and color effects. This suggests the actual inclination

is smaller and/or the mass ratio is slightly different. We correct for these visible discrepancies in the following step.

Step 2. Using the nine physical properties from Step 1, we synthesize an I-band light curve with NIGHTFALL. We then fit the simple analytic model of Gaussians (Eqn. 4.1) as done in §4.2 to the simulated NIGHTFALL light curve. In this manner, we measure the analytic parameters of the NIGHTFALL model, e.g. $\Delta I_{1,\mathrm{mod}}$, $\Theta_{1,\mathrm{mod}}$, $\Phi_{2,\mathrm{mod}}$, etc.

We adjust the properties in our physical models according to the differences between the simulated and observed analytic model parameters. The adjustments are motivated as follows. If the modeled eclipse widths $\Theta_{1,\mathrm{mod}} + \Theta_{2,\mathrm{mod}}$ are wider than the observed $\Theta_1 + \Theta_2$, we select a slightly younger age τ (and vice versa). We increase the dust extinction A_I if the simulated color $\langle V - I \rangle_{\mathrm{mod}}$ is too blue. If the modeled primary eclipse $\Delta I_{1,\mathrm{mod}} > \Delta I_1$ is too deep while the modeled secondary eclipse $\Delta I_{2,\mathrm{mod}} \leq \Delta I_2$ matches observations or is too shallow, we increase the mass ratio q and decrease the inclination i. However, if both simulated eclipses are too deep (or both too shallow), we only decrease (increase) the inclination i. Finally, we adjust e according to the position of and differences in the secondary eclipse phases Φ_2 and $\Phi_{2,\mathrm{mod}}$. In this step, we fix P, t_{o}, and ω to the values determined in Step 1. Finally, we interpolate M_1 from the stellar evolutionary tracks based on the observed mean magnitude $\langle I \rangle$ and the revised values for τ, q, and A_I.

When adjusting our physical model properties, we choose step sizes that scale with the differences between the observed and simulated analytic model parameters. After making these adjustments, we synthesize another I-band light curve with NIGHTFALL.

We iterate this step until all the analytic model parameters of the simulated and observed light curves match within a small tolerance level. In the middle panel of Fig. 4.3, we show our solution for ID-2142 at the end of Step 2 after five iterations. We therefore

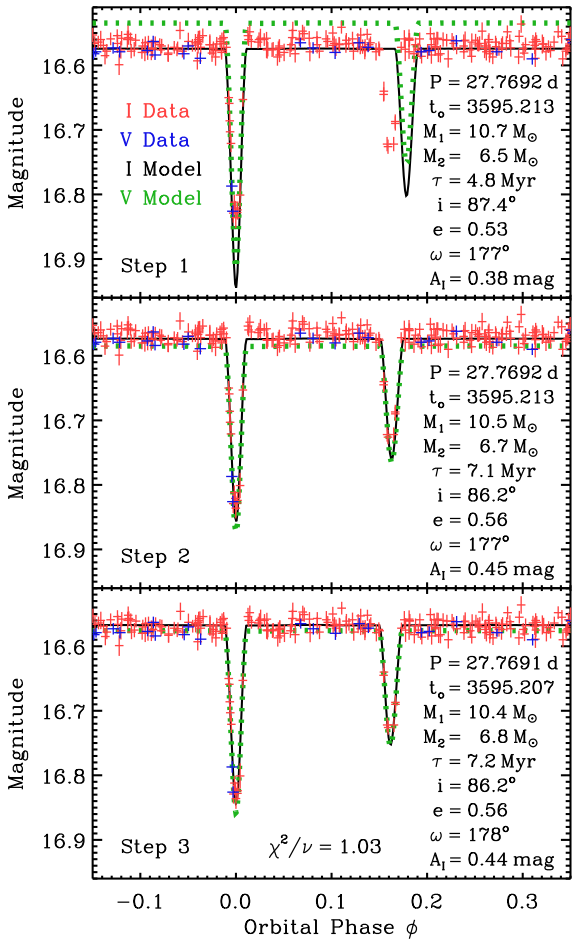

Figure 4.3: Observed and model light curves for ID-2142. We compare the I-band (red) and V-band (blue) OGLE-III LMC data to the synthesized I-band (black) and V-band (dotted green) light curves at the end of the three steps in our automated procedure. We display only the interval $-0.15 < \phi < 0.35$ that encompass the eclipses. Note how the physical model parameters vary only slightly between our initial estimate and final solution.

required only six NIGHTFALL light curve simulations during this middle step.

Step 3. This final step is essentially the procedure outlined in Paper II. We calculate the photometric correction factors $f_{\sigma,I}$ and $f_{\sigma,V}$ in both bands. Starting with initial model properties determined at the end of Step 2, we utilize a Levenberg-Marquardt technique (MPFIT, Markwardt 2009) to minimize the χ^2 statistic between the simulated and observed light curves. The Levenberg-Marquardt MPFIT algorithm operates by independently varying each of the nine physical model properties from the previous solution. The routine then measures the resulting deviations between the data and models, and then calculates a new solution. This step therefore requires ten NIGHTFALL simulations per iteration. As in Paper II, we simultaneously fit the I-band and V-band light curves. We clip up to $\mathcal{N}_{c,I} + \mathcal{N}_{c,V} \leq 3$ data points that exceed 4σ from the best-fit model. This results in $\nu = \mathcal{N}_I + \mathcal{N}_V - \mathcal{N}_{c,I} - \mathcal{N}_{c,V} - 9$ degrees of freedom.

In the bottom panel of Fig. 4.3, we display our final solution for ID-2142 after four iterations of the Levenberg-Marquardt MPFIT routine. We therefore simulated light curves with NIGHTFALL a total of 40 times in Step 3. The physical model properties changed only slightly during this final step. In fact, for ID-2142, the variations were all within the uncertainties of the physical model parameters. We emphasize that Steps 1 and 2 were crucial in guaranteeing rapid convergence toward the final solution in Step 3. Without them, this last step would have required many additional iterations or may have converged to a local minimum.

We utilize this automated procedure for all 130 detached EBs in our well-defined sample. We present our fitted model parameters, physical properties, and fit statistics for these systems in Table 4.2. For MS binaries in circular orbits, the deeper primary

eclipse ΔI_1 at time t_o always corresponds to the smaller, cooler, less massive secondary passing in front of the larger, hotter, more massive primary. For eccentric orbits, however, the situation can be reversed depending on the combination of e, ω, and i. Indeed, for 18 EBs in our well-defined sample, we determined solutions such that the less massive component was eclipsed at time t_o. To avoid confusion in nomenclature, we list properties in Table 4.2 according to the primary "p" and secondary "s" eclipse features. Namely, M_p, R_p, and T_p correspond to the component that was eclipsed at the epoch of primary eclipse t_o, and M_s, R_s, and T_s correspond to the component that was eclipsed at the secondary eclipse phase Φ_2. In the text, we refer to primary mass $M_1 = \max\{M_p, M_s\}$, secondary mass $M_2 = \min\{M_p, M_s\}$, mass ratio $q = M_2/M_1$, etc.

We measure primary masses $M_1 = 3.6\text{-}13.9\,M_\odot$, which nearly encompasses the full mass range of B-type MS stars. We determine mass ratios across the interval $q = 0.20\text{-}1.00$, which confirms the OGLE-III observations are sensitive to EBs with low-mass companions. Our measured dust extinctions cover $A_I = 0.10\text{-}0.58$ mag, which is consistent with the range of extinctions found in Paper II. Finally, we determine ages $\tau = 0.5\text{-}190$ Myr that span more than two orders of magnitude. We further discuss the EB physical properties, and their interrelations, in §4.4.

Eleven of the 130 EBs have modest fit statistics $\chi^2/\nu = 1.10\text{-}1.14$, i.e. probabilities to exceed χ^2 of $p \approx 0.01\text{-}0.05$ given $\nu \approx 530$ degrees of freedom. Seven of these EBs are extremely young with estimated ages $\tau \lesssim 0.8$ Myr (IDs 5153, 7560, 10422, 13418, 16711, 22691, and 22764). The components in these EBs have small radii, as demonstrated by their narrow eclipses (Eqn. 4.6), and are therefore consistent with the zero-age MS. The systematic uncertainties in the stellar evolutionary tracks are larger at these young ages, especially considering some of the secondaries may still be pre-MS stars (see Paper II).

Three of the 11 EBs with modest fit statistics have primaries at the tip of the MS (IDs 91, 20746, and 21518), as indicated by their wide eclipses. Again, the stellar evolutionary tracks are uncertain at the tip of the MS just prior to the rapid expansion toward the giant phase. The one last EB with a poor physical model fit (ID-17569) has $\chi^2/\nu = 1.11$ and $p \approx 0.02$. Considering our large sample of 130 EBs, we naturally expect 1 - 3 of these EBs with modest fit statistics. The remaining 119 EBs in our well-defined sample have good fit statistics $0.93 < \chi^2/\nu < 1.09$. This is testament that the nine independent physical model properties can adequately describe detached EBs with known distances and MS primaries.

Table 4.2: Physical model properties and statistics for the 130 detached EBs in the well-defined sample. We list the OGLE-III LMC EB identification number and the nine physical model properties: orbital period P (days), epoch of primary eclipse t_o (JD − 2450000), primary and secondary component masses M_p and M_s ($M_\odot$), age τ (Myr), inclination i (°), eccentricity e, argument of periastron ω (°), and dust extinction A_I (mag). We then list other physical properties including the mass ratio $q = M_2/M_1 = \min\{M_p, M_s\}/\max\{M_p, M_s\}$, orbital separation a ($R_\odot$), stellar radii R_p and R_s ($R_\odot$), and effective temperatures T_p and T_s (K). Finally, we list the fit statistics including the photometric correction factors $f_{\sigma,I}$ and $f_{\sigma,V}$, number of data points $\mathcal{N}_I$ and $\mathcal{N}_V$, and number of data points we clipped $\mathcal{N}_{c,I}$ and $\mathcal{N}_{c,V}$ in the I-band and V-band, respectively.

	Independent Physical Model Properties									Dependent Physical Properties						Fit Statistics						
ID	P	t_o	M_p	M_s	τ	i	e	ω	A_I	q	a	R_p	R_s	T_p	T_s	$f_{\sigma,I}$	$f_{\sigma,V}$	$\mathcal{N}_I$	$\mathcal{N}_V$	$\mathcal{N}_{c,I}$	$\mathcal{N}_{c,V}$	χ^2/ν
91	24.8098	3619.171	3.7	3.7	190	87.3	0.17	112	0.23	1.00	70	4.7	5.3	12,500	11,900	1.28	1.32	411	34	0	0	1.11
170	26.3719	3566.280	9.5	3.0	2.0	87.1	0.59	165	0.37	0.31	86	3.6	2.2	25,700	13,100	1.18	1.76	426	35	0	1	1.02
784	44.1198	3633.792	8.4	7.5	6.5	88.3	0.66	175	0.36	0.89	132	3.5	3.2	23,900	22,600	1.18	2.12	444	47	2	0	1.04
866	28.0132	3598.058	5.7	5.5	65	89.1	0.37	91	0.35	0.97	87	5.3	4.6	16,500	16,900	1.46	1.68	424	46	0	0	1.07
1056	30.6714	3647.865	6.1	2.8	39	89.9	0.21	89	0.32	0.46	86	3.8	1.8	19,300	13,000	1.11	1.44	444	47	0	0	1.05
1530	42.1990	3632.165	5.4	2.8	62	88.4	0.27	333	0.34	0.52	103	4.2	1.8	17,200	12,700	1.09	1.00	465	67	2	0	1.02
1968	44.8939	3627.357	5.9	3.7	49	88.5	0.11	158	0.45	0.63	113	4.2	2.3	18,300	15,100	1.33	1.16	911	41	0	0	0.99
2142	27.7691	3595.207	10.4	6.8	7.2	86.2	0.56	178	0.44	0.66	100	4.2	3.0	26,400	21,700	1.23	1.27	457	45	0	0	1.03
2277	36.5937	3616.510	6.3	4.8	37	88.6	0.05	151	0.31	0.76	103	3.9	2.8	19,500	17,400	1.32	1.03	465	67	2	0	1.02
2708	44.5972	3633.673	4.0	3.3	140	89.8	0.36	251	0.22	0.82	102	4.1	2.5	13,400	13,300	1.13	1.20	465	67	1	0	1.01
2780	27.0440	3628.753	6.3	5.0	30	89.7	0.56	107	0.14	0.80	85	3.5	2.7	19,900	17,900	1.00	1.00	446	45	0	0	1.03
3082	45.5329	3589.236	11.0	4.8	2.8	87.7	0.34	358	0.37	0.44	135	4.0	2.3	27,500	18,400	1.38	1.70	876	45	2	0	1.00
3177	20.2215	3585.256	10.2	2.4	8.7	89.2	0.40	99	0.27	0.24	73	4.3	1.6	26,000	12,200	1.13	1.33	434	42	1	1	1.02
3388	44.9699	3588.605	10.7	7.8	0.6	88.8	0.60	152	0.32	0.73	141	3.7	3.0	27,600	23,700	1.29	1.11	448	48	1	0	1.06
3557	23.8734	3592.036	7.8	3.3	20	88.6	0.08	116	0.34	0.42	78	4.0	1.9	22,400	14,300	1.46	1.49	412	32	1	0	1.01
4031	32.5105	3577.365	12.0	5.6	2.0	88.2	0.54	348	0.29	0.47	111	4.2	2.5	28,600	20,100	1.31	1.33	448	48	0	0	1.04
4399	22.9066	3624.073	5.2	3.4	83	85.9	0.23	13	0.24	0.64	70	5.9	2.2	14,900	14,000	1.03	1.00	447	43	2	0	1.03
4419	42.0952	3575.980	11.5	11.6	6.0	89.1	0.22	127	0.58	0.99	145	4.5	4.5	27,600	27,800	1.33	1.11	434	41	1	0	1.02
4721	21.8791	3592.698	4.8	3.3	96	87.2	0.07	77	0.13	0.69	66	4.8	2.3	14,800	13,800	1.03	1.04	456	44	2	0	1.03
4737	31.5717	3612.891	4.7	3.3	89	89.2	0.42	60	0.32	0.70	84	4.0	2.2	15,600	13,800	1.09	1.20	440	43	1	0	0.99
4804	23.0376	3601.269	13.0	6.5	4.9	86.8	0.06	161	0.43	0.50	92	4.8	2.9	29,300	21,400	1.34	1.16	429	41	1	0	1.01
4837	26.8054	3608.320	4.7	3.7	72	88.5	0.14	330	0.20	0.80	77	3.3	2.4	16,400	14,900	1.11	1.21	445	41	2	0	1.02
5145	47.6339	3684.852	4.6	2.8	94	86.7	0.54	183	0.21	0.62	108	3.9	1.9	15,400	12,700	1.05	1.15	445	41	0	0	1.01
5153	24.4530	3582.859	10.6	11.2	0.8	85.5	0.55	8	0.39	0.95	99	3.7	3.9	27,200	27,900	1.09	1.05	456	44	2	1	1.12
5195	39.4239	3564.495	4.8	2.5	92	89.6	0.20	241	0.13	0.52	95	4.6	1.7	15,100	11,800	1.12	1.16	445	41	2	0	0.99
5492	32.9666	3602.509	12.6	5.6	6.4	89.8	0.42	144	0.41	0.44	114	4.9	2.6	28,700	19,600	1.31	1.25	429	41	2	0	1.09
5965	20.3374	3616.352	6.0	3.0	28	88.7	0.35	36	0.21	0.50	65	3.3	1.9	19,600	13,600	1.29	1.74	439	44	3	0	1.00
6187	29.8703	3612.495	2.7	5.5	69	88.0	0.45	83	0.23	0.49	82	1.8	5.3	12,600	16,200	1.11	1.03	477	72	1	0	1.03
6555	29.0549	3591.353	4.8	4.4	77	89.5	0.39	307	0.21	0.91	83	3.7	3.1	16,200	15,900	1.16	1.10	477	72	0	0	1.02
6996	29.9282	3596.246	5.8	5.2	62	89.6	0.41	101	0.21	0.90	90	5.1	3.7	16,900	17,200	1.05	2.09	476	72	2	0	1.04
7380	31.4810	3597.752	5.8	5.2	38	87.8	0.16	51	0.33	0.89	93	3.4	3.0	18,900	18,000	1.13	1.43	468	72	2	0	1.02
7560	26.7462	3611.776	10.5	9.8	0.8	88.0	0.16	42	0.45	0.93	102	3.7	3.5	27,400	26,400	1.21	1.69	418	42	2	0	1.14
7565	29.0954	3601.066	4.2	2.8	130	88.5	0.42	307	0.36	0.67	76	4.9	2.0	13,200	12,500	1.08	1.30	477	72	0	1	0.98
7935	24.0616	3609.906	6.0	3.8	36	88.3	0.10	141	0.28	0.64	75	3.5	2.3	19,300	15,400	1.13	1.75	404	38	1	0	1.06
7975	20.1227	3615.519	2.8	8.0	21	87.1	0.46	71	0.28	0.35	69	1.8	4.3	13,200	22,500	1.11	1.29	477	72	2	0	1.05
8543	25.3381	3621.308	5.3	4.1	68	89.6	0.16	210	0.25	0.78	77	4.4	2.7	16,800	15,700	1.68	1.41	451	41	2	0	1.02
8559	42.2644	3631.167	5.8	4.4	20	89.6	0.52	140	0.23	0.77	111	2.9	2.4	19,400	16,900	1.13	1.28	468	72	2	0	1.06
8783	48.7240	3622.451	5.5	2.6	62	88.3	0.55	177	0.37	0.48	113	4.2	1.8	17,200	12,300	1.02	1.34	458	41	1	0	1.05
8903	25.6604	3637.910	7.5	7.6	19	87.3	0.15	359	0.28	1.00	90	3.8	3.8	22,200	22,200	1.89	2.05	463	66	1	0	1.03
8993	29.4599	3599.449	6.5	4.7	25	89.6	0.48	70	0.18	0.73	90	3.5	2.6	20,400	17,400	1.03	1.36	891	41	2	0	1.00
9159	48.1568	3695.292	4.3	3.5	120	89.4	0.24	37	0.25	0.81	110	4.4	2.6	14,100	13,900	1.16	1.26	466	40	0	1	1.03
9386	29.8063	3619.568	10.7	5.1	5.3	88.9	0.42	49	0.32	0.48	101	4.2	2.4	26,800	18,800	1.21	1.22	559	115	1	2	1.01
9429	20.6681	3605.551	4.6	2.3	120	88.1	0.31	81	0.33	0.50	60	5.7	1.6	13,600	11,100	1.02	1.52	476	68	1	0	1.03
9441	20.8997	3596.647	6.4	2.5	34	89.9	0.19	125	0.39	0.39	66	3.8	1.7	19,900	12,300	1.09	1.59	476	68	0	1	1.01
9953	45.5780	3730.003	6.9	6.6	3.0	87.1	0.61	168	0.21	0.95	128	2.9	2.8	22,200	21,500	1.12	1.54	490	63	2	1	1.04
10096	35.2251	3628.935	4.5	2.7	100	89.9	0.31	158	0.27	0.62	87	4.1	1.9	14,900	12,500	1.20	1.48	431	46	1	0	1.00
10422	21.1695	3586.712	6.5	8.1	0.6	85.7	0.57	9	0.22	0.81	79	2.7	3.1	22,000	24,100	1.26	1.00	612	38	2	0	1.13
10575	29.1431	3592.096	6.4	2.9	38	89.1	0.12	307	0.22	0.45	84	4.1	1.8	19,600	13,100	1.04	1.15	559	115	3	0	1.02
10953	42.2762	3610.406	7.9	3.1	31	88.3	0.41	203	0.15	0.39	113	5.8	1.9	20,500	13,700	1.34	1.00	616	38	1	0	0.99
11252	22.2402	3592.679	4.6	4.2	88	89.6	0.13	268	0.17	0.92	69	3.7	3.1	15,600	15,500	1.15	1.53	490	63	1	1	0.97
11299	39.5635	3584.917	4.0	3.6	150	89.9	0.47	177	0.30	0.91	96	4.8	3.2	12,800	13,600	1.29	1.18	1049	41	1	0	1.03
11526	49.2822	3595.336	4.5	6.5	47	88.3	0.15	150	0.28	0.69	125	2.7	5.2	16,600	18,300	1.13	1.12	477	61	1	0	1.06
11538	33.7813	3600.922	10.4	9.3	1.3	88.8	0.67	90	0.20	0.89	118	3.7	3.5	26,900	25,500	1.18	1.38	477	61	2	0	1.05
11636	31.1511	3579.505	4.0	2.8	140	90.0	0.23	40	0.29	0.69	79	4.4	2.0	13,300	12,400	1.13	1.34	474	60	1	0	1.04
11907	45.4194	3629.746	3.6	4.8	86	88.5	0.25	56	0.16	0.75	109	2.4	4.2	14,500	15,700	1.17	1.27	440	41	0	0	1.01
12170	29.1745	3586.504	4.0	3.1	120	89.6	0.17	237	0.13	0.78	77	3.6	2.3	14,300	13,200	1.09	1.21	452	88	0	0	1.01
12179	25.1022	3555.832	5.5	4.3	67	88.7	0.46	92	0.23	0.77	78	4.9	2.8	16,600	16,000	1.14	1.77	477	61	0	1	1.04
12384	25.1787	3591.907	3.9	2.3	170	87.0	0.41	193	0.29	0.60	67	6.4	1.8	11,600	11,200	1.14	1.18	476	61	2	0	1.03
12454	30.1522	3591.701	7.1	3.3	24	88.1	0.29	323	0.12	0.47	89	3.8	2.0	21,300	14,300	1.11	1.37	476	61	3	0	1.03
12832	20.1669	3551.657	7.7	8.2	16	85.8	0.12	170	0.25	0.94	78	3.7	4.0	22,600	23,100	1.30	1.21	493	90	0	0	1.03

Table 4.2 (cont.):

	Independent Physical Model Properties									Dependent Physical Properties						Fit Statistics						
ID	P	t_o	M_p	M_s	τ	i	e	ω	A_I	q	a	R_p	R_s	T_p	T_s	$f_{\sigma,I}$	$f_{\sigma,V}$	$\mathcal{N}_I$	$\mathcal{N}_V$	$\mathcal{N}_{c,I}$	$\mathcal{N}_{c,V}$	χ^2/ν
13177	40.5163	3542.688	7.3	3.7	21	88.4	0.55	24	0.29	0.50	111	3.8	2.1	21,700	15,300	1.17	1.32	477	61	2	0	1.02
13260	24.2959	3593.154	4.1	3.2	140	89.9	0.20	246	0.17	0.78	69	4.9	2.4	13,000	13,200	1.07	1.51	450	56	0	0	1.00
13390	35.7853	3571.619	4.0	5.2	53	88.5	0.41	62	0.41	0.77	96	2.5	3.5	15,700	17,700	1.15	1.26	477	61	1	0	1.01
13418	26.9107	3587.265	7.9	6.5	0.5	87.6	0.71	7	0.21	0.83	92	3.1	2.7	23,900	22,000	1.10	1.14	465	61	1	0	1.13
13441	30.6531	3593.346	5.7	3.7	51	87.8	0.19	6	0.22	0.65	87	3.9	2.3	18,100	15,000	1.24	1.48	493	90	1	0	1.03
13482	21.5789	3548.903	4.9	4.7	55	88.5	0.26	17	0.16	0.97	69	3.1	3.0	17,100	17,000	1.10	1.21	493	90	2	0	1.01
13491	21.3014	3578.037	6.2	5.1	51	87.6	0.02	0	0.43	0.83	72	5.0	3.2	18,000	17,600	1.10	1.09	477	61	2	1	1.02
13726	20.9342	3554.047	8.7	2.0	5.3	89.5	0.32	30	0.51	0.23	70	3.6	1.7	24,400	9,900	1.13	1.29	493	90	2	0	1.03
13867	21.7458	3604.872	6.6	4.3	21	88.1	0.06	101	0.30	0.65	73	3.4	2.3	20,700	16,600	1.65	1.89	831	40	1	0	1.00
14171	21.7291	3621.788	10.6	2.4	3.6	88.0	0.10	66	0.41	0.23	77	4.0	1.6	26,900	12,500	1.05	1.21	457	39	2	0	0.99
14360	30.2614	3651.358	4.1	8.4	29	87.6	0.35	66	0.32	0.48	95	2.3	6.4	16,000	20,800	1.00	1.32	540	136	1	0	1.02
14895	34.4644	3574.342	6.2	6.4	7.5	89.5	0.52	186	0.39	0.97	104	2.9	2.9	20,600	21,000	1.31	1.41	506	131	0	0	1.01
15235	28.9499	3553.094	5.9	4.2	40	88.3	0.29	174	0.19	0.70	86	3.7	2.4	19,000	16,100	1.08	1.52	726	99	2	0	1.04
15244	21.8434	3622.893	5.1	3.6	70	89.9	0.32	175	0.33	0.70	68	4.0	2.3	16,700	14,600	1.02	1.19	446	38	2	1	1.05
15380	27.6171	3624.681	6.3	8.5	4.5	85.9	0.53	25	0.24	0.74	94	2.8	3.5	20,900	24,300	1.09	2.08	325	82	0	0	1.08
15788	29.0140	3561.932	7.2	6.6	2.4	86.9	0.41	181	0.26	0.91	95	3.0	2.8	22,700	21,700	1.27	1.18	600	40	3	0	1.01
15979	28.1428	3635.584	10.0	5.3	13	88.1	0.45	296	0.23	0.53	97	4.8	2.6	25,300	18,800	1.09	1.30	449	38	1	0	1.03
16026	30.8481	3566.097	6.2	5.9	49	88.7	0.48	61	0.20	0.94	95	4.8	4.1	18,300	18,300	1.00	1.24	449	38	0	0	1.02
16126	22.2111	3609.527	5.0	4.9	45	86.5	0.50	146	0.33	0.98	71	3.0	2.9	17,600	17,400	1.58	1.00	600	40	1	1	0.98
16350	30.9797	3603.341	7.1	5.5	11	88.5	0.45	30	0.23	0.77	97	3.3	2.7	21,900	19,200	1.16	1.30	599	40	0	0	1.05
16399	39.1462	3653.058	7.7	3.9	1.4	88.2	0.63	29	0.37	0.51	110	3.1	2.0	23,400	16,400	1.00	1.08	456	39	0	0	1.07
16418	20.4167	3586.960	5.6	2.2	64	87.0	0.19	17	0.29	0.39	63	5.0	1.6	16,800	11,200	1.05	1.23	482	128	0	3	0.99
16711	26.5578	3632.442	10.5	10.7	0.5	86.4	0.57	18	0.28	0.98	104	3.7	3.7	27,400	27,600	1.02	1.67	449	38	3	0	1.10
16964	23.5422	3603.148	12.7	3.7	2.9	85.1	0.63	29	0.33	0.29	88	4.5	2.0	29,200	15,700	1.08	1.28	606	47	0	0	1.07
17067	28.1151	3592.517	4.8	8.4	17	87.2	0.43	55	0.16	0.56	92	2.5	4.3	17,700	23,300	1.24	1.25	581	36	0	0	1.03
17316	26.7748	3611.388	10.4	6.1	0.6	87.5	0.51	328	0.25	0.59	96	3.6	2.6	27,200	21,200	1.00	1.10	986	39	2	0	1.06
17361	20.9317	3562.007	3.6	3.0	190	89.8	0.31	284	0.19	0.83	60	4.5	2.5	12,100	12,500	1.00	1.04	472	54	0	0	0.98
17539	23.9095	3562.793	5.0	3.5	71	88.9	0.13	110	0.34	0.70	71	3.8	2.3	16,600	14,400	1.04	1.24	473	54	2	0	1.05
17569	22.2016	3590.999	9.0	4.4	4.8	88.5	0.19	281	0.27	0.48	79	3.6	2.2	24,900	17,300	1.18	1.06	626	66	2	1	1.11
17750	20.7084	3586.844	5.9	2.0	55	86.6	0.41	9	0.11	0.34	63	4.7	1.5	17,700	10,500	1.10	1.20	473	54	1	0	0.99
17784	25.2611	3575.386	8.0	3.6	8.8	87.2	0.36	189	0.24	0.44	82	3.5	1.9	23,300	15,100	1.28	1.50	626	66	1	0	1.02
17822	44.2711	3641.934	5.3	3.1	84	88.3	0.25	299	0.30	0.59	107	6.2	2.1	14,800	13,500	1.09	1.29	437	45	1	0	1.02
18237	20.3284	3616.374	7.4	4.3	40	88.3	0.10	254	0.15	0.58	71	6.9	2.5	18,400	16,500	1.63	1.18	588	70	1	0	0.99
18582	41.9853	3608.319	6.5	4.6	48	90.0	0.15	66	0.32	0.71	113	5.6	2.8	18,000	16,900	1.09	1.16	441	54	2	0	1.07
18659	21.4450	3594.449	5.9	4.0	51	87.8	0.35	317	0.31	0.67	70	4.2	2.4	18,200	15,600	1.19	1.61	456	50	1	0	1.06
18813	39.6988	3627.901	4.4	4.3	120	88.9	0.32	91	0.34	0.98	101	4.8	4.2	13,900	14,200	1.22	1.24	605	47	0	0	1.05
18824	33.5722	3576.497	9.2	3.0	17	89.8	0.23	115	0.27	0.32	101	4.7	1.8	24,000	13,600	1.13	1.23	626	66	1	0	1.03
18839	48.2133	3619.339	5.0	3.7	72	88.2	0.37	182	0.18	0.74	115	3.9	2.4	16,500	14,800	1.00	1.02	473	54	1	0	0.93
18859	24.5592	3624.012	4.8	4.7	81	88.5	0.36	89	0.24	0.97	75	3.9	3.6	16,000	16,000	1.08	1.36	435	45	0	0	1.06
18869	42.5786	3628.596	9.0	2.5	9.9	88.6	0.35	310	0.27	0.28	116	3.9	1.6	24,500	12,500	1.17	1.50	572	43	0	0	0.99
19083	22.2720	3600.517	9.6	2.6	11	89.8	0.03	345	0.43	0.27	77	4.3	1.6	25,200	12,700	1.26	1.39	601	70	3	0	1.06
19230	37.4005	3569.103	6.5	4.3	44	86.5	0.35	178	0.36	0.66	104	4.8	2.5	18,800	16,300	1.03	1.12	473	54	0	0	0.98
19792	29.6439	3640.471	13.9	5.6	5.5	87.4	0.07	294	0.34	0.40	109	5.2	2.6	30,000	19,600	1.52	1.43	912	55	0	0	1.01
19840	30.9701	3617.984	13.3	2.7	8.6	89.6	0.27	253	0.50	0.20	105	5.7	1.7	28,700	13,100	1.26	1.16	625	66	1	0	1.03
20309	48.2395	3694.901	3.9	3.2	140	89.9	0.11	143	0.16	0.81	107	3.7	2.4	13,800	13,300	1.00	1.00	428	40	0	0	1.01
20459	30.7410	3642.410	6.7	3.6	19	89.3	0.18	37	0.10	0.53	90	3.4	2.0	20,900	15,000	1.06	1.09	436	45	2	0	1.01
20522	27.2573	3619.602	4.2	2.6	130	88.6	0.14	117	0.28	0.62	72	4.9	1.9	13,400	12,000	1.14	1.52	423	41	1	0	1.02
20590	40.0940	3618.390	3.9	2.6	170	88.7	0.11	336	0.23	0.68	92	5.3	2.0	12,100	12,000	1.07	1.07	428	41	0	0	1.05
20646	26.0463	3620.168	5.0	3.5	89	86.9	0.25	358	0.25	0.69	75	5.5	2.4	14,800	14,200	1.09	1.53	437	42	0	0	1.00
20746	28.3718	3614.202	5.8	5.3	60	89.7	0.30	68	0.39	0.91	87	5.1	3.8	17,000	17,300	1.03	1.00	436	45	0	0	1.10
21059	25.7903	3611.139	5.5	4.1	44	87.4	0.28	9	0.38	0.75	78	3.4	2.4	18,300	16,000	1.06	1.60	428	41	0	0	0.98
21518	21.4601	3629.581	4.7	3.9	95	89.7	0.09	174	0.24	0.81	67	4.6	2.7	15,000	14,900	1.05	1.00	433	42	3	0	1.10
21621	38.5318	3576.485	4.8	4.2	86	88.9	0.44	122	0.28	0.88	100	4.1	3.0	15,700	15,500	1.00	1.39	444	42	2	0	0.98
21881	21.0055	3588.141	5.6	6.8	36	86.6	0.30	140	0.38	0.83	74	3.3	4.4	18,800	20,000	1.10	1.29	428	41	0	0	1.04
22082	33.1143	3586.180	11.2	2.7	3.7	89.0	0.41	234	0.37	0.24	104	4.2	1.6	27,600	13,100	1.08	1.50	436	45	0	0	1.02
22553	22.8430	3598.817	6.8	5.2	12	87.5	0.52	17	0.34	0.76	78	3.2	2.6	21,400	18,600	1.00	1.62	419	36	2	0	0.97
22691	31.8866	3579.269	10.6	4.7	0.7	88.3	0.63	126	0.41	0.44	105	3.7	2.5	27,400	18,400	1.26	2.26	434	37	0	0	1.11
22713	33.3752	3617.560	7.3	3.6	24	87.3	0.29	352	0.20	0.49	97	3.9	2.1	21,500	15,000	1.11	1.27	437	42	1	0	1.03
22764	29.7048	3572.591	9.8	9.0	0.6	88.8	0.59	162	0.44	0.91	107	3.5	3.3	26,500	25,400	1.13	1.26	428	37	1	0	1.12
23088	22.4310	3598.932	5.6	2.5	59	89.6	0.02	110	0.39	0.45	67	4.3	1.7	17,400	11,900	1.09	1.15	424	40	0	0	1.04
23101	46.3827	3616.722	12.0	3.9	1.0	89.7	0.68	128	0.55	0.32	137	4.1	2.8	28,900	15,000	1.02	1.39	427	37	2	0	1.04
23368	22.9011	3629.355	5.1	6.8	16	87.6	0.29	39	0.37	0.74	77	2.6	3.3	18,200	21,200	1.00	1.00	426	37	1	0	1.00
23773	35.2309	3570.983	7.3	5.5	31	89.1	0.25	144	0.40	0.75	106	4.6	3.0	20,800	18,700	1.17	1.91	428	37	0	0	1.05
24195	36.6224	3639.498	5.0	2.8	87	86.2	0.43	173	0.41	0.57	92	4.9	1.9	15,200	12,800	1.05	1.41	423	37	0	0	1.02
24580	31.1688	3608.710	12.5	5.4	1.6	88.3	0.22	252	0.39	0.43	109	4.3	2.5	29,300	19,700	1.19	1.29	844	31	1	0	1.02
24818	21.5492	3586.112	6.7	4.7	0.9	88.3	0.48	337	0.31	0.71	73	2.8	2.2	22,200	18,400	1.18	2.07	711	41	0	0	1.08
24858	45.0564	3623.441	8.2	6.5	3.2	83.6	0.77	4	0.55	0.79	131	3.3	2.8	23,900	21,500	1.03	1.19	397	48	1	0	1.03
25297	34.3873	3647.587	4.1	3.3	130	87.7	0.45	182	0.26	0.79	87	4.3	2.5	13,600	13,400	1.05	1.19	451	53	0	0	1.02
25578	21.7055	3582.825	7.5	7.0	32	88.3	0.37	150	0.18	0.93	80	5.1	4.3	20,600	20,500	1.34	1.78	423	33	2	0	1.09
26109	34.5499	3622.487	8.5	7.5	10	88.6	0.62	9	0.32	0.88	113	3.8	3.4	23,900	22,500	1.17	1.27	422	35	1	0	1.04

4.3.2 Comparison between Initial Estimates and Final Solutions

In the following, we compare the initial estimates for e, q, and R_1+R_2 in Step 1 according to Eqns. 4.3, 4.5, and 4.6, respectively, to the final solutions in Step 3 from fitting detailed NIGHTFALL light curve models to the data. We can then address the systematic uncertainties in our initial estimates and further justify the mapping between the basic EB light curve parameters to the physical model properties.

For the 130 EBs in our well-defined sample, we compare the initial values of the eccentricities e determined from the secondary eclipse phases Φ_2 and eclipse widths Θ_1 and Θ_2 (Eqn. 4.3) to the final NIGHTFALL solutions (top panel of Fig. 4.4). The initial estimates agree quite well with the true final values. The rms scatter between the two is only $\delta e = 0.03$. This validates that Eqn. 4.3 is more than sufficient for starting purposes in our fitting routine. We note that the few systems that change by more than $\Delta e > 0.07$ between Steps 1 and 3 have narrow, poorly sampled eclipses so that it is more difficult to precisely measure Θ_1 and Θ_2.

Similarly, in the bottom panel of Fig. 4.4, we compare the initial estimates of the mass ratios q determined from the eclipse depths ΔI_1 and ΔI_2 (Eqn. 4.5) to our final values obtained from NIGHTFALL light curve fittings and χ^2 minimizations. Although the population as a whole shows rough agreement between the solutions at the ends of Steps 1 and 3, individual systems can substantially deviate from the initial estimates. For example, an EB with an initial estimate of $q \approx 0.6$ may actually have a mass ratio anywhere in the interval $q = 0.3$ - 1.0. The rms deviation between the initial and final solutions is $\delta q = 0.12$, or $\delta q \,/\, q \approx 20\%$ the respective values. If we had randomly

chosen mass ratios q in Step 1 while keeping the other initial estimates unchanged, the NIGHTFALL light curve solutions in Step 3 would still converge to the same final values. We simply find that by adopting Eqn. 4.5 in Step 1 to provide initial estimates for q, the number of iterations in Steps 2 and 3 are dramatically reduced.

Finally, we evaluate the discrepancies between the values of R_1+R_2 estimated from the sum of eclipse widths $\Theta_1+\Theta_2$ and orbital periods P according to Eqn. 4.6 to the final NIGHTFALL solutions. We measure an rms deviation of $\delta(R_1+R_2) = 1.2$ R$_\odot$, or $\delta(R_1+R_2)\,/\,(R_1+R_2) \approx 20\%$ the respective values. The coefficient in Eqn. 4.6 should therefore be 7.0 ± 1.2 R$_\odot$, valid only for EBs with B-type MS primaries. As with the mass ratios q, the approximations for R_1+R_2 based on the observed light curve parameters are imprecise but sufficiently accurate to provide initial conditions for our fitting routine.

As mentioned in §4.3.1, R_1+R_2 is primarily an indictor of age τ of an EB in our sample rather than the component masses M_1 and/or M_2. For example, at age $\tau = 5$ Myr, the sum of the stellar radii must be contained on the interval $R_1+R_2 \approx 4.4$ - 8.7 R$_\odot$ given any combination of M_1 and $q \geq 0.2$ that satisfies our magnitude limits $16.0 < \langle I \rangle < 17.6$ and $-0.25 < \langle V-I \rangle < 0.20$ and measured range of dust extinctions $A_I \approx 0.1$ - 0.5 mag. Meanwhile, at age $\tau = 100$ Myr, the sum of the radii are systematically larger and confined to the interval $R_1+R_2 \approx 5.3$ - 12.3 R$_\odot$ given the same photometric requirements. Hence, EBs in our sample with $R_1+R_2 < 5.3$ R$_\odot$ must be relatively young while those with $R_1+R_2 > 8.7$ R$_\odot$ must be relatively old. We initially estimated R_1+R_2 in Step 1 from the observed sum of eclipse widths $\Theta_1+\Theta_2$ according to Eqn. 4.6. Although not as accurate as the final solutions, Eqn. 4.6 provides a model-independent measurement of R_1+R_2. The sum of radii R_1+R_2 estimated from Eqn. 4.6 is therefore a robust and

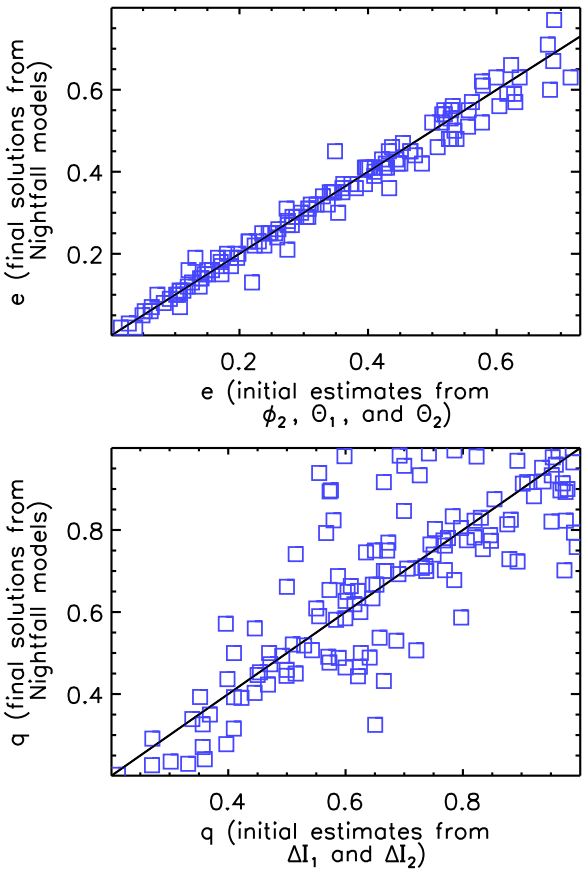

Figure 4.4: Comparison between the initial estimates in Step 1 of physical model properties based on the observed light curve parameters to the final solutions in Step 3 derived from fitting NIGHTFALL light curve models. Top panel: the initial eccentricities e determined from the phase of the secondary eclipse Φ_2 and eclipse widths Θ_1 and Θ_1 according to Eqn. 4.3 correspond quite well to the true final values. Bottom panel: the mass ratios q estimated from the eclipse depths ΔI_1 and ΔI_2 according to Eqn. 4.5 are approximate but imprecise indicators of the true mass ratios. Nonetheless, the initial estimates are sufficient for starting purposes in our fitting routine and, on average, dramatically reduce the number of iterations.

model-independent indicator of age τ.

In Fig. 4.5, we display the eccentricities e measured in Step 1 from Eqn. 4.3 as a function of the approximate sum of stellar radii R_1+R_2 estimated in Step 1 from Eqn. 4.6. Both sets of parameters are model independent and based solely on the observed light curve features. According to a Spearman rank correlation test, we find that the approximate values of e and R_1+R_2 are anticorrelated ($\rho = -0.18$) at a statistically significant level ($p = 0.04$). This suggests that EBs with larger components, which are systematically older, favor smaller eccentricities. We also compare the 19 EBs with approximate $R_1+R_2 < 5.3$ $R_\odot$, which must be relatively young, to the 27 EBs with $R_1+R_2 > 8.7$ $R_\odot$, which must be relatively old. According to a K-S test, we find these young and old populations of EBs have distributions of eccentricities that are discrepant with each other at the $p = 0.02$ significance level. The anticorrelation between R_1+R_2, which is an indicator of age τ, and e is therefore statistically significant, robust, and model independent. In §4.4, we further investigate this anticorrelation between e and τ based on the more accurate final solutions obtained from the NIGHTFALL light curve models.

4.3.3 Uncertainties

We now analyze the uncertainties in the final solutions of our NIGHTFALL light curve models (see also Paper II). For each system, we utilize MPFIT (Markwardt 2009) at the end of Step 3 (§4.3.1) to calculate the measurement uncertainties. For all 130 well-defined EBs, the nine physical model parameters have unique solutions and finite measurement uncertainties. Some of the model parameters, however, have solutions that

are correlated with each other. In addition, uncertainties in the dust reddening law, stellar evolutionary tracks, bolometric corrections, andNIGHTFALL light curve models can lead to large systematic uncertainties in the physical model parameters. In the following, we fully investigate the measurement uncertainties, parameter correlations, and systematic uncertainties in the context of a specific example EB, ID-2142. We then determine the median total uncertainties of each model parameter (Eqns. 4.9 - 4.17) for the entire population of 130 well-defined EBs.

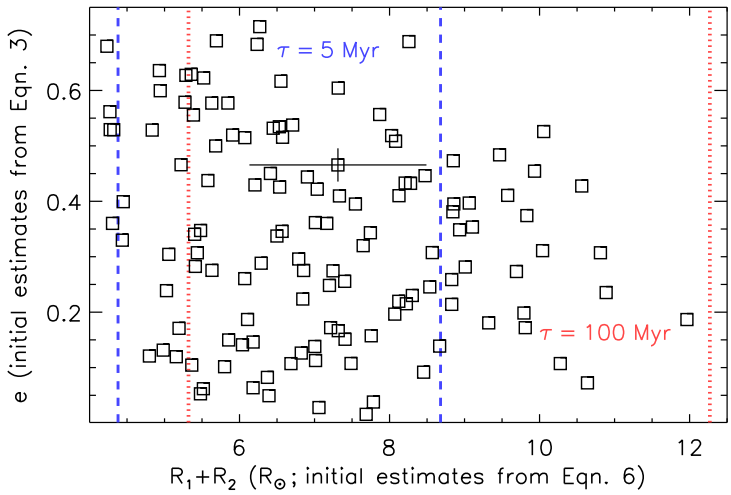

Figure 4.5: The approximate eccentricities e vs. approximate sum of stellar radii R_1+R_2 estimated in Step 1 from the basic observed light curve parameters. For an individual system, we indicate representative error bars $\delta e \approx 0.03$ and $\delta(R_1+R_2) \approx 1.2$ $R_\odot$. Young EBs with $\tau = 5$ Myr that satisfy our photometric selection criteria must have $R_1+R_2 = 4.4$ - 8.7 $R_\odot$ (dashed blue), while older EBs with $\tau = 100$ Myr must have $R_1+R_2 = 5.3$ - 12.3 $R_\odot$ (dotted red). The values of R_1+R_2, which is an indicator of age τ, and e are anticorrelated at a statistically significant level. This anticorrelation is not caused by selection effects, and is a robust and model-independent result.

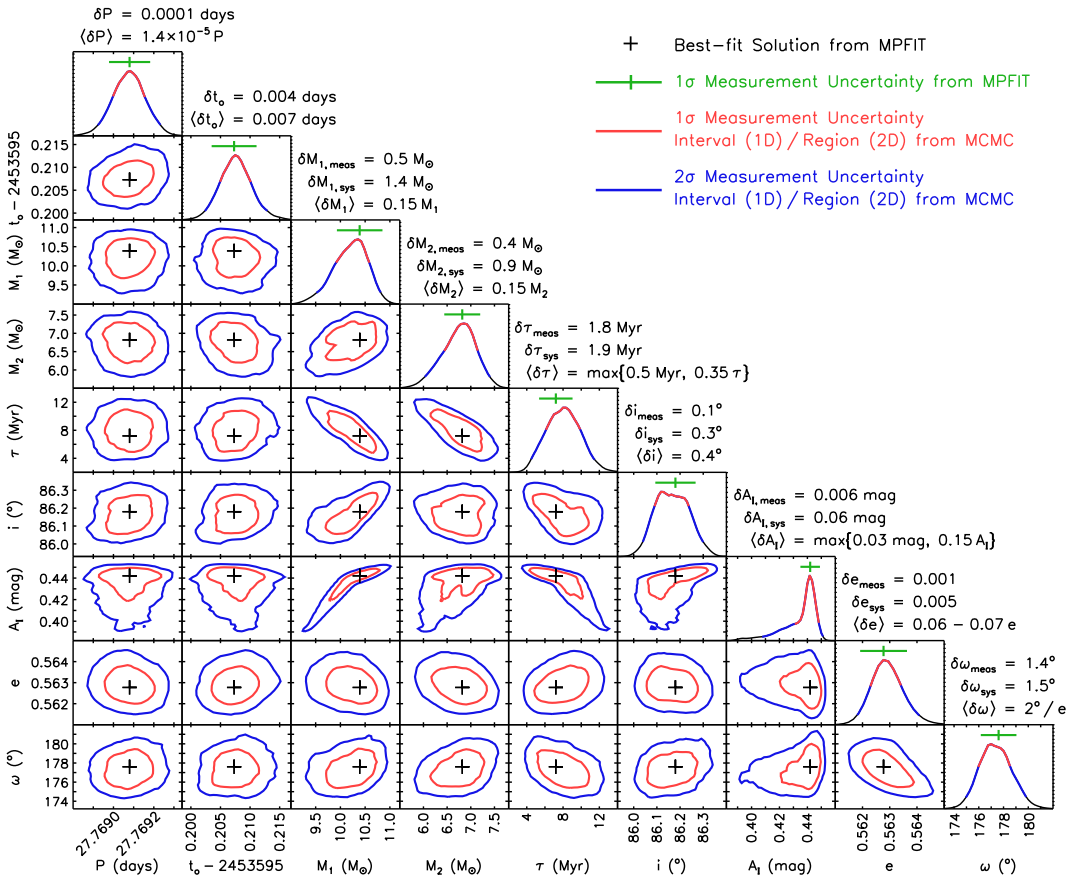

Figure 4.6: The probability density functions (diagonal panels) and joint probability distributions (off-diagonal panels) of the nine physical model parameters for ID-2142. We compare the best-fit solutions and 1σ measurement uncertainties based on the MPFIT routine (black +'s and green intervals) to the 68% (red) and 95% (blue) confidence intervals/regions determined from our MCMC technique. For each physical model parameter, we list the measurement uncertainty for ID-2142, the systematic uncertainty for ID-2142 (if any), and the median total uncertainty for all 130 well-defined EBs. These panels demonstrate: (1) the solutions are unique, (2) the uncertainties in P, t_o, e, and ω are small and primarily dictated by the sensitivity and cadence of the OGLE-III LMC observations, and (3) the measurement uncertainties for M_1, M_2, τ, i and A_I are correlated, but the systematic uncertainties in the bolometric corrections, stellar evolutionary tracks, and dust reddening law dominate the total uncertainties.

For our example EB, ID-2142, we explore the physical parameter space via a Markov chain Monte Carlo (MCMC) technique. Starting with our final solution at the end of Step 3, we implement a Metropolis-Hastings "random walk" MCMC algorithm to generate and select steps in our phase space of nine physical model parameters. At each proposed step, we synthesize aNIGHTFALL light curve model given the proposed nine physical model parameters. The probability $p \propto e^{-\Delta\chi^2/2}$ of accepting the proposed step is determined by evaluating the difference in the χ^2 statistic between the proposed step and the current solution. Obviously, if $\Delta\chi^2 < 0$, the proposed step is always taken. If the proposed step is rejected, the step length is effectively zero, i.e., the previous solution is counted again. We generate proposed steps according to a Gaussian distribution with a fixed standard deviation for each of the nine physical model parameters. We choose the standard deviation in the step sizes so that approximately one-third of the proposed steps are accepted. We simulate 32,000 proposed steps and light curves with NIGHTFALL, which exceeds the total number of models generated in §4.3.1 used to fit solutions for all 130 well-defined EBs! It is therefore quite computationally expensive to calculate robust measurement uncertainties and correlations between model parameters for an individual EB with this MCMC algorithm. The distribution of the ≈12,000 accepted steps and ≈20,000 repeated solutions provide the nine-dimensional joint probability distribution for the physical models. For each of the nine physical model parameters, we marginalize across the other eight parameters to calculate the one-dimensional probability density function. We also compute the two-dimensional joint probability distributions for each of the ${}_9C_2 = 36$ parameter combinations.

In Fig. 4.6, we display the one-dimensional probability distributions for the nine physical model parameters (diagonal panels) and the two-dimensional joint probability

distributions for the 36 parameter combinations (off-diagonal panels). Although some of the parameters are mildly to significantly correlated with each other, the measurement uncertainties are finite for all nine physical model parameters. The MCMC technique confirms the uniqueness and non-degeneracy of the physical model solutions. Moreover, the measurement uncertainties we determined from the robust MCMC algorithm are consistent with the measurement uncertainties we evaluated with the MPFIT routine. We can therefore rely on the MPFIT measurement uncertainties we calculated for all 130 well-defined EBs.

The uncertainties in the orbital parameters P and $t_{\rm o}$ are solely due to the measurement uncertainties and dictated by the sensitivity and cadence of the OGLE-III LMC observations. The solutions for P and $t_{\rm o}$ are therefore independent of the other seven model parameters (note the fairly circular contours in the first and second columns of panels in Fig. 4.6). For ID-2142, we measure 1σ uncertainties of $\delta P \approx 0.0001$ days and $\delta t_{\rm o} \approx 0.004$ days. We find the median 1σ uncertainties for the entire population of 130 well-defined EBs to be:

$$\langle \delta P \rangle \approx 1.4 \times 10^{-5} P \approx 0.0004 \text{ days} \tag{4.9}$$

$$\langle \delta t_{\rm o} \rangle \approx 0.007 \text{ days} \tag{4.10}$$

Note that our example ID-2142 has slightly smaller uncertainties than average because it is relatively bright and its eclipses are well sampled.

As with P and $t_{\rm o}$, the uncertainties in e and ω are primarily determined by the

sensitivity and cadence of the OGLE-III LMC observations. The solutions for e and ω are therefore independent of the other parameters, but are slightly correlated with each other (see last two rows in Fig. 4.6). The eclipses are sufficiently sampled to easily break this degeneracy. For ID-2142, we calculate a 95% confidence interval of $\omega = 175^{\rm o}$ - $180^{\rm o}$. Note that we measured eclipse widths $\Theta_1 = 0.0047 \lesssim \Theta_2 = 0.0050$, also indicating $\omega \lesssim 180^{\rm o}$ according to the approximations in Step 1 (Eqn. 4.3). Based on the NIGHTFALL light curve models, we calculate formal 1σ measurement uncertainties of $\delta e_{\rm meas} \approx 0.001$ and $\delta\omega_{\rm meas} \approx 1.4^{\rm o}$ for ID-2142.

For ID-2142 and some other EBs in our sample, the measurement uncertainties $\delta e_{\rm meas} \lesssim 0.005$ and $\delta\omega_{\rm meas} \lesssim 1.5^{\rm o}$ are extremely small. NIGHTFALL treats each stellar component as a three-dimensional polyhedral mesh with a finite number of flat surfaces. We suspect this finite resolution limits the true sensitivity to systematic uncertainties of $\delta e_{\rm sys} \approx 0.005$ and $\delta\omega_{\rm meas} \approx 1.5^{\rm o}$. In any case, the measurement uncertainties $\delta e_{\rm meas}$ and $\delta\omega_{\rm meas}$ increase and dominate the total uncertainties as the eccentricities e decrease. We measure median total uncertainties of $\delta e \approx 0.02$ and $\delta\omega \approx 4^{\rm o}$ for $e \gtrsim 0.5$, $\delta e \approx 0.03$ and $\delta\omega \approx 10^{\rm o}$ for $e \approx 0.3$, and $\delta e \approx 0.05$ and $\delta\omega \approx 20^{\rm o}$ for $e \approx 0.1$. Obviously, the periastron angle ω is not defined, and therefore not constrained, if the orbits are circular. For the entire population of 130 well-defined EBs, we find the following relations adequately describe the median total uncertainties:

$$\langle \delta e \rangle \approx 0.06 - 0.07e \tag{4.11}$$

$$\langle \delta\omega \rangle \approx \frac{2^{\rm o}}{e} \tag{4.12}$$

Solutions for the remaining five parameters M_1, M_2, τ, i, and A_I are all correlated with each other (see Fig. 4.6). Moreover, unlike P, t_o, e, and ω, which have relatively symmetric Gaussian errors, the probability density functions of M_1, M_2, τ, i, and A_I are mildly to significantly asymmetric. The three parameters M_1, τ, and A_I are especially correlated along the observed magnitude $\langle I \rangle$. In other words, solutions with more massive primaries M_1 require younger ages τ and higher extinctions A_I to produce the same observed I-band flux. The secondary mass M_2 is also anticorrelated with τ. Finally, the inclination i mildly depends on the three parameters M_1, τ, and A_I that are significantly correlated with each other.

Although M_1, M_2, τ, i and A_I are correlated with each other, there is sufficient information in the observed light curves and our constraints (e.g., distance, evolutionary tracks, dust reddening law) to break the degeneracies and provide unique solutions (see also §4.3.1). For example, if we were to fix the primary mass at $M_1 = 11.0$ $M_\odot$ (i.e., the 2.5σ upper limit according to the probability density function in Fig. 4.6), the other parameters would converge to $M_2 = 7.1$ $M_\odot$, $\tau = 3.6$ Myr, $i = 86.35^o$, and $A_I = 0.45$ mag with a fit statistic that is $\Delta\chi^2 = 6.7$ larger than the best-fit solution. For this larger primary mass, there is no combination of τ and A_I that can satisfactorally reproduce the observed magnitude $\langle I \rangle$ and color $\langle V - I \rangle$. Similarly, if we were to fix the primary mass at $M_1 = 9.2$ $M_\odot$ (i.e., the 2.5σ lower limit), the other parameters would converge to $M_2 = 6.1$ $M_\odot$, $\tau = 13.3$ Myr, $i = 86.08^o$, and $A_I = 0.39$ mag with a fit statistic that is $\Delta\chi^2 = 5.8$ larger than the best-fit solution. In this case, the component masses both decrease by ≈12% (to maintain the same ratio of eclipse depths $\Delta I_1/\Delta I_2$), and so the orbital separation a decreases by 4% according to Kepler's third law. The relative sum of the radii $(R_1 + R_2)/a$, which derives directly from the sum of eclipse

widths $\Theta_1 + \Theta_2$, is measured to 1% precision in our NIGHTFALL light curve models. If a decreases by 4%, then $R_1 + R_2$ must also decrease by ≈4%. According to the MS stellar evolutionary tracks, if M_1 and M_2 decrease by 12%, then the radii R_1 and R_2 decrease by 9% given the same age τ = 7.2 Myr. Hence, the age must increase to τ = 13.3 Myr so that the sum of radii $R_1 + R_2$ only decreases by 4%. If the masses decrease, the radii decrease, and the age increases, then the temperatures T_1 and T_2 both decrease according to the stellar evolutionary constraints. However, if R_1 and T_1 both decrease, it is difficult to maintain the same values of $\langle I \rangle$ and $\langle V - I \rangle$ with only one free extra paramter A_I. Hence, there is no combination of M_2, τ, and A_I that can satisfactorily reproduce the observed values of $\Delta I_1/\Delta I_2$, $\Theta_1 + \Theta_2$, $\langle I \rangle$, and $\langle V - I \rangle$ if M_1 = 9.2 $M_\odot$. This line of reasoning holds for all EBs in our sample, and so the physical model parameters will always have unique solutions with finite measurement uncertainties. For ID-2142, we measure formal 1σ measurement uncertainties of $\delta M_{1,\rm meas} \approx 0.04 M_1 \approx 0.5$ $M_\odot$, $\delta M_{2,\rm meas} \approx 0.07 M_2 \approx 0.4$ $M_\odot$, $\delta \tau_{\rm meas} \approx 0.25\tau \approx 1.8$ Myr, $\delta i_{\rm meas} \approx 0.1^{\rm o}$, and $\delta A_{I,\rm meas} \approx 0.01 A_I \approx 0.006$ mag. We find similar percentage measurement uncertainties in these parameters for the 130 well-defined EBs in our sample.

The systematic uncertainties in M_1, M_2, τ, i and A_I can be considerably larger and derive from a variety of sources. We first investigate the systematic uncertainties in the adopted bolometric corrections. Our B-type MS primaries and secondaries span a large range of temperatures $T \approx$ 10,000 - 30,000 K and therefore a broad interval of bolometric corrections $BC = M_{\rm bol} - M_V \approx -3.0$ - -0.3 mag (Pecaut & Mamajek 2013). For the hottest stars in our sample with $T \approx$ 30,000 K and $BC \approx -3.0$, the bolometric corrections are uncertain by $\delta BC \approx 0.2$ mag, i.e. $\delta BC/BC \approx 7\%$ (Bertelli et al. 2009;

Pecaut & Mamajek 2013). To propagate this systematic uncertainty into our solution for ID-2142, we decrease the absolute magnitudes of the bolometric corrections by 7% and repeat our fitting routine from §4.3.1. The NIGHTFALL light curve models now converge to a final solution of $M_1 = 9.3$ $M_\odot$, $M_2 = 6.3$ $M_\odot$, $\tau = 7.5$ Myr, $i = 86.35^o$, and $A_I = 0.40$ mag. The main effect of decreasing $|BC|$ is to decrease the masses M_1 and M_2. This is because more of the flux is radiated in the optical and so the component luminosities need to be reduced to maintain the same observed magnitude $\langle I \rangle$. Fortunately, the mass ratio $q = M_2/M_1$ is not significantly affected by the uncertainties in the bolometric corrections. The decrease in masses lead to slightly longer ages (to maintain the observed eclipse widths), higher inclinations (to maintain the observed eclipse depths), and lower extinctions (to maintain the observed color). The systematic uncertainties in the physical model parameters due to the uncertainties in the bolometric corrections are therefore $\delta M_{1,\rm BC} = 0.11 M_1 = 1.1$ $M_\odot$, $\delta M_{2,\rm BC} = 0.08 M_2 = 0.5$ $M_\odot$, $\delta \tau_{\rm BC} = 0.04\tau = 0.3$ Myr, $\delta i_{\rm BC} = 0.18^o$, and $\delta A_{I,\rm BC} = 0.1 A_I = 0.04$ mag. Because the primary mass M_1 is mainly dictated by the observed $\langle I \rangle$ and the bolometric corrections, we expect similar percentage systematic uncertainties in M_1, M_2, τ, i, and A_I for the other EBs in our sample.

We next propagate the uncertainties in the intrinsic colors, observed colors, and dust reddening law. The uncertainty in the intrinsic colors of B-type MS stars are ≈0.01 - 0.02 mag (Pecaut & Mamajek 2013), the color calibrations of stars in the OGLE-III LMC database are also uncertain by ≈0.01 - 0.02 mag (Udalski et al. 2008), and the coefficient in our adopted dust reddening law $E(V - I) = 0.70 A_I$ has a ≈10% uncertainty (Cardelli et al. 1989; Schlegel et al. 1998; Fitzpatrick 1999; Ngeow & Kanbur 2005). The systematic uncertainty in the dust extinction A_I due to dust/color uncertainties is

therefore $\delta A_{I,\rm dust/color} = \max\{0.02 \text{ mag}, 0.1A_I\}$. To confirm this estimate, we replace the dust reddening law with $E(V-I) = 0.63A_I$ in our models for ID-2142 and repeat our fitting routine from §4.3.1. As expected, we measure $A_I = 0.48$ mag, i.e. the dust extinction increased by $\delta A_I = 0.1A_I = 0.04$ mag, while the other parameters do not vary beyond the measurement uncertainties.

We finally investigate the uncertainties in the stellar evolutionary tracks, including the effects of metallicity and rotation. We replace the Z = 0.008 tracks from Bertelli et al. (2009) with the Z = 0.006 non-rotating models from Georgy et al. (2013). We refit ID-2142 and measure $M_1 = 10.5$ M$_\odot$, $M_2 = 6.8$ M$_\odot$, $\tau = 9.0$ Myr, $i = 86.38^{\rm o}$, and $A_I = 0.45$ mag. Hence, the systematic uncertainties in the stellar evolutionary models, including our ability to interpolate between the tracks, dominates the uncertainty in the age $\delta\tau_{\rm track} = 0.26\tau = 1.9$ Myr and inclination $\delta i_{\rm track} = 0.21^{\rm o}$. We then replace the evolutionary tracks with the Z = 0.006 tracks from Georgy et al. (2013) that are rotating on the zero-age MS at $v/v_{\rm crit} = 50\%$ the critical break-up velocity. We note that ≈80% of B-type MS stars are rotating at $v \lesssim 0.5v_{\rm crit} \approx 250$ km s^{-1} (Abt et al. 2002; Levato & Grosso 2013), and our EBs with intermediate orbital periods $P = 20$ - 50 days may have tidally evolved toward slower rotational velocities. B-type MS stars initially rotating at $v/v_{\rm crit} = 0.5$ have equatorial radii that are only ≈(3 - 4)% larger than their polar radii, but MS lifetimes $\tau_{\rm MS}$ that are 20% longer (Georgy et al. 2013). It is therefore the differences in the evolutionary tracks of stars with rotation, not the distortions in their shapes, that can significantly affect our model solutions. We refit ID-2142 with the rotating non-synchronized stellar models, and measure $M_1 = 10.5$ M$_\odot$, $M_2 = 6.9$ M$_\odot$, $\tau = 8.6$ Myr, $i = 86.30^{\rm o}$, and $A_I = 0.45$ mag. For ID-2142, the differences between the non-rotating and rotating tracks from Georgy et al. (2013) are within the measurement

uncertainties. This is because the tracks with $v/v_{\rm crit} = 0.5$ do not significantly deviate from their non-rotating counterparts until the ages reach $\tau > 0.8\tau_{\rm MS}$ the non-rotating MS lifetimes. For ID-2142 and the majority of EBs in our sample with primary ages $\tau < 0.8\tau_{\rm MS}$, the uncertainties due to the effects of rotation are negligible. For the few systems that are extremely young ($\tau < 1$ Myr) or old ($\tau > 0.8\tau_{\rm MS}$), we expect slightly larger systematic uncertainties in the ages and masses.

By adding the measurement uncertainties and various systematic uncertainties above in quadrature, we estimate the total median 1σ uncertainties for the 130 well-defined EBs to be:

$$\langle \delta M_1 \rangle \approx 0.15 M_1 \tag{4.13}$$

$$\langle \delta M_2 \rangle \approx 0.15 M_2 \tag{4.14}$$

$$\langle \delta \tau \rangle \approx \max\{0.5 \text{ Myr},\ 0.35\tau\} \tag{4.15}$$

$$\langle \delta i \rangle \approx 0.4^{\rm o} \tag{4.16}$$

$$\langle \delta A_I \rangle \approx \max\{0.03 \text{ mag},\ 0.15 A_I\} \tag{4.17}$$

For these five parameters, the uncertainties are dominated by the systematic uncertainties in the bolometric corrections, dust reddening law, and evolutionary tracks. For older

EBs with primary ages $\gtrsim$80% their MS lifetimes, the total uncertainties in the masses $\langle \delta M_1 \rangle \approx 0.2 M_1$ and $\langle \delta M_2 \rangle \approx 0.2 M_2$ and ages $\langle \delta \tau \rangle \approx 0.45 \tau$ are slightly larger due to the effects of rotation.

Some of our EB light curve model solutions can be biased due to contamination with a third light source, e.g., a tertiary companion or a background/foreground object along similar lines of sight. In Papers I and II, we estimated that only ≈10% of our B-type MS EBs in the LMC can be contaminated by a third light source that is bright enough to significantly contribute to the systematic uncertainties. Unlike the previously discussed sources of systematic uncertainties that contribute to all 130 well-defined EBs, contamination by a third light source affects only a small subset of our sample.

In addition to calculating the uncertainties for the nine independent physical model parameters, we also estimate the uncertainties in the dependent physical properties. The total uncertainties in M_1 and M_2 are ≈15% but slightly correlated with each other (see above). The total median uncertainty in the mass ratio is therefore $\langle \delta q \rangle = \max\{0.03,\, 0.12q\}$. Because the quantity $(R_1+R_2)/a$ is precisely constrained from the observed eclipse widths, the uncertainties in R_1, R_2, and a mainly derive from the uncertainties in M_1 and M_2 according to Kepler's third law. We measure $\langle \delta R_1 \rangle \approx 0.07 R_1 \approx 0.3 \mathrm{R}_\odot$, $\langle \delta R_2 \rangle \approx 0.07 R_2 \approx 0.2\ \mathrm{R}_\odot$, and $\langle \delta a \rangle \approx 0.06 a \approx 6\ \mathrm{R}_\odot$. Finally, given the ≈(20 - 30)% uncertainties in the luminosities (primarily due to uncertainties in the bolometric corrections) and the ≈7% uncertainties in the radii, the uncertainties in the temperatures are ≈8% according to the Stefan-Boltzmann law. Hence, the total median uncertainties are $\langle \delta T_1 \rangle \approx 0.08 T_1 \approx 1{,}500$ K and $\langle \delta T_2 \rangle \approx 0.08 T_2 \approx 1{,}100$ K.

4.4 EB Trends

In our sample of 130 EBs, several trends and correlations exist among the nine physical model properties. Most of these trends are caused by geometrical and evolutionary selection effects in our magnitude-limited sample of EBs. We correct for these selection effects in the third stage of our pipeline (§4.5). Two correlations, however, are intrinsic to the population of binaries with B-type MS primaries. In this section, we first discuss these two empirical relations we uncovered from the data, and then we explain the trends that are caused by selection effects.

In Fig. 4.7, we display the measured I-band dust extinctions A_I as a function of age τ for the 130 well-defined EBs. These two parameters are anticorrelated (Spearman rank correlation coefficient $\rho = -0.34$) at a statistically significant level (probability of independence $p = 8{\times}10^{-5}$). We fit a log-linear trend to the total population of 130 EBs (green line in Fig. 4.7):

$$A_{I,\mathrm{total}}\,(\mathrm{mag}) = 0.39 - 0.07 \log\Big(\frac{\tau}{1\,\mathrm{Myr}}\Big) \tag{4.18}$$

The slope in the above relation may be biased toward negative values due to a photometric selection effect in our magnitude-limited sample. Specifically, EBs that are intrinsically bluer and more luminous systematically contain younger, short-lived, more massive primaries. These blue, luminous, younger EBs may therefore require larger dust extinctions and reddenings to satisfy our photometric selection criteria (and vice versa). In Fig. 4.8, we show the measured absolute magnitudes M_I and intrinsic colors $\langle V-I\rangle_{\mathrm{o}}$ as a function of dust extinction A_I for our 130 well-defined EBs. We also display our

photometric selection criteria based on the observed magnitudes $16.0 < \langle I \rangle < 17.6$ and observed colors $-0.25 < \langle V - I \rangle < 0.20$ (green lines). Indeed, there are several intrinsically red, low-luminosity, older EBs with $M_I \approx -1.2$ that are in our sample only because they have small dust extinctions $A_I \approx 0.2$ mag. If they were to have slightly higher dust extinctions, they would fall below our selection limit of $\langle I \rangle = 17.6$ (see Fig. 4.8).

In §4.5, we account for our photometric selection criteria when analyzing all 130 EBs in our well-defined sample. Here, we correct for photometric selection effects by further culling our sample according to the intrinsic properties of M_I and $\langle V - I \rangle_{\rm o}$. To obtain an unbiased subsample, we can choose EBs across any interval of M_I and $\langle V - I \rangle_{\rm o}$ that also satisfies our selection criteria on observed magnitudes and colors. To retain most of the sample, we select the regions enclosed by $-2.63 < M_I < -1.35$, $-0.341 < \langle V - I \rangle_{\rm o} < -0.115$, and $0.13 < A_I\,({\rm mag}) < 0.45$ (red lines in Fig. 4.8). The 98 EBs that satisfy these extra selection criteria (filled blue systems in Fig. 4.8) represent an unbiased sample relatively free from photometric selection effects.

Even within this unbiased sample of 98 EBs, the intrinsic colors $\langle V - I \rangle_{\rm o}$ and dust extinctions A_I are still anticorrelated ($\rho = -0.25$) at a statistically significant level ($p = 0.02$). As can be observed in the bottom panel of Fig. 4.8, there are relatively few intrinsically blue systems $\langle V - I \rangle_{\rm o} \approx -0.30$ with small dust extinctions $A_I \approx 0.2$ mag. Similarly, there are few intrinsically redder EBs $\langle V - I \rangle_{\rm o} \approx -0.15$ with large dust extinctions $A_I \approx 0.4$ mag. Intrinsically bluer EBs contain hot primaries that are systematically more massive, short-lived, and younger. Hence, the anticorrelation between age τ and dust extinction A_I is real.

In Fig. 4.8, we also display τ and A_I for the 98 EBs (filled blue) in our unbiased subsample. Although not as prominent, the ages τ and dust extinctions A_I for the 98 EBs in our unbiased sample are still anticorrelated ($\rho = -0.23$) at a statistically significant level ($p = 0.02$). For example, there is a complete absence of EBs with $A_I < 0.2$ mag at $\tau < 15$ Myr. In contrast, there are many EBs in our unbiased sample

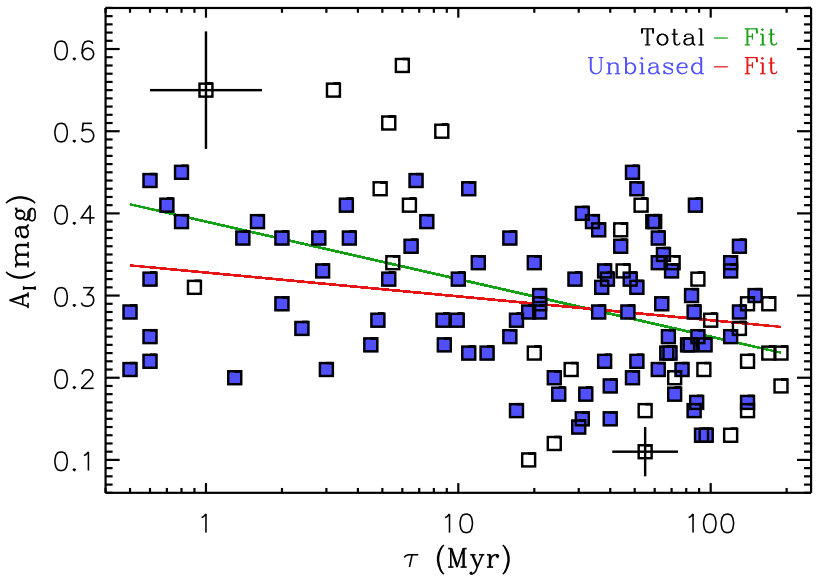

Figure 4.7: Measured I-band dust extinctions A_I and ages τ for the 130 EBs in our well-defined sample (black squares). We display representative uncertainties for two systems in opposite corners of this parameter space. We also display our unbiased subsample of 98 EBs that is relatively free from photometric selection effects (filled blue). The dust extinctions clearly diminish with age, even within our unbiased subsample, demonstrating the dust content in stellar environments systematically decreases with time. We fit a log-linear relation to the total population (green) and unbiased subsample (red). The latter is an empirical age-extinction relation that can be implemented when modeling other stellar populations.

with $A_I = 0.1$ - 0.2 mag at $\tau > 15$ Myr. The intrinsic anticorrelation between A_I and τ in our unbiased sample demonstrates a relationship between dust content and ages of

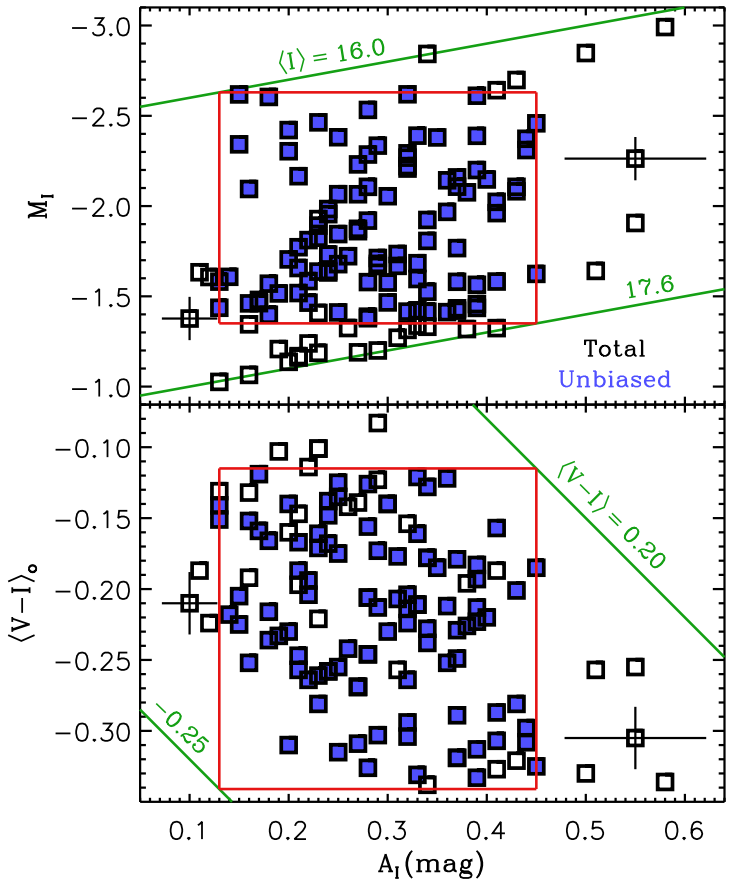

Figure 4.8: Measured absolute magnitudes M_I (top) and intrinsic colors $\langle V-I\rangle_o$ (bottom) as a function of dust extinction A_I for our 130 well-defined EBs (black squares; representative errors shown for two systems). We also display the limits on observed magnitudes $\langle I\rangle$ and observed colors $\langle V-I\rangle$ imposed by our photometric selection criteria (green lines). The 98 EBs (filled blue) that are enclosed by both red regions are relatively free from photometric selection effects. Even within our unbiased sample, intrinsically bluer EBs that contain hotter, more massive, younger primaries favor larger dust extinctions.

stellar environments. Young EBs, and young B-type MS stars in general, with $\tau \approx 1$ Myr are embedded in dusty envelopes and/or molecular clouds with photometric extinctions $A_I \approx 0.33$ mag. Meanwhile, older EBs with $\tau \approx 100$ Myr reside in less attenuating environments with $A_I \approx 0.26$ mag. We fit a log-linear trend to the unbiased sample of 98 EBs:

$$A_{I,\mathrm{unbiased}}\,(\mathrm{mag}) = 0.33 - 0.03 \log\Big(\frac{\tau}{1\,\mathrm{Myr}}\Big) \tag{4.19}$$

valid for 0.5 Myr $< \tau <$ 200 Myr (red line in Fig. 4.8). Even after accounting for selection effects, the value of and measurement uncertainty in the slope -0.029 ± 0.011 is still inconsistent with zero at the 2.6σ confidence level. This is a similar probability of significance based on the Spearman rank test above (probability of no correlation $p = 0.02$ between A_I and $\langle V - I \rangle_{\mathrm{o}}$). The ≈30% systematic uncertainty in the ages τ and ≈10% systematic uncertainty in the extinctions A_I propagate into Eqn. 4.19. The values of and total uncertainties are therefore -0.029 ± 0.014 for the slope and 0.33 ± 0.04 mag for the mean dust extinction at $\tau \approx 1$ Myr. The rms in the measured dust extinctions A_I around the above relation is $\sigma = 0.08$ mag.

It had been previously known that younger early-type stars in the LMC experience slightly higher dust extinctions than late-type stars (Zaritsky 1999; Zaritsky et al. 2004). In the present study, we have measured the relationship between age τ and dust extinction A_I. Quantifying age-dependent dust extinctions is crucial when analyzing the spectral energy distributions of unresolved stellar populations in distant galaxies (Panuzzo et al. 2007; Silva et al. 2011). Young O- and B-type stars, which dominate the ultraviolet component in star-forming galaxies, will experience systematically higher

dust extinctions than the older, redder stars. To accurately constrain the star-formation histories of these galaxies, it is imperative to account for age-dependent dust extinctions. We note that different galaxies and stellar populations will have slightly different dust extinctions as a function of age. Nonetheless, our empirical age-extinction relation (Eqn. 4.19) can provide insight when calibrating models of unresolved stellar populations.

Zaritsky et al. (2004) found that the dust extinction distribution toward young, hot stars in the LMC peaks at $A_I \approx 0.25$ mag with a long tail toward higher values. This is consistent with our total population of 130 EBs with B-type MS primaries (see Fig. 4.9). By dividing our EB population into young ($\tau \leq 12$ Myr) and old ($\tau > 12$ Myr) subsamples, we find that both subsamples can be fitted with simple Gaussians centered

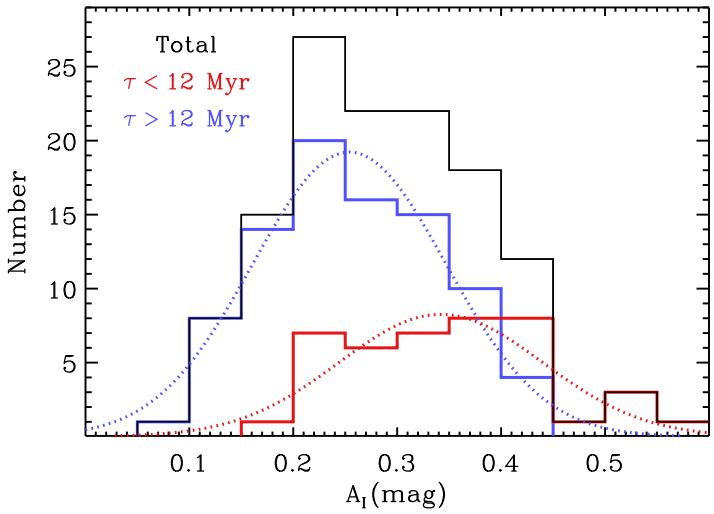

Figure 4.9: Distribution of I-band dust extinctions A_I for the total population of 130 EBs (black), 42 EBs with ages $\tau \leq 12$ Myr (red), and 88 EBs with $\tau > 12$ Myr (blue). Although the total population peaks at $A_I \approx 0.25$ mag with a long tail toward high dust extinctions, the young and old subsamples can each be accurately described with Gaussian distributions (dotted) centered at $A_I \approx 0.34$ mag and $A_I \approx 0.25$ mag, respectively.

at $A_I \approx 0.34$ mag and $A_I \approx 0.25$ mag, respectively. Hence, the non-Gaussian distribution of dust extinction may be simply due to a selection effect with age. The very young EBs, which represent a small fraction of the total population, occupy the long tail toward large dust extinctions. Meanwhile, the long-lived EBs, which comprise the majority of the sample, form the peak in the distribution at $A_I \approx 0.25$ mag.

We now examine the second physically-genuine trend in our EB population. In Fig. 4.10, we show the measured eccentricities e as a function of age τ for the 130 EBs in our well-defined sample. The eccentricities and ages are anticorrelated (Spearman rank correlation coefficient $\rho = -0.39$) at a statistically significant level (probability of no correlation $p = 5{\times}10^{-6}$).

This observed anticorrelation is primarily because eccentricities decrease with time due to tidal evolution. The observed trend may be accentuated by a secondary effect, whereby EBs with more massive, short-lived primaries favor larger eccentricities. However, this relation between primary mass M_1 and eccentricity e cannot fully explain the observed anticorrelation between τ and e. For example, the eccentricities and ages of the 32 EBs with massive primaries $M_1 \approx 8.5$ - $13.9\,\mathrm{M}_\odot$ are still anticorrelated ($\rho = -0.44$) at a statistically significant level ($p = 0.01$). Similarly, the 98 less massive EBs with $M_1 \approx 3.6$ - $8.5\,\mathrm{M}_\odot$ have eccentricities and ages that are anticorrelated ($\rho = -0.28$) at a statistically significant level ($p = 0.005$). Although EBs with early-B primaries may be born with systematically larger eccentricities, the anticorrelation between age τ and eccentricity e is dominated by tidal evolution and is observed in both early-B and late-B MS subsamples.

For late-type stars with $M \lesssim 1.3\ \mathrm{M}_\odot$, orbital energy is most efficiently dissipated

into the interior of the stars via convective eddies in the stellar atmospheres (Zahn 1977; Hut 1981; Zahn 1989; Hurley et al. 2002). This equilibrium tide model for convective damping has been tested against observations of late-type binaries in various environments with different ages (Meibom & Mathieu 2005). For more massive stars $M > 1.3$ $M_{\odot}$ with radiative envelopes, such as our B-type MS stars, tides operate dynamically via oscillations in the stellar interiors (Zahn 1975; Hurley et al. 2002). By estimating the ages of 130 early-type EBs, we have measured the evolution of binary eccentricities due to dynamical tides with radiative damping.

The slope of the observed age-eccentricity anticorrelation provides insight into the

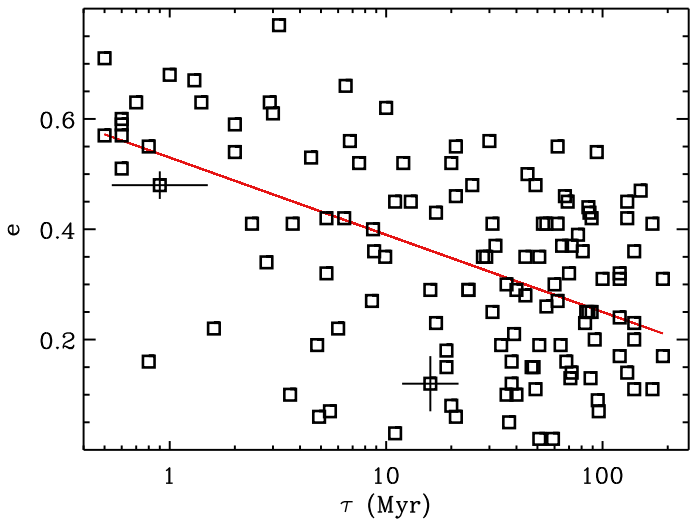

Figure 4.10: Measured eccentricities e and ages τ for the 130 EBs in our well-defined sample (black squares; representative uncertainties shown for two systems). Binaries with B-type MS primaries and intermediate orbital periods are preferentially born with large eccentricities, which suggest they formed via dynamical interactions and/or tidal capture. Moreover, the observed slope (red line) in the age-eccentricity anticorrelation provides a constraint for dynamical tides in hot MS stars with radiative envelopes.

tidal evolution of highly eccentric binaries. We fit a log-linear trend to the observations (red line in Fig. 4.10):

$$e_{\rm fit} = 0.53 - 0.14 \log\Big(\frac{\tau}{1\,{\rm Myr}}\Big) \tag{4.20}$$

The value of and measurement uncertainty in the slope is -0.14 ± 0.03. Hence, the slope is negative at the 5σ confidence level, similar to the statistical significance determined from the Spearman correlation test above. Again, systematic uncertainties in the ages τ and eccentricities e contribute to the uncertainties in the coefficients in Eqn. 4.20. After calculating the total uncertainties, we find the mean eccentricity at $\tau \approx 1$ Myr is 0.53 ± 0.05 while the slope is -0.14 ± 0.05. The rms scatter in the measured eccentricities around the above relation is $\sigma_e \approx 0.16$.

The intercept in Eqn. 4.20 implies a circularization timescale of $\tau_{\rm circ} \approx 5$ Gyr for our EBs with B-type MS primaries and moderate orbital periods $P \approx 20$ - 50 days. However, tidal damping is not as efficient when the orbits become less eccentric (Hut 1981). The true circularization timescale may therefore be longer if the age-eccentricity relation flattens beyond $\tau > 200$ Myr. Conversely, older EBs have systematically larger components (see Fig. 4.5), and so tidal damping may become more efficient as the primary fills a larger fraction of its Roche lobe. In any case, these short-lived B-type MS primaries will expand beyond $R_1 \gtrsim 10\,{\rm R}_\odot$ and evolve toward the giant branch long before the orbits are completely circularized.

Our young EBs with generally large eccentricities experience extreme tidal forces. In fact, a few of the EBs with $e > 0.6$ in our sample have modest Roche-lobe fill-factors $RLFF \approx 0.3$ at periastron. Tidal evolution of highly eccentric binaries is quite

complicated, especially considering second-order effects and non-linear terms can become quite important (Hut 1981). A full analysis of tidal evolution in our EB sample is therefore not within the scope of the present study. Nonetheless, the observed age-eccentricity anticorrelation provides a constraint for models of tidal evolution in highly eccentric early-type binaries.

In Fig. 4.11, we display the cumulative distribution function of the eccentricities for the 128 EBs with $e \leq 0.68$ (green). We do not consider the two EBs with $e = 0.71$ and 0.77 because highly eccentric binaries are not complete in our EB sample (see below and §4.5). Moreover, as discussed above, binaries with $P = 20\text{-}50$ days and $e = 0.7\text{-}0.8$ nearly fill their Roche lobes at periastron, and are expected to evolve toward smaller

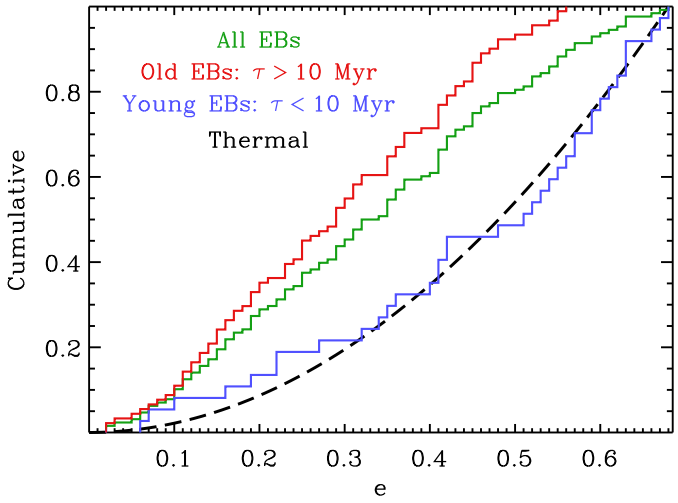

Figure 4.11: Cumulative distributions of eccentricities e for all 128 EBs with $e < 0.68$ (green) and subsamples of 91 old EBs with $\tau > 10$ Myr (red) and 37 young EBs with $\tau \leq 10$ Myr (blue). The young population is fully consistent with a thermal eccentricity distribution (dashed black), indicating early-type binaries at intermediate orbital periods were dynamically captured.

eccentricities on rapid timescales. In Fig. 4.11, we also divide our sample into the 91 old EBs with $\tau > 10$ Myr (red) and 37 young EBs with $\tau \leq 10$ Myr (blue). Using a maximum likelihood method, we fit a power-law eccentricity probability distribution $p_e \propto e^{\eta}$ to the observed EBs. We measure $\eta = 0.1 \pm 0.2$, -0.1 ± 0.2, and 0.8 ± 0.3 for the total, old, and young EB samples, respectively. Our total population of EBs ($\eta = 0.1 \pm 0.2$) is consistent with the flat distribution ($\eta = 0$) observed by Abt (2005) for his sample of binaries with B-type MS primaries and intermediate orbital periods.

If the orbital velocities and energies of a binary population follow a Maxwellian "thermal" probability distribution, then the eccentricity probability distribution $p_e = 2e\,de$ will be weighted toward large eccentricities (Ambartsumian 1937). Such a population of eccentric and thermalized binaries would suggest the binaries formed through dynamical interactions, either through tidal / disk capture, dynamical perturbations in a dense cluster, three-body exchanges, and/or Kozai cycles with a tertiary companion (Heggie 1975; Pringle 1989; Turner et al. 1995; Kroupa 1995; Kiseleva et al. 1998; Naoz & Fabrycky 2014). Surprisingly, the observed population of 37 young EBs ($\eta = 0.8 \pm 0.3$) is fully consistent with a thermal eccentricity probability distribution ($\eta = 1$; dashed black line in Fig. 4.11). This indicates that massive binaries with intermediate orbital periods formed via dynamical interactions on rapid timescales $\tau <$ 5 Myr.

Previous observations of spectroscopic (Duquennoy & Mayor 1991) and visual (Harrington & Miranian 1977) solar-type binaries have indicated a thermal eccentricity distribution. However, these studies recovered the thermal eccentricity distribution only after applying large and uncertain correction factors for incompleteness. In both the spectroscopic and visual binary surveys, the raw samples were weighted significantly

toward smaller eccentricities relative to the thermal distribution. In addition, more recent and complete observations of solar-type (Abt 2006; Raghavan et al. 2010) and early-type (Abt 2005) binaries at intermediate orbital periods have revealed a uniform eccentricity distribution that is clearly discrepant with a thermal distribution.

Our raw sample of young early-type EBs is only slightly biased toward small eccentricities. In fact, the small excess of young EBs with $e \approx 0.1$ - 0.3 relative to the thermal distribution in Fig. 4.11 would be reduced after correcting for selection effects. In other words, we expect even better agreement between our sample of young early-type EBs and the thermal eccentricity distribution after considering observational biases (§4.5). By choosing only the EBs with young ages, we have probed the initial binary properties of massive stars shortly after their formation. For the first time, we have directly observed the theoretical thermal eccentricity distribution before tides have dramatically reduced the eccentricities.

In the following, we compare other physical model parameters and examine additional trends that could be caused by observational biases. We use these observed distributions to further justify our selection criteria in §4.2. We also motivate the necessity for incompleteness corrections and Monte Carlo simulations, which we perform in §4.5.

We display the measured eccentricities e as a function of mass ratio q in Fig. 4.12. A Spearman rank test reveals no statistically significant correlation ($p = 0.25$). The mass ratios q of early-type binaries are independent of their eccentricities e at intermediate orbital periods $P = 20$ - 50 days.

In §4.2 (see item D), we removed 23 EBs with nearly identical primary and

secondary eclipses separated by ≈50% in orbital phase. We concluded the majority of these systems have half their listed orbital periods, and therefore exhibit only one eclipse per orbit. If we were to fit physical models to these systems assuming the listed orbital periods, they would all have $q > 0.84$ and $e < 0.08$ (blue diamonds within red region of Fig. 4.12). A concentration of 23 EBs in this small corner of the parameter space is highly unlikely considering the density of systems in the surrounding phase space is substantially smaller. We expect only 3 - 5 of the 23 EBs to be twins in nearly circular

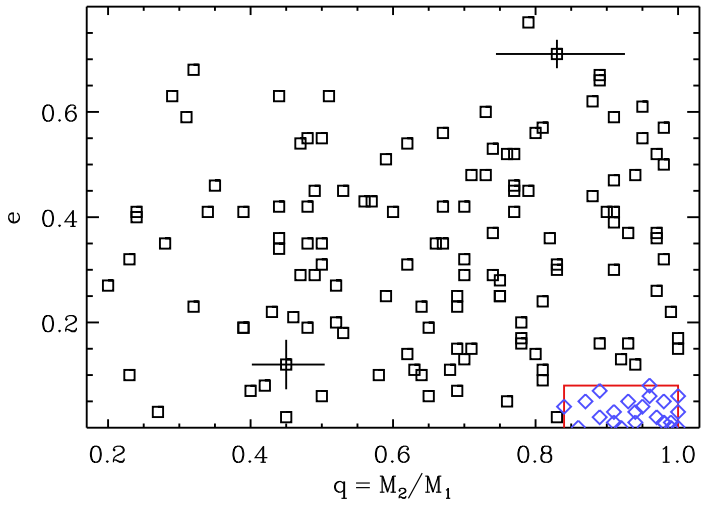

Figure 4.12: Measured eccentricities e versus mass ratios $q = M_2/M_1$ for the 130 well-defined EBs (squares; representative errors shown for two systems). There is no evidence for a statistically significant correlation between q and e in our sample. We removed 23 EBs that have ambiguous orbital periods (see item D in §4.2). If we were to fit these 23 systems using the listed periods, they would all have $q > 0.84$ and $e < 0.08$ (blue diamonds enclosed within red lines). Such a dense population in this corner of the parameter space is highly unlikely, so it was justifiable to exclude these 23 systems from our well-defined sample.

orbits with the listed orbital periods. Given only the photometric data, however, we cannot easily determine which of the systems are truly twins with small eccentricities and which have half the listed orbital periods. In §4.2, we simply excluded all 23 EBs with ambiguous periods, and we account for the incidental removal of the 3 - 5 genuine systems in §4.5. We emphasize that most of the 23 EBs with ambiguous orbital periods have half the listed values, and therefore it was appropriate to remove these systems.

In Fig. 4.13, we compare the measured eccentricities e to the arguments of periastron ω for the 130 well-defined EBs. Assuming random orientations, the periastron angle should be uniformly distributed across $0^{\rm o} \leq \omega < 360^{\rm o}$. However, the observed systems are not evenly concentrated across all ω and e. We notice two observational biases in the data, both of which are due to geometrical selection effects.

First, for modest to large eccentricities $e > 0.4$, the EBs cluster near $\omega = 0^{\rm o}$ and $\omega = 180^{\rm o}$. In fact, the two systems with $e \approx 0.7$ - 0.8 have $\omega \approx 0^{\rm o}$. For EBs with $\omega = 90^{o}$ or $\omega = 270^{o}$, one of the eclipses would occur at periastron while the other at apastron. The eclipse at periaston would be quite narrow according to Kepler's second law, and may be too narrow to be accurately measured given the cadence of the OGLE-III data (see item B in §4.2). If the inclination is not sufficiently close to edge-on, e.g. $i \approx 87^{\rm o}$, then the eclipse at apastron may be too shallow to be accurately measured (again, see item B in §4.2). If the inclination was even smaller, e.g. $i \approx 85^{\rm o}$, the projected separation at apastron could be large enough so there would be no secondary eclipse. These systems would exhibit only one eclipse per orbit such as those presented in item A of §4.2. Considering the above, it is extremely difficult to observe and measure highly eccentric EBs with eclipses that occur near periastron and apastron. As the eccentricity increases, well-defined EBs are only detected as the argument of periastron approaches

$\omega \approx 0^{\rm o}$ or $\omega \approx 180^{\rm o}$.

Second, there is an overabundance of EBs with $\omega \approx 90^{\rm o}$ relative to those with $\omega \approx 270^{\rm o}$. Quantitatively, there are 90 EBs with $0^{\rm o} < \omega < 180^{\rm o}$ and only 40 EBs with $180^{\rm o} < \omega < 360^{\rm o}$. These two values are discrepant at the 4.4σ level according to Poisson statistics. This observational bias is due to our definition of the primary eclipse minimum $t_{\rm o}$, which determines the reference frame for ω. Recall the primary eclipse $\Delta I_1 > \Delta I_2$ at $t_{\rm o}$ must be deeper than the secondary eclipse. If $e \gtrsim 0.2$, $i \lesssim 89^{\rm o}$, and the primary $M_1 > M_2$ is eclipsed closer to apastron, then the eclipse of the most massive luminous component M_1 may actually coincide with the secondary eclipse $\Delta I_2 < \Delta I_1$. Indeed, we found 18 EBs in such a configuration whereby M_1 is eclipsed at Φ_2 and M_2

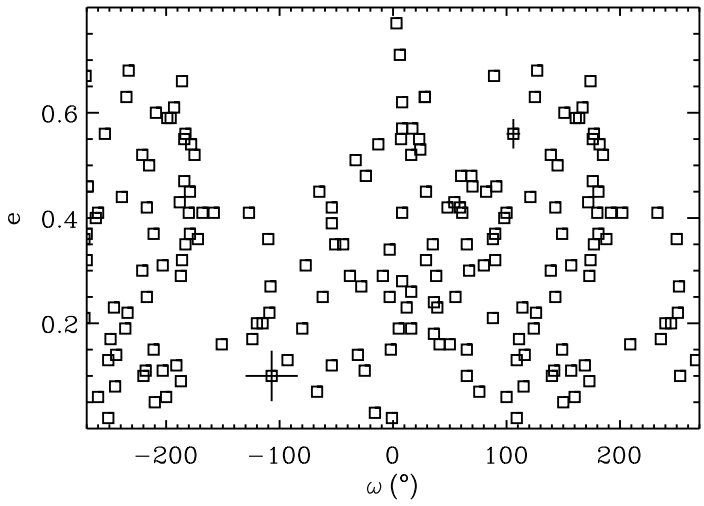

Figure 4.13: Measured eccentricities e as a function of periastron angle ω for the 130 well-defined EBs (squares; representative errors shown for two systems). Note that we display the interval $-270^{\rm o} < \omega < 270^{\rm o}$, so that some of the systems are repeated. For $e \gtrsim 0.4$, the concentration of EBs at $\omega = 0^{\rm o}$ and $\omega = -180^{\rm o} = 180^{\rm o}$ as well as deficit at $\omega = -90^{\rm o} = 270^{\rm o}$ are due to geometrical selection effects.

is eclipsed at t_o (see §4.3 and Table 4.2). Sixteen of these 18 EBs have $0^o < \omega < 180^o$. If we were to define ω according to M_1 instead of in terms of ΔI_1, then 74 EBs would have $0^o < \omega < 180^o$ and 58 EBs would have $180^o < \omega < 360^o$. These two values are now consistent with each other, i.e. they only differ at the 1.4σ significance level.

As indicated above and discussed in §4.2, we suspect the majority of the 48 EBs we removed in items A and B of §4.2 have $e > 0.4$ and either $20^o < \omega < 160^o$ or

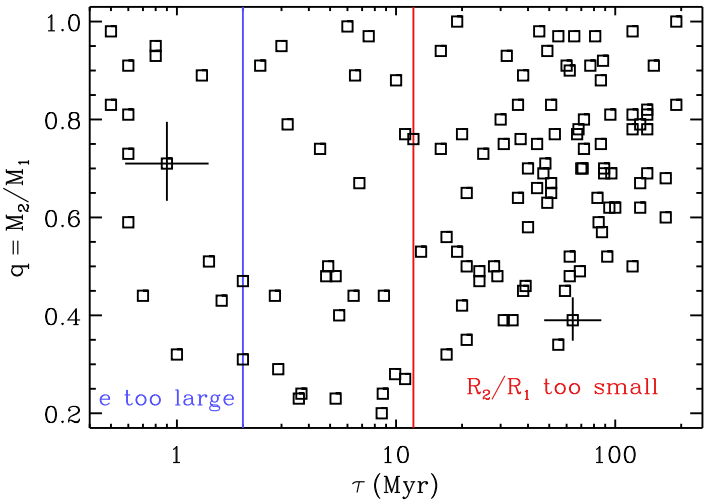

Figure 4.14: Measured mass ratios $q = M_2/M_1$ as a function of age τ for the 130 well-defined EBs (squares; representative errors shown for two systems). At young ages $\tau < 2$ Myr (left of blue line), most EBs are in highly eccentric orbits with $e \approx 0.6$. Because of geometrical selection effects, it is difficult to detect these EBs, especially if they have small, low-mass companions $q < 0.3$. At older ages $\tau > 12$ Myr (right of red line), the primaries are systematically larger. The primary eclipse depths ΔI_1, which are largely determined by R_2/R_1, are therefore shallower. Given the sensitivity of the OGLE-III data, EBs with low-mass companions $q < 0.3$ become undetectable as the primary evolves toward the upper MS.

$200^{\rm o} < \omega < 340^{\rm o}$. We test this hypothesis using the statistics of the measured systems in our well-defined sample. Of the 53 EBs with $e > 0.4$, 22 have $\omega < 20^{\rm o}$, $160^{\rm o} < \omega < 200^{\rm o}$, or $\omega > 340^{\rm o}$. If these 22 systems are complete across the specified intervals of ω, which total $80^{\rm o}$, and if the intrinsic distribution of periastron angles is uniform, then we expect $22 \times 360^{\rm o}/80^{\rm o} = 99$ EBs with $e > 0.4$. We detected only 53 EBs with $e > 0.4$, implying $99 - 53 = 46$ EBs did not satisfy our selection criteria. These 46 EBs most likeley have secondary eclipses that are too narrow, too shallow, or completely absent. This prediction of 46 missing EBs nearly matches the 48 EBs we removed in items A and B of §4.2. This consistency further demonstrates that geometrical selection effects are understood in our sample and the removal of EBs in §4.2 were well-motivated.

We compare the mass ratios q to the ages τ of our 130 EBs in Fig. 4.14. There is a lack of extreme mass-ratio binaries $q < 0.3$ at young ($\tau < 2$ Myr) and old ($\tau > 12$ Myr) ages. The former is due to geometrical selection effects. At extremely young ages, we have shown early-type binaries with intermediate orbital periods favor large eccentricities. In fact, the median eccentricity of the 16 EBs with $\tau \leq 2$ Myr is $\langle e \rangle = 0.59$. At these large eccentricities, the eclipse that occurs closest to apastron will have a larger projected distance, and may therefore have a shallower eclipse (see above). Shallow eclipses are easily missed given the sensitivity and cadence of the OGLE-III observations, especially if the EB contains a small, low-mass companion $q < 0.3$.

The bias against low-mass companions $q < 0.3$ at older ages is primarily due to an evolutionary selection effect. As the primary evolves and expands, the ratio of radii R_2/R_1 decreases and the primary eclipse depth ΔI_1 becomes shallower (see Fig. 4.5 in Paper I). At $\tau \approx 15$ Myr, only companions with $q > 0.3$ produce eclipses $\Delta I_1 \gtrsim 0.15$ mag that are deep enough to be detected given the sensitivity of the OGLE-III data. If the

primary is near the tip of the MS, then $q > 0.45$ is required to produce a visible and well-defined eclipse. Considering the above, only EBs with ages $\tau \approx 2\text{-}12$ are sensitive toward low-mass companions with $q \approx 0.2\text{-}0.3$.

We compare the primary masses M_1 to the mass ratios $q = M_2/M_1$ in Fig. 4.15. There is a clear observational bias such that massive primaries $M_1 = 12\text{-}14\,M_\odot$ contain only small mass ratios $q = 0.2\text{-}0.5$ while late-B MS primaries with $M_1 = 3.6\text{-}4.5\,M_\odot$ include only large mass ratios $q = 0.6\text{-}1.0$. This trend is simply due to the magnitude limits imposed by our photometric selection criteria. Massive MS primaries $M_1 \gtrsim 12\,M_\odot$ with luminous $q \gtrsim 0.6$ MS companions will be brighter than our selection limit of $\langle I \rangle =$

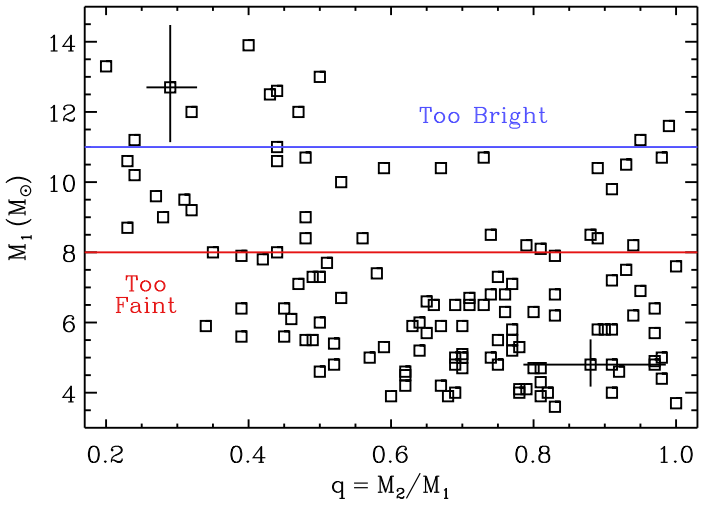

Figure 4.15: Measured primary masses M_1 versus mass ratios $q = M_2/M_1$ for the 130 well-defined EBS (squares; representative errors shown for two systems). Massive primaries $M_1 \gtrsim 11\,M_\odot$ (above blue line) with luminous companions $q > 0.6$ are too bright to be contained in our magnitude-limited sample. Similarly, low-mass primaries $M_1 < 8\ M_\odot$ (below red line) with $q = 0.2\text{-}0.3$ companions are either too faint to satisfy our photometric selection criteria and/or too old and large to produce detectable eclipses.

16.0. Similarly, low-mass primaries with $M_1 \lesssim 5\,M_\odot$ will be fainter than our detection limit of $\langle I \rangle = 17.6$ unless there is a bright companion $q \gtrsim 0.6$ that increases the total luminosity of the system.

The precise mass versus mass-ratio cutoffs in our sample also depend on the age of the binary. For example, older primaries with $M_1 \approx 5\text{-}7\,M_\odot$ on the upper MS will be bright enough $\langle I \rangle < 17.6$ to satisfy our photometric selection criteria. As stated above, EBs with small mass ratios $q = 0.2\text{-}0.3$ produce visible well-defined eclipses with $\Delta I_1 \gtrsim 0.15$ mag only when the primary is relatively small and young. However, young

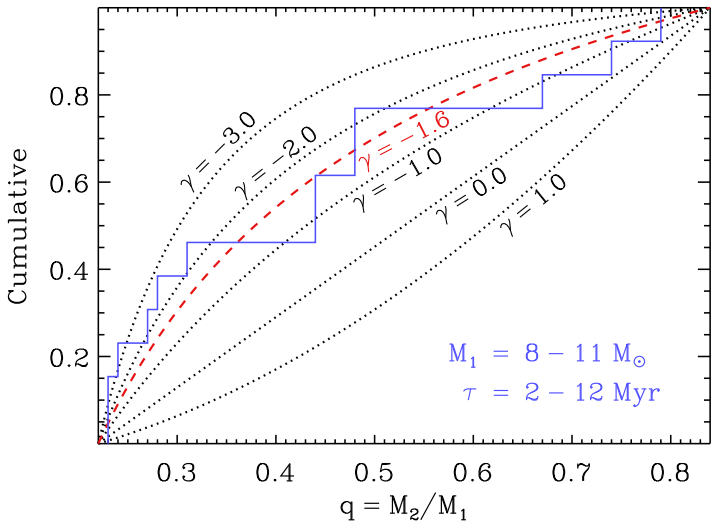

Figure 4.16: Cumulative distribution of mass ratios $q = M_2/M_1$ for the 13 EBs with $M_1 = 8\text{-}11\,M_\odot$, $\tau = 2\text{-}12$ Myr, and $q = 0.22\text{-}0.84$ that are relatively free from selection effects (blue solid line). Assuming the mass-ratio probability distribution $p_q \propto q^\gamma$ can be described by a power-law, we display curves for $\gamma = -3$, -2, -1, 0, and 1 (dotted black). For the 13 unbiased EBs, we measure $\gamma = -1.6 \pm 0.4$ (dashed red), demonstrating binaries with massive primaries $M_1 \approx 10\,M_\odot$ and orbital periods $P = 20\text{-}50$ days are weighted toward small mass ratios $q \approx 0.2\text{-}0.3$.

moderate-mass primaries $M_1 \approx 5\text{-}7\,M_\odot$ with low-luminosity companions are fainter than our detection limit of $\langle I \rangle = 17.6$. Hence, our EB sample is sensitive to extreme mass ratios $q \approx = 0.2\text{-}0.3$ only if $M_1 \gtrsim 7\,M_\odot$. To be conservative, we consider only the primary mass interval $M_1 = 8\text{-}11\,M_\odot$ to be sensitive to companions across the entire interval $q = 0.2\text{-}1.0$ (distinguished by red and blue lines in Fig. 4.15).

Considering the above, our EB sample is relatively unbiased across the mass-ratio interval $q = 0.22\text{-}0.84$ (Fig. 4.12), age interval $\tau = 2\text{-}12$ Myr (Fig. 4.14), and primary mass interval $M_1 = 8\text{-}11\,M_\odot$ (Fig. 4.15). The 13 EBs that are contained in this cube of the three-dimensional phase space therefore represent a small subsample relatively free from geometrical, evolutionary, and photometric selection effects. In Fig. 4.16, we display the cumulative distribution of mass ratios q for these 13 EBs in our unbiased subsample. Using a maximum liklihood technique, we fit a power-law mass-ratio probability distribution $p_q \propto q^\gamma$ to these 13 EBs. We measure $\gamma = -1.6 \pm 0.4$, demonstrating binaries with massive primaries favor extreme mass ratios $q \approx 0.2\text{-}0.3$ at intermediate orbital periods $P = 20\text{-}50$ days.

We emphasize this statistic is based on the small unbiased subsample of the 13 EBs, and therefore valid only for early-B MS primaries with $M_1 \approx 10\,M_\odot$. The median primary mass in our total sample of 130 EBs is $\langle M_1 \rangle \approx 6\,M_\odot$. We therefore utilize our total sample to derive more accurate statistics as well as probe the companion properties of late-B MS stars. In the following section, we correct for selection effects so that we can make full use of all EBs in our well-defined sample.

4.5 Corrected Binary Statistics (Stage III)

For the final stage of our pipeline, we recover the intrinsic binary statistics and distributions by correcting for selection effects. As done in Paper II, we first determine the probability density functions that describe the nine physical model parameters of our EBs (§4.5.1). We then calculate simple estimates for the detection efficiencies (§4.5.2), and then synthesize a large population of EBs via a Monte Carlo technique (§4.5.3). In §4.5.4, we present our results for the intrinsic binary fraction and mass-ratio distribution.

4.5.1 Probability Density Functions

We utilize probability density functions similar to those in Paper II. For example, we assume random epochs of primary eclipse minima t_o, and that the logarithmic orbital periods $\log P$ are uniformly distributed across $P = 20\text{-}50$ days (i.e., Öpik's law; Abt 1983). We select primary masses $M_1 = 3\text{-}30\,M_\odot$ and ages $\tau = 0\text{-}320\,\mathrm{Myr}$ according to the initial mass function (IMF) and star-formation history, respectively, measured for the OGLE-III LMC footprint in Paper II. In short, we fitted an IMF slope $\alpha = -2.4$ consistent with the Salpeter value and a star-formation history such that the present-day star-formation rate is approximately double the rate at earlier epochs $\tau = 40\text{-}320$ Myr. We assume random orientations, i.e. $\cos i = 0\text{-}1$ and $\omega = 0^\circ\text{-}360^\circ$ are both uniformly distributed across their respective intervals.

In the present study, we account for the empirical age-extinction and age-eccentricity anticorrelations. Given an age τ, we select dust extinctions A_I according to a Gaussian distribution:

$$p_{A_I} \propto \exp\Big(- \frac{[A_I - A_{I,\mathrm{unbiased}}(\tau)]^2}{2\sigma_{A_I}^2} \Big) \tag{4.21}$$

for $0 < A_I\,(\mathrm{mag}) < 1$ and where $A_{I,\mathrm{unbiased}}\,(\tau)$ and $\sigma_{A_I} = 0.08$ mag derive from the fit to the unbiased subsample in Eqn. 4.19. We also choose eccentricities e from an age-dependent Gaussian distribution:

$$p_e \propto \exp\Big(- \frac{[e - e_{\mathrm{fit}}(\tau)]^2}{2\sigma_e^2} \Big) \tag{4.22}$$

for $0.0 < e < 0.8$ and where $e_{\mathrm{fit}}\,(\tau)$ and $\sigma_e = 0.16$ derive from Eqn. 4.20. Finally, we consider the detection efficiencies as a continuous function of mass ratio $q = 0.2$ - 1.0.

4.5.2 Simple Estimates

Before we conduct detailed Monte Carlo simulations, we perform simple calculations to estimate the probabilities of detecting EBs with $P = 20$ - 50 days. For $q = 0.8$ - 1.0 companions, the detection efficiencies are primarily dictated by two geometrical selection effects. First, the orientations must be sufficiently close to edge-on. About 90% of our well-defined EBs have $i > 86.6^{\mathrm{o}}$, implying the probability of having the necessary inclinations to produce observable eclipses is $\mathcal{P}_i = \cos(86.6^{\mathrm{o}}) = 0.06$.

Second, EBs with longer orbital periods are more likely to be missed. Not only do binaries with longer periods require larger inclinations $i \gtrsim 87^{\mathrm{o}}$ to produce eclipses, but the eclipse widths can also become too narrow to be detected given the cadence of the OGLE-III LMC observations. We found 73 well-defined EBs with $P = 20$ - 30 days. Assuming the intrinsic distribution of log P is uniform, then we would expect ≈92

EBs with $P = 30\text{-}50$ days. Our well-defined sample includes only 57 EBs with $P = 30\text{-}50$ days, suggesting 35 systems were missed due to narrow and/or shallow eclipses. Note that this is consistent with the 32 EBs we removed in item B of §4.2 with uncertain eclipse parameters. The probability that EBs have orbital periods that are sufficiently short is therefore $\mathcal{P}_P = 130 \,/\, (130 + 35) \approx 0.8$. Considering these two factors, the probability of detecting well-defined EBs with $q \approx 0.8\text{-}1.0$ is $\mathcal{P}_i\,\mathcal{P}_P = 0.06 \times 0.8 \approx 5\%$ (red line in Fig. 4.17).

For $q = 0.2\text{-}0.3$ companions, we must also consider evolutionary and photometric selection effects. As discussed in §4.4, well-defined EBs satisfy our photometric selection criteria and are sensitive to low-mass companions only if the primaries are relatively young with ages $\tau = 2\text{-}12$ Myr (Fig. 4.14) and massive with $M_1 \approx 8\text{-}11\,\mathrm{M}_\odot$ (Fig. 4.15). Given a typical MS lifetime of $\tau_{\rm MS} \approx 30$ Myr for $M_1 \approx 8\text{-}11\,\mathrm{M}_\odot$ primaries, then the probability of having the necessary ages $\tau = 2\text{-}12$ Myr is $\mathcal{P}_\tau \approx (12-2)/30 \approx 0.3$. The smallest primary mass in our well-defined EB sample is $3.6\,\mathrm{M}_\odot$. Assuming our adopted IMF, the probability that an EB contains a massive primary $M_1 > 8\,\mathrm{M}_\odot$compared to the probability of having any B-type MS primary with $M_1 > 3.6\,\mathrm{M}_\odot$ is $\mathcal{P}_{M_1} = 0.2$. Combining these additional factors, then the probability of detecting well-defined EBs with $q \approx 0.2\text{-}0.3$ is $\mathcal{P}_i\,\mathcal{P}_P\,\mathcal{P}_\tau\,\mathcal{P}_{M_1} = 0.06 \times 0.8 \times 0.3 \times 0.2 \approx 0.3\%$ (blue line in Fig. 4.17).

4.5.3 Monte Carlo Simulations

We utilize the same technique from Paper II to correct for incompleteness across a continuous function of mass ratios q. For a given q, we select M_1, τ, and A_I from their respective probability density functions. If the simulated binary does not satisfy our

photometric selection criteria, we generate a new binary. Otherwise, we keep the binary and consider its contribution toward the total number $\mathcal{N}_{\rm sim}$ of simulated binaries. We then select the other physical parameters, i.e. $t_{\rm o}$, P, i, e, and ω, from their respective probability density functions.

With the nine physical model parameters for our simulated binary, we synthesize an I-band light curve with NIGHTFALL. We match the cadence and sensitivity of the OGLE-III LMC survey. Specifically, we sample the simulated light curve at $\langle \mathcal{N}_I \rangle = 470$ random epochs and add Gaussian noise according to:

$$\sigma_I = \left[1 + 10^{(I-17.0)/2}\right] \times 0.0075 \text{ mag} \tag{4.23}$$

This equation derives from fitting the relation between the I-band magnitudes and corrected photometric uncertainties for all 221 OGLE-III LMC EBs with intermediate orbital periods $P = 20$ - 50 days.

We then fit our analytic model of Gaussians (Eqn. 4.1) to the simulated NIGHTFALL light curve. As in §4.2, we utilize the MPFIT (Markwardt 2009) Levenberg-Marquardt routine to measure the values of and uncertainties in the eight analytic model parameters, e.g. ΔI_1, Φ_2, etc. To be considered well-defined, we impose the same selection criteria adopted in §4.2. Namely, we require the uncertainties in the eclipse depths ΔI_1 and ΔI_2 and eclipse widths Θ_1 and Θ_2 to be <20% their respective values. We also require the fitted orbital periods to be unambiguous according to Eqn. 4.2. If the synthesized binary satisfies these selection criteria, we consider its contribution toward the total number $\mathcal{N}_{\rm well}$ of well-defined EBs. Using a Monte Carlo technique, we repeat the above procedure until we simulate $\mathcal{N}_{\rm well} = 50$ well-defined EBs for each value of q. The probability of

detecting well-defined EBs is simply $\mathcal{P} = \mathcal{N}_{\rm well} \, / \, \mathcal{N}_{\rm sim}$.

By creating this mock data set of EBs, we find the measurement uncertainties in the eclipse depths and widths calculated by MPFIT are themselves uncertain by $\approx$20%. Hence, a simulated light curve with $\approx 6\sigma$ confidence in the analytic light curve parameters may be accidentally rejected, while a system with $\approx 4\sigma$ detections in the eclipse depths and widths may be included as a well-defined EB. To account for this systematic uncertainty in our selection criteria, we simulate two additional sets of EB populations. We first relax our criteria and consider EBs as well-defined if the MPFIT uncertainties in the eclipse depths ΔI_1 and ΔI_2 and eclipse widths Θ_1 and Θ_2 are $<$25% their respective values. For our final set of simulations, we impose a more stringent requirement that the MPFIT relative uncertainties are $<$15%. For each value of q, we therefore simulate a total of $3 \times \mathcal{N}_{\rm well} = 150$ well-defined EBs. In this manner, we have determined the values of and uncertainties in $\mathcal{P}(q)$.

In Fig. 4.17, we display the probabilities $\mathcal{P}$ (and their uncertainties) of detecting well-defined EBs as a function of mass ratio q. As expected, the ability to detect EBs with extreme mass ratios $q = 0.2$ - 0.3 is substantially smaller than the ability to observe EBs with mass ratios near unity. At large $q > 0.6$, the relative uncertainties in the probabilities are $\delta\mathcal{P}/\mathcal{P} \approx 11\%$, which is only slightly larger than that expected from Poisson statistics $150^{-1/2} = 8\%$. Essentially, the majority of EBs with $q > 0.6$ have deep and accurately measured eclipse properties, and so the precise definition of our selection criteria does not significantly affect which EBs are considered well-defined. At the smallest mass ratios $q = 0.2$, however, the relative uncertainties more than double to $\delta\mathcal{P}/\mathcal{P} \approx 25\%$. All extreme mass-ratio EBs have shallow eclipses (see §4.3) and are close to the detection limit, and so the probabilities $\mathcal{P}$ of detecting well-defined EBs are

more uncertain. The probabilities $\mathcal{P}$ we calculate from our Monte Carlo simulations are consistent with the simple estimates derived in §4.5.2. This demonstrates the selection effects are well-understood and the probabilities $\mathcal{P}$ are reliably measured.

4.5.4 Corrected Binary Fraction

The intrinsic binary statistics are determined by weighting each well-defined EB by the inverse of their respective probability $\mathcal{P}(q)$ of detection as displayed in Fig. 4.17. The total number of B-type MS stars with companions $q = 0.2$ - 1.0 at $P = 20$ - 50 days is

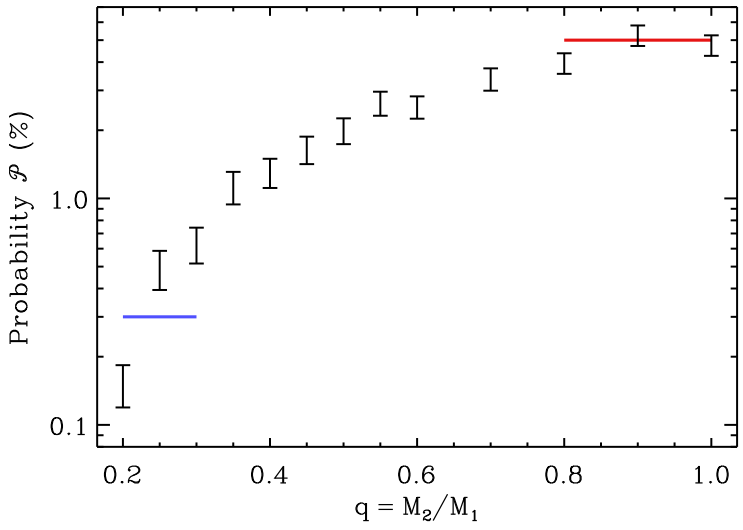

Figure 4.17: Probability $\mathcal{P}$ of detecting well-defined EBs with $P = 20$ - 50 days as a function of mass ratio $q = M_2/M_1$. The results of our detailed Monte Carlo simulations (black) are consistent with our simple estimates (blue and red). In addition to orientation effects, evolutionary and photometric selection effects in our magnitude-limited sample substantially reduce the detection efficiencies for well-defined EBs with extreme mass ratios $q \approx 0.2$ - 0.3.

simply $\mathcal{N}_{\rm comp} = \sum_{j=1}^{130} [\mathcal{P}(q_j)]^{-1} \approx 6{,}500$. Given $\mathcal{N}_{\rm B} = 96{,}000$ B-type MS primaries in our photometric sample, then $\mathcal{F} = \mathcal{N}_{\rm comp} \,/\, \mathcal{N}_{\rm B} = 6{,}500 \,/\, 96{,}000 \approx 6.7\%$ of B-type MS stars have companions with $P = 20$ - 50 days and $q = 0.2$ - 1.0. The uncertainty in this fraction derives from a variety of sources. First, the predicted number $\mathcal{N}_{0.2<q<0.3} \approx 2{,}000$ of low-mass companions with $q = 0.2$ - 0.3 is relatively large but also uncertain. In our sample of 130 well-defined EBs, only 8 systems have mass ratios $q = 0.2$ - 0.3, and so the measurement uncertainty from Poisson statistics is $8^{-1/2} \approx 35\%$. The systematic uncertainty at $q = 0.2$ - 0.3 is $\approx$25% due to the uncertainty in the probabilities $\mathcal{P}$ of detection (see above). The total relative uncertainty in the number of companions with $q = 0.2$ - 0.3 is therefore $\approx$43%, and so $\mathcal{N}_{0.2<q<0.3} = 2{,}000 \pm 900$. We repeat this calculation for the other mass ratio intervals, and find the total relative uncertainty in the number of companions is $\approx$31%, i.e. $\mathcal{N}_{\rm comp} = 6{,}500 \pm 2{,}000$. Finally, in our Monte Carlo simulations, we account for the removal of the 74 systems represented in panels A - D of Fig. 4.1 from our total initial sample of 221 EBs. We did not, however, account for the 17 EBs represented in panels E - F that exhibited variable or peculiar eclipse properties. These systems contribute a small relative uncertainty of $17/221 = 8\%$. Hence, the total relative uncertainty in the number of companions is $\approx$33%. The fraction of B-type MS stars that have companions with $P = 20$ - 50 days and $q = 0.2$ - 1.0 is therefore $\mathcal{F} = (6.7 \pm 2.2)\%$.

Surveys for double-lined spectroscopic binaries (SB2s) with early-type primaries are generally complete for modest mass ratios $q > 0.25$ and short orbital periods $P < 20$ days (Abt et al. 1990; Sana et al. 2012). In a sample of 109 B-type MS stars, Abt et al. (1990) found seven SB2s with $q > 0.25$ and $P = 2$ - 20 days. Similarly, in a sample of 71 O-type stars, Sana et al. (2012) identified 18 SB2s across the same mass-ratio and

period intervals. These statistics imply $f_{\rm logP} = 7\,/\,109 = 0.06 \pm 0.02$ and $f_{\rm logP} = 18\,/\,71 = 0.25 \pm 0.06$ companions with $q > 0.25$ per decade of orbital period at $\log P\,({\rm days}) = 0.8$ for B-type and O-type stars, respectively. As discussed in Paper II and in Chini et al. (2012), the close binary fraction dramatically increases with primary mass.

Based on our B-type MS EBs, we measure a $(5.6 \pm 1.4)\%$ corrected binary fraction across $P = 20$ - 50 days and $q > 0.25$. This results in $f_{\rm logP} = (0.056 \pm 0.014)\,/\,(\log 50 - \log 20) = 0.14 \pm 0.04$ companions with $q > 0.25$ per decade of orbital period centered at $\log P\,({\rm days}) = 1.5$. This value is consistent with the early-type spectroscopic binary fraction measured at short orbital periods $P < 20$ days, implying the intrinsic period distribution of early-type binaries closely resembles Öpik's law (Abt 1983; Abt et al. 1990).

4.5.5 Corrected Mass-ratio Distribution

In Fig. 4.18, we display the cumulative distribution of mass ratios q after weighting each well-defined EB by the inverse of their respective probability $\mathcal{P}$ of producing observable eclipses. By fitting a power-law probability distribution $p_q \propto q^{\gamma}$ to the corrected mass-ratio distribution, we measure $\gamma = -1.1 \pm 0.3$. This is consistent with our estimate in §4.4 (Fig. 4.16) of $\gamma = -1.4 \pm 0.3$ based on a relatively unbiased subsample of 13 young EBs with early-B MS primaries $M_1 \approx 10\,{\rm M}_{\odot}$. In both cases, binaries with B-type MS primaries and orbital periods $P = 20$ - 50 days favor small mass ratios $q = 0.2$ - 0.3.

Observations of early-type spectroscopic and eclipsing binaries with short orbital periods $P = 2$ - 20 days reveal a mass-ratio probability distribution that is only slightly weighted toward small values, e.g. $\gamma \approx -0.9$ - -0.2 (Abt et al. 1990; Sana et al. 2012,

Papers I and II). In addition to the power-law component, close massive binaries with $P < 20$ days exhibit a small excess of twins with $q \gtrsim 0.9$ (Tokovinin 2000; Pinsonneault & Stanek 2006, Paper I). The preponderance of close binaries with moderate mass ratios and excess of twins suggest early-type binaries with $P < 20$ days coevolved via fragmentation and competitive accretion in the circumbinary disk (Abt et al. 1990; Tokovinin 2000; Bonnell & Bate 2005; Kouwenhoven et al. 2009).

In contrast to close massive binaries with $P < 20$ days, we find early-type binaries at moderate orbital periods $P = 20$ - 50 days are even further weighted toward extreme

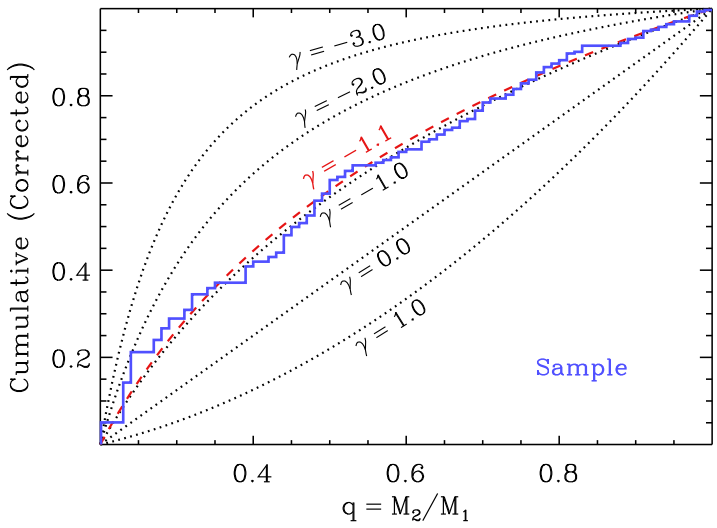

Figure 4.18: Cumulative distribution of mass ratios $q = M_2/M_1 = 0.2$ - 1.0 for the 130 EBs in our well-defined sample (blue) after weighting each system by the inverse of their respective detection probability $\mathcal{P}(q)$. Assuming the mass-ratio probability distribution can be described by a power-law $p_q \propto q^{\gamma}$, we display curves for exponents $\gamma = -3$, -2, -1, 0, and 1 (dotted from top to bottom). After correcting for selection effects, we measure $\gamma = -1.1 \pm 0.3$ (dashed red), demonstrating early-type binaries with intermediate orbital periods are weighted toward extreme mass ratios.

mass ratios, i.e. $\gamma = -1.1 \pm 0.3$ for our total sample and $\gamma = -1.6 \pm 0.4$ for early-B MS primaries. In addition, there is no evidence for an excess population of twins at intermediate orbital periods. Previous spectroscopic surveys have indicated that the mass-ratio probability distribution becomes weighted toward smaller values with increasing orbital period (Abt et al. 1990; Kobulnicky et al. 2014). However, this result is primarily based on the smaller frequency of SB2s at intermediate orbital periods, especially when compared to the frequency of single-lined spectroscopic binaries. In the present study, we have measured the mass-ratio probability distribution at intermediate orbital periods. Our results indicate that early-type binaries at slightly longer orbital periods $P = 20$ - 50 days have experienced less coevolution. In a future paper (Moe et al., in prep.), we will analyze early-type binaries discovered through other observational techniques, e.g. long-baseline interferometry, adaptive optics, common proper motion, etc., and investigate this anticorrelation between P and q in a more thorough and self-consistent manner.

4.6 Summary

Eclipsing Binary Sample (§4.2). We analyzed the 221 EBs in the OGLE-III LMC database with B-type MS primaries and orbital periods $P = 20$ - 50 days. After fitting analytic models of Gaussians to the observed light curves, we identified 130 detached EBs that exhibit two well-defined eclipses per orbit. The remaining 90 EBs have uncertain, peculiar, and/or variable eclipse properties, including 12 systems that displayed changes in the secondary eclipse parameters most likely due to orbital motion with a tertiary companion.

Physical Models (§4.3). We developed an automated procedure to robustly and quickly fit detailed physical models to the EB light curves. Our algorithm can be adapted for any population of detached EBs with known distances and MS primaries. We implemented our procedure on our 130 detached well-defined EBs to measure their intrinsic physical properties, including their ages τ, component masses M_1 and M_2, dust extinctions A_I, and eccentricities e. We incorporated various techniques to demonstrate the uniqueness and robustness of the model solutions as well as the accuracy of the model parameters.

Age-Extinction Anticorrelation (§4.4). Even after considering selection effects, we find the ages τ and dust extinctions A_I are anticorrelated ($\rho = -0.23$) at a statistically significant level ($p = 0.02$). This suggests young stars with $\tau < 10$ Myr are embedded in dusty envelopes and/or molecular clouds with $A_I \approx 0.35$ mag, while older stars with $\tau > 100$ Myr reside in less attenuating environments with $A_I \approx 0.25$ mag. This empirical relation between τ and A_I should prove beneficial when modeling stellar populations.

Age-Eccentricity Anticorrelation (§4.4). We also discover the ages τ and eccentricities e are anticorrelated ($\rho = -0.39$) at a statistically significant level ($p = 5 \times 10^{-6}$) due to tidal evolution. The slope in the observed trend provides a diagnostic for the radiative damping constant via dynamical tides in highly eccentric binaries with hot MS components. We note the tidal circularization timescales $e/\dot{e}$ in highly eccentric binaries with $e \approx 0.5$ - 0.8 may be orders of magnitude shorter than the circularization timescales when the eccentricities $e \lesssim 0.4$ are already small.

Initial Eccentricity Distribution (§4.4). We find that massive binaries at $P =$ 20 - 50 days are initially born with larger eccentricities $\langle e \rangle \approx 0.6$. Assuming a power-law

eccentricity probability distribution $p_e \propto e^{\eta}$, we measure $\eta = 0.8 \pm 0.3$ for our young early-type EBs with $\tau \leq 10$ Myr. This is consistent with a Maxwellian "thermal" eccentricity distribution ($\eta = 1$), which indicates massive binaries with intermediate orbital periods formed via dynamical interactions, either through tidal / disk capture, dynamical perturbations in a dense cluster, three-body exchanges, and/or Kozai cycles with a tertiary companion.

Binary Fraction (§4.5). After utilizing a Monte Carlo technique to correct for selection effects, we measure that $(6.7 \pm 2.2)\%$ of B-type MS stars have companions with $P = 20$ - 50 days and $q = 0.2$ - 1.0. The frequency of companions per decade of orbital period at $\log P\,(\mathrm{days}) = 1.5$ is consistent with spectroscopic observations of close massive binaries at $\log P\,(\mathrm{days}) = 0.8$. This suggests the intrinsic period distribution of binary companions to B-type MS stars closely resembles Öpik's law for $P < 50$ days.

Mass-ratio Distribution (§4.5). In our corrected binary sample with B-type MS primaries $\langle M_1 \rangle = 6\,\mathrm{M}_{\odot}$, we measure a mass-ratio probability distribution $p_q \propto q^{\gamma}$ weighted toward small values ($\gamma = -1.1 \pm 0.3$). There is a slight indication that binaries with early-B MS primaries $\langle M_1 \rangle = 10\,\mathrm{M}_{\odot}$ are even further skewed toward extreme mass ratios ($\gamma = -1.6 \pm 0.4$). Close massive binaries with $P < 20$ days favor moderate mass ratios and exhibit a small excess of twin components $q \gtrsim 0.9$. This indicates our early-type MS binaries with intermediate orbital periods $P = 20$ - 50 days have experienced substantially less coevolution via fragmentation and competitive accretion in the circumbinary disk.

Chapter 5

Mind your Ps and Qs. I. The Interrelation between Period (P) and Mass-ratio (Q) Distributions of Massive Binaries

Abstract

We compile observations of early-type binaries identified via spectroscopy, eclipses, long-baseline interferometry, adaptive optics, lucky imaging, speckle interferometry, high-contrast photometry, composite spectral energy distributions, and common proper motion. Each observational technique is sensitive to companions across a narrow parameter space of orbital periods P and mass ratios $q = M_2/M_1$. We combine the

samples from the various surveys and correct for their respective selection effects to determine a comprehensive nature of the intrinsic multiplicity statistics of O- and B-type stars. We find the properties of companions to massive stars differ among three regimes. First, at short orbital periods $P \lesssim 20$ days (separations $a \lesssim 0.3$ AU), the binaries have small eccentricities, favor modest mass ratios, and exhibit a small excess of twins $q > 0.95$, which indicate the components coevolved via competitive accretion during their formation in the circumbinary disk. Second, at intermediate periods $P \approx 20$ - 10^4 days ($a \approx 0.3$ - 20 AU), the binaries follow a Maxwellian "thermal" eccentricity distribution and have mass ratios weighted toward extreme values $q \approx 0.2$ - 0.3. These distributions suggest the components in massive binaries at intermediate orbital periods formed relatively independently and quickly evolved to their current configurations through dynamical interactions. Finally, the majority of companions at long orbital periods $P \approx 10^4$ - 10^8 days ($a \approx 20$ - 10^4 AU) are outer tertiary components in a hierarchical triple. We also reanalyze the binary statistics of solar-type primaries, taking into account that $\approx$1/3 of single-lined spectroscopic binaries likely contain white dwarf companions instead of M-dwarf secondaries. These updated multiplicity statistics serve as stepping stones to more reliably predict the rates and properties of certain channels of binary evolution via population synthesis.

5.1 Introduction

Spectral type B ($3\,M_\odot \lesssim M_1 \lesssim 16\,M_\odot$) and O ($M_1 \gtrsim 16\,M_\odot$) main-sequence (MS) primaries with closely orbiting stellar companions can evolve to produce X-ray binaries (Verbunt 1993), millisecond pulsars (Lorimer 2008), Type Ia (Wang & Han 2012) and

possibly Type Ib/c (Yoon et al. 2010) supernovae, Algols (van Rensbergen et al. 2011), short (Nakar 2007) and perhaps long (Izzard et al. 2004) gamma ray bursts, accretion induced collapse (Ivanova & Taam 2004), and sources of gravitational waves (Schneider et al. 2001). It is therefore important to constrain the binary statistics of massive stars in order to fully characterize the rates and properties of these channels of binary evolution. The close binary fraction, i.e. the fraction of primaries with stellar companions at separations $a \lesssim 1$ AU, increases dramatically between M-type and O-type MS stars (Abt 1983; Duquennoy & Mayor 1991; Fischer & Marcy 1992; Raghavan et al. 2010; Moe & Di Stefano 2015a, etc.). In fact, most massive stars with $M_1 \gtrsim 15\,\mathrm{M}_\odot$ will interact with a stellar companion before they explode as core-collapse supernovae (Sana et al. 2012). However, the interrelations among binary properties, e.g. primary mass, mass ratio, orbital period, eccentricity, age, metallicity, and environment, are only beginning to be accurately quantified. See Duchêne & Kraus (2013) for a recent review.

The precise distributions of binary properties enlightens our understanding of binary star formation. For example, a mass-ratio distribution that is consistent with random pairings drawn from the initial mass function (IMF) would suggest the companions formed relatively independently from the primaries (Abt et al. 1990; Tout 1991; McDonald & Clarke 1995). Alternatively, correlated component masses, which are expected and generally observed for close binaries (Tokovinin 2000; Raghavan et al. 2010; Sana et al. 2012), indicate coevolution during the pre-MS phase via physical processes such as fragmentation, fission, competitive accretion, and/or mass transfer through Roche lobe overflow (Bonnell & Bastien 1992; Clarke 1996; Bate & Bonnell 1997; Kratter & Matzner 2006; Kouwenhoven et al. 2009; Bate 2012). As another example, an eccentricity distribution that is weighted toward large values implies a Maxwellian

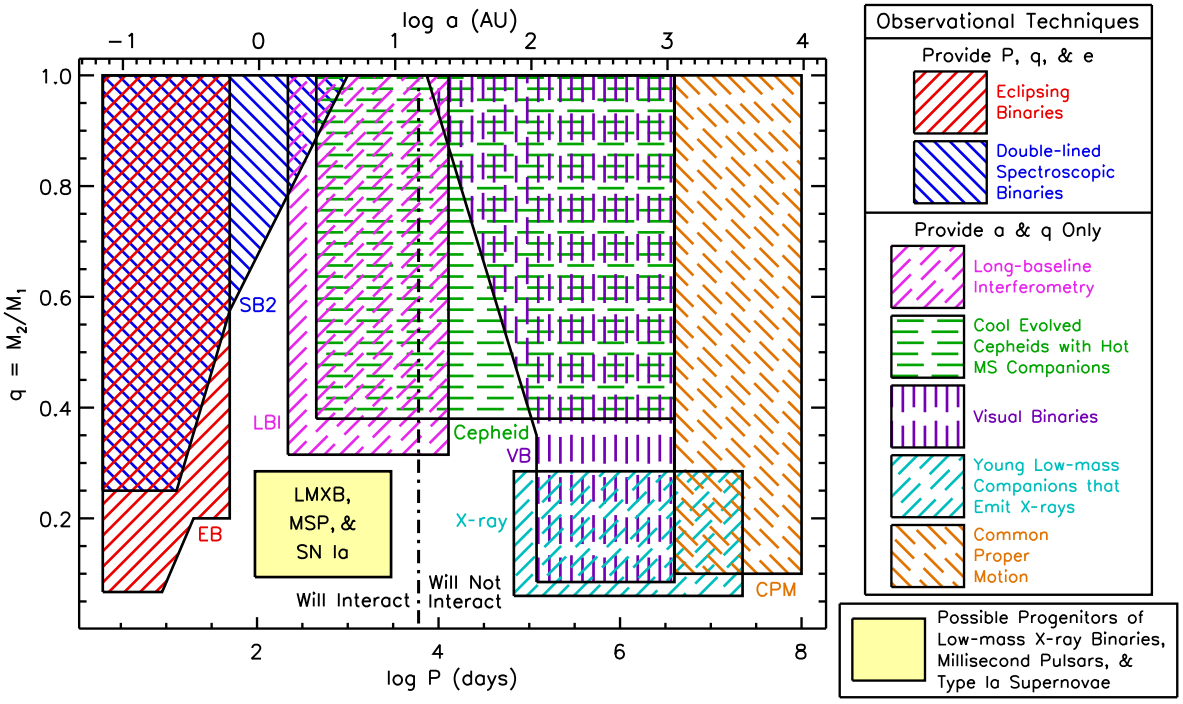

Figure 5.1: Schematic diagram of the various observational techniques (regions enclosed with solid and dashed lines) used to identify companions to early-type primaries as a function of orbital period P and mass ratio $q = M_2/M_1$. We compare the approximate parameter space of detection abilities for double-lined spectroscopic binaries (blue), eclipsing binaries (red), long-baseline interferometry (magenta), Cepheids (green), visual binaries (purple), X-ray emission (aqua), and common proper motion (orange). In this diagram, we show only observational techniques where the orbital periods P (or orbital separations a) and mass ratios q can be estimated, and the nature of the companion is reliably known to be a non-degenerate pre-MS or MS star. Assuming an average eccentricity $\langle e \rangle \approx 0.5$, only binaries with $\log P\,(\mathrm{days}) \lesssim 3.8$ (left of dot-dashed line) will substantially interact as the primary evolves toward the giant phase. Certain channels of low-mass X-ray binaries, millisecond pulsars, and Type Ia supernovae are expected to derive from early-type MS primaries with low-mass companions $q \approx 0.1$ - 0.3 at initially moderate orbital periods $P \approx 100$ - $3{,}000$ days (filled yellow region).

"thermal" orbital velocity distribution (Ambartsumian 1937). Such a population would suggest the binaries formed through dynamical interactions, possibly through tidal or disk capture, perturbations in a dense cluster, triple-star secular evolution, and/or three-body exchanges (Heggie 1975; Harrington & Miranian 1977; Pringle 1989; Turner et al. 1995; Kroupa 1995). Meanwhile, circularized orbits demonstrate tidal evolution on the MS and/or pre-MS (Zahn 1977; Zahn & Bouchet 1989b; Meibom & Mathieu 2005).

The initial conditions of MS binaries are also utilized as input parameters in binary population synthesis (Hurley et al. 2002; Belczynski et al. 2008). The predicted rates and properties of certain channels of binary evolution are highly dependent on the adopted MS binary statistics (Fryer et al. 1999; Kiel & Hurley 2006; Davis et al. 2010; Claeys et al. 2014). Moreover, MS binary distributions, such as the period and mass-ratio distributions, may be significantly correlated with each other (Abt et al. 1990). Separately adjusting the input MS binary distributions to the extremes may still not encompass the true nature of the binary population.

Companions to massive stars have been detected through a variety of methods, including spectroscopy (Sana et al. 2012), eclipses (Moe & Di Stefano 2015b), long-baseline interferometry (Rizzuto et al. 2013), adaptive optics (Shatsky & Tokovinin 2002), common-proper motion (Abt et al. 1990), etc. Each observational technique is sensitive to companions across a certain interval of orbital periods P and mass ratios $q = M_2/M_1$ (see Fig. 5.1). Despite significant advances in the observational instruments and methods, the properties of low-mass companions ($q \lesssim 0.4$) around early-type stars at intermediate orbital periods ($P \approx 20\text{-}10^4$ days) remain elusive. This region is especially interesting because low-mass X-ray binaries and millisecond pulsars that form in the galactic field (Kalogera & Webbink 1998; Kiel & Hurley 2006) as well as Type Ia

supernovae that explode in elliptical galaxies (Whelan & Iben 1973; Ruiter et al. 2011) may evolve from extreme mass-ratio binaries at initially intermediate orbital periods (Fig. 5.1). Although we investigate all portions of the binary parameter space, we are especially concerned with determining accurate companion statistics at intermediate orbital periods.

We organize the rest of this paper as follows. In §5.2, we define the parameters that describe the statistics and distributions of binary stars. We then review the various observational methods for detecting binary companions to O- and B-type MS stars, noting their specific strengths and weaknesses in filling the binary parameter space. We analyze spectroscopic binaries (§5.3), eclipsing binaries (§5.4), binaries discovered via long-baseline interferometry (§5.5), binaries containing Cepheid primaries that evolved from B-type MS stars (§5.6), and visual binaries identified through adaptive optics, lucky imaging, speckle interferometry, X-ray emission, and common proper motion (§5.7). For each observational technique and sample of early-type binaries, we account for their respective selection effects to recover the intrinsic binary statistics. To extend the baseline toward smaller masses, we parameterize the multiplicity statistics of solar-type primaries in §5.8. Finally, we combine the statistics of the corrected binary populations in §5.9 to measure the interrelations between primary mass, multiplicity frequency, mass ratio, orbital period, and eccentricity. We briefly discuss the implications for binary formation and evolution.

5.2 Definitions

In the following sections, we analyze the various observational techniques for identifying stellar companions to late-B ($M_1 \approx 3\text{-}5\,\mathrm{M}_\odot$), mid-B ($M_1 \approx 5\text{-}9\,\mathrm{M}_\odot$), early-B ($M_1 \approx 9\text{-}16\,\mathrm{M}_\odot$) and O-type ($M_1 \gtrsim 16\,\mathrm{M}_\odot$) MS stars. Unless otherwise stated, we use the stellar relations provided in Pecaut & Mamajek (2013, and references therein) to estimate the primary mass M_1 from the spectral type. For each observational sample, we recover the instrinsic distributions of orbital periods P, mass ratios q, and eccentricities e. Our aim is to measure four parameters, which we designate as $f_{\log\mathrm{P}}$, γ, $\mathcal{F}_{\mathrm{twin}}$, and η (see definitions immediately below), that describe the binary statistics and distributions.

We define $f_{\log\mathrm{P}}\,(M_1, P)$ as the frequency of companions per decade of orbital period with mass ratios $q \equiv M_{\mathrm{comp}}/M_1 > 0.1$. For example, if a sample of 100 primaries with $M_1 = 10\,\mathrm{M}_\odot$ have 15 companions with masses $M_{\mathrm{comp}} = 1\text{-}10\,\mathrm{M}_\odot$ and periods $P = 100\text{-}1{,}000$ days, then $f_{\log\mathrm{P}}\,(M_1 = 10\,\mathrm{M}_\odot, \log P = 2.5) = 0.15$. For a given mass M_1, the frequency $f_{\log\mathrm{P}}\,(P)$ provides the period distribution. Note that $f_{\log\mathrm{P}}\,(P) =$ constant is simply Öpik's law (Öpik 1924; Abt 1983), i.e. a uniform distribution with respect to logarithmic period. Integration of $f_{\log\mathrm{P}}$ gives the multiplicity frequency:

$$f_{\mathrm{mult}}\,(M_1) = \int_{0.0}^{8.0} f_{\log\mathrm{P}}\,(M_1,\, P)\, d\log P, \tag{5.1}$$

i.e. the mean number of companions with $q > 0.1$ per primary. We investigate stellar companions with $P > 1$ day that are not Roche-lobe filling and binaries with $P < 10^8$ days that are gravitationally bound according to their common proper motion (see Fig. 5.1). The multiplicity frequency f_{mult} can exceed unity if a primary star contains, on average, more than one stellar companion with $q > 0.1$.

In the present study, we do not differentiate between companions that are in binaries versus triples. We instead tabulate the corrected total frequency of MS companions $f_{\rm logP}\,(M_1, P)$, where the MS primary with mass M_1 is the most massive component of the system and P is the orbital period of the stellar companion with respect to the primary. Current observations of massive stars are not sensitive to companions in certain portions of the P and q parameter space (see Fig. 5.1), and so we must correct for incompleteness to self-consistently derive $f_{\rm logP}$. By correcting for incompleteness, we cannot evaluate the full multiplicity statistics without making assumptions. Namely, we cannot determine whether a companion that escapes detection is in a binary or is the inner or outer component of a hierarchical triple. Nonetheless, we can estimate the orbital period $P_{\rm triple}(M_1)$ beyond which the companion is most likely to be an outer tertiary component in a hierarchical triple. We define $P_{\rm triple}(M_1)$ to satisfy:

$$\int_{0.0}^{\log P_{\rm triple}(M_1)} f_{\rm logP}\,(M_1,\,P)\,d{\rm log}P = 1, \tag{5.2}$$

i.e. the orbital period beyond which the multiplicity frequency exceeds unity. The majority of companions with $P > P_{\rm triple}$ are the outer members of a hierarchical triple in which both the inner and outer companions have $q = M_{\rm comp}/M_1 > 0.1$.

Next, the parameters $\gamma\,(M_1, P)$ and $\mathcal{F}_{\rm twin}\,(M_1, P)$ describe the mass-ratio probability distribution p_q. For a given primary mass M_1 and orbital period P, the mass-ratio probability distribution integrates to unity, i.e.:

$$\int_{0.1}^{1.0} p_q\,{\rm d}q \;=\; 1, \tag{5.3}$$

across our mass-ratio interval $q = 0.1$ - 1.0 of interest. If the mass-ratio probability distribution can be described by a single power-law, then $p_q \propto q^{\gamma}$. Note that $\gamma = 0$ is

a uniform mass-ratio probability distribution while $\gamma = -2.35$ implies random pairings drawn from a Salpeter IMF.

Certain observational techniques can detect extreme mass-ratio binaries $q \approx 0.05$-0.10 (Shatsky & Tokovinin 2002; Abt et al. 1990; Moe & Di Stefano 2015a; Hinkley et al. 2015), which we exclude when quantifying $f_{\rm logP}$ and γ. Alternatively, other observational methods are sensitive to only companions above some threshold $q \gtrsim q_{\rm thresh} \approx 0.3$ (Remage Evans et al. 2013; Sana et al. 2014, see Fig. 5.1). For these samples, we measure the power-law component $\gamma_{\rm largeq}$ of the mass-ratio distribution across large mass ratios $q_{\rm thresh} < q < 1.0$. To self-consistently evaluate $f_{\rm logP}$, we correct for incompleteness down to $q = 0.1$ while taking into account the uncertainty in the mass-ratio probability distribution across $0.1 < q < q_{\rm thresh}$. If $\gamma_{\rm largeq} \approx 0$, then it is safe to assume that the uniform mass-ratio distribution continues to extend down to $q = 0.1$. If $\gamma_{\rm largeq} \approx -2$, however, the slope of the mass-ratio distribution must eventually flatten and possibly turn over toward smaller mass ratios. For such binary populations, we adopt a broken power-law with slopes:

$$\begin{aligned} \gamma = \gamma_{\rm largeq} \ \ &\text{for } q_{\rm thresh} < q < 1.0, \\ \gamma_{\rm smallq} \ \ &\text{for } 0.1 < q < q_{\rm thresh}, \end{aligned} \tag{5.4}$$

where the mass-ratio probability distribution p_q is continuous at $q = q_{\rm thresh} \approx 0.3$. If the observations are not sensitive toward small mass ratios, then we adopt $\gamma_{\rm smallq} = (0.2 \pm 0.4)\gamma_{\rm largeq}$. We then determine the correction factor for incompleteness toward small mass ratios:

$$\mathcal{C}_{\rm smallq} = \Big(\int_{q_{\rm min}}^{1.0} p_q \, {\rm d}q \Big)^{-1}. \tag{5.5}$$

For example, suppose $\mathcal{N}_{\rm comp} = 20$ companions are identified around $\mathcal{N}_{\rm prim} = 100$ primaries across orbital periods $P = 10^2$ - 10^4 days. The observations are sensitive and complete to companions with $q > q_{\rm thresh} = 0.3$, and the 20 observed binaries are adequately described by a power-law mass-ratio distribution with $\gamma_{\rm largeq} = -1.5$ across $q = 0.3$ - 1.0. We adopt $\gamma_{\rm smallq} = (0.2 \pm 0.4)\gamma_{\rm largeq} = -0.3 \pm 0.6$, which encompasses a distribution $\gamma_{\rm smallq} \approx -0.9$ that continues to be weighted toward extreme mass ratios below $q = 0.3$ as well as a power-law component $\gamma_{\rm smallq} = 0.3$ that flattens and turns over below $q = 0.3$. The correction factor for incompleteness toward small mass ratios is $\mathcal{C}_{\rm smallq} = 1.8 \pm 0.3$, where we have propagated the uncertainty in $\gamma_{\rm smallq}$. The corrected frequency of companions with $q > 0.1$ per decade of orbital period is $f_{\rm logP} = \mathcal{N}_{\rm comp} \, \mathcal{C}_{\rm smallq} / \mathcal{N}_{\rm prim} / \Delta {\rm log} P = (10 \pm \sqrt{10})(1.8 \pm 0.3)/100/(4-2) = 0.09 \pm 0.03$, where we have propagated the uncertainty from Poisson statistics and the uncertainty in the mass-ratio probability distribution across $q = 0.1$ - 0.3.

For some observed populations of close binaries, there is a clear narrow peak in the mass-ratio probability distribution at $q \gtrsim 0.95$ (Tokovinin 2000; Pinsonneault & Stanek 2006; Raghavan et al. 2010). We therefore define $\mathcal{F}_{\rm twin}$ as the excess fraction of twins with $q > 0.95$ relative to the underlying power-law component(s). For example, if 90% of the binaries are uniformly distributed across $0.1 < q < 1.0$ and the remaining 10% are evenly distributed across $0.95 < q < 1.0$, then $\gamma = 0$ and $\mathcal{F}_{\rm twin} = 0.1$. The parameter $\mathcal{F}_{\rm twin}$ is therefore the *excess* fraction, not the total fraction, of twin components with $q > 0.95$.

Finally, $\eta\,(M_1, P)$ describes the eccentricity probability distribution $p_e \propto e^{\eta}$ according to a power-law. Note that $\eta = 1$ is a Maxwellian "thermal" eccentricity distribution (Ambartsumian 1937). For a given M_1 and P, the eccentricity distribution integrates to unity, i.e.:

$$\int_0^{e_{\max}} p_e \, \mathrm{d}e = 1, \tag{5.6}$$

where the upper limit is:

$$e_{\max}\,(P) = 1 - \left(\frac{P}{2\ \mathrm{days}}\right)^{-2/3} \ \text{for}\ P\ >\ 2\ \mathrm{days}. \tag{5.7}$$

This relation guarantees the binary components have Roche-lobe fill-factors $\lesssim$70% at periastron. Some binaries may initially have $e > e_{\max}$ and nearly fill their Roche lobes at periastron, but their orbits will rapidly evolve toward smaller eccentricities due to tides. We assume all binaries with $P \leq 2$ days are circularized, which is consistent with both observations and tidal theory of early-type binaries (Zahn 1975; Abt et al. 1990; Sana et al. 2012).

According to the above definitions, we have implicitly assumed that the distributions of mass ratios q and eccentricities e are independent. At present, there is no observational evidence that q and e are correlated (Raghavan et al. 2010; Moe & Di Stefano 2015b), and so our assumption is valid. For all other parameter combinations, the above definitions allow for possible correlations between the binary physical properties and their distributions.

Only a small fraction of visual early-type binaries have measured orbital eccentricities

(Abt et al. 1990; Sana et al. 2014). Harrington & Miranian (1977) argue that visual binaries without measurable orbital solutions have systematically larger eccentricities. The subsample of visual binaries with orbital solutions is therefore biased toward smaller eccentricities. For binaries identified through spectroscopic radial velocity variations and eclipses, the eccentricities can always be measured. Only spectroscopic (§5.3) and eclipsing (§5.4) binaries can therefore be utilized to quantify an unbiased eccentricity distribution for early-type binaries (see Fig. 5.1). In each of the following sections, we measure $f_{\rm logP}\,(M_1, P)$, $\gamma\,(M_1, P)$, $\mathcal{F}_{\rm twin}\,(M_1, P)$, and, if possible, $\eta\,(M_1\,P)$.

5.3 Double-lined Spectroscopic Binaries

5.3.1 Sample Selection

Multi-epoch spectroscopic radial velocity observations are capable of detecting companions to massive MS stars with the shortest orbital periods (Wolff 1978; Garmany et al. 1980; Levato et al. 1987; Abt et al. 1990; Sana et al. 2012; Chini et al. 2012; Kobulnicky et al. 2014). The mass ratio of a double-lined spectroscopic binary (SB2) can be directly measured from the observed ratio of velocity semi-amplitudes $q = M_2/M_1 = K_1/K_2$. The orbital eccentricity e of an SB2 simply derives from fitting the radial velocities as a function of orbital phase.

We initially analyze 44 SB2s with orbital periods $P = 2$ - 500 days from four surveys of early-type stars: Levato et al. (1987, 81 B-type primaries; $\langle M_1 \rangle \approx 5\,{\rm M}_\odot$; 3 SB2s), Abt et al. (1990, 109 B2 - B5 primaries; $\langle M_1 \rangle \approx 8\,{\rm M}_\odot$; 9 SB2s), Kobulnicky et al. (2014, 83 B0 - B2 primaries; $\langle M_1 \rangle \approx 12\,{\rm M}_\odot$; 8 SB2s), and Sana et al. (2012, 71 O-type

Table 5.1: Binary statistics based on four spectroscopic surveys containing 44 early-type SB2s with $\log P\,(\mathrm{days}) = 0.3$ - 2.7.

Survey	Primary Mass	Period Interval	Statistic
All Four	$\langle M_1 \rangle = 16 \pm 8\,\mathrm{M}_\odot$	$\log P\,(\mathrm{days}) = 0.75 \pm 0.25$	$\eta = -0.3 \pm 0.2$
		$\log P\,(\mathrm{days}) = 1.85 \pm 0.85$	$\eta = 0.6 \pm 0.3$
		$\log P\,(\mathrm{days}) = 0.8 \pm 0.5$	$\gamma_{\mathrm{largeq}} = -0.3 \pm 0.3$
			$\mathcal{F}_{\mathrm{twin}} = 0.08 \pm 0.03$
		$\log P\,(\mathrm{days}) = 2.0 \pm 0.7$	$\gamma_{\mathrm{largeq}} = -1.5 \pm 0.4$
			$\mathcal{F}_{\mathrm{twin}} < 0.03$
Levato et al. (1987)	$\langle M_1 \rangle = 5 \pm 2\,\mathrm{M}_\odot$	$\log P\,(\mathrm{days}) = 0.8 \pm 0.5$	$f_{\mathrm{logP}} = 0.07 \pm 0.04$
Abt et al. (1990)	$\langle M_1 \rangle = 8 \pm 2\,\mathrm{M}_\odot$		$f_{\mathrm{logP}} = 0.10 \pm 0.04$
Kobulnicky et al. (2014)	$\langle M_1 \rangle = 12 \pm 3\,\mathrm{M}_\odot$		$f_{\mathrm{logP}} = 0.12 \pm 0.05$
Sana et al. (2012)	$\langle M_1 \rangle = 28 \pm 8\,\mathrm{M}_\odot$		$f_{\mathrm{logP}} = 0.31 \pm 0.08$
Abt et al. (1990) & Kobulnicky et al. (2014)	$\langle M_1 \rangle = 9 \pm 3\,\mathrm{M}_\odot$	$\log P\,(\mathrm{days}) = 1.8 \pm 0.5$	$f_{\mathrm{logP}} = 0.10 \pm 0.06$
Sana et al. (2012)	$\langle M_1 \rangle = 28 \pm 8\,\mathrm{M}_\odot$	$\log P\,(\mathrm{days}) = 2.0 \pm 0.7$	$f_{\mathrm{logP}} = 0.19 \pm 0.09$

primaries; $\langle M_1 \rangle \approx 28\,\mathrm{M}_\odot$; 24 SB2s). We list the multiplicity statistics based on these four surveys in Table 5.1. In Figs. 2 and 3, we display the eccentricities e and mass ratios q, respectively, of the 44 SB2s as a function of orbital period. Sana et al. (2012) and Kobulnicky et al. (2014) identified additional SB2s with $q > 0.55$ at $P > 500$ days, which confirms that spectroscopic observations can reveal moderate mass-ratio binaries at intermediate orbital periods. However, spectroscopic binaries become increasingly less complete and biased toward larger q at longer P (see §5.3.3 and Fig. 5.3), so we limit our sample selection to SB2s with $P < 500$ days when discussing these four surveys.

We also examine the 23 detached SB2s with primary spectral types O and B, luminosity classes III-V, orbital periods $P = 8$ - 40 days, and measured mass ratios $q = K_1/K_2$ and eccentricities e from the Ninth Catalog of Spectroscopic Binaries (SB9; Pourbaix et al. 2004). This sample includes 10 systems with O9-B3 primaries ($\langle M_1 \rangle \approx 14\,\mathrm{M}_\odot$) and 13 systems with B5-B9.5 primaries ($\langle M_1 \rangle \approx 4.5\,\mathrm{M}_\odot$). We report

the multiplicity statistics based on these 23 SB2s in Table 5.2. The spectroscopic binaries contained in the SB9 catalog are compiled from a variety of surveys and samples, and so the cadence and sensitivity of the spectroscopic observations are not as homogeneous. We therefore consider only the SB2s with $P < 40$ days, which are relatively complete regardless of the instruments utilized. Unfortunately, we cannot infer the intrinsic frequency of companions per primary based on the SB9 catalog because the number

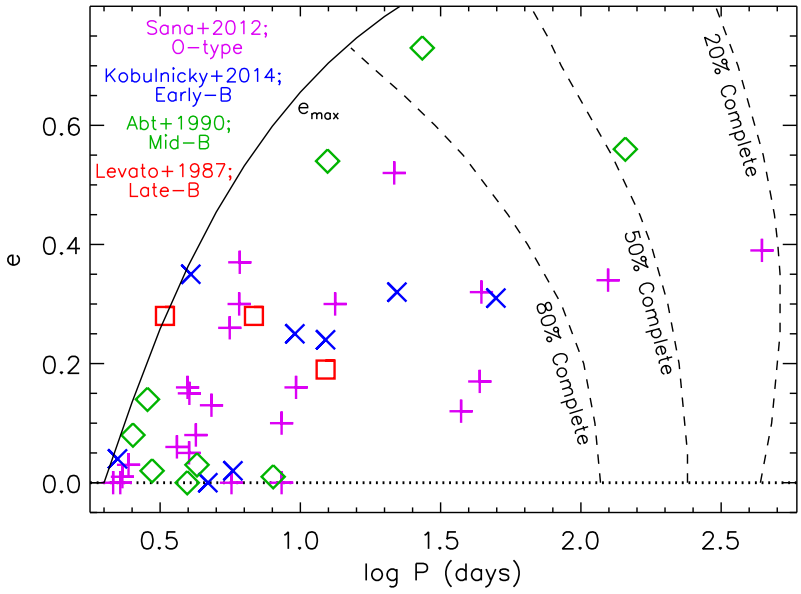

Figure 5.2: Eccentricities e of 44 SB2s as a function of orbital period P from four spectroscopic surveys: Sana et al. (2012, magenta pluses), Kobulnicky et al. (2014, blue crosses), Abt et al. (1990, green diamonds), and Levato et al. (1987, red squares). We display the maximum expected eccentricity $e_{\rm max}(P)$ according to Eqn. 5.7 (black line). Assuming $M_1 = 10\,{\rm M}_\odot$, $q = 0.4$, random orientations, and the median cadence and sensitivity of the spectroscopic surveys, we show completeness levels of 80%, 50%, and 20% (dashed). Note that many SB2s with $P < 10$ days are circularized ($e = 0$; dotted), while all early-type SB2s with $P > 10$ days are in eccentric orbits.

of primaries are not reported. Nonetheless, the sample of 23 early-type SB2s can be utilized to measure the eccentricity and mass-ratio distributions, and their variations with primary mass.

For SB2s, the secondary must be comparable in luminosity to the primary in order for both components to be visible in the combined spectrum. Because MS stars follow a steep mass-luminosity relation, SB2s with early-type MS primaries can only reveal moderate mass ratios $q > q_{\rm thresh} \approx 0.25$ (Figs. 1 & 3). For single-lined spectroscopic binaries (SB1s) with low-luminosity companions, a lower limit to the mass ratio can be estimated from the observed reflex motion of the primary. A statistical mass-ratio distribution can be recovered for SB1s by assuming the intrinsic binary population has random orientations (Mazeh et al. 1992a). However, SB1s with early-type MS primaries may not necessarily have low-mass A-K type stellar companions. Instead, many SB1s with O- and B-type primaries may contain 1 - 3 $M_\odot$ stellar remnants such as white dwarfs, neutron stars, or even black holes (Wolff 1978; Garmany et al. 1980). It is imperative to never implicitly assume that early-type SB1s contain two MS components. In the context of spectroscopic binaries with massive primaries, only SB2s provide a reliable uncontaminated census of unevolved companions (Moe & Di Stefano 2015a). At the very least, SB1s can provide a self-consistency check and an upper limit to the frequency of stellar companions with $q \approx 0.10$ - 0.25, but only as long as the SB1 samples are complete toward all companions in this mass-ratio interval.

5.3.2 Corrections for Incompleteness

The ability to detect spectroscopic binaries not only depends on the resolution of the spectrograph, the signal to noise ratio of the spectra, and the cadence of the observations, but also on the physical properties of the binary. Early-type stars, including those in binaries with $P \gtrsim 10$ days where tidal synchronization is inefficient, are rotationally

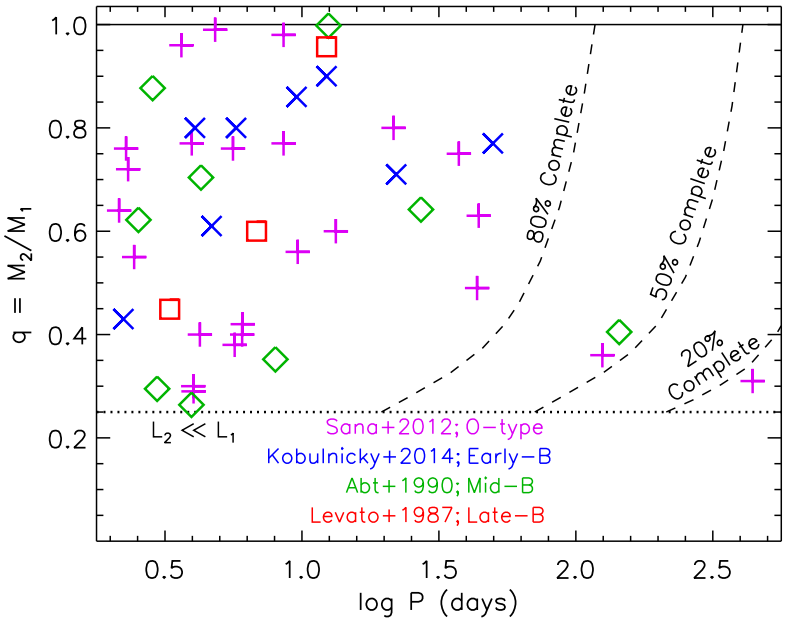

Figure 5.3: Similar to Fig. 5.2, but for the mass ratios $q = M_2/M_1$ as a function of orbital period P. Early-type SB2s with MS components can only reveal companions with $q > 0.25$ (above dotted line). Assuming $M_1 = 10\,\mathrm{M}_\odot$, $e = 0.5e_{\max}$, and the median cadence and sensitivity of the spectroscopic surveys, we show completeness levels of 80%, 50%, and 20% (dashed). Short-period SB2s with $P < 20$ days span the entire observable mass-ratio interval $q \approx 0.25$ - 1.0. Alternatively, long-period systems with $P = 100$ - 500 days include only SB2s with $q \approx 0.3$ - 0.4, even though the spectroscopic surveys are substantially incomplete in this corner of the parameter space.

Table 5.2: Binary statistics based on 23 early-type SB2s with $\log P\,(\text{days}) = 1.3 \pm 0.3$ contained in the SB9 catalog.

Sample	Primary Mass	Statistic
Spectral Types O9 - B3	$\langle M_1 \rangle = 14 \pm 4\,\mathrm{M}_\odot$	$\eta = 0.9 \pm 0.4$
		$\gamma_{\rm largeq} = -0.6 \pm 0.7$
Spectral Types B5 - B9.5	$\langle M_1 \rangle = 4.5 \pm 1.5\,\mathrm{M}_\odot$	$\eta = -0.3 \pm 0.2$
		$\gamma_{\rm largeq} = -1.0 \pm 0.6$

broadened by $\langle v_{\rm rot} \rangle \approx 100$ - 200 km s^{-1} (Abt et al. 2002; Levato & Grosso 2013). The primary's orbital velocity semi-amplitude must therefore be $K_1 \gtrsim 10$ - 15 km s^{-1} in order for the orbital reflex motion of the primary to be detectable (Levato et al. 1987; Abt et al. 1990; Sana et al. 2012; Kobulnicky et al. 2014). In addition, for SB2s, the atmospheric absorption features of both the primary and secondary components need to be distinguishable. Due to blending of the broad absorption features, early-type SB2s require an even higher threshold of $K_1 \approx 20$ - 30 km s^{-1} to be observed. The primary's velocity semi-amplitude K_1 decreases toward wider separations a, smaller mass ratios q, and lower inclinations i. Lower mass companions at longer orbital periods will more readily be missed in the spectroscopic binary surveys. Finally, highly eccentric binaries spend only a small fraction of time near periastron while exhibiting appreciable radial velocity variations. Considering the finite cadence of spectroscopic observations, very eccentric binaries with long orbital periods are not easily detected.

To measure the detection efficiencies and correct for incompleteness, we utilize a Monte Carlo technique to generate a large population of binaries with different primary masses M_1, mass ratios q, and orbital configurations P and e. For each binary, we assume random orientations, i.e. an inclination i distribution such that $\cos i = [0, 1]$ is uniform and a distribution of periastron angles $\omega = [0^{\rm o}, 360^{\rm o}]$ that is also uniform.

The velocity semi-amplitude K_1 criterion does not adequately describe the detection efficiencies of eccentric binaries due to the finite number of spectroscopic observations. For each binary, we instead synthesize radial velocity measurements $v_{1,r}$ and $v_{2,r}$ at 20 random epochs, which is the median cadence of the spectroscopic binary surveys (Levato et al. 1987; Abt et al. 1990; Sana et al. 2012; Kobulnicky et al. 2014). For simplicity, we assume the systemic velocity of the binary is zero. In an individual spectrum of a early-type star, the radial velocities can be centroided to an accuracy of $\approx$2 - 3 km s^{-1}. However, atmospheric variations limit the true sensitivity across multiple epoch to $\delta v_{1,r} \approx 3$ - 5 km s^{-1} (Levato et al. 1987; Abt et al. 1990; Sana et al. 2012; Kobulnicky et al. 2014). In order for a simulated binary to have an orbital solution that can be fitted, and therefore an eccentricity and mass ratio that can be measured, we require a minimum number of radial velocity measurements of the primary $v_{1,r}$ to significantly differ from the systemic velocity. We impose that at least 5 of the 20 measurements satisfy $|v_{1,r}| \gtrsim (3\text{-}5)\,\delta v_{1,r} \approx 15$ km s^{-1} in order to provide a precise and unique orbital solution for the primary. In addition, the rotationally broadened spectral features of both the primary and secondary must be distinguishable to be cataloged as an SB2. At the very least, the primary's absorption features must not only shift during the orbit, but also have velocity profiles that visibly change due to the moving absorption lines from the orbiting secondary (De Becker et al. 2006; Sana et al. 2012). We therefore require that at least 3 of the 20 measurements satisfy $|v_{1,r} - v_{2,r}| \gtrsim \langle v_{\rm rot} \rangle / 2 \approx 75$ km s^{-1}. This velocity threshold is valid for both O-type and B-type primaries because the mean rotational velocities $\langle v_{\rm rot} \rangle \approx 150$ km s^{-1} do not significantly vary as a function of primary mass for early-type stars (Abt et al. 2002; Levato & Grosso 2013). We keep track of the fraction of binaries that satisfy these criteria. In this manner, we calculate the detection

efficiencies $\mathcal{D}(P, M_1, q, e)$ of SB2s as a function of the physical properties of the binary.

In Fig. 5.4, we display the detection efficiencies $\mathcal{D}$ as a function of orbital period P for various combinations of M_1, q, and e. The sample of SB2s are relatively complete

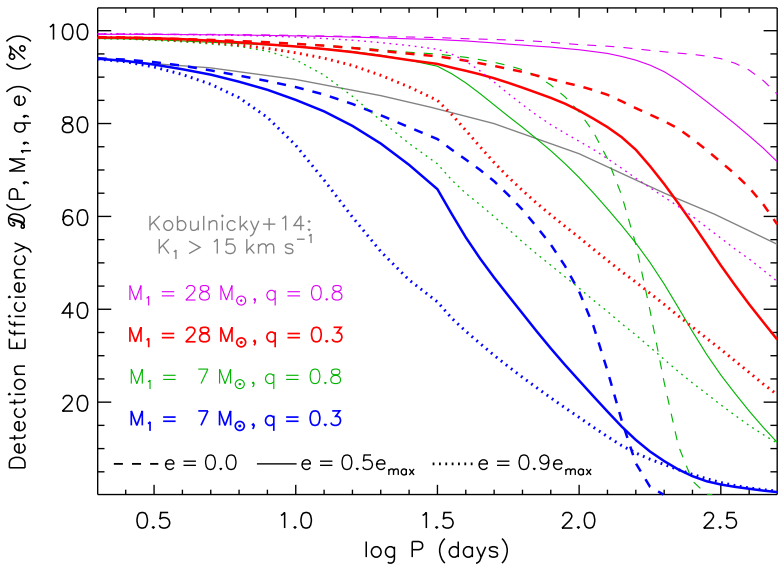

Figure 5.4: The detection efficiencies $\mathcal{D}(P, M_1, q, e)$ of SB2s assuming random orientations and the sensitivity and cadence of the spectroscopic observations. As a function of orbital period P, we display the completeness levels for $M_1 = 28$ M$_\odot$ (O-type) primaries with $q = 0.8$ (thin magenta) and $q = 0.3$ (thick red) companions as well as $M_1 = 7$ M$_\odot$ (B-type) primaries with $q = 0.8$ (thin green) and $q = 0.3$ (thick blue) companions. For each combination of M_1 and q, we compare the detection efficiencies for circular orbits (dashed), intermediate eccentricities $e = 0.5e_{\rm max}$ (solid), and large eccentricities $e = 0.9e_{\rm max}$ (dotted). SB2s at $P < 10$ days are relatively complete, while the detection efficiencies of longer period systems considerably vary and critically depend on the primary mass, mass ratio, and eccentricity. We also display the completeness levels as calculated by Kobulnicky et al. (2014, grey), who assumed a sensitivity of $K_1 = 15$ km s^{-1} for both SB1s and SB2s and that the intrinsic binary population has a flat mass-ratio distribution ($\gamma = 0.0$) and a flat eccentricity distribution ($\eta = 0.0$).

at short orbital periods $P < 10$ days, while the longer period systems have detection efficiencies considerably less than unity. As expected, binaries with small mass ratios $q \approx 0.3$ are less complete than systems with large mass ratios $q \approx 0.8$. Because of Kepler's laws, SB2s with lower mass mid-B and late-B primaries are less complete than SB2s with more massive O-type and early-B primaries. As expected, eccentric binaries with $P = 10$ - 200 days have smaller detection efficiencies than their counterparts in circular orbits due to the finite cadence of observations. At the longest orbital periods $P \gtrsim 200$ days, however, only eccentric binaries near periastron produce detectable radial velocity variations.

We also compare in Fig. 5.4 our detection efficiencies $\mathcal{D}$ to the completeness levels as computed by Kobulnicky et al. (2014, dashed line in their Fig. 26). For this calculation, Kobulnicky et al. (2014) assumed a sensitivity threshold of $K_1 = 15$ km s^{-1} for both SB1s and SB2s, and that the intrinsic binary population has an underlying flat mass-ratio distribution ($\gamma = 0$) and flat eccentricity distribution ($\eta = 0$). Although these choices of $\gamma = 0$ and $\eta = 0$ are consistent with observations of short-period spectroscopic binaries ($P \lesssim 20$ days) where the observations are relatively complete (see below), the longer period systems may have different mass-ratio and eccentricity distributions. To correct for incompleteness, it is best to calculate the detection efficiency $\mathcal{D}(P, M_1, q, e)$ for each individual SB2. The binary's relative contribution to the total sample is then determined by the statistical weight $w = 1/\mathcal{D}$. In other words, for every one system observed with detection efficiency $\mathcal{D}(P, M_1, q, e)$, there are $w = 1/\mathcal{D}$ total systems with similar properties in the intrinsic population.

Our calculated detection efficiencies $\mathcal{D}$ have some level of uncertainty, especially considering the uncertainties in our adopted detection criteria (e.g., five observations

with $|v_{1,r}| > 15$ km s^{-1} and three observations with $|v_{1,r} - v_{2,r}| > 75$ km s^{-1}). We vary our detection criteria within reasonable limits and estimate the uncertainty in $\mathcal{D}$ to be ≈10%. We propagate this uncertainty into the statistical weights $w = 1/\mathcal{D}$. For example, if $\mathcal{D} = 0.6$, then $w \approx 1.7 \pm 0.3$, while for smaller detection efficiencies $\mathcal{D} = 0.3$, the uncertainties in the weights $w = 3.3^{+1.7}_{-0.8}$ become larger and asymmetric.

In Fig. 5.2, we compare the observed SB2s to the detection efficiencies $\mathcal{D}(P, M_1, q, e)$ as a function of P and e while assuming a primary mass $M_1 = 10$ M$_\odot$ and mass ratio $q = 0.4$. Similarly, in Fig. 5.3, we compare the observed SB2s to the detection efficiencies $\mathcal{D}$ as a function of P and q while assuming an eccentricity $e = 0.5e_{\rm max}$ and the same primary mass $M_1 = 10\,{\rm M}_\odot$. These completeness levels are for illustration purposes only, as we calculate $\mathcal{D}(P, M_1, q, e)$ for each system in the full four-dimensional parameter space. For example, the longest period SB2 in Figs. 5.2 - 5.3 (i.e., the system with the O-type primary, $\log P \approx 2.6$, $q \approx 0.3$, $e \approx 0.4$) has a detection efficiency $\mathcal{D} \approx 0.37$ and statistical weight $w \approx 2.7^{+1.0}_{-0.6}$. Meanwhile, the second longest period system (i.e., the SB2 with the mid-B primary, $\log P \approx 2.2$, $q \approx 0.4$, $e \approx 0.6$) has an even smaller detection efficiency $\mathcal{D} \approx 0.23$ and therefore larger weight $w \approx 4.3^{+3.3}_{-1.3}$. We compute w for each of the 44 early-type SB2s from the four surveys and for the 23 early-type SB2s from the SB9 catalog. By weighting each observed SB2 by w, we can now calculate the intrinsic eccentricity and mass-ratio distributions.

5.3.3 Eccentricity Distributions

To investigate the intrinsic eccentricity distribution as a function of orbital period, we divide the SB2s from the four surveys into short-period ($P = 3$ - 10 days) and long-period

(P = 10 - 500 days) subsamples. To ensure the distributions are not significantly affected by tidal evolution, we consider only systems with $e < 0.3$ and $e < 0.6$ in the short-period and long-period subsamples, respectively. In Fig. 5.5, we display the cumulative distribution of eccentricities for these two subsamples of SB2s after correcting for incompleteness. The length of each vertical step in the cumulative distribution is proportional to the statistical weight w of the SB2 it represents.

Our short-period subsample of 20 SB2s is relatively complete with statistical weights all below $w < 1.4$. For this population, we measure the power-law exponent of the eccentricity distribution to be $\eta = -0.3 \pm 0.2$ (see Table 5.1 and top panel of Fig. 5.5.). The uncertainty in η derives from the quadrature sum of the uncertainties from Poisson sample statistics and the uncertainties in the statistical weights w. Our result of $\eta = -0.3 \pm 0.2$ is consistent with the measurement of $\eta = -0.4 \pm 0.2$ by Sana et al. (2012), whose O-type spectroscopic binary sample is dominated by short-period systems.

For our long-period subsample of 13 SB2s with P = 10 - 500 days, we measure $\eta = 0.6 \pm 0.3$ after correcting for selection effects (Table 5.1). Although the statistical weights w = 1.2 - 4.3 of the SB2s in this long-period subsample are relatively large and uncertain, our measurement of $\eta = 0.6 \pm 0.3$ is still robust. For example, if we were to set all the weights to $w = 1$, we would still measure $\eta > 0.2$. Regardless of how we correct for selection effects, early-type SB2s at intermediate orbital periods are weighted toward larger values of η relative to the shorter-period systems.

The sample of SB2s from the four spectroscopic surveys is not large enough to measure changes in η as a function of M_1. We therefore investigate the 23 early-type

SB2s with $P = 8\text{-}40$ days from the SB9 catalog. To easily compare the eccentricity distributions, we analyze the distributions of $e/e_{\rm max}$, where $e_{\rm max}(P)$ is determined for each SB2 according to Eqn. 5.7. Because we only include SB2s with $P < 40$ days from the SB9 catalog, the detection efficiencies are $\mathcal{D} > 60\%$ for all our systems, i.e, the

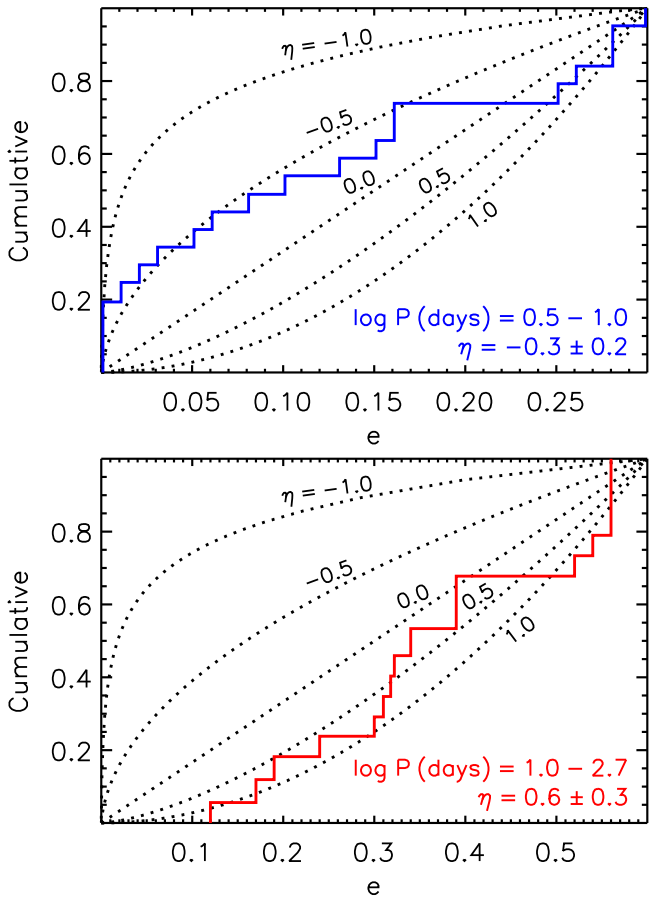

Figure 5.5: After accounting for incompleteness, we show the corrected cumulative distributions of eccentricities e for short-period (top; blue) and long-period (bottom; red) early-type SB2s from the combined sample of four spectroscopic surveys. The long-period subsample not only contains SB2s with larger eccentricities, but is also weighted toward larger values of η.

individual weights are $w < 1.7$. Even if the sensitivities of the various surveys that comprise the SB9 catalog are slightly different, the true statistical weights of the 23 selected SB2s will not significantly differ from our adopted values.

After correcting for incompleteness, we display in Fig. 5.6 the cumulative distributions of $e/e_{\rm max}$ for the 10 early (O9 - B3) and 13 late (B5 - B9.5) SB2s we selected from the SB9 catalog. Early-type SB2s with more massive primaries are clearly weighted toward larger values of η. For the O9 - B3 subsample, we measure $\eta = 0.9 \pm 0.4$. Meanwhile, for the B5 - B9.5 subsample, we measure $\eta = -0.3 \pm 0.2$ (Table 5.2). The observed differences between these two distributions may suggest more massive binaries form with systematically larger eccentricities. Alternatively, both early-B and late-B binaries may initially be born with $\eta \approx 0.9$, but the long-lived late-B binaries have had more time to tidally evolve toward smaller eccentricities. Based on the early-type SB2 observations alone, we cannot differentiate which of these two scenarios is the most likely explanation.

5.3.4 Mass-ratio Distributions

In a magnitude-limited survey, binaries with equally-bright twin components are probed across larger distances compared to single stars and binaries with faint companions. This Malmquist bias, typically called the Öpik effect in the context of binary stars, can lead to an artificial peak near unity in the mass ratio distribution (Öpik 1923). Fortunately, the four spectroscopic binary surveys have already accounted for the Öpik effect, either by targeting early-type stars in open clusters / stellar associations with fixed distances or by removing distant twin binaries that do not reside in a volume-limited sample. We

can therefore weight each observed SB2 by their respective values of w to correct for incompleteness.

After accounting for selection effects, we show in Fig. 5.7 the corrected cumulative distributions of mass ratios q for the 34 short-period ($P = 2$ - 20 days) and 10 long-period ($P = 20$ - 500 days) SB2s from the four spectroscopic surveys. Assuming the mass-ratio distribution can be described by a power-law across $0.25 < q < 1.0$, we measure $\gamma_{\rm largeq} = 0.1 \pm 0.3$ for the short-period subsample of early-type SB2s. This is consistent with the result of $\gamma = -0.1 \pm 0.6$ by Sana et al. (2012), whose O-type binary sample is dominated by short-period systems with $P = 2$ - 20 days. A simple power-law

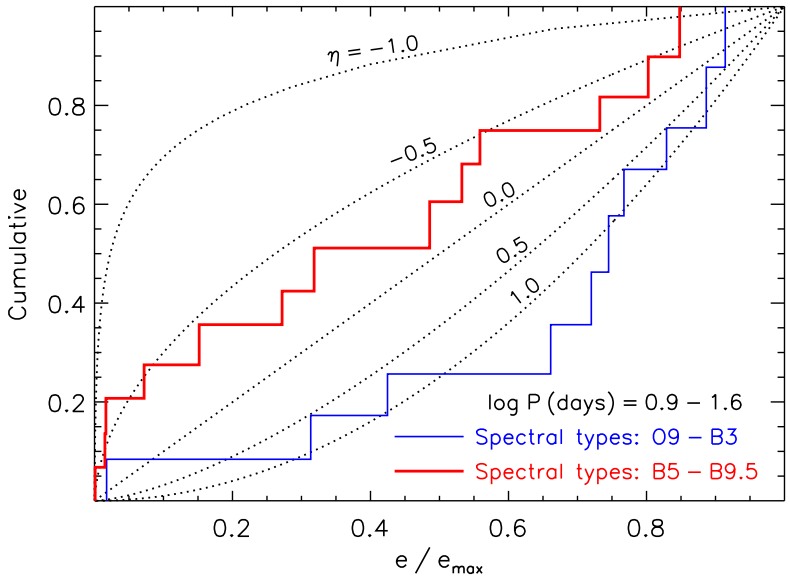

Figure 5.6: After accounting for selection effects, we compare the corrected cumulative distributions of $e/e_{\rm max}$ for the O9 - B3 (thin blue) and O9 - B3 (thick red) subsamples of SB2s with $P = 8$ - 40 days from the SB9 catalog. Long-lived late-B SB2s are weighted toward smaller values of η, either because they are initially born with and/or have tidally evolved toward smaller eccentricities.

distribution, however, does not fully describe the data. Allowing for an excess fraction of twin components with $q > 0.95$, we measure $\gamma_{\rm largeq} = -0.3 \pm 0.3$ and $\mathcal{F}_{\rm twin} = 0.08 \pm 0.03$ for our short-period subsample (see Table 5.1 and Fig. 5.7). For early-type binaries with $P = 2$ - 20 days, the frequency of companions with $q = 0.95$ - 1.00 is larger than the frequency of companions with $q = 0.90$ - 0.95 at the 2.6σ significance level. We emphasize that this twin excess is real considering the four spectroscopic binary surveys

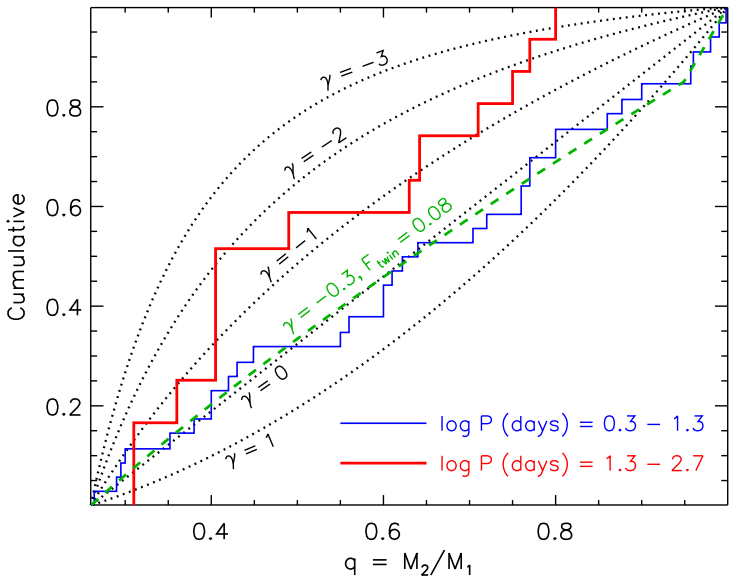

Figure 5.7: After accounting for incompleteness, we show the corrected cumulative distributions of mass ratios $q = M_2/M_1$ for short-period (thin blue) and long-period (thick red) early-type SB2s from the combined sample of four spectroscopic surveys. The short-period subsample is best fitted by a two-parameter model (dashed green) with a power-law component of $\gamma \approx -0.3$ and a small excess twin fraction of $\mathcal{F}_{\rm twin} \approx 0.08$. There is no indication of an excess twin population in the long-period subsample, which is adequately described by a power-law distribution with $\gamma = -1.5$ that is weighted toward small mass ratios.

have already accounted for the Öpik effect. Nonetheless, this excess twin fraction of $\mathcal{F}_{\rm twin} = 0.08$ is quite small; the remaining 92% of companions in this orbital period range follow a power-law distribution with $\gamma \approx -0.3$ across the broad interval $q = 0.1$ - 1.0.

After correcting for selection effects, it is clear from Fig. 5.7 that the long-period subsample of early-type SB2s is weighted toward small mass ratios. We measure $\gamma_{\rm largeq} = -1.5 \pm 0.4$ and an excess twin fraction that is consistent with zero. The 1σ upper limit on the excess twin fraction is $\mathcal{F}_{\rm twin} < 0.03$ (Table 5.1). The large uncertainty in the power-law exponent γ is mainly due to the small sample size, not the uncertainties in the large correction factors w. For example, if we were to set the weights $w = 1$ for all ten long-period SB2s, we would still measure $\gamma_{\rm largeq} = -0.5$. The detection efficiencies of binaries with small mass ratios are certainly smaller (§5.3.2), and so $\gamma_{\rm largeq} < -0.5$ is a robust upper limit. Hence, early-type SB2s become weighted toward smaller mass ratios $q \approx 0.2$ - 0.4 with increasing orbital period. This trend is already seen in the observed population of early-type SB2s (Fig. 5.3). By correcting for incompleteness, the intrinsic population of binaries with longer orbital periods are even further skewed toward smaller mass ratios compared to what is already observed in the raw sample. Our result is consistent with the conclusions of Abt et al. (1990), who also found that early-B spectroscopic binaries become weighted toward smaller mass ratios with increasing separation.

We next investigate the mass-ratio distributions inferred from the SB2s with $P = 8$ - 40 days we selected from the SB9 catalog. Unlike the four spectroscopic binary surveys, the SB9 catalog is still affected by the Öpik effect. We therefore consider only the SB2s from the SB9 catalog with $q < 0.9$ in order to remove any bias toward binaries with equally-bright components. Although we cannot quantify the excess twin fraction

$\mathcal{F}_{\rm twin}$, we can still measure the power-law component $\gamma_{\rm largeq}$ of the SB2s in the SB9 catalog.

After correcting for incompleteness, we display in Fig. 5.8 the cumulative distribution of mass ratios across $q = 0.35$ - 0.90 for the O9-B3 and B5-B9.5 subsamples from the SB9 catalog. We measure $\gamma_{\rm largeq} = -0.6 \pm 0.7$ for the O9 - B3 subsample and $\gamma_{\rm largeq} = -1.0 \pm 0.6$ for the B5 - B9.5 subsample (Table 5.2). These two subsamples are consistent with each other, especially considering the errors bars are rather large due to the small sample sizes. The measured values of $\gamma_{\rm largeq} \approx -1.0$ - -0.6 for these SB2s at intermediate orbital periods are between the values of $\gamma_{\rm largeq} \approx -0.3$ and $\gamma_{\rm largeq} \approx -1.5$

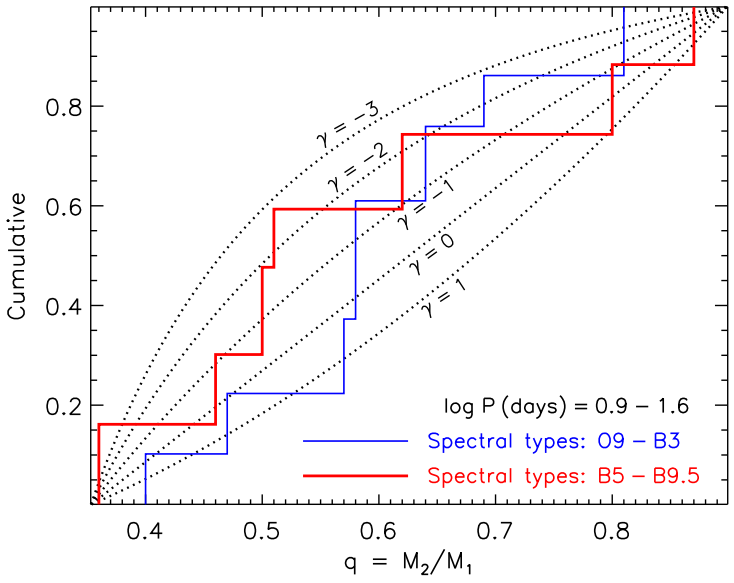

Figure 5.8: After accounting for selection effects, we compare the corrected cumulative distributions of mass ratios $q = M_2/M_1$ for the O9 - B3 (thin blue) and O9 - B3 (thick red) subsamples of SB2s with $P = 8$ - 40 days from the SB9 catalog. For these orbital periods, the O-type/early-B ($\gamma \approx -0.7$) and late-B ($\gamma \approx -1.0$) subsamples have mass-ratio distributions that are consistent with each other.

we measured above for the short-period and long-period SB2 subsamples, respectively.

5.3.5 Companion Frequencies

Now that we have measured the SB2 detection efficiencies and the corrected mass-ratio distributions, we can calculate the intrinsic frequency $f_{\rm logP}\,(M_1, P)$ of companions with $q > 0.1$ per decade of orbital period. In the Sana et al. (2012) sample of $\mathcal{N}_{\rm prim} = 71$ O-type primaries, there are $\mathcal{N}_{\rm SB2} = 18$ SB2s with $q > 0.25$ and $P = 2\text{-}20$ days. The detection efficiencies of these 18 SB2s are nearly 100%, and so the correction factor due to incompletness of binaries with $q > 0.25$ is $\mathcal{C}_{\rm largeq} = \sum_{j=1}^{\mathcal{N}_{\rm SB2}} w_j/\mathcal{N}_{\rm SB2} \approx 1.0$. We must still account for incompleteness of extreme mass-ratio binaries $q = 0.10\text{-}0.25$ that are only visible as SB1s. At short orbital periods, we measure the power-law component of the mass-ratio distribution to be $\gamma_{\rm largeq} = -0.3 \pm 0.3$ across $0.25 < q < 1.0$. We adopt a power-law slope of $\gamma_{\rm smallq} = (0.2 \pm 0.4)\gamma_{\rm largeq} = -0.1 \pm 0.2$ across $0.10 < q < 0.25$, which provides a correction factor of $\mathcal{C}_{\rm smallq} = 1.24 \pm 0.09$ for incompleteness toward small mass ratios (see §5.2). We note that Sana et al. (2012) identified $\mathcal{N}_{\rm SB1} = 3$ SB1s with $P = 2\text{-}20$ days in their O-type spectroscopic binary sample. If these three SB1s have stellar companions with $q = 0.10\text{-}0.25$, then $\mathcal{C}_{\rm smallq} = (\mathcal{N}_{\rm SB1}+\mathcal{N}_{\rm SB2})/\mathcal{N}_{\rm SB2} = (3+18)/18 = 1.16$, which is consistent with our measurement. The intrinsic frequency of companions with $q > 0.1$ per decade of orbital period is $f_{\rm logP} = \mathcal{N}_{\rm SB2}\,\mathcal{C}_{\rm smallq}\,\mathcal{C}_{\rm largeq}/\mathcal{N}_{\rm prim}/\Delta{\rm log}P$ $= (18 \pm \sqrt{18})\times 1.0 \times (1.25 \pm 0.09)/71/(1.3 - 0.3) = 0.31 \pm 0.08$ for O-type primaries and short orbital periods (Table 5.1). In other words, $(31 \pm 8)\%$ of O-type primaries have a companion with $P = 2\text{-}20$ days and $q > 0.1$.

We perform similar calculations for the samples of short-period companions to

B-type MS primaries. There is no indication that close binaries with B-type MS primaries have statistically different mass-ratio distributions than those with O-type primaries (§5.3.4), and so we assume the same correction factor $\mathcal{C}_{\rm smallq} = 1.25 \pm 0.09$ due to incompleteness of extreme mass-ratio binaries. For B-type primaries, however, the correction factor $\mathcal{C}_{\rm largeq}$ is slightly larger than unity because the detection efficiencies of SB2s with lower mass primaries are smaller (see §5.3.2). We find $\mathcal{C}_{\rm largeq} = 1.2 \pm 0.1$, 1.3 ± 0.1, and 1.4 ± 0.2 for the early-B, mid-B, and late-B subsamples, respectively. Following the same approach as above, we measure $f_{\rm logP} = 0.12 \pm 0.05$, 0.10 ± 0.04, and 0.07 ± 0.04 for the early-B, mid-B, and late-B subsamples, respectively, at short orbital periods (Table 5.1). The frequency of companions with $q > 0.1$ and $P < 20$ days is ≈4 - 5 times larger for O-type primaries than for late-B primaries. This trend is consistent with the conclusions of Chini et al. (2012), who find the spectroscopic binary fraction increases by a factor of ≈5 - 7 between B9 and O5 primaries (see their Fig. 5.3).

We next utilize the $\mathcal{N}_{\rm SB2} = 6$ SB2s with O-type primaries and $\log P\,({\rm days}) = 1.3$ - 2.7 to estimate $f_{\rm logP}$ at intermediate orbital periods. We measure the correction factor for incompleteness of $q > 0.25$ companions to be $\mathcal{C}_{\rm largeq} = \sum_{j=1}^{\mathcal{N}_{\rm SB2}} w_j / \mathcal{N}_{\rm SB2}$ $= 1.7 \pm 0.3$. For early-type SB2s at these longer orbital periods, we measure the power-law component of the mass-ratio probability distribution to be $\gamma_{\rm largeq} = -1.5 \pm 0.4$ across $q = 0.25$ - 1.0 (§5.3.4). We adopt $\gamma_{\rm smallq} = -0.3 \pm 0.6$ toward smaller mass ratios, which provides $\mathcal{C}_{\rm smallq} = 1.8 \pm 0.3$ (§2). The intrinsic frequency of companions with $q > 0.1$ per decade of orbital period is $f_{\rm logP} = \mathcal{N}_{\rm SB2}\,\mathcal{C}_{\rm largeq}\,\mathcal{C}_{\rm smallq} / \mathcal{N}_{\rm prim} / \Delta \log P$ $= (6 \pm \sqrt{6})(1.7 \pm 0.3)(1.8 \pm 0.3)/71/(2.7 - 1.3) = 0.19 \pm 0.09$ for O-type stars and intermediate orbital periods (Table 5.1).

For O-type primaries, the frequency of companions with $q > 0.25$ that are visible as

SB2s dramatically decreases with increasing orbital period. This is consistent with the results of Sana et al. (2012), who find that the period distribution of massive binaries are skewed toward shorter periods. However, the mass-ratio probability distribution becomes weighted toward smaller values with increasing separation (§5.3.4 and Abt et al. 1990). Kobulnicky et al. (2014) speculate there are many more SB1s with extreme mass ratios at intermediate orbital periods that are hiding below the spectroscopic detection limits. By accounting for the interrelation between P and q, we find the total frequency of companions with $q > 0.1$ to O-type stars only modestly decreases from $f_{\rm logP} = 0.31 \pm 0.08$ at $\log P\,({\rm days}) \approx 0.8$ to $f_{\rm logP} = 0.19 \pm 0.09$ at $\log P \approx 2.0$.

Finally, we combine the $\mathcal{N}_{\rm SB2} = 4$ SB2s with $P = 20$ - 200 days from the samples of $\mathcal{N}_{\rm prim} = 109 + 83 = 192$ early-B and mid-B primaries. We measure a large correction factor $\mathcal{C}_{\rm largeq} = \sum_{j=1}^{\mathcal{N}_{\rm SB2}} w_j / \mathcal{N}_{\rm SB2} = 2.5 \pm 0.6$ because spectroscopic binary surveys of B-type primaries are significantly incomplete at intermediate orbital periods (see Fig. 5.4). The uncertainties in the mass-ratio distribution are similar, and so we adopt the same value of $\mathcal{C}_{\rm smallq} = 1.8 \pm 0.3$ for incompleteness toward small mass ratios. We measure $f_{\rm logP} = (4 \pm \sqrt{4})(2.5 \pm 0.6)(1.8 \pm 0.3)/192/(2.3 - 1.3) = 0.10 \pm 0.06$ for early/mid B-type stars at intermediate orbital periods (Table 5.1). This is consistent with the frequecy $f_{\rm logP} \approx 0.10$ - 0.12 at shorter periods $\log P\,({\rm days}) \approx 0.8$, indicating the period distribution of companions to early-mid B-type stars approximately obeys Öpik's law across $P = 2$ - 200 days.

5.4 Eclipsing Binaries

Eclipsing binaries (EBs) with MS components are generally observed at short orbital periods $P \lesssim 50$ days. This is partially because of geometrical selection effects, but also due to the finite cadence of the observations (Söderhjelm & Dischler 2005). EBs offer an independent assessment of the close binary properties of massive stars. Deep and wide-field surveys, such as the third phase of the Optical Gravitational Lensing Experiment (OGLE-III Graczyk et al. 2011), have identified thousands of early-type EBs in the Magellanic Clouds. Despite the geometrical selection effects, we can achieve EB samples at short and intermediate orbital periods that are 1 - 2 orders of magnitude larger than the spectroscopic binary samples. In addition, unlike early-type SB2s, which can be observed only if $q > 0.25$, binaries with $q \approx 0.07$ - 0.25 can produce detectable eclipses if the orientations are sufficiently close to edge-on and the ratio of radii $R_2/R_1 \gtrsim 0.3$ are adequately large (Moe & Di Stefano 2015a). The parameter space of early-type EBs in terms of orbital periods P and mass ratios q are presented as the red region in Fig. 5.1.

In several papers (Moe & Di Stefano 2013, 2015a,b), we have analyzed OGLE-III EBs with B-type MS primaries in the Large Magellanic Cloud (LMC). By utilizing the known distance to the LMC and the calibrated evolutionary tracks of B-type MS stars, we have measured the physical properties of OGLE-III LMC EBs based solely on the photometric light curves. We also corrected for geometrical and evolutionary selection effects to recover the intrinsic multiplicity statistics. Please see the methods and discussions in these three papers, as we only report the main results pertinent to the present study (Table 5.3).

In Moe & Di Stefano (2013), we analyzed the eclipse depth and period distributions

Table 5.3: Binary statistics based on previous analysis of OGLE-III LMC EBs with B-type MS primaries and $P = 2\text{-}50$ days.

Reference	Primary Mass	Period Interval	Statistic
Moe & Di Stefano (2013)	$\langle M_1 \rangle = 10 \pm 3\,\mathrm{M}_\odot$	$\log P\,(\mathrm{days}) = 0.8 \pm 0.5$	$f_{\mathrm{logP}} = 0.22 \pm 0.05$
			$\gamma = -0.9 \pm 0.3$
			$\mathcal{F}_{\mathrm{twin}} = 0.07 \pm 0.05$
Moe & Di Stefano (2015a)	$\langle M_1 \rangle = 10 \pm 4\,\mathrm{M}_\odot$	$\log P\,(\mathrm{days}) = 0.7 \pm 0.2$	$f_{\mathrm{logP}} = 0.14 \pm 0.05$
			$\gamma = -0.7 \pm 0.3$
Moe & Di Stefano (2015b)	$\langle M_1 \rangle = 7 \pm 3\,\mathrm{M}_\odot$	$\log P\,(\mathrm{days}) = 1.5 \pm 0.2$	$\eta = 0.5 \pm 0.4$
			$\gamma_{\mathrm{largeq}} = -1.1 \pm 0.3$
			$\mathcal{F}_{\mathrm{twin}} < 0.02$
	$\langle M_1 \rangle = 10 \pm 3\,\mathrm{M}_\odot$		$f_{\mathrm{logP}} = 0.23 \pm 0.08$
			$\eta = 0.8 \pm 0.3$
			$\gamma_{\mathrm{largeq}} = -1.6 \pm 0.4$
			$\mathcal{F}_{\mathrm{twin}} < 0.04$

of EBs with early-B primaries and $P = 2\text{-}20$ days. Across this orbital period interval, we recovered an intrinsic binary fraction of $(22 \pm 5)\%$ with $q > 0.1$, i.e., $f_{\mathrm{logP}} = 0.22 \pm 0.05$, a mass-ratio distribution weighted toward small values with $\gamma = -0.9 \pm 0.3$, and a small excess fraction of twins $\mathcal{F}_{\mathrm{twin}} = 0.07 \pm 0.05$ (Table 5.3). At these short orbital periods, the early-B companion frequency $f_{\mathrm{logP}} \approx 0.22$ measured from EBs is about halfway between the O-type companion frequency $f_{\mathrm{logP}} \approx 0.31$ and the early/mid B-type companion frequency $f_{\mathrm{logP}} \approx 0.10\text{-}0.12$ calculated from SB2s.

In Moe & Di Stefano (2015a), we identified and measured the physical properties of young EBs with early/mid B-type MS primaries, low-mass pre-MS companions ($q \approx 0.07$-0.36), and short orbital periods $P = 3.0\text{-}8.5$ days. We found that $(2.0 \pm 0.6)\%$ of B-type MS stars have extreme mass-ratio companions $q < 0.25$ with $P = 3.0\text{-}8.5$ days, and that these systems constitute $\approx 0.3\text{-}0.4$ of all companions to B-type primaries across the same period interval. This translates to $f_{\mathrm{logP}} \approx (0.020 \pm 0.006)/(0.35 \pm 0.05)/(\log 8.5 - \log 3.0) = 0.14 \pm 0.05$ and $\gamma = -0.7 \pm 0.3$

(Table 5.3). The relatively large frequency of close, low-mass stellar companions to B-type MS primaries dictates the majority of early-type SB1s contain stellar non-degenerate secondaries Moe & Di Stefano (2015a).

In Moe & Di Stefano (2015b), we analyzed the properties of EBs with B-type MS primaries and intermediate orbital periods $P = 20\text{-}50$ days. For the entire population of EBs, which is dominated by relatively older and long-lived mid-B primaries, we measured $\eta = 0.1 \pm 0.2$. We also discovered the ages τ and eccentricities e of the EBs are anticorrelated at a statistically significant level due to tidal evolution. By selecting only the young systems with $\tau < 10$ Myr that have not yet tidally evolved toward smaller eccentricities, we found that companions to early-B primaries at these orbital periods are initially born with $\eta = 0.8 \pm 0.3$ (Table 5.3). We measured a statistically significant anticorrelation between τ and e for both early-B and mid-B subsamples. We currently select the 29 EBs from Moe & Di Stefano (2015b) with measured primary masses $M_1 = 5\text{-}9\,M_\odot$, ages $\tau < 30$ Myr, and eccentricities $e < 0.7$. Based on this subsample, we find binaries with mid-B primaries and intermediate orbital periods are born with $\eta = 0.5 \pm 0.4$ (Table 5.3).

After correcting for selection effects in Moe & Di Stefano (2015b), we measured $\gamma_{\rm largeq} = -1.1 \pm 0.3$ and $\mathcal{F}_{\rm twin} < 0.02$ for mid-B primaries and intermediate orbit periods (Table 5.3). The data also indicate that EBs with slightly more massive primaries favor smaller mass ratios, i.e., $\gamma_{\rm largeq} = -1.6 \pm 0.4$ and $\mathcal{F}_{\rm twin} < 0.04$ (Table 5.3). As found for SB2s, early-type binaries with slightly longer orbital periods $P > 20$ days favor smaller mass ratios, i.e., smaller values of γ and $\mathcal{F}_{\rm twin}$.

In Moe & Di Stefano (2015b), we estimated that $(6.7 \pm 2.2)\%$ of mid-B primaries

have companions with $q > q_{\rm thresh} = 0.2$ and $P = 20$ - 50 days. In the present study, we adopt a power-law slope $\gamma_{\rm smallq} = (0.2 \pm 0.4)\gamma_{\rm largeq} = (0.2 \pm 0.4)(-1.1 \pm 0.3)$ $= -0.2 \pm 0.5$ for the mass-ratio distribution across $0.1 < q < q_{\rm thresh} = 0.2$. This provides the correction factor $\mathcal{C}_{\rm smallq} = 1.4 \pm 0.1$ for incompleteness toward small ratios (see §5.2). The intrinsic frequency of companions with $q > 0.1$ is therefore $f_{\rm logP} = (0.067 \pm 0.022) \times (1.4 \pm 0.1)/(\log 50 - \log 20) = 0.23 \pm 0.08$ for mid-B stars and intermediate orbital periods (Table 5.3).

5.5 Long-Baseline Interferometry

Long-baseline interferometry (LBI) can reveal binary companions at extremely small angular separations ≈5 - 100 mas (Rizzuto et al. 2013; Sana et al. 2014). Given the typical distances $d \approx 0.1$ - 2 kpc to early-type MS stars, these angular separations correspond to physical projected separations $\rho \approx 1.5$ - 30AU, i.e. intermediate orbital periods $2.3 \lesssim \log P\,({\rm days}) \lesssim 4.3$. LBI is limited by the brightness contrasts $\Delta{\rm m} \lesssim 4$ mag between the binary components, so the secondaries must be comparable in luminosity to the primaries to be detected. Unlike SB2s, which become biased toward larger q with increasing P, the sensitivity of LBI is nearly constant with respect to orbital separation (see Fig. 5.4 in Rizzuto et al. 2013 and Fig. 5.7 in Sana et al. 2014). LBI can therefore provide an unbiased sample of moderate mass-ratio companions $q \gtrsim 0.3$ at intermediate orbital periods $2.3 \lesssim \log P\,({\rm days}) \lesssim 4.3$ (magenta region in our Fig. 5.1).

5.5.1 Early-B Primaries

For a sample of $\mathcal{N}_{\rm prim} = 58$ B0-B5 MS primaries in the Sco-Cen OB association ($d \approx 130$ pc), Rizzuto et al. (2013) used LBI to identify 24 companions with angular separations 7 - 130 mas. They measured the brightness contrasts Δm of the binary components at wavelengths $\lambda = 550$ - 800 nm, and then estimated the mass ratios q from Δm according to stellar evolutionary tracks. Rizzuto et al. (2013) report $\mathcal{N}_{\rm comp} = 18$ companions with $q \geq 0.3$ and projected orbital separations $\rho = 1.5$ - 30 AU, which correspond to orbital periods $2.3 \lesssim \log P\,({\rm days}) \lesssim 4.3$. This subsample is relatively complete across the specified mass-ratio and period interval. In Fig. 5.9, we display the cumulative distribution of mass ratios for these 18 systems. The mass-ratio distribution of the 18 binaries are fitted to high accuracy by a single power-law distribution with $\gamma_{\rm largeq} = -2.5 \pm 0.4$. The upper limit on the excess twin fraction is $\mathcal{F}_{\rm twin} < 0.02$ (Table 5.4). Companions to early-B primaries at intermediate orbital periods are weighted toward extreme mass ratios. For $q \gtrsim 0.3$, the binary mass ratios are surprisingly consistent with random pairings drawn from a Salpeter IMF ($\gamma = -2.35$).

Rizzuto et al. (2013) do not directly state that their binaries discovered through long-baseline interferometry strongly favor small mass ratios. They instead compile observations of short-period spectroscopic and long-period visual companions to the 58 early-B MS stars in their sample. They then report a mass-ratio distribution with $\gamma \approx -0.5$ that is averaged across all orbital periods. We emphasize that the binary distributions of P and q are not necessarily uncorrelated. LBI offers a unique perspective into the binary properties of massive stars at intermediate periods, and should therefore be treated independently.

We wish to evaluate the robustness of our measurement of $\gamma_{\rm largeq} = -2.5 \pm 0.4$, and so we estimate the systematic uncertainties in deriving q from Δm. We calculate our own values of q from the measured brightness contrasts Δm reported in Rizzuto et al. (2013) by incorporating different stellar evolutionary tracks, ages, and atmospheric parameters. We also apply a similar method to the O-type binary sample of Sana et al. (2014), who currently report only the brightness contrasts Δm (see 5.2).

In Fig. 5.10, we compare the brightness contrasts Δm to the mass ratios q calculated by Rizzuto et al. (2013) for the 20 binaries in their sample with $\rho = 1.5$ - 30 AU. This

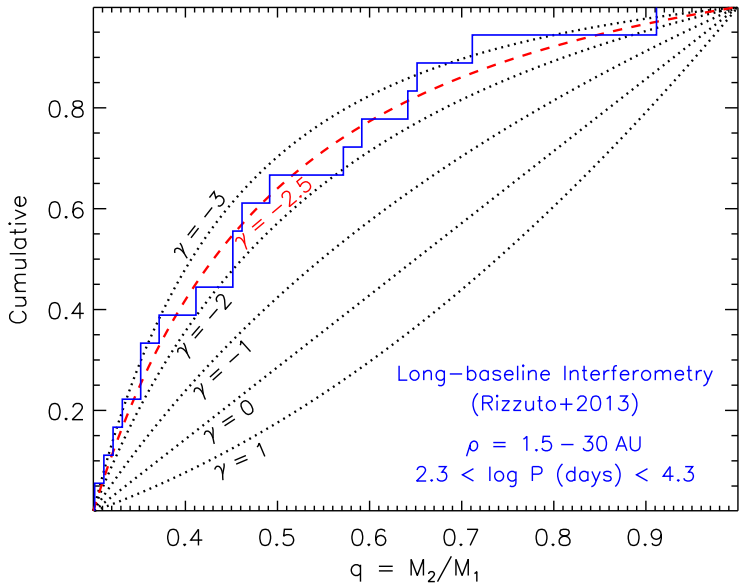

Figure 5.9: Cumulative distribution of mass ratios q for the 18 companions (blue) to 58 early-B MS stars with $q \geq 0.3$ and projected separations $\rho = 1.5$ - 25 AU ($2.3 \lesssim \log P \lesssim 4.3$) identified through long-baseline interferometry (Rizzuto et al. 2013). In this parameter space, the companions are relatively complete and described by a single power-law mass-ratio distribution $p_q \propto q^{\gamma}$ with $\gamma = -2.5 \pm 0.4$ (dashed red). For $q > 0.3$, this is surprisingly consistent with random pairings drawn from a Salpeter IMF ($\gamma = -2.35$).

subsample includes the 18 systems with $q \geq 0.3$ incorporated above as well as two additional systems with $q \approx 0.26$ - 0.29 near the detection limit. Rizzuto et al. (2013) report an uncertainty of 10% in the mass ratios, which we indicate in our Fig. 5.10. Eighteen of the 20 binaries have relatively unevolved MS primaries with B0 - B5 spectral types and IV - V luminosity classes. Two systems, ϵ-Cen and κ-Sco, have ≈B1III spectral

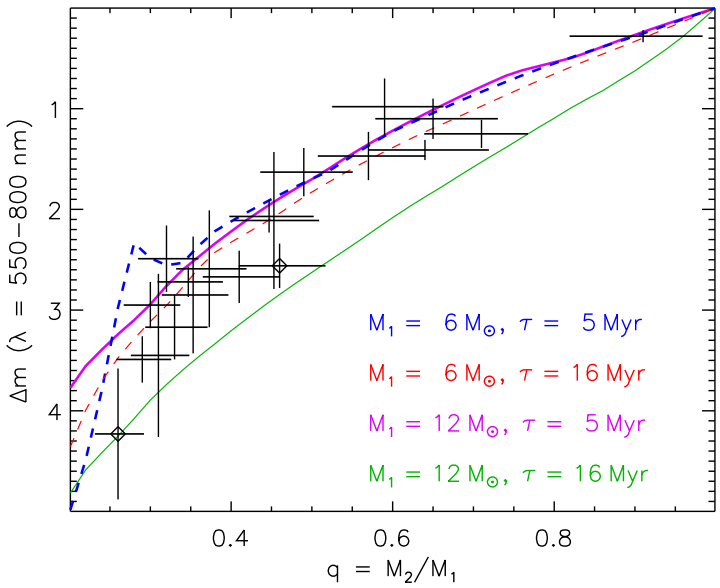

Figure 5.10: Measured mass ratios $q = M_2/M_1$ and brightness contrasts Δm (mag) at $\lambda = 550$ - 800 nm for the 20 companions to early-B primaries with projected separations $\rho = 1.5$ - 30 AU as reported by Rizzuto et al. (2013). Eighteen of the binaries have MS primaries with luminosity classes of IV-V, while two systems (shown with diamond symbols) have primaries with luminosity classes of III. We model the brightness contrasts ΔR_c in the red band for a primary mass $M_1 = 6\,M_\odot$ (dashed) and ages $\tau = 5$ Myr (thick blue) and $\tau = 16$ Myr (thin red) and for a primary mass $M_1 = 12\,M_\odot$ (solid) and ages $\tau = 5$ Myr (thick magenta) and $\tau = 16$ Myr (thin green). Our models are consistent with the mass ratios provided in Rizzuto et al. (2013).

types and are therefore on the upper MS or giant branch (shown in our Fig. 5.10 as the two systems with diamond symbols). Given the same brightness contrast Δm, binaries with older primaries on the upper MS have larger mass ratios.

To determine our own values of q from the brightness contrasts Δm, we utilize the solar-metallicity pre-MS and MS stellar evolutionary tracks from (Tognelli et al. 2011) and (Bertelli et al. 2009), respectively. We consider two primary masses, $M_1 = 12\mathrm{M}_\odot$ and $M_1 = 6\,\mathrm{M}_\odot$, which are representative of B1V and B5V MS stars, respectively. We model the brightness contrasts at two different ages, $\tau = 5$ Myr and $\tau = 16$ Myr, which span the estimated ages of the stellar subgroups within the Sco-Cen OB association (Rizzuto et al. 2013). We incorporate the bolometric corrections and color indices from (Pecaut & Mamajek 2013) to calculate the red $\mathrm{R_c}$-band magnitudes from the stellar luminosities and effective temperatures. In Fig. 5.10, we plot our derived brightness contrasts $\Delta\mathrm{R_c}$ as a function of q for the four different combinations of primary mass and age. Our models are consistent with the mass ratios reported by Rizzuto et al. (2013). In fact, the two systems with ≈B1III primaries, which systematically lie below the trend of the IV-V primaries in Fig. 5.10, match our massive, older model with $M_1 = 12\,\mathrm{M}_\odot$ and $\tau = 16$ Myr (green line in Fig. 5.10).

To estimate the systematic uncertainties in γ_{largeq}, we utilize the red line in Fig. 5.10 to calculate our own values of q. Based on this model, we find mass ratios q are slightly smaller than those reported by Rizzuto et al. (2013). We find 16 systems (instead of 18) with $q > 0.3$. By fitting a power-law mass-ratio distribution to these 16 binaries, we measure $\gamma_{\mathrm{largeq}} = -2.3 \pm 0.5$. This nearly matches the previous result of $\gamma_{\mathrm{largeq}} = -2.5 \pm 0.4$ from using the mass ratios q directly provided by Rizzuto et al. (2013). The systematic uncertainty $\delta\gamma_{\mathrm{sys}} \approx 0.2$ is smaller than the measurement uncertainty

Table 5.4: Companion statistics based on long-baseline interferometric observations of early-B stars (Rizzuto et al. 2013) and O-type stars (Sana et al. 2014).

Reference and Primary Mass / Period Interval	Statistic
Rizzuto et al. (2013);	$\gamma_{\rm largeq} = -2.5 \pm 0.4$
$\langle M_1 \rangle = 10 \pm 3\,{\rm M}_\odot$;	$\mathcal{F}_{\rm twin} < 0.02$
$\log P\,({\rm days}) = 3.3 \pm 1.0$	$f_{\rm logP} = 0.40 \pm 0.14$
Sana et al. (2014);	$\gamma_{\rm largeq} = -1.3 \pm 0.4$
$\langle M_1 \rangle = 28 \pm 8\,{\rm M}_\odot$;	$\mathcal{F}_{\rm twin} < 0.03$
$\log P\,({\rm days}) = 3.5 \pm 1.0$	$f_{\rm logP} = 0.36 \pm 0.09$

$\delta\gamma_{\rm meas} \approx 0.4$. Our conclusion that binaries with early-B primaries and intermediate orbital periods are weighted toward extreme mass ratios is robust.

We extend the mass-ratio probability distribution down to $q = 0.1$ with a power-law slope of $\gamma_{\rm smallq} = (0.2 \pm 0.4)\gamma_{\rm largeq} = -0.5 \pm 1.0$ across $0.1 < q < 0.3$. This implies a correction factor of $\mathcal{C}_{\rm smallq} = 2.6 \pm 0.7$ for incompleteness toward small mass ratios (§5.2). The frequency of companions with $q > 0.1$ per decade of orbital period is $f_{\rm logP} = \mathcal{N}_{\rm comp}\,\mathcal{C}_{\rm smallq}/\mathcal{N}_{\rm prim}/\Delta{\rm log}P = (18 \pm \sqrt{18})(2.6 \pm 0.7)/58/(4.3 - 2.3) = 0.40 \pm 0.14$ for early-B primaries and $\log P\,({\rm days}) \approx 3.3$ (Table 5.4). The dominant source of uncertainty is due to the large error in $\mathcal{C}_{\rm smallq} \approx = 2.6 \pm 0.7$, i.e., the uncertainty in the mass-ratio distribution below $q < 0.3$. Nevertheless, even after considering the uncertainties, at least half of early-B MS stars have a companion with $2.3 < \log P\,({\rm days}) < 4.3$.

5.5.2 O-type Primaries

Sana et al. (2014) recently surveyed ≈100 O-type stars with near-infrared magnitudes $H < 7.5$ in the southern hemisphere using both long-baseline interferometry (LBI) and sparse aperture masking (SAM) techniques. The combination of these observational

methods provide a relatively complete sample of companions with angular separations 2 - 60 mas and brightness contrasts ΔH < 4.0 mag (see Fig. 5.7 in Sana et al. 2014). Sana et al. (2014) also resolved additional companions at wider separations $\gtrsim 0.3''$ with adaptive optics, which we examine in §5.7.

It is difficult to reliably measure the mass ratios and correct for incompleteness for binaries with supergiant primaries. In our current analysis, we consider only the 56 O-type primaries in the Sana et al. (2014) sample that were observed by both LBI and SAM methods and have luminosity classes II.5 - V (see their Fig. 5.1). Their survey is magnitude-limited, so we must correct for the Öpik effect / Malmquist bias toward binaries with equally bright components. We remove the two detected binaries (HD 93222 and HD 123590) with observed total magnitudes $H \approx 7.2$ - 7.5 and brightness contrasts ΔH $\lesssim 0.3$ mag. These two systems would be fainter than the $H = 7.5$ limit if we were to consider the luminosity from the primaries alone. Our culled sample from the Sana et al. (2014) survey contains $\mathcal{N}_{\rm prim} = 54$ O-type MS primaries.

From this subsample of 54 O-type MS primaries, Sana et al. (2014) identified 25 companions with angular separations 2 - 60 mas and brightness contrasts ΔH < 4.0 mag. Given the typical distances $d = 1$ - 2 kpc to the O-type stars with luminosity classes II.5 - V in the Sana et al. (2014) sample (see their Fig. 5.3), the angular separations correpond to projected separations $\rho \approx 3$ - 90 AU, i.e. $2.5 < \log P\,(\text{days}) < 4.5$. In Fig. 5.11, we show the measured brightness constrasts ΔH and their uncertainties for the 25 binaries as reported by Sana et al. (2014). For the few systems with multiple measurements of the brightness contrast, we display a weighted average and uncertainty.

We employ a method similar to that described in §5.5.1 to measure the binary

mass ratios from the observed brightness contrasts ΔH. For our 25 O-type binaries, we utilize the calibrated relations for galactic O-type stars in Martins et al. (2005) to estimate the primary mass, effective temperature, and absolute M_V magnitude according to the primary's spectral type and luminosity class. We then calculate the near-infrared

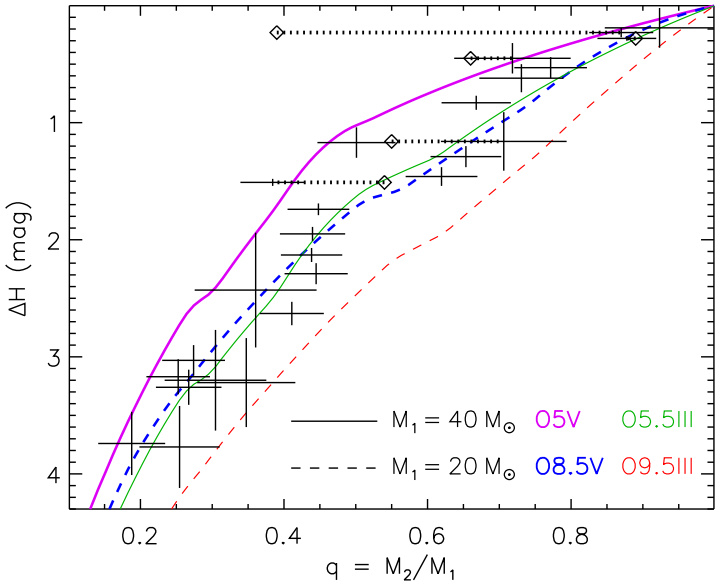

Figure 5.11: Near-infrared brightness contrasts ΔH versus binary mass ratios q. We model the brightness contrasts ΔH for $M_1 = 40\,M_\odot$ (solid) and $M_1 = 20\,M_\odot$ (dashed) primaries. On the MS, these masses correspond to O5V (thick magenta) and O8.5V (thick dashed blue) primaries. As giants, they will appear as O5.5III (thin green) and O9.5III (thin dashed red). For the 25 O-type binaries from Sana et al. (2014) with ΔH < 4.0 mag, angular separations 2 - 60 mas, and primaries with II.5-V luminosity classes, we utilize our models to measure the mass ratios q according to the observed ΔH and the spectral types and luminosity classes of the primaries. Five of the 25 binaries are SB2s (diamonds), where we link the dynamical mass ratios to our measurements inferred from the brightness contrasts (black dotted lines).

magnitude H according to the temperature-dependent color indices $(V-H)(T_{\rm eff})$ reported in Pecaut & Mamajek (2013). If the secondary is also an O-type star with $M_2 \gtrsim 16\,{\rm M}_\odot$, then we use this same technique to estimate its own value of H. For these O-type + O-type binaries, we assume the secondary is alway a MS star with luminosity class V if $q < 0.6$. For $q > 0.6$, we smoothly interpolate the secondary's luminosity class between V at $q = 0.6$ and the luminosity class of that of the primary at $q = 1.0$. If the secondary is a B-type star with $M_2 \lesssim 16\,{\rm M}_\odot$, we interpolate the solar-metallicity stellar evolutionary tracks of Bertelli et al. (2009) to determine the secondary's near-infrared magnitude H. For these O-type + B-type binaries, we adopt an age appropriate for the spectral type and luminosity class of the primary.

In Fig. 5.11, we display our modeled brightness contrasts ΔH as a function of mass ratio q for $M_1 = 20\,{\rm M}_\odot$ (dashed) and $M_1 = 40\,{\rm M}_\odot$ (solid) primaries. On the MS, these masses correspond to O8.5V (thick dashed blue) and O5V (thick solid magenta), respectively. The magenta model corresponding to the O5V primary is flatter than the dashed blue model of the O8.5V primary because the MS mass-luminosity relation flattens toward larger primary masses. For example, a 40 $M_\odot$ MS star is $\Delta{\rm H} \approx 1.0$ mag brighter than a 20 $M_\odot$ MS star (value of magenta curve at $q = 0.5$), while a 20 $M_\odot$ MS star is $\Delta{\rm H} \approx 1.7$ mag brighter than a 10 $M_\odot$ MS star (value of dashed blue curve at $q = 0.5$). The $M_1 = 20\,{\rm M}_\odot$ primary will increase in brightness by $\Delta{\rm H} \approx 1.0$ mag as it evolves into an O9.5III giant (thin dashed red line in Fig. 5.11). Meanwhile, the $M_1 = 40\,{\rm M}_\odot$ primary increases in brightness by only $\Delta{\rm H} \approx 0.6$ mag as it becomes an O5.5III star (thin green). This is why the green and magenta solid curves that correspond to the $M_1 = 40\,{\rm M}_\odot$ primary differ by $\Delta{\rm H} \approx 0.6$ mag at $q \lesssim 0.4$, while the blue and red dashed models that represent the $M_1 = 20\,{\rm M}_\odot$ primary differ by $\Delta{\rm H} \approx 1.0$ mag toward

small mass ratios.

For the 25 binaries we have selected from Sana et al. (2014), we determine the mass ratios q from our models according to the listed brightness contrasts ΔH and spectral types and luminosity classes of the primaries. We propagate the measurement uncertainties in ΔH as well as errors of $\approx$0.5 in the spectral subtypes and luminosity classes to derive our uncertainties in q. We display our solutions for the mass ratios of the 25 systems in Fig. 5.11. Twenty-three of the binaries are between our O5V (magenta) and O9.5III (dashed red) models. The two remaining systems have $\approx$O4V primaries and lie just above the magenta curve.

Five of the 25 O-type binaries resolved with LBI/SAM in our subsample are also long-period SB2s with independent measurements of the mass ratio (Sana et al. 2014). The SB2s with dynamical mass ratio measurements are HD 54662 ($q = 0.39$, Boyajian et al. 2007), HD 150136 ($q = 0.54$, Mahy et al. 2012), HD 152246 ($q = 0.89$, Nasseri et al. 2014), HD 152314 ($q = 0.55$, Sana et al. 2012), and HD 164794 ($q = 0.66$, Rauw et al. 2012). We display the five spectroscopic mass ratios as diamond symbols in Fig. 5.11. For these five systems, we also plot thick dotted lines between the SB2 measurements and the mass ratios we determined from the brightness contrasts ΔH.

Three of the five SB2s have dynamical mass ratios consistent with our values, i.e. they are discrepant at $<2\sigma$ significance level. We adopt the SB2 dynamical mass ratios for these three systems because they are measured to higher precision. For one of the two remaining systems, HD 150136, we measure $q = 0.38 \pm 0.05$ according to the moderate brightness contrast ΔH = 1.5 mag, while the SB2 dynamical measurements provide $q \approx 0.54$. HD 150136 is a triple system where the tertiary component resolved

with LBI orbits an inner binary of spectral types O3-3.5V ($M_1 \approx 64\,M_\odot$) and O5.5-6V ($M_2 \approx 40\,M_\odot$) in a $P = 2.7$ day orbit (Mahy et al. 2012). The additional luminosity from the inner companion increases the brightness contrast ΔH between the inner binary and tertiary, which biases our mass ratio measurement toward smaller values. However, Mahy et al. (2012) assumed the tertiary component was coplaner with the inner binary to derive a dynamical mass of $M_3 \approx 35\ M_\odot$. Based on the observed spectral type O6.5-7V of the tertiary alone, the mass is $M_3 \approx 27\,M_\odot$ (Mahy et al. 2012). This implies a mass ratio of $q = M_3/M_1 \approx 0.42$. We adopt $q = 0.47$ for the tertiary companion in HD 150136, which is between the dynamical (coplaner) measurement of $q \approx 0.54$ and the spectroscopic and (biased) brightness contrast measurements of $q = 0.42$ and $q = 0.38$, respectively. Finally, for HD 54662, we measure $q \approx 0.87$ based on the small brightness contrast ΔH = 0.2 mag, while Boyajian et al. (2007) report an SB2 dynamical mass ratio of $q = K_1/K_2 = 0.39$. The spectroscopic absorption features of the binary components in HD 54662 are significantly blended (Boyajian et al. 2007), and so the velocity semi-amplitudes are rather uncertain. Moreover, Boyajian et al. (2007) fit O6.5V and O9V spectral types for the binary components with an optical flux ratio of $F_2/F_1 \approx 0.5$. These spectral types and optical brightness contrast imply a much larger mass ratio of $q \approx 0.7$. For HD 54662, we adopt this spectroscopic measurement of $q = 0.70$, which is between the brightness contrast measurement of $q = 0.89$ and the uncertain dynamical measurement of $q = 0.39$.

For the 20 companions resolved at intermediate orbital periods without spectroscopic mass measurements, we adopt the mass ratios measured from the brightness contrasts ΔH. As shown in Fig. 5.11, the detection limit of ΔH = 4.0 mag is sensitive to companions with $q > 0.25$ for O-type primaries with luminosity classes III-V. For the

$\mathcal{N}_{\rm prim} = 54$ O-type primaries with luminosity classes II.5 - V in Sana et al. (2014), we find $\mathcal{N}_{\rm comp} = 24$ companions with $q > 0.25$ and $2.5 < \log P\,({\rm days}) < 4.5$, which represent a relatively complete subsample.

We display the cumulative distribution of mass ratios for these 24 systems in Fig. 5.12. We fit the mass-ratio probability distribution and measure $\gamma_{\rm largeq} = -1.3 \pm 0.4$ and $\mathcal{F}_{\rm twin} < 0.03$ (Table 5.4). Although not as steep as the measurement of $\gamma_{\rm largeq} = -2.5$ for LBI companions to early-B primaries, the mass-ratio distribution for O-type binaries is still weighted toward small mass ratios. Moreover, companions to O-type stars at intermediate orbital periods $2.5 < \log P < 4.5$, which are described by $\gamma_{\rm largeq} = -1.3$ and $\mathcal{F}_{\rm twin} \approx 0.0$, clearly favor smaller mass ratios compared to companions at short orbital periods $\log P < 1.3$, which are modeled by $\gamma_{\rm largeq} = -0.3$ and $\mathcal{F}_{\rm twin} \approx 0.08$ (see §5.3 and §5.9).

For the mass-ratio probability distribution across $0.10 < q < 0.25$, we adopt a power-law slope of $\gamma_{\rm smallq} = (0.2 \pm 0.4)\gamma_{\rm largeq} = -0.3 \pm 0.6$ (see §5.2). This provides a correction factor of $\mathcal{C}_{\rm smallq} = 1.6 \pm 0.2$ for incompleteness toward small mass ratios. For O-type primaries, the intrinsic frequency of companions with $q > 0.1$ and intermediate orbital periods $\log P\,({\rm days}) \approx 3.5$ is $f_{\rm logP} = \mathcal{N}_{\rm comp}\,\mathcal{C}_{\rm smallq}/\mathcal{N}_{\rm prim}/\Delta{\rm log}P = (24 \pm \sqrt{24})(1.6 \pm 0.2)/54/(4.5 - 2.5) = 0.36 \pm 0.09$ (Table 5.4). This is slightly larger than but consistent with our SB2 measurements of $f_{\rm logP} = 0.31$ and $f_{\rm logP} = 0.19$ for O-type stars at $\log P \approx 0.8$ and $\log P \approx 2.0$, respectively.

5.6 Cepheids

The majority of Cepheid giant variables evolve from mid-B MS stars with $\langle M_1 \rangle \approx 4\text{-}8\,M_\odot$ (Turner 1996; Remage Evans et al. 2013). B-type MS stars with close stellar companions at $\log P\,(\text{days}) \lesssim 2.6$, i.e., $P \lesssim 1$ yr, will fill their Roche lobes before they can expand into the instability strip (Remage Evans et al. 2013). Many of the mid-B primaries with close binary companions are unlikely to evolve into Cepheid variables.

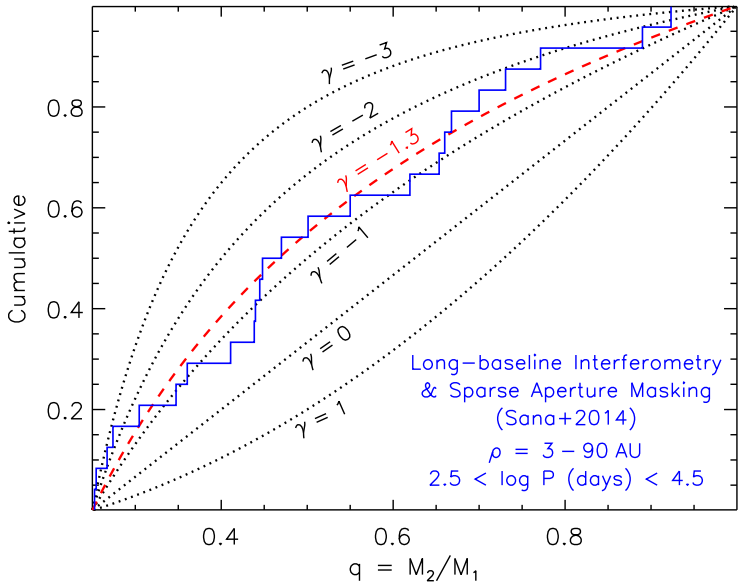

Figure 5.12: Cumulative distribution of mass ratios q for the 24 companions (blue) to 54 O-type MS stars with $q \geq 0.25$ and projected separations $\rho = 3\text{-}90$ AU ($2.5 \lesssim \log P \lesssim 4.5$) identified through long-baseline interferometry and sparse aperture masking (Sana et al. 2014). For this relatively complete subsample, we measure the power-law component of the mass-ratio probability distribution $p_q \propto q^\gamma$ to be $\gamma = -1.3 \pm 0.4$ (dashed red). Although favoring small mass ratios $q \approx 0.25\text{-}0.40$, the observed mass-ratio distribution is inconsistent with random pairings of the IMF.

The Cepheid population can, however, offer invaluable insight into the frequency and properties of companions to intermediate-mass stars at longer orbital periods $\log P \gtrsim 2.6$. Although the orbits may have tidally evolved toward smaller eccentricities, the masses of detached binaries with Cepheid primaries and MS companions have not significantly changed from their original zero-age MS values (Remage Evans et al. 2013). In addition, unlike their B-type MS progenitors, which have rotationally and pressure broadened spectra (see §5.3), Cepheid giants have narrow absorption lines. Companions that produce small velocity semi-amplitudes $K_1 \approx 2$ km s^{-1} can be detected once the primary evolves into a Cepheid (Remage Evans et al. 2015). Spectroscopic surveys of Cepheid primaries are therefore more sensitive toward companions with smaller masses and longer orbital periods.

Remage Evans et al. (2013) took advantage of the temperature differences between cool Cepheid giants and hot late-B/early-A companions that are still on the MS. For a magnitude-limited sample of $\mathcal{N}_{\rm Cepheid} = 76$ Cepheids, they compiled all known massive companions with $M_2 \gtrsim 2\,{\rm M}_\odot$ and $T_2 \gtrsim 10{,}000$ K that exhibit a UV excess. Remage Evans et al. (2013) measured the masses M_1 of the primaries according to a mass-luminosity relation for Cepheids, and the masses M_2 of the hot MS companions from their UV spectral features. This technique is sensitive to all companions with $q \gtrsim 0.35$ that are hot enough to produce a UV excess, regardless of the orbital separation. Remage Evans et al. (2013) also utilized spectroscopic and photometric follow-up observations to estimate the orbital periods of the binaries in their sample. They found 16 companions with $2.7 < \log P\,({\rm days}) < 6.5$ and $q \geq 0.35$, which is relatively complete in this parameter space (green region in our Fig. 5.1).

Table 5.5: Companion statistics based on observations of Cepheid variables that evolved from mid-B MS primaries ($\langle M_1 \rangle = 6 \pm 2\,\mathrm{M}_\odot$).

Reference and Period Interval	Statistic
Remage Evans et al. (2013); $\log P\,(\mathrm{days}) = 5.3 \pm 1.2$	$\gamma_{\mathrm{largeq}} = -2.1 \pm 0.5$
	$\mathcal{F}_{\mathrm{twin}} < 0.04$
	$f_{\mathrm{logP}} = 0.08 \pm 0.03$
Remage Evans et al. (2015); $\log P\,(\mathrm{days}) = 3.1 \pm 0.5$	$\gamma_{\mathrm{largeq}} = -2.3 \pm 0.5$
	$\gamma_{\mathrm{smallq}} \approx 0.4$
	$\mathcal{F}_{\mathrm{twin}} < 0.04$
	$f_{\mathrm{logP}} = 0.18 \pm 0.06$

5.6.1 Wide Companions

We initially examine the $\mathcal{N}_{\mathrm{longP}} = 8$ long-period companions with $4.1 < \log P < 6.5$ and $q > 0.3$ in the Remage Evans et al. (2013) sample. We display in Fig. 5.13 the cumulative distribution of mass ratios q for these 8 wide binaries. This subsample is relatively complete across the specificed mass-ratio interval. We measure $\gamma_{\mathrm{largeq}} = -2.1 \pm 0.5$ and $\mathcal{F}_{\mathrm{twin}} < 0.04$ (Table 5.5). We find that wide companions to intermediate-mass stars have mass ratios $q \gtrsim 0.3$ consistent with random pairings drawn from a Salpeter IMF ($\gamma = -2.35$).

For $q = 0.1$ - 0.3, we adopt a power-law slope of $\gamma_{\mathrm{smallq}} = (0.2 \pm 0.4)\gamma_{\mathrm{largeq}} = -0.4 \pm 0.8$, and so the correction factor for incompleteness toward small mass ratios is $\mathcal{C}_{\mathrm{smallq}} = 2.3 \pm 0.5$. We also account for the fact that many mid-B MS primaries with close companions $\log P\,(\mathrm{days}) < 2.6$ are unlikely to evolve into Cepheids. In the previous sections, we measured $f_{\mathrm{logP}} \approx 0.10$ - 0.15 companions with $q > 0.1$ per decade of orbital period for mid B-type MS primaries and $0.3 < \log P \lesssim 2.6$. We estimate that $\Delta \log P \times f_{\mathrm{logP}} = (2.6 - 0.3) \times (0.12 \pm 0.04) = (30 \pm 10)\%$ of mid B-type

MS stars will interact with a binary companion at log $P < 2.6$. A small fraction of these systems, i.e., those with $q \approx 0.1$ - 0.3 and $P \lesssim 10$ days, are likely to merge while the primary is still on the MS (Hurley et al. 2002; Belczynski et al. 2008), thereby allowing the rejuvenated primary to continue its evolution toward the Cepheid giant phase. The majority of the close binaries, however, will undergo stable mass transfer or common envelope evolution, thereby preventing the primary from evolving into a Cepheid. We estimate that $(25 \pm 15)\%$ of mid-B primaries will interact with a close stellar companion in such a manner that it does not evolve into a Cepheid. The remaining $\mathcal{F}_{\rm Cepheid} = 0.75 \pm 0.15$ of mid-B MS stars are capable of evolving into Cepheid variables. Because only a subset of mid-B MS stars evolve into Cepheids, the frequency of *wide* companions to B-type MS stars is *smaller* than the frequency of wide companions to Cepheids. We calculate $f_{\rm logP} = \mathcal{N}_{\rm longP}\,\mathcal{C}_{\rm smallq}\,\mathcal{F}_{\rm Cepheid}/\mathcal{N}_{\rm Cepheid}/\Delta{\rm log}P$ $= (8 \pm \sqrt{8})(2.3 \pm 0.5)(0.75 \pm 0.15)/76/(6.5 - 4.1) = 0.08 \pm 0.03$ for mid-B MS stars and long orbital periods (Table 5.5).

5.6.2 Companions at Intermediate Orbital Periods

We next examine the companions to Cepheids at intermediate orbital periods. In a recent follow-up paper, Remage Evans et al. (2015) identified all spectroscopic binary companions to Cepheids, including those that did not necessarily exhibit a UV excess. Given $\langle M_1 \rangle \approx 6{\rm M}_\odot$ and the sensitivity $K_1 \approx 2$ km s^{-1} of their radial velocity measurements, the Remage Evans et al. (2015) sample is relatively complete for $q \gtrsim 0.08$ and for $P \approx 1$ - 10 yrs, i.e. $2.6 <$ log P (days)< 3.6 (see their Figs. 4 & 5). At slightly longer orbital periods $P > 10$ yr, the Remage Evans et al. (2015) survey most

likley misses low-mass companions due to the limited sensitivity and cadence of the spectroscopic observations. We analyze the $\mathcal{N}_{\rm comp} = 17$ companions reported in Table 8 of Remage Evans et al. (2015) that have $P = 1\text{-}10$ yr and measured or upper limits on the mass ratios.

Of the 17 intermediate-period companions to Cepheids, 9 have measured mass ratios $q > 0.35$ based on the observed UV excess from the hot MS companions. We plot the

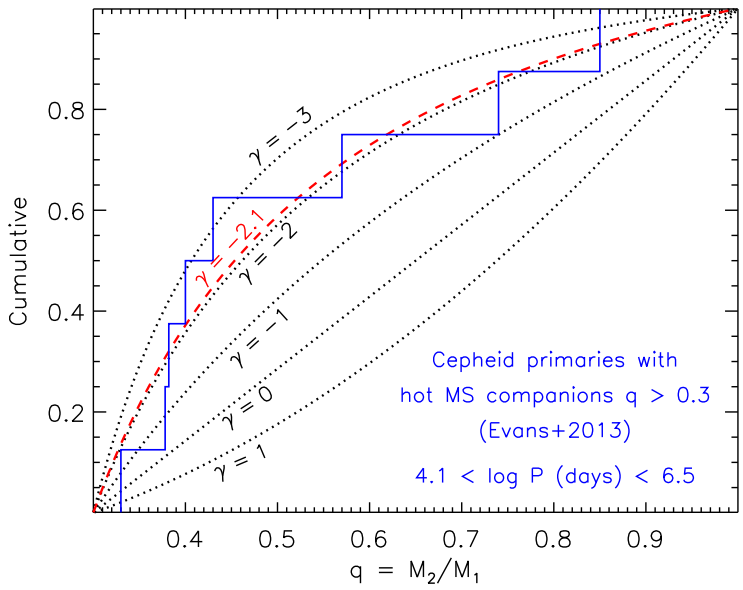

Figure 5.13: Cumulative distribution of mass ratios q for the 8 wide companions (blue) to 76 Cepheid primaries ($\langle M_1 \rangle = 6 \pm 2\,{\rm M}_\odot$) with $\log P\,({\rm days}) = 4.1\text{-}6.5$ and $q > 0.3$ as listed in Remage Evans et al. (2013). Hot MS companions to cool Cepheid primaries produce a detectable UV excess if $q \gtrsim 0.3$. This subsample is therefore relatively complete, where we measure the power-law component of the mass-ratio probability distribution $p_q \propto q^\gamma$ to be $\gamma = -2.1 \pm 0.5$ (dashed red). Cepheids, which evolved from mid-B MS primaries, have wide companions with mass ratios $q > 0.3$ that are consistent with random pairings drawn from a Salpeter IMF ($\gamma = -2.35$).

cumulative distribution of mass ratios for these 9 systems in Fig. 5.14, and measure $\gamma_{\rm largeq} = -2.3 \pm 0.5$ and $\mathcal{F}_{\rm twin} < 0.04$ (Table 5.5). Like the wide companions, companions to Cepheids at intermediate orbital periods have mass ratios $q \gtrsim 0.35$ consistent with random pairings drawn from the IMF.

Of the 8 remaining companions to Cepheids at intermediate orbital periods, two have measured mass ratios $q = 0.27$ - 0.31 near the detection limit. The other six do not have detectable UV excesses, and therefore have upper limits $q < 0.30$ - 0.38 assuming they are MS companions (see Table 8 in Remage Evans et al. 2015). These six companions are observed as SB1s, and so must have $q \gtrsim 0.08$ given the sensitivity $K_1 = 2$ km s^{-1} of

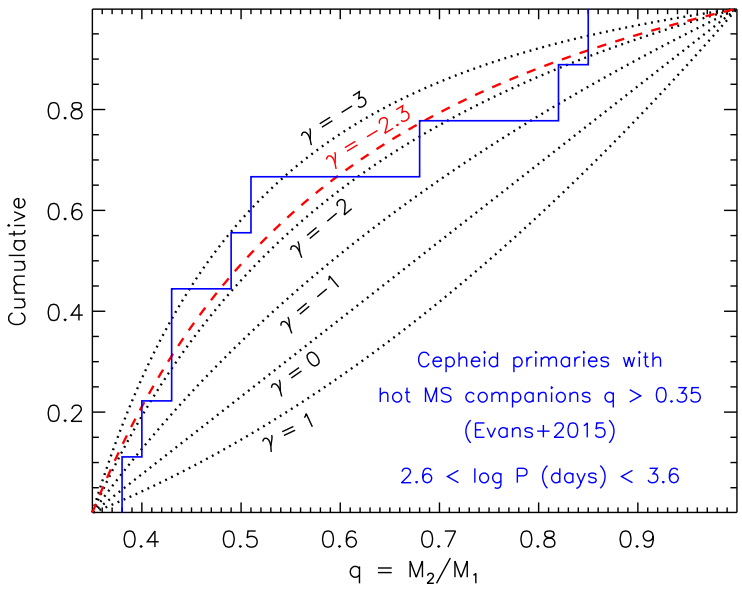

Figure 5.14: Similar to Fig. 5.13, but for the 9 companions (blue) to Cepheids with $q > 0.35$ and intermediate orbital periods $2.6 < \log P\,(\text{days}) < 3.6$ (Remage Evans et al. 2015). We measure $\gamma = -2.3 \pm 0.5$ (dashed red) for $q > 0.35$, which is consistent with our measurement at long orbital periods ($\gamma = -2.1$) as well as random pairings drawn from a Salpeter IMF ($\gamma = -2.35$).

the spectroscopic radial velocity observations. Unfortunately, we do not reliably know the nature of the six SB1s, i.e., whether they are F-K type MS companions or compact remnants.

Nonetheless, we can utilize the six SB1s to place a lower limit on $\gamma_{\rm smallq}$ (see §5.2 and §5.3). If $\gamma_{\rm largeq} = -2.3$ across $0.35 < q < 1.0$, and if there are $\mathcal{N}_{\rm largeq} = 9$ companions with $0.35 < q < 1.0$, and if there are $\mathcal{N}_{\rm smallq} = 8$ stellar companions (including the six SB1s) with $0.10 < q < 0.35$, then the slope of the mass-ratio distribution must turn over to $\gamma_{\rm smallq} = 0.4$ across $0.10 < q < 0.35$. The slope $\gamma_{\rm smallq}$ will be even larger if any of the SB1s contain compact remnants. Without the additional SB1 information, we would normally adopt $\gamma_{\rm smallq} = (0.2 \pm 0.4)\gamma_{\rm largeq} = -0.4 \pm 0.9$ to describe the mass-ratio distribution across $q = 0.10$ - 0.35 (see §5.2). Although this assumption encompasses the inferred lower limit, the observed population of SB1s clearly dictate that the power-law slope $\gamma_{\rm smallq}$ must turn over below $q = 0.35$. The statistics of spectroscopic binaries (§5.3) and eclipsing binaries (§5.4) suggest the majority of short-period SB1s contain stellar companions. Similarly, the Cepheid binary population indicates the majority of low-mass companions to intermediate-mass stars at moderate orbital periods are also stellar in nature.

Considering the above, we assume all spectroscopic binaries with Cepheid primaries and orbital periods $P = 1$ - 10 yrs contain stellar MS companions with $q > 0.1$. In a magnitude-limited sample of $\mathcal{N}_{\rm Cepheid} = 49$ Cepheids that were inspected for spectroscopic variability, Remage Evans et al. (2015) identified $\mathcal{N}_{\rm comp} = 12$ companions with $P = 1$ - 10 yrs, i.e. $2.6 < \log P\,({\rm days}) < 3.6$. After accounting for the B-type MS stars that do not evolve into Cepheids (see above), then the frequency of companions with $q > 0.1$ per decade of orbital period is $f_{\rm logP} = \mathcal{N}_{\rm comp}\,\mathcal{F}_{\rm Cepheid}/\mathcal{N}_{\rm Cepheid}/\Delta{\rm log}P =$

$(12 \pm \sqrt{12})(0.75 \pm 0.15)/49/(3.6 - 2.6) = 0.18 \pm 0.06$ for mid-B MS stars and intermediate orbital periods (Table 5.5). This is consistent with the frequencies $f_{\rm logP} \approx 0.1$ - 0.2 we measured for mid-B MS stars at short orbital periods based on observations of SB2s (§5.3) and EBs (§5.4).

5.7 Visual Binaries

Because O- and B-type MS stars have low space densities, we must study these primaries over large distances $d \gtrsim 100$ pc to achieve an adequate sample size. Companions to early-type stars can therefore be visually resolved only at larger orbital separations $a \gtrsim 20\,{\rm AU}$, i.e. $P \gtrsim 10^4$ days, even with speckle interferometry (Mason et al. 1998; Preibisch et al. 1999; Mason et al. 2009), adaptive optics (Duchêne et al. 2001; Shatsky & Tokovinin 2002; Sana et al. 2014), and lucky imaging (Peter et al. 2012). MS binaries with large brightness contrasts $\Delta{\rm m} > 4$ mag, and therefore small mass ratios $q = M_2/M_1 \lesssim 0.3$, can only be detected at even longer orbital periods $P \gtrsim 10^5$ days (see purple region in our Fig. 5.1). At wide separations $a >$ 1,000 AU, i.e. angular separations $\gtrsim 5''$, confusion with background and foreground stars becomes non-negligible. Continuous astrometric observations can help confirm that wide visual binaries are gravitationally bound according to their common proper motion (Abt et al. 1990, orange region in our Fig. 5.1). However, it is also possible that two young individual stars are only loosely associated because they recently formed in the same cluster (Abt & Corbally 2000). It is therefore difficult to select a window of angular separations that is complete toward low-mass companions while simultaneously not significantly biased toward optical doubles.

In addition to common proper motion, the spectral energy distributions of visual binaries can help confirm their physical association. For example, Shatsky & Tokovinin (2002) utilized theoretical stellar isochrones and the observed near-infrared colors to differentiate optical doubles from physical pairs that share the same age, distance, and dust reddening. As another example, late-B MS stars are typically X-ray quiet, while young and magnetically active G-M MS and pre-MS stars can emit X-rays (Evans et al. 2011). Late-B MS stars that appear to be X-ray bright probably have young low-mass companions with $q \approx 0.05$ - 0.40 (Hubrig et al. 2001; Stelzer et al. 2003; Evans et al. 2011). Indeed, $(43 \pm 6)\%$ of X-ray bright late-B and early-A MS stars were resolved with adaptive optics to have low-mass companions at angular separations $0.3''$ - $26''$ (De Rosa et al. 2011), i.e. $4.7 \lesssim \log P\,(\mathrm{days}) \lesssim 7.4$ (aqua region in our Fig. 5.1). The remaining $\approx$57% of the X-ray bright late-B/early-A stars most likely contain low-mass companions with $\log P < 4.7$ that cannot be spatially resolved. Unfortunately, the precise orbital periods of these putative extreme mass-ratio binaries have not yet been measured. We therefore do not know the intrinsic frequency of low-mass, X-ray emitting companions to late-B stars as a function of orbital period.

In the following, we examine the statistics of visual binary companions to B-type and O-type stars. We avoid the separation-contrast bias by analyzing only the systems with separations $\gtrsim 0.5''$ where the observations are complete to $q = 0.1$ companions. In this manner, we can directly measure f_{logP}, γ, and $\mathcal{F}_{\mathrm{twin}}$ across the entire interval $0.1 < q < 1.0$ without having to correct for incompleteness.

5.7.1 Late-B Primaries

For a sample of $\mathcal{N}_{\rm prim} = 115$ B-type stars in the Sco OB2 association ($d \approx 145$ pc), Shatsky & Tokovinin (2002) utilized near-infrared adaptive optics to search for visual companions across 0.3″ - 6.4″, i.e. $a = 45$ - 900 AU. Their sample of B0-B9 stars is dominated by the IMF so that the average primary mass is $\langle M_1 \rangle = 5 \pm 2\,{\rm M}_\odot$. Shatsky & Tokovinin (2002) measured the mass ratios q from the infrared colors and brightness contrasts according to stellar isochrones. Adaptive optics are sensitive to $q = 0.1$ companions for angular separations >0.5″, while incompleteness due to the limited field of view becomes important beyond >4″ (Shatsky & Tokovinin 2002, see their Fig. 5.8). We therefore select the $\mathcal{N}_{\rm comp} = 17$ companions with angular separations 0.5″ - 4.0″ and measured mass ratios $q > 0.1$, which represent a relatively complete subsample. The 17 companions have projected separations $\rho = 70$ - 600 AU, i.e. $4.9 < \log P\,({\rm day}) < 6.3$. The frequency of companions with $q > 0.1$ per decade of orbital period is simply $f_{\rm logP} = \mathcal{N}_{\rm comp}/\mathcal{N}_{\rm prim}/\Delta{\rm log}P = (17 \pm \sqrt{17})/115/(6.3 - 4.9) = 0.11 \pm 0.03$ (Table 5.6).

We display in Fig. 5.15 the cumulative distribution of mass ratios for the 17 companions. We fit the parameters of the mass-ratio distribution to be $\gamma = -0.9 \pm 0.3$ and $\mathcal{F}_{\rm twin} < 0.03$ across the interval $0.1 < q < 1.0$ (Table 5.6). Our measurement is steeper than the slope $\gamma = -0.5$ reported by Shatsky & Tokovinin (2002), even though the measurements are based on the same observations. This is because we fit the power-law slope γ for only companions with $q > 0.1$, while Shatsky & Tokovinin (2002) fit the entire range $0 < q < 1$. Like the IMF, the mass-ratio probability distribution p_q cannot be described by a single power-law across all mass ratios $0 < q < 1$. As we have parameterized in the present study (see §5.2), the mass-ratio distribution is more

accurately described by a power-law down to some minimum mass ratio, i.e. $q = 0.1$ in our case, and/or as a broken power-law that flattens and possibly turns over below some threshold, i.e. $q_{\rm thresh} \approx 0.3$.

5.7.2 Mid-B Primaries

For a sample of $\mathcal{N}_{\rm prim} = 109$ B2-B5 primaries ($\langle M_1 \rangle = 8 \pm 2\,{\rm M}_\odot$), Abt et al. (1990) provide the secondary masses M_2 and projected separations / orbital periods for 49 visual companions (see their Table 5.5). The 49 visual binaries exhibit common proper motion,

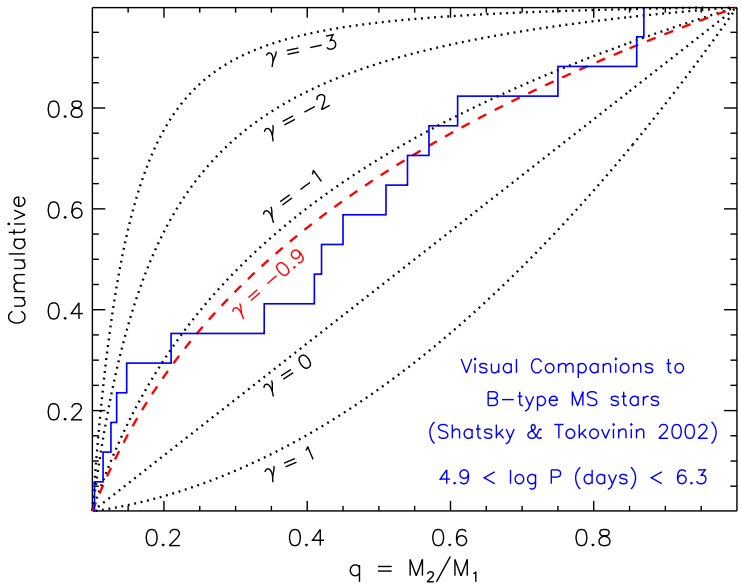

Figure 5.15: Cumulative distribution of mass ratios $q > 0.1$ for the 17 visual companions (blue) to 115 B-type MS primaries ($\langle M_1 \rangle = 5 \pm 2\,{\rm M}_\odot$) resolved at angular separations $0.5''$ - $4.0''$ with adaptive optics (Shatsky & Tokovinin 2002). For this relatively complete subsample, we measure the power-law component of the mass-ratio probability distribution $p_q \propto q^\gamma$ to be $\gamma = -0.9 \pm 0.3$ for $0.1 < q < 1.0$ (dashed red).

Table 5.6: Companion statistics based on visually resolved companions to early-type MS stars.

Reference and Primary Mass / Period Interval	Statistic
Shatsky & Tokovinin (2002);	$\gamma = -0.9 \pm 0.3$
$\langle M_1 \rangle = 5 \pm 2\,\mathrm{M}_\odot$;	$\mathcal{F}_{\rm twin} < 0.03$
$\log P\,(\mathrm{days}) = 5.6 \pm 0.7$	$f_{\rm logP} = 0.11 \pm 0.03$
Abt et al. (1990);	$\gamma = -2.1 \pm 0.5$
$\langle M_1 \rangle = 8 \pm 2\,\mathrm{M}_\odot$;	$\mathcal{F}_{\rm twin} < 0.04$
$\log P\,(\mathrm{days}) = 6.0 \pm 0.8$	$f_{\rm logP} = 0.06 \pm 0.02$
Sana et al. (2012);	$\gamma = -2.0 \pm 0.5$
$\langle M_1 \rangle = 28 \pm 8\,\mathrm{M}_\odot$;	$\mathcal{F}_{\rm twin} < 0.04$
$\log P\,(\mathrm{days}) = 6.8 \pm 0.5$	$f_{\rm logP} = 0.13 \pm 0.05$

have orbital solutions, and/or are have sufficiently small angular separations $<5''$ to ensure the systems are physically associated. Their sample is relatively complete down to $M_2 \approx 1.0\,\mathrm{M}_\odot$ secondaries ($q \gtrsim 0.13$) for angular separations $>0.65''$ ($P \gtrsim 400$ yrs). We therefore select the $\mathcal{N}_{\rm comp} = 9$ companions from Abt et al. (1990) with listed secondary masses $M_2 > 0.9\,\mathrm{M}_\odot$ and angular separations $0.65''$ - $8''$, i.e. $5.2 \lesssim \log P\,(\mathrm{days}) \lesssim 6.8$. Beyond $8''$, the binaries may be spurious associations or dynamically unstable, even if they exhibit common proper motion (Abt & Corbally 2000; Shatsky & Tokovinin 2002).

In Fig. 5.16, we display the cumulative distribution of mass ratios for these $\mathcal{N}_{\rm comp} = 9$ visual companions. We measure $\gamma = -2.1 \pm 0.5$ and $\mathcal{F}_{\rm twin} < 0.04$ across $q = 0.13$ - 1.0, which nearly encompasses our entire mass-ratio interval of interest (Table 5.6). For $q \gtrsim 0.1$, this mass-ratio distribution is consistent with random pairings drawn from a Salpeter IMF ($\gamma = -2.35$). Abt et al. (1990) examined all visual and common proper motion binaries across $5 \lesssim \log P\,(\mathrm{days}) \lesssim 9$ in their sample, and also concluded that the mass ratios are consistent with random pairings from the IMF. The widest systems, however, may be contaminated by faint spurious companions. Nevertheless, we have shown that $\gamma \approx -2.1$ applies for relatively close visual companions $5.2 < \log P < 6.8$

that are most probably gravitationally bound and dynamically stable.

To measure $f_{\rm logP}$, we assume a small correction factor $\mathcal{C}_{\rm smallq} = 1.2 \pm 0.1$ for incompleteness toward small mass ratios $q = 0.10$ - 0.13. For mid-B primaries, the frequency of companions with $q > 0.1$ per decade of orbital period is $f_{\rm logP} = \mathcal{N}_{\rm comp}\,\mathcal{C}_{\rm smallq}/\mathcal{N}_{\rm prim}/\Delta{\rm log}P = (9 \pm \sqrt{9})(1.2 \pm 0.1)/109/(6.8 - 5.2) = 0.06 \pm 0.02$ at $\log P \approx 6.0$ (Table 5.6). As expected, the frequency of companions diminishes toward the longest orbital periods.

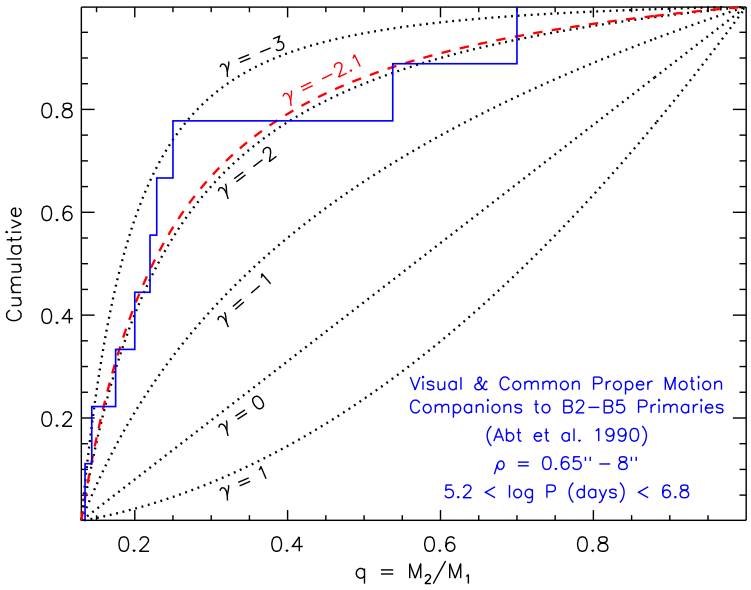

Figure 5.16: Cumulative distribution of mass ratios q for the 9 visual companions (blue) to 109 B2 - B5 MS primaries ($\langle M_1 \rangle = 8 \pm 2\,{\rm M}_\odot$) with angular separations 0.65″-8.0″ and $q > 0.13$ (Abt et al. 1990). We measure the power-law component of the mass-ratio probability distribution $p_q \propto q^\gamma$ to be $\gamma = -2.1 \pm 0.5$ (dashed red). For a broad range of mass ratios $0.1 \lesssim q < 1.0$, companions to mid-B MS stars at long orbital periods have a mass-ratio distribution consistent with random pairings drawn from the IMF.

5.7.3 O-type Primaries

In addition to long-baseline interferometry and sparse aperture masking, Sana et al. (2014) utilized near-infrared adaptive optics to search for visual companions to the O-type stars in their sample. We follow the same procedure from §5.5.2 to select O-type MS binaries and measure their mass ratios from the observed brightness contrasts ΔH. According to our adopted stellar isochrones, companions to O-type MS stars with $q > 0.1$ have brightness contrasts $\Delta\mathrm{H} \gtrsim 5.2$ mag (see Fig. 5.11). The adaptive optics survey of Sana et al. (2014) is sensitive to $\Delta\mathrm{H} = 5.2$ mag binaries for angular separations $>0.7''$ (see their Fig. 7), while confusion with background and foreground stars becomes non-negligible beyond $>3''$. From the same sample of $\mathcal{N}_{\rm prim} = 54$ O-type stars with luminosity classes II.5 - V we investigated in §5.5.2, 10 have companions with separations $0.7'' - 3.0''$ and brightness contrasts $\Delta\mathrm{H} < 5.2$ mag (Sana et al. 2012). Given the average distance $\langle d \rangle = 1.5$ kpc to these O-type binaries, the angular separations correspond to $\rho =$ 1,000-5,000 AU, i.e., $6.3 < \log P\,(\mathrm{days}) < 7.3$ days.

By incorporating our stellar models from §5.5.2, we measure the mass ratios of our 10 selected visual binaries according to the observed brightness contrasts ΔH and the spectral types and luminosity classes of the primaries. Of the 10 companions, three have mass ratios $q < 0.1$. These three systems have $\Delta\mathrm{H} \approx 5$ mag and O-type primaries with luminosity classes of V, dictating they have quite extreme mass ratios. The remaining $\mathcal{N}_{\rm comp} = 7$ visual companions have $q > 0.1$, providing $f_{\rm logP} = \mathcal{N}_{\rm comp}/\mathcal{N}_{\rm prim}/\Delta\log P$ $= (7 \pm \sqrt{7}/54/(7.3-6.3) = 0.13 \pm 0.05$ for O-type primaries at long orbital periods (Table 5.6).

We plot the cumulative distribution of mass ratios for the seven visual binaries

with $q > 0.1$ in Fig. 5.17. We measure $\gamma = -2.0 \pm 0.5$ and $\mathcal{F}_{\rm twin} < 0.04$. Again, the mass-ratio distribution of wide companions to O-types primaries are consistent with random pairings drawn from a Salpeter IMF ($\gamma = -2.35$).

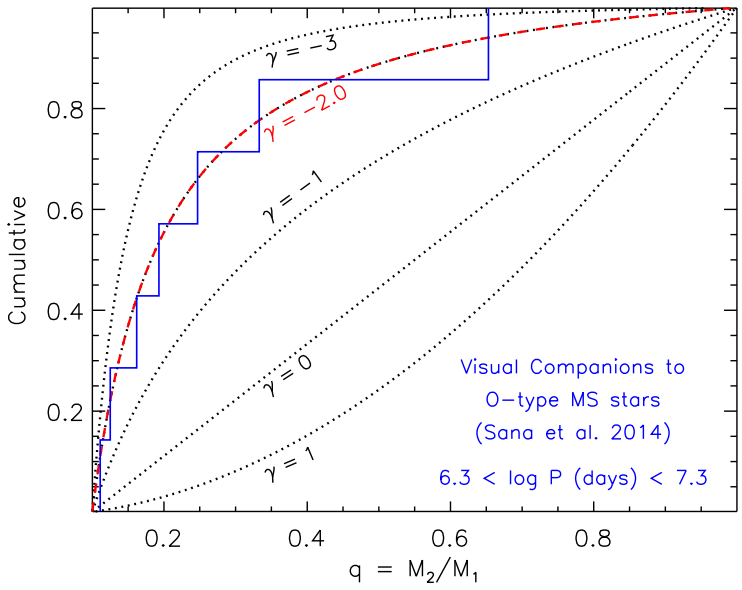

Figure 5.17: Cumulative distribution of mass ratios q for the 7 visual companions (blue) to 54 O-type MS primaries ($\langle M_1 \rangle = 28 \pm 8\,{\rm M}_\odot$) with angular separations 0.7″-3.0″ (Sana et al. 2014) and mass ratios $q > 0.1$ we measured from the observed brightness contrasts ΔH. We measure the power-law component of the mass-ratio probability distribution $p_q \propto q^\gamma$ to be $\gamma = -2.0 \pm 0.5$ (dashed red). Like mid-B binaries, companions to O-type MS stars at long orbital periods have a mass-ratio distribution consistent with random pairings drawn from the IMF across a broad range of mass ratios $0.1 < q < 1.0$.

5.8 Solar-type Binaries

5.8.1 Sample Selection

To extend the baseline toward smaller primary masses, we now investigate the companion properties to solar-type primaries. The most complete solar-type binary sample derives from Raghavan et al. (2010), who updated and extended the sample of Duquennoy & Mayor (1991). Raghavan et al. (2010) combined various observational techniques to search for companions around $\mathcal{N}_{\rm prim} = 454$ F6 - K3 type primaries ($\langle M_1 \rangle = 1.0 \pm 0.2$) located within 25 pc. We note the companion properties to solar-type primaries may differ in young star-forming environments (Duchêne et al. 2007; Connelley et al. 2008; Kraus et al. 2011), dense open clusters (Patience et al. 2002; Köhler et al. 2006; Geller & Mathieu 2012; King et al. 2012), or at extremely low metallicities (Abt 2008; Gao et al. 2014; Hettinger et al. 2015). For the purposes of binary population synthesis, we are mostly interested in the overall companion statistics of typical primaries at typical ages. Most solar-type stars are near solar-metallicity, in the galactic field, and are several Gyr old. The volume-limited sample of solar-type primaries in Raghavan et al. (2010) is therefore most representative of the majority of solar-type stars in the Milky Way.

We display in Fig. 5.18 the 168 confirmed companions from Raghavan et al. (2010) with measured orbital periods $0.0 < \log P\,({\rm days}) < 8.0$ and mass ratios $0.1 < q < 1.0$. We utilize the same methods as in Raghavan et al. (2010) to estimate the orbital periods P from projected separations and the stellar masses from spectral types. Our Fig. 5.18 is therefore similar to Figs. 11 & 17 in Raghavan et al. (2010). However, in the case of triples and higher-order multiples, we always define the period and mass ratio

$q = M_{\rm comp}/M_1$ of the companion with respect to the solar-type primary (see §5.2), which is slightly different than the definitions adopted in Raghavan et al. (2010). For example, consider a triple in a (Aa, Ab) - B hierarchical configuration: a $M_{\rm Aa} = M_1 = 1.0\,{\rm M}_\odot$ primary and $M_{\rm Ab} = 0.3\,{\rm M}_\odot$ companion are in a short-period orbit of $P = 100$ days, and a longer-period tertiary component with $M_{\rm B} = 0.5\,{\rm M}_\odot$ orbits the inner binary with a period of $P = 10^5$ days. This system would contribute two data points in Fig. 5.18: one with $q = M_{\rm Ab}/M_{\rm Aa} = 0.3$ and $\log P = 2.0$, and one with $q = M_{\rm B}/M_{\rm Aa} = 0.5$ and $\log P = 5.0$. Next, consider a triple in a A - (Ba, Bb) hierarchical configuration where a solar-type $M_{\rm A} = M_1 = 1.0\,{\rm M}_\odot$ primary is in a long-period $P = 10^5$ day orbit around a close, low-mass binary with $M_{\rm Ba} = 0.5\,{\rm M}_\odot$, $M_{\rm Ba} = 0.3\,{\rm M}_\odot$, and $P = 100$ days. In this situation, only the wide system with $q = M_{\rm Ba}/M_{\rm A} = 0.5$ and $\log P = 5.0$ would contribute to our Fig. 5.18. We do *not* consider the low-mass inner binary with $\log\ P = 2.0$ and $M_{\rm Ba}/M_{\rm Bb} = 0.6$ because neither component Ba nor Bb is a solar-type star. Only if component Ba itself has a F6 - K3 spectral type do we include the close (Ba, Bb) pair in our sample. Nearly half of the twins with $q \approx 1.00$ in Figs. 11 & 17 of Raghavan et al. (2010) actually contain late-K or M-dwarf equal-mass binaries in a long-period orbit with a solar-type primary in a A - (Ba, Bb) hierarchical configuration. Our Fig. 5.18 therefore does not contain as many twin components as displayed in Figs. 11 & 17 of Raghavan et al. (2010).

5.8.2 Corrections for Incompleteness

Sensitivity of Observations

The Raghavan et al. (2010) sample is relatively complete except for two regions of the parameter space of P versus q. First, the survey is not sensitive to detecting companions with $\log P \approx 6.0$ - 6.6 and $q \approx 0.1$ - 0.2 (green region in our Fig. 5.18). As shown in Fig. 11 of Raghavan et al. (2010), companions that occupy this portion in the parameter space will be missed by both adaptive optic and common proper motion techniques. Considering the density of systems in the immediately surrounding regions where the observations are relatively complete, we estimate ≈4 additional systems occupy this gap in the parameter space (four green systems in Fig. 5.18).

The second region of incompleteness occurs at $q \lesssim 0.5$ and $\log P \lesssim 4.5$ (blue region in our Fig. 5.18). The optical brightness contrast between binary components is an even steeper function of mass ratio for F - M type stars. Solar-type SB2s with sufficiently luminous secondaries are observed only if $q \gtrsim 0.40$ - 0.55, depending on the orbital period. Spectroscopic binaries with lower-mass companions will generally appear as SB1s and therefore not have mass ratios that can be readily measured. Of the four spectroscopic binaries with $\log P < 3.0$ and $q < 0.4$ shown in Fig. 5.18, only one is an SB2 with $P \approx 4$ days and a mass ratio $q \approx 0.38$ close to the detection limit. The other three systems are SB1s in a hierarchical triple where the tertiary itself has an orbital solution. The total mass of the SB1 is measured dynamically, and so the mass of the companion in the SB1 can be estimated. The few observed systems with $3.0 < \log P < 4.5$ and $q < 0.4$ are sufficiently nearby and have favorable orientations for the companion to be resolved with adaptive optics. In general, companions below the blue line in our Fig. 5.18 are

unresolved.

We estimate the number of missing systems in the blue region of Fig. 5.18 as follows. Raghavan et al. (2010) identified 27 confirmed and candidate binaries that do not have

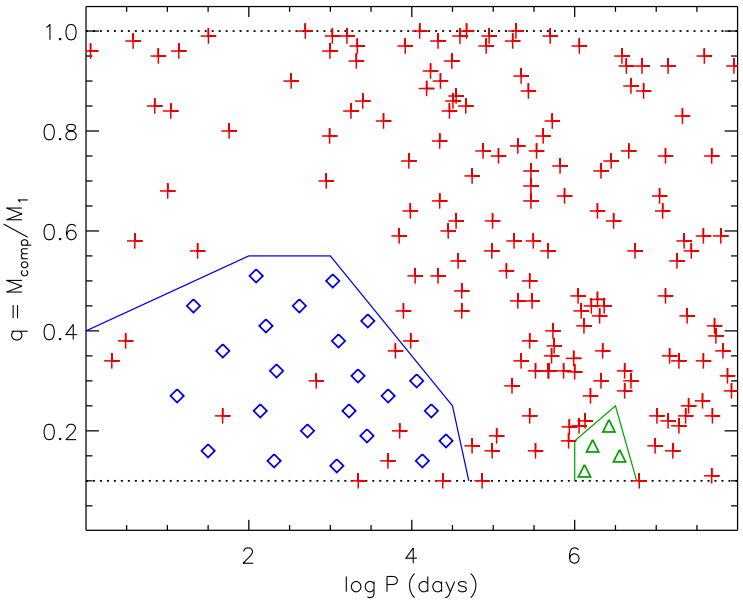

Figure 5.18: The companions to $\mathcal{N}_{\rm prim} = 454$ solar-type primaries ($\langle M_1 \rangle = 1.0 \pm 0.2\,{\rm M}_\odot$) from the Raghavan et al. (2010) survey as a function of P and $q = M_{\rm comp}/M_1$. We display the 168 confirmed systems (red pluses) with measured mass ratios $0.1 < q < 1.0$ and periods $0 < \log P\,({\rm days}) < 8$. Two regions (blue and green lines) of this parameter space are incomplete, either because the various observational techniques are insensitive to these systems and/or the systems in these regions are detectable but have periods and/or mass ratios that cannot be readily measured (e.g., SB1s, radial velocity variables, and companions implied through proper motion acceleration). We estimate 23 (blue diamonds) and 4 (green triangles) additional stellar companions located within these blue and green regions, respectively.

measurable mass ratios, e.g., SB1s, radial velocity variables, and companions implied through proper motion acceleration of the primary. A few of the seven radial velocity variables may contain substellar companions with $q < 0.1$, but the SB1s and companions identified through proper motion acceleration must have $q \gtrsim 0.1$ to produce the measured signal. There is also a small gap at $\log P = 3.5$ - 4.5 and $q = 0.10$ - 0.25 where neither spectroscopic radial velocity surveys nor adaptive optic surveys are complete (see Fig. 11 of Raghavan et al. 2010). Considering the density of low-mass companions at slightly longer orbital periods, we estimate ≈3 - 5 additional systems that escaped detection in this region. Finally, only spectroscopic radial velocity surveys are sensitive to closely orbiting low-mass companions, but only ≈80% of the sample of $\mathcal{N}_{\rm prim} = 454$ primaries were searched for such radial velocity variations. We estimate an additional ≈20%, or ≈4 - 6 SB1s, to be present around primaries that were not surveyed for spectroscopic variability. In total, we estimate ≈35 additional unresolved companions with $q > 0.1$ and $\log P \lesssim 4.5$.

Frequency of White Dwarf Companions

Like early-type binaries, we do not implicitly assume that unresolved SB1s contain stellar non-degenerate secondaries. For solar-type binaries, unresolved compact remnant companions are predominantly white dwarfs (WDs) instead of neutron stars or black holes (Hurley et al. 2002; Belczynski et al. 2008). Fortunately, we can estimate the frequency of such close Sirius-like systems observationally using three different independent methods.

Method 1. First, we rely on the catalog of Holberg et al. (2013), who compiled all known Sirius-like binaries with A - K type primaries and WD companions. Their sample contains $\mathcal{N}_{\rm hotWD} = 7$ systems with separations $a < 25$ AU ($\log P \lesssim 4.5$), distances $d < 50$ pc, and components that were originally identified due to the UV excess from the hot, closely orbiting WD companion. This subsample is relatively complete as long as the temperature $T_{\rm WD} > 15{,}000$ K of the WD is sufficiently hotter than the temperature $T_1 \approx 5{,}000$-$10{,}000$ K of the A - K type primary. According to evolutionary tracks, a WD cools to $T_{\rm WD} \approx 15{,}000$ K in $t_{\rm cool} \approx 0.15$ - 0.60 Gyr, depending on its mass and composition (Fontaine et al. 2001). There are $\mathcal{N}_{\rm prim} = 6{,}000$ A - K type stars in the Hipparcos catalog with parallactic distances $d < 50$ pc (Perryman et al. 1997). Assuming an average age of $\langle \tau \rangle = 5$ Gyr for the A - K type primaries in the galactic field, then the fraction of solar-type stars that have WD companions with $\log P < 4.5$ is $\mathcal{F}_{\rm solar+WD,logP<4.5} = \mathcal{N}_{\rm hotWD}\, \langle \tau \rangle / (\mathcal{N}_{\rm prim}\, t_{\rm cool}) = (2.5 \pm 1.5)\%$.

Method 2. Second, we use the observed MS companion statistics to estimate the fraction of systems that will evolve into closely orbiting solar-type + WD binaries. For a late-B MS primary with $M_1 \approx 5\,{\rm M}_\odot$, the companion must have $q \approx 0.15$ - 0.25 ($M_2 \approx 0.75$-$1.25\,{\rm M}_\odot$) to be capable of evolving into a solar-type + WD binary. However, not all late-B + solar-type binaries will evolve into Sirius-like systems. For example, a $M_1 = 5\,{\rm M}_\odot$ primary with a $M_2 \approx 1\,{\rm M}_\odot$ secondary in a short-period orbit of $\log P < 1.5$ will most likely merge (Hurley et al. 2002; Belczynski et al. 2008). The $M_1 = 5\,{\rm M}_\odot$ primary must first evolve into a large giant with a compact core before filling its Roche lobe in order for the $M_2 = 1{\rm M}_\odot$ companion to survive common envelope (CE) evolution. This requires the initial orbital period to be $\log P > 1.5$. Based on the early-type MS binary statistics measured in the previous sections, we estimate $\mathcal{F}_{\rm B+solar,logP>1.5} =$

Table 5.7: Companion statistics of solar-type primaries ($\langle M_1 \rangle = 1.0 \pm 0.2$) based on Raghavan et al. (2010) survey of $\mathcal{N}_{\rm prim} = 454$ F6 - K3 primaries and corrected sample of $\mathcal{N}_{\rm comp} = 195$ stellar companions with $q > 0.1$ and $0 < \log P\,({\rm days}) < 8$.

$\log P$ (days)	$\mathcal{N}_{\rm comp}$	$f_{\rm logP}$	γ	$\mathcal{F}_{\rm twin}$	η
0.5 ± 0.5	7	0.015 ± 0.006	0.4 ± 0.4	0.35 ± 0.08	-0.8 ± 0.2
1.5 ± 0.5	11	0.024 ± 0.007	0.0 ± 0.3	0.18 ± 0.06	-0.4 ± 0.3
2.5 ± 0.5	13	0.029 ± 0.008	-0.3 ± 0.3	0.15 ± 0.05	0.2 ± 0.3
3.5 ± 0.5	25	0.055 ± 0.011	-0.5 ± 0.3	0.13 ± 0.04	0.6 ± 0.4
4.5 ± 0.5	35	0.077 ± 0.013	-0.1 ± 0.3	0.10 ± 0.03	0.3 ± 0.3
5.5 ± 0.5	39	0.086 ± 0.014	-0.2 ± 0.3	0.05 ± 0.03	-
6.5 ± 0.5	33	0.073 ± 0.013	-0.7 ± 0.3	0.04 ± 0.03	-
7.5 ± 0.5	32	0.070 ± 0.012	-0.6 ± 0.3	< 0.04	-

$(13 \pm 3)\%$ of late-B primaries have solar-type companions with $\log P > 1.5$. Hence, $\approx$13% of systems with late-B primaries will eventually evolve into solar-type + WD binaries.

About half of these systems, i.e., $\mathcal{F}_{\rm B+solar,1.5<logP<4.5} = (6 \pm 2)\%$, have orbital periods $1.5 < \log P < 4.5$ and will therefore emerge as closely orbiting solar-type + WD binaries with $\log P \lesssim 4.5$. B-type + solar-type binaries in nearly circular orbits with $3.8 \lesssim \log P \lesssim 4.5$ will expand beyond $\log P > 4.5$ due to the substantial mass loss of the B-type MS primary as it evolves into a WD. If the orbits are highly eccentric, however, solar-type companions with $4.5 < \log P \lesssim 5.2$ may be tidally captured into a shorter orbit with $\log P < 4.5$ despite the mass loss. For simplicity, we assume these two effects cancel, especially considering the intrinsic eccentricity distribution of early-type binaries have not yet been reliably measured at $\log P \approx 4.5$.

Similarly, a $M_1 = 1.25$ mid-F primary with a $q = 0.6$ - 1.0 ($M_2 = 0.75$ - $1.25\,{\rm M}_\odot$) companion can evolve into a Sirius-like binary. Given our necessary level of precision, the Raghavan et al. (2010) sample of F6 - K3 primaries is sufficiently representative of

the binary statistics of $M_1 = 1.25$ primaries. We count 72 companions with $q > 0.6$ and $\log P > 1.5$, 27 of which have $1.5 < \log P < 4.5$. We therefore compute $\mathcal{F}_{\rm solar+solar,logP>1.5} = 72/454 = (16 \pm 2)\%$ and $\mathcal{F}_{\rm solar+solar,1.5<logP<4.5} = 27/454 = (6 \pm 1)\%$. Although the total frequency of companions increases with primary mass, the fraction of primaries that have solar-type companions with $M_2 = 0.75$ - $1.25\,{\rm M}_\odot$ remains relatively constant.

Using a Monte Carlo technique and the input MS binary statistics determined above, we calculate the fraction of solar-type primaries that currently have a closely orbiting WD companions. For the galactic field, we assume a constant star formation rate during the past 10 Gyr, i.e. each system has a random age in the interval 0 Gyr $< \tau <$ 10 Gyr. We select primary masses $0.75 < M_1 < 8{\rm M}_\odot$ across our interval of interest according to a Kroupa et al. (2013) IMF with slope $\alpha = -2.3 \pm 0.3$. The probabilities that $M_1 = 1.25\,{\rm M}_\odot$ and $M_1 = 5\,{\rm M}_\odot$ primaries have $M_2 = 0.75$ - $1.25\,{\rm M}_\odot$ companions with $\log P > 1.5$ is $\mathcal{F}_{\rm solar+solar,logP>1.5} = (16 \pm 2)\%$ and $\mathcal{F}_{\rm B+solar,logP>1.5} = (13 \pm 3)\%$, respectively. By definition, the probability that a $M_1 = 0.75\,{\rm M}_\odot$ primary has a $M_2 = 0.75$-$1.25\,{\rm M}_\odot$ companion is 0%. We interpolate these probabilities with respect to M_1. We calculate similar probabilities for binaries with solar-type companions and $1.5 < \log P < 4.5$ according to $\mathcal{F}_{\rm solar+solar,1.5<logP<4.5} = (6 \pm 1)\%$ and $\mathcal{F}_{\rm B+solar,1.5<logP<4.5} = (6 \pm 2)\%$. We select secondary masses uniformly across $0.75{\rm M}_\odot < M_2 < \min\{1.25{\rm M}_\odot, M_1\}$. The precise distribution of companions within this narrow range does not affect our results. If a simulated binary has an initial orbital period $1.5 < \log P < 4.5$, is old enough $\tau > \tau_{\rm MS}(M_1)$ for the original primary to evolve into a WD, and is young enough $\tau < \tau_{\rm MS}(M_2)$ for the original solar-type secondary (now primary) to still be on the MS, then we count its contribution toward the number $\mathcal{N}_{\rm solar+WD,logP<4.5}$ of short-period solar-type + WD binaries. We compare this value to

the total number $\mathcal{N}_{\rm solar}$ of solar-type MS stars, including those that are single stars, those in binaries with lower-mass MS companions, and those in binaries with WD companions across all orbital periods. We determine $\mathcal{F}_{\rm solar+WD,logP<4.5} = \mathcal{N}_{\rm solar+WD,logP<4.5}/\mathcal{N}_{\rm solar} = (3.8 \pm 1.6)\%$. The dominant source of uncertainty derives from the slope $\alpha = -2.3 \pm 0.3$ of the IMF. Larger values of α favor more B-type MS primaries, including those with solar-type companions, and therefore more systems that can evolve into solar-type + WD binaries.

The above calculation of $\mathcal{F}_{\rm solar+WD,logP<4.5} = (3.8 \pm 1.6)\%$ applies only for solar-type stars in the galactic field that have a broad distribution of ages $0 < \tau < 10$ Gyr centered on $\langle\tau\rangle = 5$ Gyr. For a coeval $\tau = 500$ Myr population, e.g., an intermediate-age open cluster, this fraction decreases to $\mathcal{F}_{\rm solar+WD,logP<4.5} \approx 1.3\%$. For a young coeval $\tau = 50$ Myr population, the fraction is $\mathcal{F}_{\rm solar+WD,logP<4.5} = 0\%$ because the most massive stars $M_1 \approx 8\,{\rm M}_\odot$ that produce WDs have not yet evolved off the MS.

Method 3. Finally, we estimate $\mathcal{F}_{\rm solar+WD,logP<4.5}$ based on the observed frequency of barium stars. Barium stars are G-K type giants with mild to strong Ba II absorption features (MacConnell et al. 1972). About 80% of barium stars are observed to be in SB1s with companions at intermediate orbital periods $P \approx 200$ - 6,000 days, i.e. $2.3 < \log P < 3.8$ (Boffin & Jorissen 1988; Jorissen et al. 1998). The remaining ≈20% are also expected to be in binaries, but with face-on orientations and/or orbital periods $P >$ 6,000 days too long to produce detectable radial velocity variations. The general consensus is that barium stars were originally solar-type MS stars that accreted s-process rich material from asymptotic giant branch (AGB) donors (Boffin & Jorissen 1988; Jorissen et al. 1998; Karakas et al. 2000). The companions to barium stars are therefore the carbon-oxygen white dwarf remnants of the AGB donors. Not only did the solar-type

MS stars accrete barium, but sufficient mass to become hotter and more massive A-F type MS stars. Because Ba II absorption features cannot readily be detected when $T_{\rm eff} \gtrsim 6{,}000$ K, the accretors must first evolve into cooler G-K type giants to be observed as barium stars.

About $\mathcal{F}_{\rm Ba} = (1.0 \pm 0.5)\%$ of G-K type giants are barium stars (MacConnell et al. 1972; Jorissen et al. 1998; Karakas et al. 2000). At a minimum, $\gtrsim$1% of solar-type MS stars must have WD companions with $\log P < 4.5$. Not all solar-type MS stars with WD companions accreted material from an AGB donor. Solar-type MS companions at initially shorter periods $1.5 < \log P < 2.3$ will undergo CE evolution when the primary is on the red giant branch (Hurley et al. 2002; Belczynski et al. 2008). These systems will leave behind helium WD remnants with solar-type MS companions that are not chemically enriched with barium. Similarly, companions at longer orbital periods $3.8 < \log P < 4.5$ are less likely to accrete enough material from the AGB donor to appear as barium stars. Assuming the period distribution of solar-type companions approximately follows Öpik's law in the interval $1.5 < \log P < 4.5$, then the ratio of all close WD companions with solar-type MS primaries to those that will become barium stars is $\mathcal{C}_{\rm Ba} \approx (4.5-1.5)/(3.8-2.3) \approx 2.0 \pm 0.5$. This correction factor is sufficiently accurate even if the period distribution substantially deviates from Öpik's law. Based on these estimates, we calculate that $\mathcal{F}_{\rm solar+WD,logP<4.5} = \mathcal{F}_{\rm Ba}\,\mathcal{C}_{\rm Ba} = (2.0 \pm 1.1)\%$ of solar-type MS stars have WD companions with $\log P < 4.5$.

The three methods described above result in values $\mathcal{F}_{\rm solar+WD,logP<4.5} = (2.5 \pm 1.5)\%$, $(3.8 \pm 1.6)\%$, and $(2.0 \pm 1.1)\%$ that are consistent with each other. We adopt an average value of $\mathcal{F}_{\rm solar+WD,logP<4.5} = (2.8 \pm 1.0)\%$. In the Raghavan et al. (2010) sample of $\mathcal{N}_{\rm prim} = 454$ solar-type MS stars, there should be $\mathcal{N}_{\rm WD,logP<4.5} = \mathcal{F}_{\rm solar+WD,logP<4.5}\,\mathcal{N}_{\rm prim}$

$= 13 \pm 4$ WD companions with $\log P < 4.5$. Only one of these suspected systems, HD 13445, was barely resolved to have a WD secondary with $\log P = 4.4$. The remaining 12 ± 4 solar-type MS + WD binaries with $\log P < 4.5$ remain unresolved, but most likely appear as SB1s and/or systems that exhibit proper motion acceleration. Of the ≈35 additional companions with $\log P < 4.5$ and $q > 0.1$ we estimated in §5.8.2, 12 ± 4 are most likely WDs. In other words, $(34 \pm 10)\%$ of solar-type primaries that are SB1s and/or exhibit proper motion acceleration actually contain WD companions. The remaining 23 binaries contain M-dwarf companions with $q \approx 0.1$ - 0.5 and $\log P \lesssim 4.5$.

Corrected Population

The blue region in Fig. 5.18 is quite large, and so we distribute the estimated 23 additional M-dwarf companions based on the nature of the systems. The SB1s have known orbital periods, generally $1.0 < \log P\,(\mathrm{days}) < 3.5$. There are only two additional SB1s with $0 < \log P < 1$, and these two systems most likely contain post-CE WD companions (see above). The radial velocity variables and companions implied through proper motion acceleration probably have $2.5 < \log P < 4.7$ (Raghavan et al. 2010). The ≈3 - 5 systems that escaped detection lie in the interval $3.5 < \log P < 4.7$. We therefore expect four, seven, eight, and four additional stellar companions in the logarithmic period intervals $\log P = 1$ - 2, 2 - 3, 3 - 4, and 4.0 - 4.7, respectively.

In terms of mass ratios q, we simply assume the 23 additional systems are evenly distributed between $q = 0.1$ and the detection limit at $q = 0.40$ - 0.55 as indicated by the blue line in Fig.5.18. Weighting the additional systems toward smaller or larger mass ratios in this interval does not affect our overall statistical measurements. We display

the 23 additional systems as the blue diamonds in Fig. 5.18.

5.8.3 Intrinsic Multiplicity Statistics

We measure the intrinsic binary statistics of solar-type primaries according to the corrected sample of $\mathcal{N}_{\rm comp} = 195$ companions in Fig. 5.18. The total multiplicity frequency per our definition (see §5.2) is simply $f_{\rm mult}(M_1 = 1\,{\rm M}_\odot) = \mathcal{N}_{\rm comp}/\mathcal{N}_{\rm prim}$ $= 195/454 = 0.43 \pm 0.03$, where the uncertainty derives from Poisson statistics. A solar-type MS primary has, on average, 0.43 stellar companions with $q > 0.1$ that directly orbit it with a period of $0 < \log P\,({\rm days}) < 8$. This statistic does not include substellar companions, WD companions, companions at shorter or longer periods, or tertiary companions that orbit late-K or M-dwarf secondaries.

The frequency $f_{\rm logP}$ of companions with $q > 0.1$ per decade of orbital period derives from dividing the number of companions in Fig. 5.18 in each of the eight bins of logarithmic period by $\mathcal{N}_{\rm prim} = 454$. We display $f_{\rm logP}$ in Table 5.7 and in the top panel of Fig. 5.19, where the uncertainties derive from Poisson statistics. As found in Duquennoy & Mayor (1991) and Raghavan et al. (2010), $f_{\rm logP}$ for solar-type primaries can be adequately described by a log-normal period distribution:

$$f_{\rm logP}(M_1 = 1{\rm M}_\odot,\, P) = f_{\rm peak} \exp\Big[- \frac{(\log P - \mu_{\rm logP})^2}{2\sigma^2_{\rm logP}}\Big] \qquad \text{for } 0 < \log P\,({\rm days}) < 8 \tag{5.8}$$

where $f_{\rm peak} = 0.084$, $\mu_{\rm logP} = 5.6$, and $\sigma_{\rm logP} = 2.6$ (red dashed line in top panel of Fig. 5.19). Our fitted parameters differ slightly from those reported in Raghavan et al.

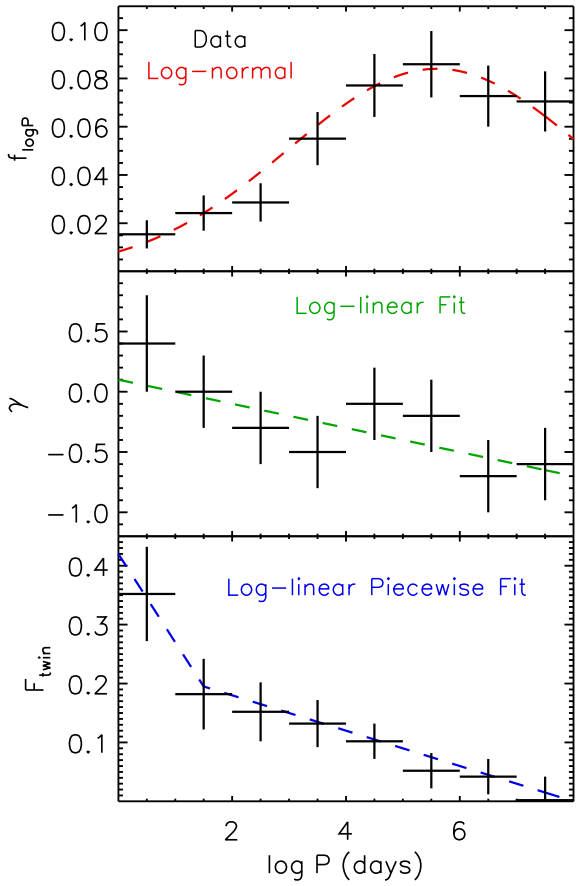

Figure 5.19: Measured companion statistics of corrected solar-type binary sample as a function of log P. Top panel: the frequency $f_{\rm logP}$ of companions with $q > 0.1$ per decade of orbital period. The data is adequately described by a log-normal period distribution with a peak of $f_{\rm peak} = 0.084$ at $\mu_{\rm logP} = 5.6$ and a standard deviation of $\sigma_{\rm logP} = 2.6$ (dashed red). Middle panel: the power-law component γ of the mass-ratio probability distribution $p_q \propto q^{\gamma}$ across the interval $0.1 < q < 1.0$. The overall mass-ratio distribution becomes weighted toward smaller values of q with increasing P. Specifically, the power-law component decreases from $\gamma = 0.1$ at log $P = 0$ to $\gamma = -0.7$ at log $P = 8$ (dashed green). Bottom panel: the excess fraction $\mathcal{F}_{\rm twin}$ of twins with $0.95 < q < 1.00$ relative to the underlying power-law component of the mass-ratio distribution. The excess twin fraction dramatically decreases from $\mathcal{F}_{\rm twin} \approx 0.35$ at $P = 3$ days to $\mathcal{F}_{\rm twin} \approx 0.19$ at $P = 30$ days. The excess twin fraction then continues to decrease linearly according to log P until it reaches $\mathcal{F}_{\rm twin} \approx 0$ at log $P \approx 8$ (dashed blue).

(2010) because we count companions differently (see above) and do not fit the tail of the Gaussian distribution at $\log P > 8$.

Using a maximum likelihood method, we measure the parameters γ and $\mathcal{F}_{\rm twin}$ that describe the mass-ratio probability distribution. We calculate these two parameters for each of the eight bins of decade of orbital period. We present the results in Table 5.7 and in the middle and bottom panels of Fig. 5.19. We also display in Fig. 5.20 the cumulative distributions of mass ratios for the intervals $\log P = 0$ - 2, 2 - 6, and 6 - 8.

The mass-ratio distribution p_q clearly becomes weighted toward smaller values of q with increasing orbital period P. We find the power-law component decreases from $\gamma \approx 0.1$ at $\log P = 0$ - 2, to $\gamma = -0.2$ at $\log P = 2$ - 6, and then down to $\gamma = -0.6$ at $\log P =$ 6-8 (Fig. 5.20). We fit a log-linear trend to the data (dashed green line in middle panel of Fig. 5.19):

$$\gamma(M_1 = 1{\rm M}_\odot,\, P) = 0.1 - 0.1 \log P \quad \text{for } 0 < \log P\,({\rm days}) < 8. \tag{5.9}$$

A simple power-law distribution does not adequately describe the mass ratios of solar-type binaries, especially those with short orbital periods. In the interval $0 < \log P < 1$, for example, there are three twin systems with $q = 0.95$ - 1.00 and only four other binaries with $q < 0.95$ (see Fig. 5.18). Raghavan et al. (2010) found two additional SB1s in this period interval, but we suspect that one or both have WD companions (§5.8.2). We measure an excess twin fraction $\mathcal{F}_{\rm twin} \approx 0.35 \pm 0.08$ at $0 < \log P < 1$ (Fig. 5.19). The excess fraction of twins dramatically decreases to

$\mathcal{F}_{\rm twin} \approx 0.18 \pm 0.06$ by $\log P \approx 1.5$, and then slowly declines to zero by $\log P \approx 8$. There are only two twin systems ($q \geq 0.95$) with $6 < \log P < 7$ and only one with $7 < \log P < 8$ (see Fig. 5.18). We find the excess fraction of twins to solar-type primaries is adequately described by a piecewise linear trend with respect to logarithmic orbital period (dashed blue line in bottom panel of Fig. 5.19):

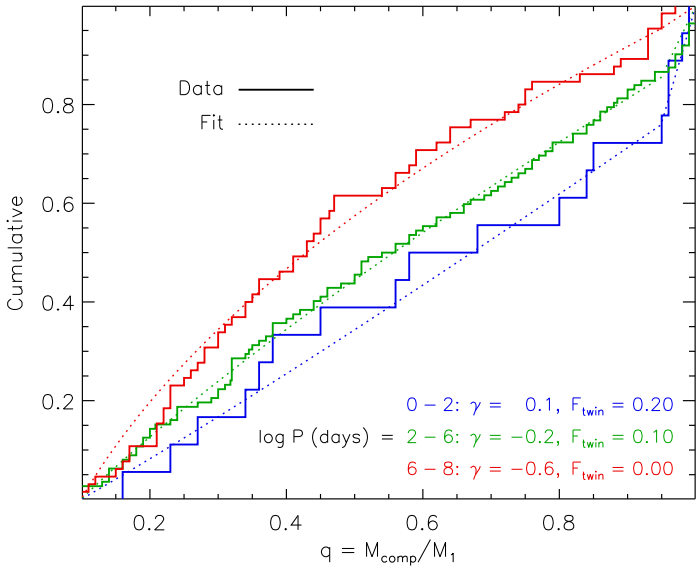

Figure 5.20: Cumulative distribution of mass ratios q of solar-type binaries divided into three logarithmic period intervals. We compare the data (solid lines) after correcting for incompleteness to the two-parameter fits (dotted). The short-period systems (blue) with $0 < \log P$ (days) < 2 are weighted toward large mass ratios with a positive power-law component $\gamma = 0.1$ and a large excess fraction $\mathcal{F}_{\rm twin} = 0.20$ of twins with $q = 0.95$ - 1.00. The intermediate-period systems (green) with $2 < \log P < 6$ have $\gamma = -0.2$ and a modest excess twin fraction $\mathcal{F}_{\rm twin} = 0.10$. The long-period systems (red) with $6 < \log P < 8$ are weighted toward smaller mass ratios with $\gamma = -0.6$ and no statistically significant excess twin fraction.

$$\mathcal{F}_{\rm twin}(M_1 = 1{\rm M}_\odot,\, P) =$$
$$0.42 - 0.15 \log P \;\; \text{for } 0.0 < \log P\,(\text{days}) < 1.5,$$
$$0.24 - 0.03 \log P \;\; \text{for } 1.5 < \log P\,(\text{days}) < 8.0. \qquad (5.10)$$

5.8.4 Eccentricity Distribution

We next measure the eccentricity probability distributions $p_e \propto e^\eta$ of solar-type binaries as a function of orbital period P. In Fig. 5.21, we plot e versus P for the 97 solar-type binaries in the Raghavan et al. (2010) sample with spectroscopic and/or visual orbit solutions and $0 < \log P\,(\text{days}) < 5$. Our Fig. 5.21 is therefore quite similar to Fig. 14 in Raghavan et al. (2010). However, we do not include the data points that actually represent the orbits of late-K and M-dwarf binaries. For example, the two systems near $e = 0.12$ and $\log P \approx 3.9$ in Fig. 14 of Raghavan et al. (2010) are the orbits of low-mass binaries with tertiary solar-type primaries in a A - (Ba, Bb) hierarchical configuration (see §5.8.1). We remove these two systems and four additional low-mass binaries with $4 < \log P\,(\text{days}) < 5$ in the Raghavan et al. (2010) survey from our sample.

In the previous subsections, we eliminated SB1s that most likely contained WD companions. The inclusion of these systems would bias our multiplicity measurements toward larger values of $f_{\rm logP}$ and smaller values of γ and $\mathcal{F}_{\rm twin}$. Considering the small sample of binaries per decade of orbital period, we find the inclusion of solar-type SB1s does not affect our measurements of η to a statistically significant level. We therefore include all spectroscopic binaries in our analysis of the eccentricity distributions, especially considering $\approx$2/3 of solar-type SB1s contain stellar M-dwarf companions (see

§5.8.2).

All 44 detected companions to solar-type primaries with $0 < \log P\,(\mathrm{days}) < 3$ have measured eccentricities according to spectroscopic and/or visual orbit solutions. At $3 < \log\ P < 4$ and $4 < \log\ P < 5$, however, three and two detected companions, respectively, do not have measured eccentricities. At even longer orbital periods $\log P\,(\mathrm{days}) > 5$, i.e. $P \gtrsim 300$ yrs, a significant fraction of solar-type binaries do not have visual orbits. The intrinsic eccentricity distributions can therefore not be readily measured at $\log P\,(\mathrm{days}) > 5$ for solar-type binaries, so we only consider systems with

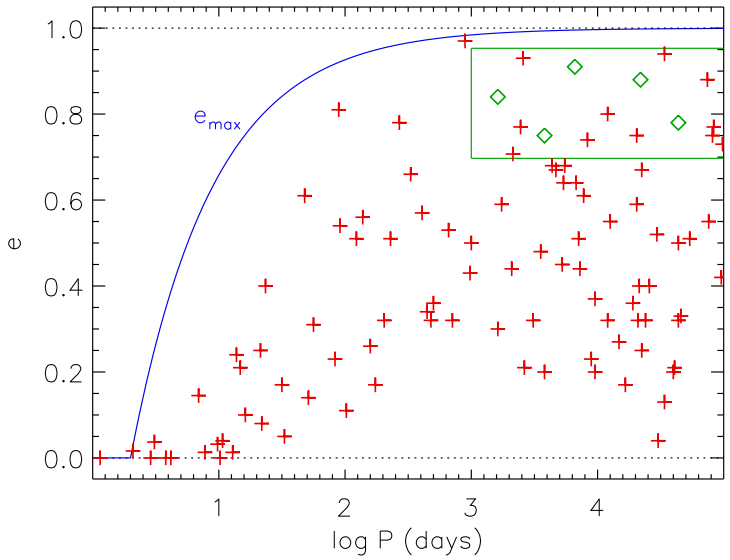

Figure 5.21: Eccentricities e versus orbital periods P for solar-type binaries from the (Raghavan et al. 2010) sample. We display the 97 binaries (red +'s) with spectroscopic and/or visual orbit solutions. Five additional detected systems with $3 < \log P\,(\mathrm{days}) < 5$ do not have visual orbits and most likely have $e \approx 0.70$ - 0.95 (five green systems within green region). Solar-type binaries with $\log\ P < 1$ have been tidally circularized, while longer period systems are weighted toward large eccentricities.

log $P < 5$. Harrington & Miranian (1977) demonstrated that visual binaries which do not have reliable orbital solutions generally have large eccentricities $e \gtrsim 0.7$. We assume

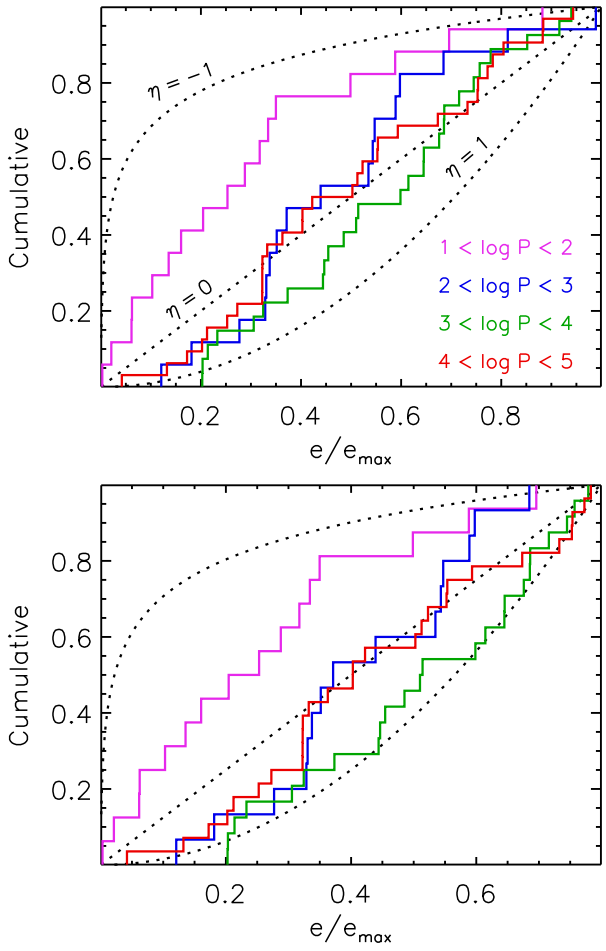

Figure 5.22: Cumulative distribution of eccentricities e for solar-type binaries with $\log P\,(\mathrm{days}) = 1\text{-}2$ (magenta), 2-3 (blue), 3-4 (green), and 4-5 (red). We compare the data to power-law probability distributions $p \propto (e/e_{\max})^{\eta}$ (dotted). Top panel: by fitting all solar-type binaries, we measure $\eta = -0.4$, 0.1, 0.4, and 0.2 for $\log P = 1\text{-}2$, 2-3, 3-4, and 4-5, respectively. Bottom panel: by fitting only those systems with $e < 0.8e_{\max}$ that have not been as severely affected by tidal evolution, we measure $\eta = -0.4$, 0.3, 0.8, and 0.4 for $\log P = 1\text{-}2$, 2-3, 3-4, and 4-5, respectively.

the five visual binaries with intermediate periods $3 < \log P < 5$ but without orbital solutions are evenly distributed across $e \approx 0.70$ - 0.95 (green systems in Fig. 5.21).

In Fig. 5.21, we display the maximum eccentricity $e_{\rm max}$ as a function of P according to Eqn. 5.7. As expected, all detected systems have $e < e_{\rm max}$. In fact, the majority of systems with $\log P < 1$ have been tidally circularized. In this interval, we measure the power-law component $\eta = -0.8 \pm 0.2$ of the eccentricity distribution to be weighted toward small values (Table 5.7). Solar-type binaries at longer orbital periods $\log P > 1$ not only contain systems with large eccentricities, but exhibit a deficit of binaries with small eccentricities $e \lesssim 0.15$. In the top panel of Fig. 5.22, we display the cumulative distributions of $e/e_{\rm max}$ for four different logarithmic period intervals. We measure $\eta = -0.4$, 0.1, 0.4, and 0.2 for $\log P = 1$ - 2, 2 - 3, 3 - 4, and 4 - 5, respectively.

Even after considering the five systems that do not have visual orbits, there is a deficit of very eccentric binaries ($e > 0.8$) relative to those that are moderately eccentric ($0.6 < e < 0.8$) at $\log P \gtrsim 2$ (see Fig. 5.21). At these wide separations, the tidal circularization timescales are orders of magnitude longer than the ages $\langle \tau \rangle \approx 5$ Gyr of solar-type binaries (Zahn 1977; Hut 1981). However, solar-type binaries initially born with $e > 0.8$ and $\log P > 2$ may tidally evolve toward smaller eccentricities $e < 0.8$ on shorter timescales. In the bottom panel of Fig. 5.22, we display the cumulative distribution of eccentricities for only those systems with $e/e_{\rm max} < 0.8$ that are not as severely affected by tidal effects. By fitting the power-law component η across $0 < e/e_{\rm max} < 0.8$, we measure $\eta = -0.4$, 0.3, 0.8, and 0.4 for the intervals $\log P = 1$ - 2, 2 - 3, 3 - 4, and 4 - 5, respectively.

We average the two methods of determining η, and report $\eta = -0.4 \pm 0.3$, 0.2 ± 0.3,

0.6 ± 0.4, and 0.3 ± 0.3 for log P = 1 - 2, 2 - 3, 3 - 4, and 4 - 5, respectively, in Table 5.7. For solar-type binaries, the power-law component η of the eccentricity distribution increases with orbital period. Nonetheless, the measured values of $\eta \approx 0.2$ - 0.6 at intermediate periods log P = 2 - 5 are mildly discrepant with a thermal eccentricity distribution ($\eta = 1$).

5.9 Comparison and Discussion

In Fig. 5.23, we display all the statistics from Tables 5.1 - 5.7 we have measured for the various binary samples after correcting for their respective selection effects. In the four panels, we plot the parameters $f_{\rm logP}$, γ (or $\gamma_{\rm largeq}$ in the cases the observations are only sensitive down to $q = q_{\rm thresh} \approx 0.3$), $\mathcal{F}_{\rm twin}$, and η as a function of orbital period. We distinguish primary mass according to color, e.g. solar-type (red), late-B (orange), mid-B (green), early-B (blue), and O-type (magenta) primaries.

We begin by discussing the frequency $f_{\rm logP}$ of companions. In the top panel of Fig. 5.23, we compare the observations to Opik's law normalized to $f_{\rm logP} = 0.1$, which is the canonical assumption in binary population synthesis (Claeys et al. 2014). At long orbital periods $\log P\,({\rm days}) > 5$, all the observations are consistent with this value, regardless of the primary mass. At short orbital periods $\log P\,({\rm days}) < 4$, however, only binaries with $M_1 \approx 5.0$ $M_\odot$ primaries follow Opik's law with $f_{\rm logP} = 0.1$. Solar-type binaries diminish rapidly toward shorter periods, reaching $f_{\rm logP} = 0.02$ at log $P = 1$ (see §5.5.7). Meanwhile, mid-B, early-B, and O-type binaries have measurements that range from $f_{\rm logP} = 0.1$ - 0.3 at log $P \approx 1$ and even larger values of $f_{\rm logP} = 0.2$ - 0.4 at log $P \approx 3$. Although the total binary fraction increases with primary mass, this is almost

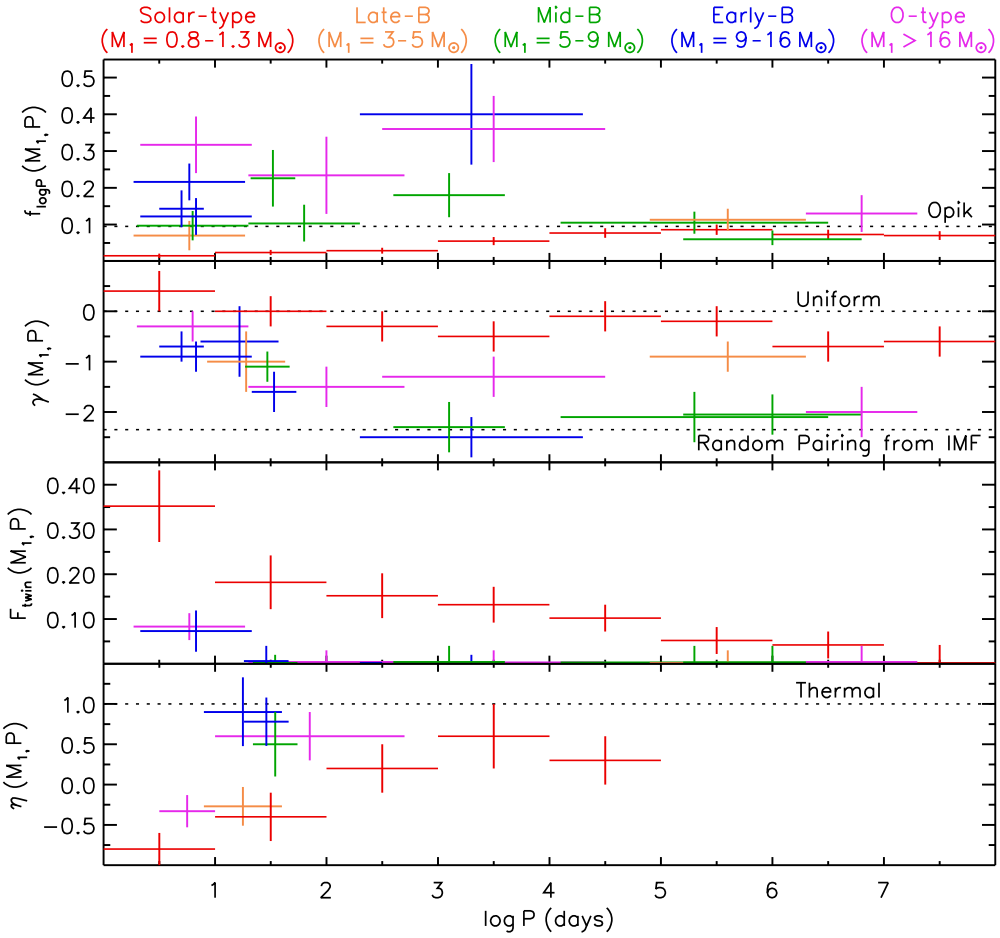

Figure 5.23: The four binary statistics as a function of logarithmic orbital period (x-axis) and primary mass (color) based on all samples investigated in this paper after correcting for selection effects in a self-consistent manner. Top panel: the frequency $f_{\rm logP}$ of companions with $q > 0.1$ per decade of orbital period. We also display Opik's law normalized to $f_{\rm logP} = 0.1$ (dotted line). Second panel: the power-law component γ of the mass-ratio probability distribution $p_q \propto q^{\gamma}$. We indicate a uniform mass-ratio distribution with $\gamma = 0.0$ (top dotted) and a mass-ratio distribution implied by random pairings drawn from a Salpeter IMF with $\gamma = -2.35$ (bottom dotted). Third panel: the excess fraction $\mathcal{F}_{\rm twin}$ of twin components with $q = 0.95$ - 1.00 relative to the underlying power-law component of the mass-ratio distribution. Bottom panel: the power-law component η of the eccentricity distribution $p_e \propto e^{\eta}$. We compare the observations to a thermal eccentricity distribution with $\eta = 1.0$ (dotted).

completely due to the increase in close companions with $\log P < 5$. This indicates that formation of wide binaries is relatively insensitive to the mass of the system, while close binaries form quite differently depending on the primary mass. We suspect the long lived primordial disks of solar-type stars, which scale to tens of AU, are the culprits for the deficit of companions at separations $a < 10$ AU. If a low-mass companion migrates inward through the disk at the time of formation, it will merge with the primary unless it can accrete sufficient mass and orbital angular momentum to stabilize into a short orbit. Only the few companions with moderate mass ratios can survive, while many of the low-mass companions, including all of the brown dwarf companions, fall into the primary. Meanwhile, more massive stars have rapid infall times and short disk photoevaporation timescales. The rapid evolution of the disk allows many more companions, including low-mass companions, to stabilize into short orbits. Moreover, more massive binaries have more orbital angular momentum, which further impedes the ability to merge.

By integrating $f_{\rm logP}$, we calculate the total multiplicity frequency $f_{\rm mult}$, i.e. the frequency of companions with $q > 0.1$ per primary (see §5.5.2). We measure $f_{\rm mult} = 0.43 \pm 0.03$ for solar-type primaries up to $f_{\rm mult} = 2.0 \pm 0.2$ for O-type primaries. Hence, O-type stars form almost exclusively in triples and/or higher order multiples. The companion frequency $f_{\rm logP} \approx 0.2$ - 0.4 to O-type stars at short orbital orbital periods is already quite high. Integrating $f_{\rm logP}$ for O-type primaries implies the multiplicity frequency $f_{\rm mult} > 1.0$ exceeds unity beyond $\log P\,({\rm days}) > 4$. The majority of companions to O-type stars with $\log P > \log P_{\rm triple} > 4$ are therefore the tertiary components in a hierarchical triples.

We next examine the parameters γ and $\mathcal{F}_{\rm twin}$ which describe the mass-ratio probability distribution. As discussed in §5.5.7, the power-law component for solar-type

binaries gradually diminishes from $\gamma = 0.4$ at $\log P = 0.5$ to $\gamma = -0.7$ at $\log P = 7$. The excess fraction of twins initially declines quickly from $\mathcal{F}_{\rm twin} = 0.35$ at $\log P = 0.5$ to $\mathcal{F}_{\rm twin} = 0.18$ at $\log P = 1.5$, and then tapers off gradually to $\mathcal{F}_{\rm twin} = 0.0$ by $\log P = 7.5$. Meanwhile, for O-type, early-B, and midB binaries, the power-law component rapidly declines from $\gamma = -0.5$ at $\log P = 0.7$ to $\gamma = -1.5$ at $\log P = 2.0$, and then continues to decline down to $\gamma = -2.0$ for $\log P > 4$. The single data point for late-B binaries of $\gamma = -0.9$ is between the solar-type value of $\gamma = -0.2$ and O - mid-B values of $\gamma \approx -2.0$. Five of the six samples of O - mid-B binaries with $\log P > 3$ have mass-ratio distribution consistent with random pairings drawn from a Salpeter IMF ($\gamma = -2.35$). Also for early-type binaries, only systems with $\log P < 1.3$ exhibit a marginal excess fraction of twins $\mathcal{F}_{\rm twin} = 0.08$. All other samples of early-type binaries show no indication for an excess fraction of twins beyond $\log P > 1.3$. We again interpret these results in the context of competitive accretion in the circumbinary disk. Both solar-type and early-type binaries show a trend of decreasing γ and $\mathcal{F}_{\rm twin}$ with increasing $\log P$. This effect is quite gradual for solar-type binaries. Solar-type stars have long lived disks than span large separation scales. Companions to solar-type stars are therefore more likely to coevolve via competitive accretion at these wider separations. However, the disks of early-type stars rapidly infall and quickly photoevaporate. Only close early-type binaries are capable of coevolving toward correlated component masses, leading to moderate value of $\gamma = -0.5$ and a measurable excess fraction of twins $\mathcal{F}_{\rm twin} = 0.08$ for $\log P < 1.3$. Meanwhile, companions to early-type stars at wider separations formed relatively independently and are weighted toward extreme mass ratios.

Finally, we examine the eccentricity distribution according to η. For both solar-type and early-type binaries, the eccentricity distribution becomes weighted toward larger

values with increasing orbital period. For O, early-B, and mid-B primaries, this transition is much more rapid, approaching a thermal distribution of $\eta = 1$ beyond $\log P > 1$. For solar-type binaries, the eccentricity distribution reaches $\eta \approx 0.5$ for $\log P \approx 4.0$, and may reach a thermal distribution at longer orbital periods. Complete samples of both solar-type and early-type binaries with visual orbits are needed to more accurately measure the eccentricity distribution at intermediate orbital periods.

In a follow-up paper, we fit analytic functions to these measured binary statistics. We use these functions to generate a realistic population of binaries, noting the differences between the typical methods and those motivated by these recent measurements. In another follow-up paper, we will use these updated initial conditions to more reliably predict the rates and properties of certain channels of binary evolution.

Chapter 6

Future Directions and Conclusions

More work needs to be done to model the observed distributions of binary star properties. In the future, I plan to fit analytic functions to the data in Chapter 5. These analytic functions will be used to generate more realistic populations of binary stars. In addition, the analytic functions will include free parameters that can be varied in order to encompass the uncertainties in the observations. In turn, these initial conditions, and their uncertainties, will be utilized to more accurately predict the rates and properties of various channels of binary evolution.

Despite not yet having these analytic functions, it is tantalizing to speculate the implications of Fig. 5.23 on the predicted rates of SNe Ia and LMXBs. Most BPS studies assume a uniform mass ratio distribution ($\gamma = 0.0$) and Opik's period distribution normalized to $f_{\log P} = 0.1$ companions per decade of orbital period (Claeys et al. 2014). Fig. 5.23 demonstrates that the primary mass, binary fraction, period distribution, and mass ratio distribution are all interrelated. In the following, we estimate the relative changes in the rates of SNe Ia and LMXBs implied by the updated multiplicity statistics.

The changes in the relative rates simply depend on the changes in the frequency of the progenitors, i.e. the density of systems with the specified values of M_1, q and P.

In the Introduction, I discussed how SD SNe Ia that explode after long delay times with red giant donors evolve from $M_1 = 6\text{-}7\,\mathrm{M}_\odot$ primaries with $M_2 = 1.0\text{-}1.3\,\mathrm{M}_\odot$ secondaries ($q = 0.15\text{-}0.20$) and initial orbital periods $P \approx 1{,}000$ days. We use our own multiplicity statistics to determine the changes in the relative frequency of binaries with these values of M_1, q, and P. According to Fig. 5.23, we are predicting an intrinsic companion frequency of $f_{\mathrm{logP}} = 0.2$ for mid-B primaries and intermediate orbital periods. Compared to Opik's law normalized to $f_{\mathrm{logP}} = 0.1$, we are estimating $\mathcal{C}_f \approx 2$ times the companion frequency. We are also finding a mass-ratio distribution weighted toward extreme values ($\gamma = -1.3\text{-}-2.3$) for intermediate orbital periods and mid-B, early-B, and O-type primaries. Compared to a uniform mass-ratio distribution with $\gamma = 0.0$, we estimate there to be $\mathcal{C}_q = 3\text{-}5$ times more companions with $q \approx 0.15\text{-}0.20$. The range in $\mathcal{C}_q = 3\text{-}5$ derives from the uncertainty in the slope of the mass ratio distribution across $q = 0.1\text{-}0.3$. Finally, BPS studies typically select primary stars from the IMF and subsequently select companions from the mass-ratio distribution. However, the IMF represents the distributions of all stars, including single stars, the primaries in binaries, and the secondaries in binaries (Kroupa et al. 2013). It is therefore more accurate to select primary stars from the primary star mass function, i.e. the distribution of single stars and the primaries in binaries. The primary star mass function is weighted toward larger masses because it does not contain the lower mass secondaries. Kroupa et al. (2013) found the normalization of the primary mass function to be $\mathcal{C}_{M1} \approx 2$ times larger than the IMF for O-type and B-type stars.

After combining these three factors, then we predict $\mathcal{C}_f\,\mathcal{C}_q\,\mathcal{C}_{M1} = 12\text{-}20$ times more

SD SNe Ia that explode in elliptical galaxies after long delay times. The kink in the theoretical delay time distribution of SD SNe Ia found by previous studies may therefore be due to incorrect initial conditions. The corrected predicted rate of SD SNe Ia at long delay times is now consistent with the observations as well as with the predictions of the DD scenario. I am not claiming that SNe Ia derive from SD systems. I am simply stating that, given the uncertainties in the binary physical processes and by incorporating updated initial conditions of binary stars, we cannot use the SN Ia delay time distribution to test progenitor models.

Similarly, we expect more LMXBs than originally predicted. These systems derive from even more massive early-B and O-type primaries with companions at $P \approx 1{,}000$ days (see Introduction). According to the top panel of Fig. 5.23, the companion frequency is $\mathcal{C}_f \approx 3$ - 4 times higher than that predicted by Opik's law. LMXBs also derive from even more extreme mass ratios $q < 0.15$. There may be even more of these systems, but we adopt the same correction factor $\mathcal{C}_q = 3$ - 5 from above due to the uncertainty in the slope of the mass-ratio distribution below $q < 0.3$. We therefore expect $\mathcal{C}_f \mathcal{C}_q \mathcal{C}_{M1} = 18$ - 40 times more LMXBs than typically predicted by BPS. Kiel & Hurley (2006) found that by implementing canonical input assumptions into BPS, the predicted rates of LMXBs are one to two orders of magnitudes smaller than the rates implied by observations. However, they minimized the discrepancy by adjusting the descriptions for the physical process, e.g, changing the supernova kick velocity distribution, making the common envelope efficiency parameter more efficient, etc. In contrast, we find the discrepancy between BPS and observations may derive completely from improper initial conditions. Indeed, I look forward to this summer / fall so I can perform more robust calculations to see if these initial estimates hold up.

In summary, I hope I have convinced you that eclipsing binaries are wonderful astrophysical tools. We can use eclipsing binaries to explore parts of the binary parameter space that were previously unattainable, namely massive binaries with low metallicities, extreme mass ratios, and intermediate orbital periods. By knowing the distances to EBs in the LMC, we can measure their physical properties, e.g. masses M_1 and M_2, ages τ, line-of-sight dust extinctions A_I, etc., based solely on the photometric light curves. By using EBs at age indicators, we have revealed the long-term evolution of H II regions, tidal evolution in massive binaries, and evolution of dust content in young stellar populations. We combined our EB measurements with other samples of binaries to determine a comprehensive picture of binary statistics. These binary distributions provide invaluable insight into the formation of binary stars as well as robust initial conditions for binary population synthesis. In the future, LSST will find millions of eclipsing binaries (Prša et al. 2011a), and GAIA will measure the distances to a larger fraction of them. With our automated pipeline, we will collect a treasure trove of information on the physical properties of these systems. I am no longer worried as I anticipate the future. I hope you too will learn to stop worrying and love eclipsing binaries.

References

Abt, H. A. 1983, ARA&A, 21, 343

—. 2005, ApJ, 629, 507

—. 2006, ApJ, 651, 1151

—. 2008, AJ, 135, 722

Abt, H. A., & Corbally, C. J. 2000, ApJ, 541, 841

Abt, H. A., Gomez, A. E., & Levy, S. G. 1990, ApJS, 74, 551

Abt, H. A., Levato, H., & Grosso, M. 2002, ApJ, 573, 359

Alecian, E., Goupil, M.-J., Lebreton, Y., Dupret, M.-A., & Catala, C. 2007, A&A, 465, 241

Alonso-Albi, T., Fuente, A., Bachiller, R., Neri, R., Planesas, P., Testi, L., Berné, O., & Joblin, C. 2009, A&A, 497, 117

Ambartsumian, V. A. 1937, Astron. Zh., 14, 207

Armitage, P. J., & Bonnell, I. A. 2002, MNRAS, 330, L11

Asplund, M., Grevesse, N., Sauval, A. J., & Scott, P. 2009, ARA&A, 47, 481

Badenes, C., & Maoz, D. 2012, ApJ, 749, L11

Bally, J., & Zinnecker, H. 2005, AJ, 129, 2281

Barlow, B. N., et al. 2013, MNRAS, 430, 22

Bate, M. R. 2012, MNRAS, 419, 3115

Bate, M. R., & Bonnell, I. A. 1997, MNRAS, 285, 33

Bate, M. R., Bonnell, I. A., & Bromm, V. 2002, MNRAS, 336, 705

Belczynski, K., Kalogera, V., Rasio, F. A., Taam, R. E., Zezas, A., Bulik, T., Maccarone, T. J., & Ivanova, N. 2008, ApJS, 174, 223

Bellazzini, M., Pasquali, A., Federici, L., Ferraro, F. R., & Pecci, F. F. 1995, ApJ, 439, 687

Berger, E. 2009, ApJ, 690, 231

Bertelli, G., Girardi, L., Marigo, P., & Nasi, E. 2008, A&A, 484, 815

Bertelli, G., Nasi, E., Girardi, L., & Marigo, P. 2009, A&A, 508, 355

Bica, E. L. D., Schmitt, H. R., Dutra, C. M., & Oliveira, H. L. 1999, AJ, 117, 238

Boffin, H. M. J., & Jorissen, A. 1988, A&A, 205, 155

Bond, H. E. 2000, in Astronomical Society of the Pacific Conference Series, Vol. 199, Asymmetrical Planetary Nebulae II: From Origins to Microstructures, ed. J. H. Kastner, N. Soker, & S. Rappaport, 115

Bonnell, I., & Bastien, P. 1992, ApJ, 401, 654

Bonnell, I. A., & Bate, M. R. 2005, MNRAS, 362, 915

Bouy, H., Brandner, W., Martín, E. L., Delfosse, X., Allard, F., & Basri, G. 2003, AJ, 126, 1526

Boyajian, T. S., et al. 2007, ApJ, 664, 1121

Branch, D. 1976, ApJ, 210, 392

Butkevich, A. G., Berdyugin, A. V., & Teerikorpi, P. 2005, MNRAS, 362, 321

Cantiello, M., & Braithwaite, J. 2011, A&A, 534, A140

Cao, Y., et al. 2015, Nature, 521, 328

Cardelli, J. A., Clayton, G. C., & Mathis, J. S. 1989, ApJ, 345, 245

Casey, B. W., Mathieu, R. D., Vaz, L. P. R., Andersen, J., & Suntzeff, N. B. 1998, AJ, 115, 1617

Chini, R., Hoffmeister, V. H., Nasseri, A., Stahl, O., & Zinnecker, H. 2012, MNRAS, 424, 1925

Chomiuk, L., et al. 2012, ApJ, 750, 164

Chu, Y.-H., & Kennicutt, Jr., R. C. 1994, Ap&SS, 216, 253

Cichowolski, S., Romero, G. A., Ortega, M. E., Cappa, C. E., & Vasquez, J. 2009, MNRAS, 394, 900

Claeys, J. S. W., Pols, O. R., Izzard, R. G., Vink, J., & Verbunt, F. W. M. 2014, A&A, 563, A83

Claret, A. 2001, MNRAS, 327, 989

Clarke, C. J. 1996, MNRAS, 283, 353

Connelley, M. S., Reipurth, B., & Tokunaga, A. T. 2008, AJ, 135, 2526

Cooper, M. C., Newman, J. A., & Yan, R. 2009, ApJ, 704, 687

Cox, A. N. 2000, Allen's astrophysical quantities (-)

Crowther, P. A. 2013, MNRAS, 428, 1927

Daflon, S., & Cunha, K. 2004, ApJ, 617, 1115

Davis, P. J., Kolb, U., & Willems, B. 2010, MNRAS, 403, 179

De Becker, M., Rauw, G., Manfroid, J., & Eenens, P. 2006, A&A, 456, 1121

de la Fuente Marcos, R., & de la Fuente Marcos, C. 2004, "New Astronomy", 9, 475

de Marchi, F., et al. 2007, A&A, 471, 515

De Rosa, R. J., et al. 2011, MNRAS, 415, 854

de Wit, W. J., Testi, L., Palla, F., Vanzi, L., & Zinnecker, H. 2004, A&A, 425, 937

Devor, J. 2005, ApJ, 628, 411

Devor, J., & Charbonneau, D. 2006, Ap&SS, 304, 351

Devor, J., Charbonneau, D., O'Donovan, F. T., Mandushev, G., & Torres, G. 2008, AJ, 135, 850

di Criscienzo, M., Ventura, P., & D'Antona, F. 2009, A&A, 496, 223

Di Stefano, R. 2010, ApJ, 712, 728

Di Stefano, R., Voss, R., & Claeys, J. S. W. 2011, ApJ, 738, L1

Dotter, A., Chaboyer, B., Jevremović, D., Kostov, V., Baron, E., & Ferguson, J. W. 2008, ApJS, 178, 89

Dray, L. M. 2006, MNRAS, 370, 2079

Duchêne, G., Bontemps, S., Bouvier, J., André, P., Djupvik, A. A., & Ghez, A. M. 2007, A&A, 476, 229

Duchêne, G., & Kraus, A. 2013, ARA&A, 51, 269

Duchêne, G., Simon, T., Eislöffel, J., & Bouvier, J. 2001, A&A, 379, 147

Duquennoy, A., & Mayor, M. 1991, A&A, 248, 485

Eggleton, P. P. 1983, ApJ, 268, 368

Eggleton, P. P., & Kiseleva-Eggleton, L. 2002, ApJ, 575, 461

Ekström, S., Meynet, G., Chiappini, C., Hirschi, R., & Maeder, A. 2008a, A&A, 489, 685

Ekström, S., Meynet, G., Maeder, A., & Barblan, F. 2008b, A&A, 478, 467

Evans, C. J., Lennon, D. J., Smartt, S. J., & Trundle, C. 2006, A&A, 456, 623

Evans, N. R., et al. 2011, ApJS, 194, 13

Farinella, P., & Paolicchi, P. 1978, Ap&SS, 54, 389

Fischer, D. A., & Marcy, G. W. 1992, ApJ, 396, 178

Fitzpatrick, E. L. 1999, PASP, 111, 63

Fontaine, G., Brassard, P., & Bergeron, P. 2001, PASP, 113, 409

Fragos, T., & McClintock, J. E. 2015, ApJ, 800, 17

Frederiksen, T. F., Hjorth, J., Maund, J. R., Rodney, S. A., Riess, A. G., Dahlen, T., & Mobasher, B. 2012, ApJ, 760, 125

Fryer, C. L., Woosley, S. E., & Hartmann, D. H. 1999, ApJ, 526, 152

Fryer, C. L., et al. 2007, PASP, 119, 1211

Gao, S., Liu, C., Zhang, X., Justham, S., Deng, L., & Yang, M. 2014, ApJ, 788, L37

Garmany, C. D., Conti, P. S., & Massey, P. 1980, ApJ, 242, 1063

Geller, A. M., & Mathieu, R. D. 2012, AJ, 144, 54

Georgy, C., Ekström, S., Granada, A., Meynet, G., Mowlavi, N., Eggenberger, P., & Maeder, A. 2013, A&A, 553, A24

Graczyk, D., et al. 2011, Acta Astron., 61, 103

Grebel, E. K., & Chu, Y.-H. 2000, AJ, 119, 787

Grether, D., & Lineweaver, C. H. 2006, ApJ, 640, 1051

Grocholski, A. J., Cole, A. A., Sarajedini, A., Geisler, D., & Smith, V. V. 2006, AJ, 132, 1630

Gullikson, K., & Dodson-Robinson, S. 2013, AJ, 145, 3

Gummersbach, C. A., Kaufer, A., Schaefer, D. R., Szeifert, T., & Wolf, B. 1998, A&A, 338, 881

Halbwachs, J. L. 1981, A&A, 102, 191

Halbwachs, J. L., Arenou, F., Mayor, M., Udry, S., & Queloz, D. 2000, A&A, 355, 581

Halbwachs, J. L., Mayor, M., Udry, S., & Arenou, F. 2003, A&A, 397, 159

Hall, D. S., & Garrison, Jr., L. M. 1969, PASP, 81, 771

Harrington, R. S., & Miranian, M. 1977, PASP, 89, 400

Harris, J., & Zaritsky, D. 2009, AJ, 138, 1243

Hartmann, L. 2009, Accretion Processes in Star Formation: Second Edition (Cambridge University Press)

Haschke, R., Grebel, E. K., & Duffau, S. 2011, AJ, 141, 158

—. 2012, AJ, 144, 107

Heggie, D. C. 1975, MNRAS, 173, 729

Hettinger, T., Badenes, C., Strader, J., Bickerton, S. J., & Beers, T. C. 2015, ApJ, 806, L2

Hillenbrand, L. A., & White, R. J. 2004, ApJ, 604, 741

Hinkley, S., et al. 2015, ApJ, 806, L9

Holberg, J. B., Oswalt, T. D., Sion, E. M., Barstow, M. A., & Burleigh, M. R. 2013, MNRAS, 435, 2077

Howarth, I. D. 2013, A&A, 555, A141

Huang, S. S., & Struve, O. 1956, AJ, 61, 300

Hubrig, S., Le Mignant, D., North, P., & Krautter, J. 2001, A&A, 372, 152

Hurley, J. R., Tout, C. A., & Pols, O. R. 2002, MNRAS, 329, 897

Hut, P. 1981, A&A, 99, 126

Iben, Jr., I., & Tutukov, A. V. 1987, ApJ, 313, 727

Imara, N., & Blitz, L. 2007, ApJ, 662, 969

Indu, G., & Subramaniam, A. 2011, A&A, 535, A115

Ivanova, N. 2006, ApJ, 636, 979

Ivanova, N., & Taam, R. E. 2004, ApJ, 601, 1058

Izzard, R. G., Ramirez-Ruiz, E., & Tout, C. A. 2004, MNRAS, 348, 1215

Jorissen, A., Van Eck, S., Mayor, M., & Udry, S. 1998, A&A, 332, 877

Kallrath, J., & Milone, E. F. 2009, Eclipsing Binary Stars: Modeling and Analysis

Kalogera, V., & Webbink, R. F. 1998, ApJ, 493, 351

Karakas, A. I., Tout, C. A., & Lattanzio, J. C. 2000, MNRAS, 316, 689

Keller, S. C., & Wood, P. R. 2006, ApJ, 642, 834

Kiel, P. D., & Hurley, J. R. 2006, MNRAS, 369, 1152

Kim, D.-W., Fabbiano, G., Ivanova, N., Fragos, T., Jordán, A., Sivakoff, G. R., & Voss, R. 2013, ApJ, 764, 98

King, R. R., Goodwin, S. P., Parker, R. J., & Patience, J. 2012, MNRAS, 427, 2636

Kiseleva, L. G., Eggleton, P. P., & Mikkola, S. 1998, MNRAS, 300, 292

Kistler, M. D., Stanek, K. Z., Kochanek, C. S., Prieto, J. L., & Thompson, T. A. 2011, ArXiv e-prints

Klagyivik, P., et al. 2013, ApJ, 773, 54

Kobayashi, C., Tsujimoto, T., Nomoto, K., Hachisu, I., & Kato, M. 1998, ApJ, 503, L155

Kobulnicky, H. A., & Fryer, C. L. 2007, ApJ, 670, 747

Kobulnicky, H. A., et al. 2014, ArXiv e-prints

Köhler, R., Petr-Gotzens, M. G., McCaughrean, M. J., Bouvier, J., Duchêne, G., Quirrenbach, A., & Zinnecker, H. 2006, A&A, 458, 461

Korn, A. J., Becker, S. R., Gummersbach, C. A., & Wolf, B. 2000, A&A, 353, 655

Kouwenhoven, M. B. N., Brown, A. G. A., Goodwin, S. P., Portegies Zwart, S. F., & Kaper, L. 2009, A&A, 493, 979

Kouwenhoven, M. B. N., Brown, A. G. A., Portegies Zwart, S. F., & Kaper, L. 2007, A&A, 474, 77

Kratter, K. M., & Matzner, C. D. 2006, MNRAS, 373, 1563

Kraus, A. L., Ireland, M. J., Martinache, F., & Hillenbrand, L. A. 2011, ApJ, 731, 8

Kroupa, P. 1995, MNRAS, 277, 1507

Kroupa, P., Weidner, C., Pflamm-Altenburg, J., Thies, I., Dabringhausen, J., Marks, M., & Maschberger, T. 2013, The Stellar and Sub-Stellar Initial Mass Function of Simple and Composite Populations (-), 1–115

Kuznetsova, N., et al. 2008, ApJ, 673, 981

Lee, J. W., Kim, S.-L., Kim, C.-H., Koch, R. H., Lee, C.-U., Kim, H.-I., & Park, J.-H. 2009, AJ, 137, 3181

Lefèvre, L., Marchenko, S. V., Moffat, A. F. J., & Acker, A. 2009, A&A, 507, 1141

Levato, H., & Grosso, M. 2013, PASP, 125, 1191

Levato, H., Malaroda, S., Morrell, N., & Solivella, G. 1987, ApJS, 64, 487

Lodders, K. 2003, ApJ, 591, 1220

Lorimer, D. R. 2008, Living Reviews in Relativity, 11, 8

Luck, R. E., Moffett, T. J., Barnes, III, T. G., & Gieren, W. P. 1998, AJ, 115, 605

Lucy, L. B. 2006, A&A, 457, 629

Lyubimkov, L. S., Rostopchin, S. I., Rachkovskaya, T. M., Poklad, D. B., & Lambert, D. L. 2005, MNRAS, 358, 193

MacConnell, D. J., Frye, R. L., & Upgren, A. R. 1972, AJ, 77, 384

Machida, M. N. 2008, ApJ, 682, L1

Mahy, L., Gosset, E., Sana, H., Damerdji, Y., De Becker, M., Rauw, G., & Nitschelm, C. 2012, A&A, 540, A97

Maoz, D., Sharon, K., & Gal-Yam, A. 2010, ApJ, 722, 1879

Margutti, R., et al. 2012, ApJ, 751, 134

Markwardt, C. B. 2009, in Astronomical Society of the Pacific Conference Series, Vol. 411, Astronomical Data Analysis Software and Systems XVIII, ed. D. A. Bohlender, D. Durand, & P. Dowler, 251

Martins, F., Schaerer, D., & Hillier, D. J. 2005, A&A, 436, 1049

Mason, B. D., Gies, D. R., Hartkopf, W. I., Bagnuolo, Jr., W. G., ten Brummelaar, T., & McAlister, H. A. 1998, AJ, 115, 821

Mason, B. D., Hartkopf, W. I., Gies, D. R., Henry, T. J., & Helsel, J. W. 2009, AJ, 137, 3358

Massey, P., & Hunter, D. A. 1998, ApJ, 493, 180

Mathieu, R. D. 1994, ARA&A, 32, 465

Mazeh, T., & Goldberg, D. 1992, ApJ, 394, 592

Mazeh, T., Goldberg, D., Duquennoy, A., & Mayor, M. 1992a, ApJ, 401, 265

—. 1992b, ApJ, 401, 265

Mazeh, T., Tamuz, O., & North, P. 2006, MNRAS, 367, 1531

McCully, C., et al. 2014, Nature, 512, 54

McDonald, J. M., & Clarke, C. J. 1995, MNRAS, 275, 671

McGowan, K. E., et al. 2008, MNRAS, 383, 330

Meibom, S., & Mathieu, R. D. 2005, ApJ, 620, 970

Miszalski, B., Acker, A., Moffat, A. F. J., Parker, Q. A., & Udalski, A. 2009, A&A, 496, 813

Moe, M., & Di Stefano, R. 2013, ApJ, 778, 95

—. 2015a, ApJ, 801, 113

—. 2015b, ArXiv e-prints

Moeckel, N., & Bally, J. 2007, ApJ, 656, 275

Morales-Calderón, M., et al. 2012, ApJ, 753, 149

Nakar, E. 2007, Phys. Rep., 442, 166

Naoz, S., & Fabrycky, D. C. 2014, ArXiv e-prints

Nasseri, A., et al. 2014, A&A, 568, A94

Nelemans, G., Toonen, S., & Bours, M. 2013, in IAU Symposium, Vol. 281, IAU Symposium, ed. R. Di Stefano, M. Orio, & M. Moe, 225–231

Ngeow, C.-C., & Kanbur, S. M. 2005, MNRAS, 360, 1033

Nomoto, K., Saio, H., Kato, M., & Hachisu, I. 2007, ApJ, 663, 1269

Nordstrom, B., & Johansen, K. T. 1994, A&A, 282, 787

O'Dell, C. R., Henney, W. J., Abel, N. P., Ferland, G. J., & Arthur, S. J. 2009, AJ, 137, 367

Olling, R. P., et al. 2015, Nature, 521, 332

Öpik, E. 1923, Publications of the Tartu Astrofizica Observatory, 35, 6

—. 1924, Publications of the Tartu Astrofizica Observatory, 25, 1

Paczyński, B. 1971, ARA&A, 9, 183

Pakmor, R., Kromer, M., Taubenberger, S., Sim, S. A., Röpke, F. K., & Hillebrandt, W. 2012, ApJ, 747, L10

Palla, F., & Stahler, S. W. 1990, ApJ, 360, L47

—. 2001, ApJ, 553, 299

Panuzzo, P., Granato, G. L., Buat, V., Inoue, A. K., Silva, L., Iglesias-Páramo, J., & Bressan, A. 2007, MNRAS, 375, 640

Parker, R. J., & Goodwin, S. P. 2007, MNRAS, 380, 1271

Patat, F., et al. 2007, Science, 317, 924

Patience, J., Ghez, A. M., Reid, I. N., & Matthews, K. 2002, AJ, 123, 1570

Pawlak, M., et al. 2013, Acta Astron., 63, 323

Pecaut, M. J., & Mamajek, E. E. 2013, ApJS, 208, 9

Peimbert, A., & Peimbert, M. 2010, ApJ, 724, 791

Perryman, M. A. C., et al. 1997, A&A, 323, L49

Peter, D., Feldt, M., Henning, T., & Hormuth, F. 2012, A&A, 538, A74

Phillips, M. M. 1993, ApJ, 413, L105

Phinney, E. S., & Kulkarni, S. R. 1994, ARA&A, 32, 591

Piatti, A. E., & Geisler, D. 2013, AJ, 145, 17

Pietrukowicz, P., et al. 2013, Acta Astron., 63, 115

Pietrzyński, G., et al. 2013, Nature, 495, 76

Pinsonneault, M. H., & Stanek, K. Z. 2006, ApJ, 639, L67

Podsiadlowski, P. 1991, Nature, 350, 136

Podsiadlowski, P., Rappaport, S., & Pfahl, E. D. 2002, ApJ, 565, 1107

Popper, D. M. 1987, ApJ, 313, L81

Pourbaix, D., et al. 2004, A&A, 424, 727

Preibisch, T., Balega, Y., Hofmann, K.-H., Weigelt, G., & Zinnecker, H. 1999, New Astronomy, 4, 531

Press, W. H., & Teukolsky, S. A. 1977, ApJ, 213, 183

Pringle, J. E. 1989, MNRAS, 239, 361

Prša, A., Guinan, E. F., Devinney, E. J., DeGeorge, M., Bradstreet, D. H., Giammarco, J. M., Alcock, C. R., & Engle, S. G. 2008, ApJ, 687, 542

Prša, A., Pepper, J., & Stassun, K. G. 2011a, AJ, 142, 52

Prša, A., & Zwitter, T. 2005, ApJ, 628, 426

Prša, A., et al. 2011b, AJ, 141, 83

Raghavan, D., et al. 2010, ApJS, 190, 1

Rappaport, S., Deck, K., Levine, A., Borkovits, T., Carter, J., El Mellah, I., Sanchis-Ojeda, R., & Kalomeni, B. 2013, ApJ, 768, 33

Rauw, G., Sana, H., Spano, M., Gosset, E., Mahy, L., De Becker, M., & Eenens, P. 2012, A&A, 542, A95

Reid, W. A., & Parker, Q. A. 2010, MNRAS, 405, 1349

Remage Evans, N., Bond, H. E., Schaefer, G. H., Mason, B. D., Karovska, M., & Tingle, E. 2013, AJ, 146, 93

Remage Evans, N., et al. 2015, ArXiv e-prints

Rest, A., et al. 2008, ApJ, 680, 1137

Ritter, H., Zhang, Z.-Y., & Kolb, U. 2000, A&A, 360, 969

Rizzuto, A. C., et al. 2013, MNRAS, 436, 1694

Rolleston, W. R. J., Trundle, C., & Dufton, P. L. 2002, A&A, 396, 53

Romaniello, M., Primas, F., Mottini, M., Groenewegen, M., Bono, G., & François, P. 2005, A&A, 429, L37

Ruiter, A. J., Belczynski, K., & Fryer, C. 2009, ApJ, 699, 2026

Ruiter, A. J., Belczynski, K., Sim, S. A., Hillebrandt, W., Fryer, C. L., Fink, M., & Kromer, M. 2011, MNRAS, 417, 408

Sana, H., et al. 2012, Science, 337, 444

—. 2013, A&A, 550, A107

—. 2014, ApJS, 215, 15

Schaefer, B. E., & Pagnotta, A. 2012, Nature, 481, 164

Schlegel, D. J., Finkbeiner, D. P., & Davis, M. 1998, ApJ, 500, 525

Schmidt, B. P., et al. 1998, ApJ, 507, 46

Schneider, R., Ferrari, V., Matarrese, S., & Portegies Zwart, S. F. 2001, MNRAS, 324, 797

Shatsky, N., & Tokovinin, A. 2002, A&A, 382, 92

Shen, K. J., Guillochon, J., & Foley, R. J. 2013, ApJ, 770, L35

Siess, L., Dufour, E., & Forestini, M. 2000, A&A, 358, 593

Silva, L., et al. 2011, MNRAS, 410, 2043

Smith, R. C., Points, S. D., Chu, Y.-H., Winkler, P. F., Aguilera, C., Leiton, R., & MCELS Team. 2005, in Bulletin of the American Astronomical Society, Vol. 37, American Astronomical Society Meeting Abstracts, 1200

Söderhjelm, S., & Dischler, J. 2005, A&A, 442, 1003

Stassun, K. G., Mathieu, R. D., Cargile, P. A., Aarnio, A. N., Stempels, E., & Geller, A. 2008, Nature, 453, 1079

Stelzer, B., Huélamo, N., Hubrig, S., Zinnecker, H., & Micela, G. 2003, A&A, 407, 1067

Sullivan, M., et al. 2010, MNRAS, 406, 782

Taam, R. E., & Sandquist, E. L. 2000, ARA&A, 38, 113

Teerikorpi, P. 1997, ARA&A, 35, 101

Tognelli, E., Prada Moroni, P. G., & Degl'Innocenti, S. 2011, A&A, 533, A109

Tohline, J. E. 2002, ARA&A, 40, 349

Tokovinin, A., Thomas, S., Sterzik, M., & Udry, S. 2006, A&A, 450, 681

Tokovinin, A. A. 2000, A&A, 360, 997

Tomita, A., Ohta, K., Nakanishi, K., Takeuchi, T. T., & Saito, M. 1998, AJ, 116, 131

Torres, G., Andersen, J., & Giménez, A. 2010, A&A Rev., 18, 67

Tout, C. A. 1991, MNRAS, 250, 701

Turner, D. G. 1996, JRASC, 90, 82

Turner, J. A., Chapman, S. J., Bhattal, A. S., Disney, M. J., Pongracic, H., & Whitworth, A. P. 1995, MNRAS, 277, 705

Turner, N. H., ten Brummelaar, T. A., Roberts, L. C., Mason, B. D., Hartkopf, W. I., & Gies, D. R. 2008, AJ, 136, 554

Tutukov, A., & Yungelson, L. 1996, MNRAS, 280, 1035

Udalski, A., Szymanski, M., Kubiak, M., Pietrzynski, G., Soszynski, I., Wozniak, P., & Zebrun, K. 2000, Acta Astron., 50, 307

Udalski, A., Szymanski, M., Kubiak, M., Pietrzynski, G., Wozniak, P., & Zebrun, K. 1998, Acta Astron., 48, 147

Udalski, A., et al. 2008, Acta Astron., 58, 89

van den Heuvel, E. P. J. 1984, Journal of Astrophysics and Astronomy, 5, 209

van Rensbergen, W., de Greve, J. P., Mennekens, N., Jansen, K., & de Loore, C. 2011, A&A, 528, A16

Verbunt, F. 1993, ARA&A, 31, 93

Wagner-Kaiser, R., & Sarajedini, A. 2013, MNRAS

Wang, B., & Han, Z. 2012, New Astronomy Reviews, 56, 122

Webbink, R. F. 1984, ApJ, 277, 355

Weidemann, V. 2000, A&A, 363, 647

Whelan, J., & Iben, Jr., I. 1973, ApJ, 186, 1007

Wilson, R. E. 1972, Ap&SS, 19, 165

Wilson, R. E., & Devinney, E. J. 1971, ApJ, 166, 605

Windemuth, D., Herbst, W., Tingle, E., Fuechsl, R., Kilgard, R., Pinette, M., Templeton, M., & Henden, A. 2013, ApJ, 768, 67

Wolff, S. C. 1978, ApJ, 222, 556

Woosley, S. E., & Kasen, D. 2011, ApJ, 734, 38

Wyrzykowski, L., et al. 2003, Acta Astron., 53, 1

—. 2004, Acta Astron., 54, 1

Yoon, S.-C., Woosley, S. E., & Langer, N. 2010, ApJ, 725, 940

Yorke, H. W. 1986, ARA&A, 24, 49

Zahn, J.-P. 1975, A&A, 41, 329

—. 1977, A&A, 57, 383

—. 1989, A&A, 220, 112

Zahn, J.-P., & Bouchet, L. 1989a, A&A, 223, 112

—. 1989b, A&A, 223, 112

Zaritsky, D. 1999, AJ, 118, 2824

Zaritsky, D., Harris, J., Thompson, I. B., & Grebel, E. K. 2004, AJ, 128, 1606

Zaritsky, D., Harris, J., Thompson, I. B., Grebel, E. K., & Massey, P. 2002, AJ, 123, 855